UNIVERSITY OF SOUTHAMPTON

FACULTY OF ENGINEERING, SCIENCE & MATHEMATICS

Institute of Sound and Vibration Research

RANDOM VIBRATION RESPONSE STATISTICS FOR FATIGUE ANALYSIS OF NONLINEAR STRUCTURES

by

Karl Albert Sweitzer

Thesis for the degree of Doctor of Philosophy

March 2006

UNIVERSITY OF SOUTHAMPTON

ABSTRACT

FACULTY OF ENGINEERING, SCIENCE & MATHEMATICS

Institute of Sound and Vibration Research

Doctor of Philosophy

RANDOM VIBRATION RESPONSE STATISTICS FOR FATIGUE ANALYSIS OF NONLINEAR STRUCTURES

by Karl Albert Sweitzer

Statistical analysis methods are developed for determining fatigue time to failure for nonlinear structures when subjected to random loading. The change in the response, as structures progress from a linear regime to a large amplitude nonlinear regime, is studied in both the time and frequency domains. The analyses in the two domains are shown to compliment each other, allowing keen understanding of the physical fundamentals of the problem.

Analysis of experimental random vibration data, obtained at Wright Patterson Air Force Base, is included to illustrate the challenge for a real, multi-mode, nonlinear structure. The reverse path frequency response identification method was used with the displacement and strain response to estimate nonlinear frequency response functions. The coherence functions of these estimates provided insight into nonlinear models of the system. Time domain analysis of the nonlinear data showed how the displacement and strain departed from a normal distribution. Inverse distribution function methods were used to develop functions that related the linear to the nonlinear response of the structure. These linear to the nonlinear functions were subsequently used to estimate probability density functions that agreed well with measured histograms.

Numerical simulations of a nonlinear single degree of freedom system were produced to study other aspects of the large deflection structural response. Very large sample size data sets of displacement, velocity, acceleration and stress were used to quantify the rate of convergence of several random response statistics. The inverse distribution function method was also applied to the simulation results to estimate normal and peak linear to nonlinear functions. These functions were shown to be useful for probability density function estimates and for estimating rates of response zero crossings.

Fatigue analysis was performed on the experimental and simulated linear and nonlinear data. The time to failure estimates for the nonlinear results was shown to increase dramatically when compared to the linear results. The nonlinear stresses have significant positive mean values due to membrane effects, that when used with fatigue equations that account for mean stresses, show reductions in time to failure. Further studies of the nonlinear increase in the frequency of stress response are included in the fatigue analysis.

TABLE OF CONTENTS

ACKNOWLEDGEMENTS

I would like to express my utmost gratitude to my supervisor Dr Neil Ferguson for all of his professional assistance and personal hospitality while I was a student at the ISVR. Neil responded to my inquiries throughout this period with outstanding recommendations and advice in an extremely timely fashion. Thanks also to my review committee, Professor Brian Mace and Dr Tim Waters, for their comments and suggestions.

I am truly thankful that Dr Neil Bishop and Dr Stuart Kerr recommended that I perform graduate research at the ISVR based on research that we started as part of an US Air Force SBIR contract. Financial assistance from my employer Eastman Kodak Company (and later ITT Industries, Inc.) made this an outstanding opportunity.

Thanks to S. Michael Spottswood and Joseph Hollkamp, of the Structural Mechanics Branch at Wright Patterson Air Force Base, for the experimental data they provided.

Special thanks to Ronald Lambert who was a friend and professional mentor to me in my early career. I would like to express appreciation for the technical assistance that Allan Piersol and David Smallwood have provided over the many years I have been acquainted with them. I would also like to express gratitude to Norm Dowling, Amanda and Scott Hanford, Cindy Lewis, William McKinley, Marc Mignolet, Ronald Miles, Adam Przekop, Steve Rizzi, Shahram Sarkani, and Randy VanVranken who have assisted me over the course of this research. I am also grateful to Sharon Ryan for her excellent and timely editorial and word processing assistance.

Last but not least, I must acknowledge my family who has supported me throughout this demanding period in my life. My wife, Melissa, and daughters Alice and Elizabeth have cheered me on from the start. My father, Maurice, has always encouraged me in the pursuit of higher education. My sister, Rhoda and brother-in-law Larry Danforth, have also supported me while their own daughter and son-in-law have also been pursuing PhD degrees in engineering. My father-in-law Dr. Earl Gale, who also earned his PhD in engineering while working full time, and my mother-in-law, Jane Gale, a retired schoolteacher, were also inspirational.

LIST OF SYMBOLS

English symbols

Upper case

A cross-sectional area; m^2

sinusoidal fatigue strength coefficient at one cycle

state space system state matrix

B bandwidth; Hz

state space input matrix

C narrow-band random fatigue strength coefficient at one cycle

D damage ratio; $D = 1$ failure of median sample

E elastic (Young's) modulus; MPa

$E[\ ]$ expected value

$F(\ )$ distribution function (cumulative distribution function (CDF))

$F^{-1}(\ )$ inverse distribution function (IDF)

F force; N

expected frequency

$\mathrm{F}(\ ), \mathrm{F}^{-1}(\ )$ Fourier transform, inverse Fourier transform

$G, G(\ )$ one-sided auto spectrum (power spectral density (PSD)); normally $unit^2/Hz$

$H, H(f), H(\omega)$ frequency response function

$H(s)$ transfer function (in Laplace domain)

I second moment of area; m^4

K stress concentration factor

chi-squared degrees of freedom

$L, L(\ )$ frequency response function with uncorrelated inputs

N number of data points

P probability of occurrence

R stress ratio

S tensile force; N

$S(\ )$ two-sided auto spectrum

T time period; s

$U(\ )$ frequency domain variable

W histogram or PDF bin width

$X(\ )$ frequency domain variable

$Y(\ )$ frequency domain variable

Lower case

a acceleration; m/s^2

b bias
fatigue strength exponent (slope of stress – life curve)

c viscous damping constant; N s/m

erf, erf^{-1}, erfc error function, inverse error function, complementary error function

$\exp(x)$ e^x

f frequency; Hz

g acceleration due to gravity; approximately 9.806 m/s^2 at sea level

$g(\ )$ function, typically on the right hand side of the equal sign

$h(\ )$ function, typically on the left hand side of the equal sign

h height (thickness); mm

k instrument gain
stiffness; N/m

l length; mm

ln natural logarithm

m mass; kg

m_n spectral moment; $unit/s^n$

n number of cycles

$p(\,)$ probability density function (PDF)

s complex frequency

t time; s

v velocity; m/s

x linear displacement; m
general variable

y nonlinear displacement; m

z standardized variable; $(w\text{-}\mu_w)/\sigma_w$
state vector

Greek symbols

Upper case

Δ incremental change in value

$\Phi[\,x\,]$ rate of x; Hz

Γ gamma function

Lower case

α modal force; m/s^2
nonlinear acceleration; m/s^2
Duffing equation linear response term
hypothesis acceptance value

β Duffing equation squared response term

χ^2 chi-squared statistic

δ logarithmic decrement

ε error
strain; m/m

γ Walker equation fitting exponent
Duffing equation cubic response term

γ^2 coherence function

ι skew

φ transient response decay factor

κ kurtosis

μ mean value
van der Pol nonlinear damping term

μ_n spectral moment; unit/s^n

ρ probability of occurrence
density; kg/m^3

θ angle

σ standard deviation

σ^2 variance

σ stress; MPa

ϖ ratio of zero crossings to peaks

ω frequency; rad/s

ψ mean squared value

ζ viscous damping ratio

Subscripts

$_a$ amplitude

$_{alt}$ alternating, fully reversed stress

$_{a0}$ amplitude, mean

$_b$ bias (error)

$_{bend}$ bending

block	data block (record, or file)
bot	bottom surface value
cube	response cubed
dif	difference
eq	equivalent
f	failure
i, j	integer indices
lin	linear
max	maximum
mB	Morrow fatigue equation with true fracture (Brickman) stress
memb	membrane
mi	Morrow fatigue equation with SN curve intercept stress
min	minimum
mM	minimum, maximum
n	natural
nb	narrow-band
nl	nonlinear
nl norm	nonlinear transformed normal
nl peak	nonlinear transformed peak
nl ray	nonlinear transformed Rayleigh
norm	normal
nyq	Nyquist
ode	from Ordinary Differential Equation
p+, -p+, +p+	positive peaks: negative valued, positive valued
peak	peak distribution
r	random (error)

$_{ray}$ Rayleigh distribution

$_{rfc}$ rainflow cycle

$_{square}$ response squared

$_{sum}$ summation

$_{top}$ top surface value

$_{total}$ response total; combined result of several effect

$_{w}$ Walker fatigue equation

$_{wb}$ wide-band

$_{xx}$ complex frequency domain variable with respect to itself

$_{xy}$ complex frequency domain variable of input x with respect to output y

$_{0}$ mean value of a variable

$_{1:2}$ input value 1 that is uncorrelated with input 2

$_{3:2!}$ input value 3 that is uncorrelated with inputs 2 and 1 (or 2!)

$_{5}$ modified Walker fatigue equation from MMPDS-1 (replacement for MIL-HDBK-5)

1 INTRODUCTION AND LITERATURE REVIEW

The main motivation for this research is the need to predict fatigue lives for structures that exhibit nonlinear response to random loading. A nonlinear response is indicated by a change in response that is not proportional to a change in the input load. It can be observed in the time domain or the frequency domain; the latter can show that the response spectrum contains frequencies that were not present in the excitation. Fatigue life estimates based on linear theory may be either very conservative or, for some nonlinear structures, very optimistic. Rigorous analysis techniques need to be developed to either take advantages of the longer lives or to ensure that premature failures do not occur. Random loading dictates an analysis technique that includes the probabilistic nature of the random response. Nonlinear random response cannot be assumed to be Gaussian even if Gaussian loading can be assumed. The non-Gaussian response requires a further level of analysis sophistication.

Common examples of nonlinear random response are lightweight aerospace structures subjected to acoustic pressure loadings. Very high levels of acoustic pressures can be generated near rocket or jet engines. When applied to lightweight panels, either curved or flat, these acoustic excitations can induce geometric nonlinear behavior when the deflection is large enough in proportion to the geometry. Membrane forces in panels tend to increase the stiffness of a structure and can add tensile mean stresses. Curved panels can have further nonlinearities that may result in asymmetric response levels and in extreme cases "snap through" behavior. Elevated temperatures from exhaust or from supersonic flow at space re-entry can further complicate the nonlinear response analysis by introducing the need to consider nonlinear material properties.

This thesis will discuss methods to estimate the response statistics, with an emphasis on the resulting fatigue life, for nonlinear structures subjected to random loading. Examples of predicted and measured nonlinear response due to large deflections of beams will be used extensively throughout this thesis. Data from clamped-clamped experiments will be used to illustrate frequency and time domain analysis techniques that have been shown to be useful for identifying and quantifying the nonlinear behavior. Additional numerical simulations will be used to further the analysis and

investigation of the nonlinear response. Fatigue life estimates, based on the nonlinear strain response, are compared to baseline linear response estimates. The times to failure for this class of stress stiffening nonlinear structure are shown to be longer than those based on linear estimates.

Cyclic fatigue is considered in this thesis to be the ultimate failure mode of the structural material when subjected to large numbers of stress cycles. The random loading can lead to large deflections and high peak stresses, and repeated loading that accumulate damage resulting in fatigue failure. Aerospace structures typically are subjected to short periods of intense loading mixed with longer periods of reduced loading. Take-off and landing events are typically where the loads are the greatest. Supersonic events or brief bursts of gunfire vibration are other high load conditions. The combined effects of all the accumulated cycles need to be included in the fatigue analysis to help ensure satisfactory service life. Economic factors that lead to the desire for continued service from older equipment, or the desire to have reusable vehicles are additional reasons for requiring long times to fatigue failures.

1.1 Nonlinear structural analysis

There are many reasons why structures can exhibit nonlinear and/or non-Gaussian random responses. This section will review the various parameters that can lead to nonlinear system response and discuss methods to identify and predict the nonlinear response.

1.1.1 Nonlinear system parameters

Physical systems often can be described by linear system parameters, but often some nonlinear terms can have a significant impact on the total response. These nonlinear terms are grouped into categories and discussed in the following sections.

1.1.1.1 Mechanical system with nonlinear restoring force

The physical geometry of systems comprised of linear materials can lead to system properties that result in nonlinear response. The classic example of this is when the

1.1.1.1 Mechanical system with nonlinear restoring force

The physical geometry of systems comprised of linear materials can lead to system properties that result in nonlinear response. The classic example of this is when the structural change in shape results in modifications to the system restoring force. This case is often known as the large deflection problem.

A very common example of a nonlinear large deflection problem is a simple pendulum, oscillating under the force of gravity (see for example [1]). The free vibration equation of motion is

$$\ddot{\theta} + \frac{g}{l}\sin\theta = 0 \tag{1.1}$$

A power series expansion of the sin function, keeping the first two terms is

$$\ddot{\theta} + \frac{g}{l}\left(\theta - \frac{\theta^3}{6}\right) = 0 \tag{1.2}$$

where g is the gravitational acceleration, l is the length and θ is the angle from vertical. The resonance frequency of the pendulum tends to decrease as the angle increases.

Another basic large deflection case is the vibration of a tensioned string (or wire) with central mass m, fixed between two points; as the mass deflects a distance x from its nominal position, the length of the string has to increase, thereby increasing the restoring force. This change in length and restoring force is a nonlinear relationship of the change in lateral position (see for example [1])

$$m\ddot{x} + \left(S + AE\frac{x^2}{2l^2}\right)\frac{2x}{\sqrt{l^2 + x^2}} = 0 \tag{1.3}$$

where S is the initial tension, A is the cross-sectional area, and E is the elastic modulus of the string (wire). The simplified free vibration equation of this system for moderate lateral displacements is

$$m\ddot{x} + \frac{2Sx}{l} + AE\frac{x^3}{l^3} = 0 \tag{1.4}$$

The nonlinear stiffness increase in this case tends to increase the resonance frequency of the string. These two approximate equations can be generalized by the Duffing equation [2]

$$\ddot{x} + \alpha x + \beta x^2 + \gamma x^3 = 0 \tag{1.5}$$

The pendulum approximate solution has $\beta = 0$ and $\gamma < 0$, while the string mass system approximation has $\beta = 0$ and $\gamma > 0$.

The natural extension of the large deflection string problem is when the material dimensions increase enough to require the addition of bending stiffness terms; the string becomes a beam. If the boundary conditions are fixed at both ends, the lateral displacement again leads to a change in length that causes a tensile axial force. The stiffness of the fixed-fixed beam system is a nonlinear combination of bending and axial terms (see [3-7]). The large deflection beam stiffness non-linearity can be assumed to act like a Duffing oscillator (see for example [8, 9]). A review article [10] summarizes the status of analysis techniques as of 2000.

Curved beam geometry under large deflections can also result in non-symmetric stiffness (i.e. lateral deflections toward the center of curvature tend to have reduced stiffness, while deflections away from the center of curvature tend to increase stiffness). The curved beam approximate Duffing solution will have $\beta \neq 0$. Very large deflections of curved beams can lead to an unstable "snap through" condition. One example of a curved beam used in engineering applications is the coiled wire rope isolator.

As the beam material dimensions increase, additional in-plane terms are added as the beam becomes a plate or shell. The shell is a natural extension of the string problem where the axial force translates to a membrane force. The large deflection plate problem will include nonlinear bending and membrane effects. Curved plates have nonlinear properties similar to curved beams [11, 12].

Further examples of nonlinear restoring force under large deflections can be described with bi-linear stiffness due to additional materials coming into contact as gaps close [1]. A physical example of this is a spring or isolator that has a snubber (additional stiffness) mounted to it to limit large deflections.

1.1.1.2 Mechanical system with nonlinear damping

Another category of nonlinear system parameter is nonlinear damping. The classic example of this is the nonlinear damped van der Pol oscillator [13]

$$\ddot{x} + \mu\left(1 - x^2\right)\dot{x} + x = 0 \tag{1.6}$$

The periodic forced response van der Pol equation

$$\ddot{x} + \mu\left(1 - x^2\right)\dot{x} + x = a\sin\left(2\pi\nu\tau\right) \tag{1.7}$$

can lead to highly nonlinear results, the study of which has opened up several areas of research (see, for example [14, 15]). Damping for structural models can take various forms (e.g. viscous, hysteretic, etc.), and in this research project, the issue of nonlinear damping is not of concern compared to nonlinear stiffness.

1.1.1.3 Mechanical system with nonlinear stress

Linear structures are often assumed to have stress and strains that are linear functions of displacement. Large deflection cases often have nonlinear displacement to strain relationships. One example that will be discussed in detail in this thesis is the nonlinear displacement to strain function for beams and plates that involves a combination of bending and membrane terms. These are often discussed for static loading conditions [3]. One approximation of the displacement to strain (or stress) function is [16]

$$\varepsilon = C_1 y + C_2 y^2 \tag{1.8}$$

where y is the nonlinear displacement, and C_1 and C_2 are constants. Note: this is a nonlinear instantaneous relationship, not a nonlinear differential equation.

1.1.1.4 Nonlinear materials

Materials can often have basic properties that are nonlinear functions of displacement, temperature or strain rate. Elastomer materials (e.g. rubber) are common examples that exhibit nonlinear load deflection responses as bulk materials. Plastic and elastomeric

materials often have a complex shear modulus (or complex modulus) that changes with temperature and loading frequency. The experimental methods for determining complex modulus are well-established [17].

1.1.1.5 Non Gaussian loads

Many random noise sources in nature and engineering applications can be considered Gaussian as a first approximation. There are however, some random loading conditions that have been shown to be non-Gaussian. Non-Gaussian environmental loads that are of concern in the field of civil engineering are due to wind [18, 19] and waves [20-27]. Additional non-Gaussian loads that are of concern for aerospace engineers are due to turbulent boundary flow [28, 29], supersonic flow [30] and thermal acoustic conditions [31, 32]. Non-stationary random loads from different types of road or ground surfaces over the life of a vehicle can also be considered as non-Gaussian operating loads [33, 34]. The response of linear systems to non-Gaussian inputs have been documented [35-37]. Methods to generate non-Gaussian loads time histories may be of interest to the reader [38-42]).

1.1.2 Analysis methods for nonlinear response prediction

The study of solutions to nonlinear differential equations has been active since the early 1900's. Work by Kelvin [43], Duffing [2], van der Pol [13], Hamel [44] and others (see summary articles [14, 45]) have laid the foundation for the mathematical theory. This section will review the analytic and approximate methods developed to analyze nonlinear and non-Gaussian responses.

1.1.2.1 Analytic solutions

Recent work in the area of general nonlinear differential solutions can be found in many references [46-55]. Additional work in the area of non-stationary random process can be found in [56-58]. Chaos theory has also been applied to engineering problems [59, 60].

Of particular interest to this thesis is the study of level crossings and extreme values. The seminal work by Rice [61] was followed by the early study of nonlinear statistics

by Lin [16] Crandall [62] and others [63-65]. Recent work in the area with particular interest to nonlinear, non-Gaussian responses has continued to advance the theory [66-73]. Level crossings and extremes based on time domain moments have been developed, most notably by Winterstein and associates [74-76]. Probability distributions based on Non-Gaussian variables have also been developed [26, 69, 77-83].

1.1.2.2 Equivalent & stochastic linearization

Approximate methods to solving systems of nonlinear differential equations have been proposed since the first work to solve them. A method known as equivalent linearization has been researched and applied to random vibration problems for more than 40 years [5, 84-94]. An equivalent linearization technique solves for equivalent linear model stiffnesses for a given magnitude of load, with the goal of minimizing the error in the system response standard deviation. This method has been shown to also produce good estimates of the change in system modal frequencies, but it cannot estimate changes in response probability density functions or harmonic distortion of the resonances. The equivalent linearization method has been extended to higher order powers of the response in an effort to estimate extremes of the nonlinear response [95]. Another alternative to the equivalent linearization method, the probabilistic linearization technique, has been proposed whereby the error in a approximate probability density function of the response is minimized with respect to the nonlinear probability density function [96, 97]. Challenges to the standard linearization method are well-documented (see [98, 99]).

Linear and nonlinear analysis methods based on stochastic moments and cumulants have been proposed as an alternative to solving the nonlinear Fokker-Planck equations [100, 101]. Other methods to predict nonlinear response are based on linear systems with stochastic system properties. Several methods have been proposed to estimate the power spectral density (PSD) of the nonlinear response by treating the system natural frequency [102, 103] and other system parameters [104, 105] as random variables. Modal methods have also been proposed as methods to estimate PSDs of nonlinear systems [106-108].

1.1.2.3 Reduced order nonlinear differential equations

The need to develop larger and more detailed models of engineering structures has led to efficient techniques to reduce the order of the models for subsequent dynamic simulations. Modal analysis methods have proven to be a very effective way to predict the time and frequency domain behavior of linear systems. Recently modal methods have been applied as a technique to reduce the order of nonlinear systems [109-114]. The basic idea is to first find the linear reduced order modal properties of the system, and then to use them to develop a nonlinear ordinary differential equation (ODE) model of the system. Once the reduced order nonlinear ODE has been solved numerically, the full model results can be estimated by expanding back from modal coordinates to physical coordinates. Since this method solves the nonlinear ODE in the time domain, it has the benefit of allowing estimation of time domain statistical parameters, in particular probability density functions of the response. The reduced order nonlinear models also allow inclusion of nonlinear physical behavior such as membrane stiffness. Similar methods have been employed using nonlinear modal representations of substructures of larger system [115].

1.1.2.4 Nonlinear Laplace and Fourier transforms

The related field of communication theory has several applications of nonlinear functions, particularly in the area of detectors for receivers. The behavior of signals and background noise in nonlinear communication systems has been documented in classic books by Middleton [116] and Davenport and Root [117]. These texts should be consulted for a through development of nonlinear Laplace and Fourier transforms as well as advanced developments of the statistical behavior of nonlinear systems.

1.1.3 Nonlinear frequency domain identification

Advances in experimental signal processing and analysis have led to methods that can be used to estimate nonlinear properties of systems. This has been a very active area of research in the last 10 years [118-140]. Nonparametric models, that require no knowledge of the system or excitation, have been developed [141, 142]. The "reverse path" technique [125, 143], where the response is transformed into nonlinear functions

and used as the input to a multi conditioned input spectral analysis, will be presented and used extensively in the rest of this thesis.

1.2 Fatigue and damage analysis

Cyclic fatigue is one of the most important failure modes for structures that are required to withstand repeated applications of dynamic loads. This section will give a review of fatigue theory, with emphasis on random, non-Gaussian stress cases (e.g. sonic fatigue). The following sections will give a brief review of early fatigue work, but will also concentrate on recent theoretical developments. Fatigue equations and notation will be introduced in chapter 2.

1.2.1 Sinusoidal fatigue

The study of fatigue in materials can be traced to Wöhler [144] in the late 1800's. Research in the early 1900's led to an exponential relationship between stress amplitude and life by Basquin [145] and a secondary effect on life due to mean stresses by Goodman [146]. A recent paper by Dowling [147] reviews sinusoidal fatigue equations, comparing the predictions of various equations that include mean stress to experimental data. Another recent paper [148] discusses bi-linear fatigue models (attributed to discrete changes in the slope of S-N curves, and total strain life models (see also [147])) that attempt to more accurately predict the sinusoidal fatigue life of materials. Mean stress effects for fatigue in welds [149] due to sinusoidal and random loading have also been documented.

Some engineering materials, most notably rubber, exhibit highly nonlinear elastic isotropic behavior with incompressibility. Sinusoidal fatigue analysis methods for rubber, based on strain and strain energy, have shown to match experimental results well [150].

1.2.2 Variable amplitude fatigue

Many situations in engineering fatigue problems cannot be considered as constant amplitude sinusoidal loading. A simple example is a machine that operates at different

speeds, with different structural forces at each speed, whilst complex examples include transient and random loading. Methods that have been developed to determine the time-to-failure or damage for variable amplitude loading will be discussed next.

1.2.2.1 Linear cumulative damage

The founding theory of variable amplitude loading is attributed to Palmgren [151] and later Miner [152] will be described in this thesis as a linear cumulative damage rule. It simply states that damage is cumulative, and that each stress cycle contributes to damage as a function of the number of cycles to failure for that cycle amplitude. Linear cumulative damage neglects any sequence effects (e.g. low amplitude followed by high amplitude vs. high amplitude followed by low amplitude) that may change fatigue life.

1.2.2.2 Narrowband random fatigue

The Palmgren-Miner linear damage rule was extended to narrow band random fatigue by Miles [153] in the mid 1950's. Miles extended the linear summation of damage to an integral of stress peaks scaled by the probability density function of stress peaks, which, for a narrowband random system, was known to be a Rayleigh distribution. The resulting damage equation was a function of the sinusoidal stress versus number of cycles to failure (SN curve) fatigue properties and the standard deviation of stress. Similar derivations with reference to Miles work can be found in [4, 154, 155]. The same derivation was developed independently again later by Lambert [156], who extended the development to include statistical properties of the stress-probability density function (PDF) integrand as well as equations for random fatigue life with variable stress or strength.

Seminal work with nonlinear response probability density functions and their effect on fatigue can be traced to two papers in 1963 by Lin [16] and Crandall [62]. Lin developed relationships for nonlinear stress PDFs based on a quadratic displacement to stress equation, with the additional assumption that the displacement PDF was also nonlinear. The number of peaks and troughs were developed, with attention to the formation of negative stress peaks in the nonlinear structure. Lin's concluding remarks still apply today: "...analytically determined distribution of stress peaks in a nonlinear

structure shows marked differences from that in a linear structure, especially in the regions of negative stress peaks...". In particular for this thesis, "...it is suggested that further research be carried out with special attention to nonlinear response". Crandall developed equations for the rates of zero crossings for nonlinear, non-Gaussian systems, plus peak PDFs for nonlinear Duffing "hardening spring" oscillators and other systems with nonlinear restoring forces. Recent derivations of random fatigue due to nonlinear stress peak PDFs have been developed [157-160].

1.2.2.3 Wideband random fatigue

The special case of narrowband random loading was extended to arbitrary stress cycles in the 1960's, using cycle versus amplitude counting methods. The de-facto standard that emerged was called the Rainflow cycle method, attributed to Matsuishi and Endo [161]. Research showed that the Rainflow cycle method combined with the linear damage model gave the most accurate estimates of fatigue life [162]. The rainflow counting technique was later redefined in more mathematical terms by Rychlik [163-165] and Bishop [166, 167]. It should be stated here that rainflow cycle counting is a time domain method that is computationally intensive.

Parallel work with multimode responses was published based on probability theory. Lambert extended his narrow band theories to multi-degree of freedom random damage functions [168] based on published one and two degree of freedom experimental data. Other methods have also been proposed to fit a rainflow range PDF [169-173].

The difficulties with the computation of rainflow cycles distributions from time domain data has led to the development of frequency domain techniques. The seminal work by Rice [61] and research since has shown that the PDF of peak response can be determined from moments of the frequency domain response power spectral density (PSD) (also called spectral moments), and that the peak PDF is a combination of a Gaussian and a Rayleigh PDF. Dirlik [174] developed an empirical equation for a rainflow PDF by performing numerical experiments. This method was applied to engineering problems (see for example [175]). A review of the spectral moment technique theory and applications of it to random fatigue problems can be found in several recent papers [176-179]. Reviews of the Dirlik equation and other published

rainflow PDF empirical equations [180] have been published by several authors [181, 182]. Alternative methods of estimating the rainflow PDF using spectral moments have recently been proposed [183, 184].

A second aspect of wideband random fatigue is that stress cycles can have mean values that are not zero (compared to the ideal narrowband case). Sinusoidal testing has shown for over 100 years that the addition of a tensile mean stress can reduce the fatigue life. It is therefore theoretically advantageous to extend the rainflow cycle amplitude PDF to a multi-dimensional PDF. Two multi-dimensional rainflow cycle PDF formats have been proposed: 2D PDF of amplitude (or range) and mean values [185-187], and 2D PDF of minimum (or trough) and maximum (or peak) values [34, 165, 188, 189].

A slightly different approach to the cycle counting methods using Markov chain models has been proposed [188, 190-192]. This Markov chain method is especially useful for including sequence effects in damage models.

A natural extension to the uni-axial cycle counting methods has been proposed to include multiaxial states of stress (see [193] for a summary review as of 1998). Recent papers that operate in the time [194] and frequency domain [195-197] are also of interest.

1.2.2.4 Non-Gaussian random fatigue

The area of research for this thesis is the specific topic of non-Gaussian random fatigue. One of best examples of engineering problems in this area is the study of acoustic fatigue. Summary reports [198, 199] review the state of acoustic fatigue in 1987 and 1994, and propose plans for future theoretical and experimental work. One of the prime motivations for the research documented in this thesis was earlier theoretical work by the author for the US Air Force, under a Small Business Independent Research (SBIR) contract F33615-02-M-3236, titled Rapid Fatigue Life Prediction for Nonlinear Loading and Structures. Other research in this area can be found in [34, 189, 200-209].

Sarkani et al. [158] developed a nonlinear transformation of the narrowband Rayleigh distribution and used this to estimate fatigue damage for various nonlinear exponents (and their resulting kurtosis values) and material SN fatigue exponents.

1.2.2.5 Nonlinear cumulative damage

Although this thesis assumes the linear Palmgren-Miner damage rule, as stated above and detailed in the following chapters, there are challenges to the linear theory that should be noted. Experimental and in service failures in the 1950's gave rise to the field of fracture mechanics which concentrates on crack growth rather than overall structural fatigue (see the summary article [210]). One of the basic findings of fracture mechanics is that the crack growth rate is a nonlinear function of the current crack length, the surrounding material geometry and the applied load. Recent work on fracture mechanics with application to random loads may be of interest for future research [211-218]. Fracture mechanics analysis has in some ways replaced more classic fatigue analysis, but the nonlinear sequence effect of stress on life is difficult to treat stochastically in closed form.

Parallel work with multi level fatigue testing also challenges linear Palmgren-Miner damage theory. A comprehensive review of the linear and nonlinear cumulative damage theories was published in 1998 [219]. Additional publications since then may be of interest [220-227]. Comments by one author [226] in the introduction of his article summarize the situation well. In short, the linear theory "...is the most often used due to its simplicity." "Moreover, the final mathematical expressions of many (nonlinear) prediction rules are so complex that they are simply not suitable for random loading applications, especially in analytical form." There is clearly a need for more research and practical engineering approaches to the problem.

1.2.3 Reliability due to fatigue

The field of reliability has a strong link to the study of fatigue. The famous author Weibull began his work by developing a statistical theory for the static strength of materials [228], and then extended it to the fatigue strength of materials [229]. Reliability analysis has branched out into many fields of applications, but the underlying physics of the problems often has material fatigue as its root. Later work by Weibull [230] addressed the joint effect of cyclic and random peak loading, noting that the data did not follow the linear Palmgren-Miner damage rule.

Work by other researchers is of interest. Lambert [231] developed a random fatigue failure model based on a simultaneous variance of strength and stress. Random service loading, with the inherent scatter and uncertainty in limited measurements, has been studied by several authors [33, 232-235]. Practical discussions of reliability predictions for mechanical structures are a topic of continued interest [236-239]. Structural fatigue life with system uncertainty is another area of recent work [240, 241]. Recently, methods to model complex, large-size stochastic mechanics problems have been developed [242-246]).

1.3 Summary

This introductory chapter has presented a review of the nonlinear random vibration literature and the response failure criteria of cyclic fatigue. The field of nonlinear random vibration has many important applications in modern engineering problems and is an active area of research and practical development. The field of random fatigue is also an active area of research. Methods for fatigue analysis based on extensions to sinusoidal linear damage fatigue theory have been presented, whilst still other methods, based on more recent nonlinear damage theory (e.g. fracture mechanics), have been cited.

1.4 Thesis objectives and overview of the content

The thesis topic, "Random Vibration Response Statistics for Fatigue Analysis of Nonlinear Structures", will be explored in the following chapters using a combination of experimental test and numerical simulation results. The goal of this work will be to introduce analysis techniques that will show by example how the resulting fatigue life estimates of one important case of nonlinear structures changes as more nonlinear terms are included. The findings of this work are applicable to improving the time-to-failure estimates for modern engineering structures.

This thesis will continue in chapter 2 by briefly introducing equations and techniques for random linear and nonlinear signal analysis. The topic of probability density and distribution functions will be stressed, and the use of the inverse distribution function

method to estimate linear to nonlinear functions will be presented. Frequency domain analysis techniques such as spectral moments and the reverse path nonlinear frequency response function identification technique will be introduced. Additional sections on random fatigue equations for use with non-Gaussian response will be presented.

The thesis will then explore the nonlinear random vibration problem using experimental results from a clamped-clamped beam experiment performed at Wright Patterson Air Force Base (WPAFB) [7]. Frequency and time domain methods will be used to identify some of the nonlinear properties of the experiment. Strain data from the experiments will also be used to estimate fatigue life using a baseline alternating stress equation and several damage equations that include mean stress terms. This experimental study is presented in chapter 3.

Additional linear and nonlinear differential equation numerical simulations are presented in chapter 4. This chapter will explore additional statistical analysis of the Duffing style nonlinear problem. The models are based on the nonlinear identification of the parameters from the WPAFB experiments. The numerical simulations allow for additional insight into the velocity and acceleration response states for various damping levels over very long time periods.

Nonlinear strain and stress estimates, based on nonlinear displacements determined numerically from nonlinear differential equations, will be presented in chapter 5. The nonlinear strain displacement parameters used in this analysis are derived from the results presented in chapter 3. Time domain cycle counting method results will be compared to nonlinear stress PDFs determined using PDF transforms. The time to failure estimates based on linear and nonlinear results are presented to show the importance of each nonlinear term.

The final chapter 6 will summarize the thesis, highlighting the original and novel contributions, and suggest areas for future research. References used in this thesis will be given at the end.

2 RANDOM DATA, NONLINEAR ANALYSIS, AND FATIGUE REVIEW

This chapter will briefly introduce relationships and techniques for random linear and nonlinear signal analysis. Time and frequency domain techniques are given here as a way to introduce the notation and to familiarize the reader with the methods that are used extensively throughout the rest of the thesis. Fatigue theory for sinusoidal and random loading will complete the review.

Probability density and distribution functions will be stressed, and the use of the novel inverse distribution function method to estimate linear to nonlinear functions is presented. The probability density function (PDF) transform method is introduced as a method to estimate the PDF of a related signal given a function relationship between the two signals. This PDF transform method is used extensively throughout the rest of the thesis to estimate nonlinear PDFs for displacement and stress response.

Frequency domain analysis techniques are reviewed with special attention to spectral moments. The spectral moments introduced here will be used later in this thesis to estimate rates of zero crossings and peaks and to also estimate peak PDFs of Gaussian signals. The reverse-path nonlinear frequency response function identification technique introduced in this chapter will be used in the following chapter to estimate nonlinear parameters from clamped-clamped beam experiments.

The final section of this chapter reviews basic sinusoidal fatigue equations and their extension to random fatigue, based on the Palmgren-Miner linear damage theory. Equations that estimate fatigue life with the addition of nonzero mean stress will be presented.

2.1 Time domain analysis

Time domain methods for analysis of random signals are the preferred method for estimating basis statistics, such as expected values and moments of the data. This

section will also briefly review PDFs, distribution functions, inverse distribution functions, and the PDF transform method.

2.1.1 Expected values and moments

The mean value (expected value) μ of x is given for a continuous function by

$$\mu_x = E[x] = \int_{-\infty}^{\infty} x\, p(x)\, dx \tag{2.1}$$

where $p(x)$ is the PDF of x (see, for example, (2.18) for the PDF of a Gaussian signal). This equation can be thought of as the first moment of the PDF. For a discrete signal, the estimated mean value is calculated by

$$\hat{\mu}_x = \left(\frac{1}{N}\right)\sum_{j=1}^{N} x_j \tag{2.2}$$

where x_j are discrete values and N is the number of data points in the signal. The higher-order n_{th} expected values (or PDF moments) of x are defined by

$$\mu_x^n = E\left[x^n\right] = \int_{-\infty}^{\infty} x^n p(x)\, dx \tag{2.3}$$

or for a discrete signal

$$\hat{\mu}_x^n = \left(\frac{1}{N}\right)\sum_{j=1}^{N} x_j^n \tag{2.4}$$

For example, the mean squared value of a discrete signal x is

$$\hat{\psi}_x = \left(\frac{1}{N}\right)\sum_{j=1}^{N} x_j^2 \tag{2.5}$$

The second central moment (variance) about the mean is defined by

$$\sigma_x^2 = E\left[(x-\mu_x)^2\right] = \int_{-\infty}^{\infty} (x-\mu_x)^2\, p(x)\, dx \tag{2.6}$$

or for a discrete signal

$$\hat{\sigma}_x^2 = \left(\frac{1}{N}\right)\sum_{j=1}^{N}\left(x_j - \mu_x\right)^2 \tag{2.7}$$

The variance can be expanded to yield a relationship with the mean values

$$\sigma_x^2 = \psi_x - \mu_x^2 \tag{2.8}$$

The standard deviation σ (RMS for a zero mean) is

$$\sigma_x = \sqrt{\sigma_x^2} \tag{2.9}$$

For higher-order central moments, it is convenient to work with the standard variable z, defined as

$$z = \frac{x - \mu_x}{\sigma_x} \tag{2.10}$$

Two named higher central moments (in terms of the standardized variable z) are of interest. The third central moment, skew ι, is defined as

$$\iota = E\left[z^3\right] = \int_{-\infty}^{\infty} z^3\, p(z)\, dz \tag{2.11}$$

or for a discrete signal

$$\hat{\iota} = \left(\frac{1}{N}\right)\sum_{j=1}^{N} z_j^3 \tag{2.12}$$

A symmetric PDF (e.g., a Gaussian), will have skew equal to zero. A non-symmetric PDF will have positive or negative skew. The fourth central moment, kurtosis κ is

$$\kappa = E\left[z^4\right] = \int_{-\infty}^{\infty} z^4\, p(z)\, dz \tag{2.13}$$

or for a discrete signal

$$\hat{\kappa} = \left(\frac{1}{N}\right)\sum_{j=1}^{N} z_j^4 \tag{2.14}$$

For Gaussian random signals, kurtosis is equal to three. For non-Gaussian systems, kurtosis can take on positive values less or greater than three.

2.1.2 Distribution and probability density functions

The distribution function of x (or $F(x)$) (also referred to as the cumulative distribution function (CDF)) is defined as the probability of occurrence ρ of the variable x taking a value less than or equal to a

$$F(x) = \text{Prob}[x \le a] = \rho \tag{2.15}$$

The distribution function monotonically increases from $F(-\infty) = 0$ to $F(\infty) = 1$. The probability density function is defined as

$$p(x) = \lim_{\Delta x \to 0} \left[\frac{\text{Prob}[x < x_j \le x + \Delta x]}{\Delta x} \right] \tag{2.16}$$

The distribution function is related to the PDF by

$$F(x) = \int_{-\infty}^{x} p(\alpha) d\alpha \tag{2.17}$$

Two common PDFs are the Gaussian (or normal) PDF (for zero mean)

$$p_{norm}(x) = \frac{1}{\sigma_x \sqrt{2\pi}} \exp\left(\frac{-x^2}{2\sigma_x^2} \right) \tag{2.18}$$

where exp(x) is the value e raised to the power x, and the Rayleigh PDF

$$p_{ray}(x) = \frac{x}{\sigma_x^2} \exp\left(\frac{-x^2}{2\sigma_x^2} \right) \tag{2.19}$$

The Rayleigh function is useful for studying the peak response of narrowband Gaussian signals. Also of interest is the generalized peak function, defined here for the standardized variable z, which gives the peak PDF for any normal random signal [247, 248]

$$p_{peak}(z,\varpi)=\left(\frac{k_1}{\sqrt{2\pi}}\right)\exp\left(\frac{-z^2}{2k_1^2}\right)+\varpi z\exp\left(\frac{-z^2}{2}\right)\left[1-Q_2\left(\frac{z}{k_2}\right)\right] \tag{2.20}$$

where ϖ is the ratio of the rates of zero crossings to peaks (defined in Section 2.1.4). The additional terms k_n and Q_n are functions of the ratio ϖ (which has values $0 \le \varpi \le 1$)

$$k_1^2=1-\varpi^2 \quad k_2=k_1/\varpi \quad Q_n\left(\frac{z}{k_n}\right)=\frac{1}{2}\mathrm{erfc}\left(\frac{z}{k_n\sqrt{2}}\right) \tag{2.21}$$

where erfc is the complimentary error function [249]

$$\mathrm{erfc}(x)=\frac{2}{\sqrt{\pi}}\int_x^\infty \exp\left(-v^2\right)dv \tag{2.22}$$

Note that the generalized peak PDF equation (2.20) is a weighted sum of a Gaussian and Rayleigh PDF; at the limits

$$p_{peak}(z,0)=p_{norm}(z); \quad p_{peak}(z,1)=p_{ray}(z) \tag{2.23}$$

The generalized peak PDFs for various values of the ratio ϖ are shown in Figure 2.1. Common distribution functions are also useful. The normal distribution function is [249]

$$F_{norm}(x)=\frac{1}{2}\left[1+\mathrm{erf}\left(\frac{x}{\sigma_x\sqrt{2}}\right)\right] \tag{2.24}$$

where erf is the error function [249]

$$\mathrm{erf}(\mathrm{x})=\frac{2}{\sqrt{\pi}}\int_0^x \exp\left(-v^2\right)dv \tag{2.25}$$

The error function and complimentary error function are related [249]

$$\mathrm{erfc}(x)=1-\mathrm{erf}(x) \tag{2.26}$$

The Rayleigh distribution function is [248]

$$F_{ray}(x) = 1 - \exp\left(-\frac{1}{2}\left(\frac{x}{\sigma_x}\right)^2\right) \tag{2.27}$$

The generalized peak distribution function is [248]

$$F_{peak}(z,\varpi) = 1 - Q_1\left(\frac{z}{k_1}\right) - \varpi \exp\left(-\frac{z^2}{2}\right)\left[1 - Q_2\left(\frac{z}{k_2}\right)\right] \tag{2.28}$$

2.1.3 Inverse distribution function

The inverse distribution function (IDF) or $F^{-1}(\rho)$ determines the corresponding x value of a distribution function given a value of probability of occurrence [42, 250]

$$F^{-1}(\rho) = F^{-1}(F(x)) = x \tag{2.29}$$

The IDF for a normal distribution can be determined explicitly from equation (2.24) as

$$F_{norm}^{-1}(\rho) = \sigma\sqrt{2}\,\mathrm{erf}^{-1}(2\rho - 1) = x \tag{2.30}$$

where erf^{-1} is the inverse error function $x = \mathrm{erf}^{-1}(y)$, which satisfies $y = \mathrm{erf}(x)$ for $-1 \le y \le 1$ and $-\infty \le x \le \infty$ [251]. The IDF for a Rayleigh distribution is determined from (2.27) as

$$F_{ray}^{-1}(\rho) = \sigma\sqrt{-2\ln(1-\rho)} = x \tag{2.31}$$

The IDF will be used extensively in the following chapters to determine functional relationships between linear and nonlinear data sets. A simple example of the IDF method is shown in Figure 2.2. In this example a distribution function (or CDF) from a nonlinear response is compared to the CDF of a linear normal distribution. For this example, two values of the probability of occurrence $\rho = 0.75, 0.97$ are shown with their corresponding linear and nonlinear response data points x, y.

2.1.4 Response rates

The rates of zero crossings and peaks are very important for peak response and fatigue analysis. They can be estimated (for linear or nonlinear random data) by sampling the time domain data. The rate of positive zero crossings can be interpreted as the apparent or dominant frequency of the data record, while the rates of peaks can help one understand the frequency of the highest periodic component of the data. Narrowband data is characterized by having one periodic component that has equal rates of peaks and zero crossings. Wideband data has many periodic components which mean that the rates of peaks will be much higher than the rates of zero crossings.

Realizing that there can be both positive and negative slope level crossings, the rates of positive slope zero crossings $\Phi\left[0^+\right]$ is assumed to be one half of the total number of zero crossings

$$\Phi\left[0^+\right]=\frac{N_0}{2T_{block}} \tag{2.32}$$

where N_0 is the number of level (level = 0) crossings and T_{block} is the length of the analysis time block. The rates of positive peaks $\Phi\left[P^+\right]$ can be determined by finding the total number of positive peaks N_p, i.e.,

$$\Phi\left[P^+\right]=\frac{N_p}{T_{block}} \tag{2.33}$$

The ratio of zeros to peaks ϖ (also know as the statistical irregularity) is

$$\varpi=\frac{\Phi\left[0^+\right]}{\Phi\left[P^+\right]} \tag{2.34}$$

One method of determining response rates for Gaussian data, based on spectral moments, is discussed later in Section 2.2.2.

2.1.5 Probability density function transforms

The PDF $p(x)$, of a data set x, can be transformed to $p(y)$ of a different data set y using the PDF transform [125, 250]

$$p(y) = \frac{p(x)}{|dy/dx|} \tag{2.35}$$

where there is a one-to-one monotonic relationship between x and y, and where

$$y = g(x) \tag{2.36}$$

which will be referred to as a right hand side (RHS) function. The PDF transform can also be expressed for a left hand side (LHS) monotonic function

$$h(y) = x \tag{2.37}$$

by

$$p(y) = |dx/dy|\, p(x) = |h'(y)|\, p(h(y)) \tag{2.38}$$

As an example, determine the normal PDF for a zero mean standardized variable (see equation (2.10))

$$z = g(x) = \frac{x-0}{\sigma_x} \tag{2.39}$$

The normal PDF, in terms of the standardized variable z, using equations (2.18), (2.35), and (2.39) is

$$p_{norm}(z) = \frac{p_{norm}(z\sigma_x)}{|1/\sigma_x|} = \frac{\sigma_x}{\sigma_x\sqrt{2\pi}} \exp\left(\frac{-(z\sigma_x)^2}{2\sigma_x{}^2}\right) = \frac{1}{\sqrt{2\pi}} \exp\left(\frac{-z^2}{2}\right) \tag{2.40}$$

The PDF transform will be used extensively in the next chapters to transform PDFs of linear data to PDFs of nonlinear data. The method is especially useful for predicting the PDF of a nonlinear system when there is some knowledge of the linear to nonlinear functions (see equations (2.36) and (2.37)). The IDF method, from section 2.1.3, is

throughout the rest of this thesis to predict these linear to nonlinear functions for use with PDF transforms.

An example is a nonlinear Rayleigh PDF transform for a LHS function equation (2.37) using equation (2.19) and (2.38)

$$p_{nl\,ray}(y) = |h'(y)|\, p_{ray}(h(y)) = |h'(y)| \frac{h(y)}{\sigma_x^2} \exp\left(\frac{-(h(y))^2}{2\sigma_x^{\,2}} \right) \tag{2.41}$$

The PDF transform method can also be used successively to perform multiple transforms, as will be shown in Chapter 5.

2.2 Frequency domain analysis

Frequency domain analysis techniques are often used to characterize periodic and Gaussian random signals. This section will give a brief overview of techniques that will be applied later. The reverse-path nonlinear frequency response function estimation technique will also be introduced.

2.2.1 Fourier transform, auto-spectrum and power spectral density

The Fourier transform F is defined as

$$X(f) = \int_{-\infty}^{\infty} x(t) e^{i2\pi f t} dt = \mathrm{F}(x(t)) \tag{2.42}$$

and the inverse Fourier transform F^{-1} is

$$x(t) = \int_{-\infty}^{\infty} X(f) e^{-i2\pi f t} df = \mathrm{F}^{-1}(X(f)) \tag{2.43}$$

The autocorrelation function that defines how a signal is correlated with itself, with a time separation τ is

$$R_{xx}(\tau) = \int_{-\infty}^{\infty} x(t) x(t+\tau) dt = E[x(t) x(t+\tau)] \tag{2.44}$$

The autocorrelation and auto-spectrum $S_{xx}(f)$ (or power spectral density (PSD)) functions are related by the Fourier transform pair

$$S_{xx}(f) = \int_{-\infty}^{\infty} R_{xx}(\tau) e^{j\omega\tau} d\tau \tag{2.45}$$

$$R_{xx}(\tau) = \int_{-\infty}^{\infty} S_{xx}(f)\, e^{-j\omega\tau} d\omega \tag{2.46}$$

The one-sided PSD $G_{xx}(f)$, defined for $0 \leq f < \infty$, is

$$G_{xx}(f) = 2S_{xx}(f) \tag{2.47}$$

At $f = 0$, G_{xx} and S_{xx} are equal to the mean value of the data.

2.2.2 Spectral moments and expected rates

A review of spectral moment and derivative process calculation is given briefly below. For a full treatment of the subject, see [248] and [177-179]. Spectral moments are calculated from the one-sided PSD $G(f)$ (in units of Hertz) or the two-sided PSD $S(\omega)$ (where $\omega = 2\pi f$ in units of radians) using

$$m_n = \int_0^{\infty} f^n G(f) df \tag{2.48}$$

$$\mu_n = \int_{-\infty}^{\infty} \omega^n S(\omega) d\omega = m_n (2\pi)^n \tag{2.49}$$

It is important to note that μ_1 and μ_3 are zero, but m_1 and m_3 are not. Remember that μ_n is calculated by integrating from -∞ and +∞, and m_n is calculated by integrating from 0 to +∞. Typically, the moments m_0, m_1, m_2, and m_4 are calculated. The spectral moments can be used to estimate the rates of response of Gaussian random signals [248] and [177-179]. The expected rate of positive (or negative) slope zero crossings for this type of signal is

$$E[0]=\left[\frac{m_2}{m_0}\right]^{1/2} \tag{2.50}$$

and the rates of positive (or negative) peaks, P, and points of inflection, PI are

$$E[P]=\left[\frac{m_4}{m_2}\right]^{1/2} \tag{2.51}$$

$$E[PI]=\left[\frac{m_6}{m_4}\right]^{1/2} \tag{2.52}$$

A useful relationship for estimating the ratio of rates of zero crossings to peaks ϖ_{norm} for a normally distributed signal is

$$\varpi_{norm}=\frac{E[0]}{E[P]}=\frac{m_2}{\sqrt{m_0 m_4}} \tag{2.53}$$

This ratio can be used in the generalized peak PDF (2.20) or distribution function (2.28) equations.

2.2.3 Random time history from PSD using IFT

Often when working in test or analysis conditions, it is useful to generate random time histories with a prescribed PSD. Starting with the definition of a finite time auto spectral density function

$$S_{xx}(f,T)=\frac{1}{T}X^*(f,T)X(f,T) \tag{2.54}$$

where:

$$X(f,T)=\int_0^T x(t)e^{-i2\pi ft}dt=\mathrm{F}\left(x(t,T)\right) \tag{2.55}$$

and $T = 1/\Delta f$. The finite Fourier transform is defined from $-f_{nyq} \leq f \leq f_{nyq}$ where the Nyquist frequency is determined by $f_{nyq} = 1/(2\ \Delta t)$. Determine the magnitude of the Fourier transform for each value of f based on the prescribed PSD S_{xx} by

$$\left|X(f,T)\right| = \sqrt{TS_{xx}(f,T)} \tag{2.56}$$

At each positive frequency, determine a uniformly distributed random-phase angle $\Phi_f \in [0, 2\pi)$ such that

$$X(f,T) = A_f(f,T) + iB_f(f,T) \tag{2.57}$$

and $\tan \Phi_f = B_f / A_f$. At negative frequencies assign $X(f,T) = A_f(-f,T) - iB_f(-f,T)$. The time domain signal, with normally distributed magnitude and prescribed PSD, is determined using the inverse Fourier transform

$$x(t,T) = \int_{-f_{nyq}}^{f_{nyq}} X(f,t) e^{-i2\pi f t} df = \mathrm{F}^{-1}\left(X(f,T)\right) \tag{2.58}$$

where the limits of integration of the inverse Fourier transform are the Nyquist frequency determined by $f_{nyq} = 1/(2\ \Delta t)$.

2.2.4 Frequency response and coherence functions

The single input x, single output y relationships for a linear system h, in terms of Fourier transforms, are

$$Y(f) = H_{xy}(f) X(f) \tag{2.59}$$

or in terms of their spectral and cross-spectral densities

$$\begin{aligned} S_{yy}(f) &= \left|H_{xy}(f)\right|^2 S_{xx}(f) \\ S_{xy}(f) &= H_{xy}(f) S_{xx}(f) \end{aligned} \tag{2.60}$$

or also in terms of the one sided PSDs

$$G_{yy}(f) = |H_{xy}(f)|^2 G_{xx}(f)$$
$$G_{xy}(f) = H_{xy}(f) G_{xx}(f) \tag{2.61}$$

These equations can be used to estimate the linear frequency response function

$$H_{xy}(f) = \frac{G_{xy}(f)}{G_{xx}(f)} = \frac{G_{yy}(f)}{G_{yx}(f)} \tag{2.62}$$

More general equations relating multi-input, multi-output systems can also be developed (see for example [143, 248]).

The coherence function between the ideal single input and output,

$$\gamma_{xy}^2(f) = \frac{|G_{xy}(f)|^2}{G_{xx}(f) G_{yy}(f)} = \frac{|S_{xy}(f)|^2}{S_{xx}(f) S_{yy}(f)} \tag{2.63}$$

is a real valued function that ranges between 0 and 1. A coherence value of 1 indicates that the output is completely determined by a linear function of the input. Coherence values less than 1 indicate the presence of noise or other contributions to the output (e.g., nonlinear response terms).

2.2.5 Multi-input single-output frequency response function estimation

The single-input single-output frequency response function estimation method described above can be extended to multi-input single-output (MISO) problems [143, 248]. The MISO frequency response function method will be used extensively later in this thesis for estimating nonlinear frequency response functions (see Section 2.2.6). The basic MISO frequency domain formula for determining the response Y for multiple inputs X_i (excluding noise sources) is

$$Y(f) = \sum_{i=1}^{n} H_i(f) X_i(f) \tag{2.64}$$

This equation is shown in block diagram form in Figure 2.3(a). When one wants to estimate the frequency response functions H_i, it is very desirable to have the multiple

inputs X_i uncorrelated. If the inputs are uncorrelated, then the frequency response functions can be estimated as before by

$$H_i(f) = \frac{G_{iy}(f)}{G_{ii}(f)} \tag{2.65}$$

If the inputs are correlated, then the recommended technique is to precondition the data to form new inputs U_i that are uncorrelated.

In [143] there is a development (see Chapters 8 and 10) of a general MISO technique that determines multiple frequency response functions based on a method using conditioned (i.e., mutually uncorrelated) inputs (see Figure 2.3(b) based on Figure 10.2 of [143]). This general MISO technique is based on removing that part of the second input that is correlated with the first input (with notation $X_{2:1}$). The third conditioned input, is formed by removing that part which is correlated with the first two inputs (with notation $X_{3:21}$), and so on. Once the uncorrelated inputs are determined, linear frequency response functions for each path can be found using simple frequency domain calculations. Next, recursive relationships are presented that allow the originally correlated input problem to be related to the transformed uncorrelated input problem.

For purposes of illustration (and later use), consider a triple input X_i single output Y model of a system shown in Figure 2.3(a). The transformed uncorrelated equivalent to this model is shown in Figure 2.3(b) where the second and third inputs are now uncorrelated with the first two, and the frequency response functions H_{iy} are replaced with related frequency response functions L_{iy}.

Frequency domain formula for determining these frequency response functions are detailed in Chapters 8 and 10 of [143], and are given here for the illustrated problem. The first frequency response function L_{1y}, between the Fourier transform of the first input $X_1 = U_1$, and the Fourier transform of output Y, is given by the ratio of spectra

$$L_{1y} = \frac{G_{1y}}{G_{11}} \tag{2.66}$$

shown using the one-sided form G. The frequency response function L between the first two correlated inputs is

$$L_{12} = \frac{G_{12}}{G_{11}} \tag{2.67}$$

and the coherence function between these two inputs is

$$\gamma_{12}^2 = \frac{G_{12}^* G_{12}}{G_{11} G_{22}} \tag{2.68}$$

Note that in equations (2.67) and (2.68) as well as the equations that follow, the subscript 2 refers to the original input X_2. The uncorrelated input U_2 (i.e., the input determined by removing the part of input X_2 correlated to the input X_1) is found by

$$U_2 = X_{2:1} = X_2 - L_{12} X_1 \tag{2.69}$$

The frequency response function between the uncorrelated input U_2 and the output Y is

$$L_{2y} = \frac{G_{u_2 y}}{G_{u_2 u_2}} = L_{2y:1} = \frac{G_{2y:1}}{G_{22:1}} = \frac{G_{2y} - L_{1y} G_{21}}{G_{22}\left(1 - \gamma_{12}^2\right)} \tag{2.70}$$

The right hand side of equation (2.70) can be determined from the original inputs. The uncorrelated input U_3 is found by

$$U_3 = X_{3:2!} = X_{3:1} - L_{23} X_{2:1} = X_3 - L_{13} X_1 - L_{23} U_2 \tag{2.71}$$

and

$$L_{3y} = \frac{G_{u_3 y}}{G_{u_3 u_3}} \tag{2.72}$$

A flow diagram of this process of determining the uncorrelated inputs U_i is shown in Figure 2.4(a). The frequency response functions H of the original nonlinear model are recursively related to frequency response functions L by

$$
\begin{aligned}
H_{3y} &= L_{3y} \\
H_{2y} &= L_{2y} - L_{23}H_{3y} \\
H_{1y} &= L_{1y} - L_{12}H_{2y} - L_{13}H_{3y}
\end{aligned}
\tag{2.73}
$$

This recursive process of determining the frequency response functions H_{iy} is shown in Figure 2.4(b). The coherence functions between the Fourier transforms of the uncorrelated inputs U_i and the output Y are calculated by

$$
\gamma_{u_i y}^2 = \frac{\left|G_{u_i y}\right|^2}{G_{u_i u_i} G_{yy}}
\tag{2.74}
$$

This brief illustration is given full development in the text [143, 248] and should be studied in detail. The text goes into great detail to develop the methodology for determining the MISO frequency response functions and spectra for general models with any number of inputs.

2.2.6 Nonlinear frequency response functions

Methods to determine frequency response functions for nonlinear systems have recently been developed [118-140] and offer many options for modeling the nonlinear behavior of the system. One method [125, 143], which uses a "reverse-path," model will be discussed here and applied in later chapters. The input to the model is in the form of a combined linear and nonlinear MISO problem with the standard inputs and outputs being reversed (see Figure 2.5(a) based on Figure 13.15 of [143]). Here the linear or nonlinear dynamic response is used as a "mathematical input" to a MISO problem where the "mathematical output" is the known and specified force. Examples in Chapter 13 of [143] are given for a Duffing SDOF nonlinear system as well as other nonlinear SDOF and MDOF systems.

There are two main parts to the reverse-path nonlinear model system identification technique. The first is to define an equivalent nonlinear model that has nonlinear operators in series with linear frequency response functions. The second is to estimate the frequency response functions for each path of the model.

Bendat [125, 143] proposes an equivalent nonlinear system (to that shown in Figure 2.5(a)), based on a straightforward squaring and cubing of the mathematical input. In general, arbitrary nonlinear functions could be used, but for some systems, including the Duffing system, it is known a priori that the nonlinear response contains higher order powers such as cubic terms. The nonlinear model (see Figure 2.5(b) based on Figure 13.5 of [143]) now has three paths: a linear path with a linear frequency response function $H_{1Y}(f)$ and two nonlinear paths. The nonlinear paths have a nonlinear function in series with the linear frequency response functions: one path squares the input first then multiplies it by a linear frequency response function $H_{2Y}(f)$, the other path cubes the input before multiplying by a linear frequency response function $H_{3Y}(f)$. The authors also point out that this realization of the nonlinear model is general and convenient but not unique, i.e., other nonlinear operators can be used on the mathematical input (see for example [138]).

The next step in the method is to realize that this model can now be considered a MISO problem where, for this illustration, the frequency domain inputs are

$$\begin{aligned} X_1(f) &= \mathrm{F}\left(x(t)\right) \\ X_2(f) &= \mathrm{F}\left(x^2(t)\right) \\ X_3(f) &= \mathrm{F}\left(x^3(t)\right) \end{aligned} \tag{2.75}$$

This representation is shown in Figure 2.5(b) (based on Figure 13.10 of [143]). Note: the square and cubic transformations are normally performed in the time domain before Fourier transforming them to the frequency domain. Unfortunately, the inputs can, in general, be correlated. The method to transform the problem to one with uncorrelated inputs is discussed in the previous section, which can then be used to form a system as shown in Figure 2.3(b). Equations (2.67) through (2.72) are therefore used to find the frequency response functions L_i for each path. The original correlated input frequency response functions H_i are determined using equation (2.73). These nonlinear frequency response methods will be used extensively in the next chapters.

2.3 Statistical errors in basic estimates of linear random processes

Much of this thesis is devoted to estimating statistical measures of linear and nonlinear response data. An important part of this estimation process is to quantify the statistical errors (or uncertainties) for a given experimental or simulation time period. This section will briefly review equations used to estimate the errors for normal (Gaussian) random signals that will serve as a baseline for non-Gaussian random signals. Most of the material in this section is taken from Bendat and Piersol [248] Chapter 8, and will be presented with a minimum of discussion.

To begin, for a statistical measure ϕ, the estimate of the measure will be shown as $\hat{\phi}$. The normalized random error (standard deviation) of the estimate is (from [248], equation 8.9a)

$$\varepsilon_r = \frac{\sigma\left[\hat{\phi}\right]}{\phi} = \frac{\sqrt{E\left[\hat{\phi}^2\right] - E^2\left[\hat{\phi}\right]}}{\phi} \tag{2.76}$$

and the normalized bias error of the estimate is ([248], equation 8.9b)

$$\varepsilon_b = \frac{b\left[\hat{\phi}\right]}{\phi} = \frac{E\left[\hat{\phi}\right]}{\phi} - 1 \tag{2.77}$$

The combined RMS error is

$$\varepsilon = \frac{\sqrt{\sigma^2\left[\hat{\phi}\right] + b^2\left[\hat{\phi}\right]}}{\phi} = \frac{\sqrt{E\left[\left(\hat{\phi} - \phi\right)^2\right]}}{\phi} \tag{2.78}$$

The errors in estimates of standard deviations and PDFs are given below based on a number of samples N, the data record time period T, and the signal bandwidth B. Numerical simulations in Chapter 4 were run multiple times to develop large sample size estimates of the statistical measures that are important for fatigue and damage.

2.3.1 Estimates of standard deviation

The normalized random error for the estimate of standard deviation of a normal random signal is ([248], equation 8.65)

$$\varepsilon_r\left[\hat{\sigma}_x\right]=\frac{1}{2\sqrt{BT}} \tag{2.79}$$

The time and number of data points required for a specified random error ε_r is

$$T_r=\frac{1}{4B_s\varepsilon_r^2};\ N=\frac{1}{2\varepsilon_r^2} \tag{2.80}$$

where the statistical bandwidth (B_s) of the data is ([248], equation 8.52)

$$B_s=\frac{\left[\int_0^\infty G_{xx}(f)\,df\right]^2}{\int_0^\infty G_{xx}^2(f)\,df}=\frac{\left[\int_0^\infty |H(f)|^2\,df\right]^2}{\int_0^\infty |H(f)|^4\,df} \tag{2.81}$$

2.3.2 Estimates of probability distribution and density functions

The estimates of probability distribution and density functions begin by estimating the probability that some variable x takes on a value between $x-(W/2)$ and $x+(W/2)$ of a number of samples N, i.e., ([248], equation 8.66)

$$\hat{P}\left[x,W\right]=\text{Prob}\left[\left(x-\frac{W}{2}\right)\le x_j\le\left(x+\frac{W}{2}\right)\right] \tag{2.82}$$

where W is the sampling bin width. This probability is commonly estimated using histograms such that

$$\hat{P}\left[x,W\right]=\frac{N_j}{N} \tag{2.83}$$

where N_j is the number of sample values in each bin j, and N is the total number of samples. The distribution function is estimated at each bin from the cumulative sum of a histogram by

$$\hat{F}\left[x_j\right] = \frac{1}{N}\sum_{j=1}^{n} N_j \tag{2.84}$$

The distribution function estimate is unbiased when evaluated at the positive bin edge (x_j+(W/2)).

The probability density function can also be estimated from histograms ([248], equation 8.69) by

$$\hat{p}(x) = \frac{N_j}{NW} = \frac{\hat{P}\left[x, W\right]}{W} \tag{2.85}$$

Unfortunately, the numerical estimate of probability density functions can have significant bias errors. A first-order approximation (based on a Taylor series expansion) for the normalized bias error term is a function of the "shape" of the PDF ([248], equation 8.82)

$$\varepsilon_b\left[\hat{p}(x)\right] \approx \frac{W^2 p''(x)}{24 p(x)} \tag{2.86}$$

where $p''(x)$ is the second derivative of $p(x)$ with respect to x. The normalized random error in PDF estimates is a function of the bandwidth B and duration of the sample T

$$\varepsilon_r^2\left[\hat{p}(x)\right] = \frac{c^2}{2BTWp(x)} \tag{2.87}$$

where c is a constant that is dependant on the sampling of the signal; in [248], c is assigned a value of approximately 0.3 based on experimental studies. The bias (2.86) and random (2.87) errors can be combined to estimate the RMS error ε of the PDF ([248], equation 8.88)

$$\varepsilon^2\left[\hat{p}(x)\right]=\frac{c^2}{2BTWp(x)}+\frac{W^4}{576}\left[\frac{p''(x)}{p(x)}\right]^2 \tag{2.88}$$

Both error estimates are a function of W; the bias error has W in the numerator and the random error has W in the denominator. This apparent conflict is usually solved by first setting W to a conservative amount (typically <0.2 σ) and then determining the time T required to reach a target random error with an assumed value of $p(x)$. This relationship gives additional insight into the importance of large data records (long sample periods) for determining quality estimates of PDFs.

2.4 Fatigue analysis

There are several failure methods for systems that vibrate, but fatigue is considered the most catastrophic. The theory of cyclic fatigue was developed first based on cyclic loading (of constant amplitude), but it has been extended to account for a summation of loads at different levels. The discussion of fatigue in this chapter will present the evolution of equations starting with sinusoidal fatigue and ending with fatigue of wideband random responses.

2.4.1 Sinusoidal fatigue

The standard sinusoidal stress life power law fatigue model is

$$\begin{gathered}\sigma_a=\sigma_f'\left(2N_f\right)^b=AN_f^b \\ A=\sigma_f'2^b\end{gathered} \tag{2.89}$$

where σ_a is the fully reversed alternating stress amplitude, and N_f is the median cycles to failure. The power law slope b (fatigue strength exponent) and the stress intercept σ'_f, at one reversal (fatigue strength coefficient), or A at one cycle, are determined experimentally. The symbol σ (**bold**, not italic) is used here to denote stress instead of σ (*italic*, not bold), which is used to denote the standard deviation. The life (number of cycles to failure) N_f that is expected for a given alternating stress under zero mean stress is

$$N_{f\,alt} = \left(\frac{\sigma_a}{A} \right)^{1/b} \tag{2.90}$$

Note, the number of cycles to failure is also a random variable, and the value predicted with these equations is assumed to be a median value based on a curve fit of experimental results. Recent work of interest by Lutes et al. [252, 253] present theory for optimal experimental design for determining the material fatigue properties if the measured life is considered a random variable.

2.4.2 Sinusoidal fatigue life with mean stress

A recent review paper by Dowling [147] describes several methods that have been developed over the past century to determine fatigue life for alternating stresses combined with mean stresses. This section summarizes the currently accepted methods.

The Morrow equation for the number of cycles to failure with mean stress σ_0 is

$$N_{f\,mi} = \left[\sigma_a \Big/ A \left(1 - \frac{\sigma_0}{\sigma_f'} \right) \right]^{1/b} \tag{2.91}$$

For nonferrous materials, a modification using the true stress at fracture $\tilde{\sigma}_{fB}$ is

$$N_{f\,mB} = \left[\sigma_a \Big/ A \left(1 - \frac{\sigma_0}{\tilde{\sigma}_{fB}} \right) \right]^{1/b} \tag{2.92}$$

The Walker equation is

$$N_{f\,w} = \left[\frac{\sigma_{max}}{A} \left(\frac{1-R}{2} \right)^{\gamma} \right]^{1/b} \tag{2.93}$$

where γ is a fitting exponent and R is the ratio of minimum and maximum stress (σ_{min}, σ_{max}) values at the minima and maxima of the cycle, defined by

$$R = \sigma_{min} \Big/ \sigma_{max} \tag{2.94}$$

The fully reversed zero mean case is when $R = -1$. Note, equation (2.93) reduces to (2.90) when the exponent $\gamma = 1.0$. The special case of the Walker equation for $\gamma = 0.5$ gives the Smith-Watson-Topper [254] equation:

$$N_{fswt} = \left[\frac{\sigma_{max}}{A}\left(\frac{1-R}{2}\right)^{0.5}\right]^{1/b} = \left[\frac{\sigma_{max}}{A}\sqrt{\frac{1-R}{2}}\right]^{1/b} \tag{2.95}$$

A modified version of the Walker equation is used in MMPDS-01 [255], (the replacement for MIL-HDBK-5), based on the stress ratio R and an equivalent stress σ_{eq}, where:

$$\begin{aligned} \log\left(N_{f5}\right) &= A_1 + A_2 \log\left(\sigma_{eq} - A_4\right) \\ \sigma_{eq} &= \sigma_{max}\left(1-R\right)^{A_3} \end{aligned} \tag{2.96}$$

The term A_4 represents the fatigue limit stress or endurance limit. Section 9.6.1.4 from [255] gives a thorough discussion of equation (2.96).

2.4.3 Palmgren-Miner linear cumulative damage rule

The Palmgren-Miner, [151] and [152] respectively, linear cumulative damage rule is

$$D = \sum_{k=1}^{n} \frac{n_k}{N_{fk}} \tag{2.97}$$

where D is the summation of damage, n_k are the number of cycles for load case k, and N_{fk} are the number of cycles to failure for case k. $D = 1$ indicates a probability of failure of 0.5 (i.e., half of a population is expected to have failed). As stated in Chapter 1, the linear cumulative damage model neglects any sequence effects that may change fatigue life.

2.4.4 Random fatigue and damage

The number of cycles to failure for a narrowband random process N_{fnb} (see [4, 153, 155, 156]) is

$$N_{fnb} = \int_0^\infty (\sigma_a / A)^{1/b} p(\sigma_a) d\sigma_a \tag{2.98}$$

where $p(\sigma_a)$ is the PDF of stress peaks. For a narrowband response, $p(\sigma_a)$ is assumed to be Rayleigh. It has been shown [4, 153, 155, 156] that (2.98) reduces to

$$N_{fnb} = \left(\frac{\sqrt{2}\sigma_\sigma}{A} \right)^{1/b} \Big/ \Gamma\left(1 - \frac{1}{2b}\right) \tag{2.99}$$

where σ_σ is the standard deviation of stress, and Γ is the gamma function [249]. This equation can be solved for σ_σ to give a narrowband random fatigue equation (similar to sinusoidal fatigue equation (2.89))

$$\sigma_\sigma = \frac{A}{\sqrt{2}} \left[N_{fnb} \Gamma\left(1 - \frac{1}{2b}\right) \right]^b = C N_{fnb}^b \tag{2.100}$$

where the narrowband random fatigue strength coefficient C [156] is

$$C = \frac{A}{\sqrt{2}} \left[\Gamma\left(1 - \frac{1}{2b}\right) \right]^b = \frac{\sigma_f'}{\sqrt{2}} \left[2\Gamma\left(1 - \frac{1}{2b}\right) \right]^b \tag{2.101}$$

When one considers a narrowband Gaussian random process, the expected value of damage for a given random load case reduces to

$$E[D_{nb}] = E[0]\, T \int_0^\infty (\sigma_a / A)^{-1/b} p(\sigma_a) d\sigma_a = E[0]\, T \left(\frac{\sigma_\sigma}{C} \right)^{1/b} \tag{2.102}$$

where $E[0]$ is the expected rate of zero crossings (see equation (2.50)), and T is the duration of the load.

2.4.5 Wideband random fatigue

A wideband random process is more interesting; the distribution of peak amplitudes diverges from the Rayleigh PDF, and the response will include maxima with negative values (see [248] and cited references) and minima with positive values. The de-facto

method for evaluating wideband random fatigue is the time domain rainflow cycle (RFC) counting method [161, 162].

The RFC is defined as follows [163, 165] (see Figure 2.6 from [256]): From a time history, find each local maxima M_i. Consider data less than M_i in the domain backward (left) or forward (right) of M_i. The minima m_i with the smallest downward excursion sets the range of the rainflow cycle. A rainflow cycle is defined in this thesis to have stress minima and maxima (σ_{min}, σ_{max}) or, equivalently, stress amplitude and mean (σ_a, σ_0). A rainflow stress range $\Delta\sigma$ is defined here to be two times (2×) the stress amplitude with no associated mean.

The damage equation based on rainflow cycles in terms of stress minima and maxima is

$$E[D_{mM}] = E[P]T \int_{-\infty}^{\infty}\int_{0}^{\infty} g\left(\sigma_{mM}/A_{mM}\right)^{-1/b} p\left(\sigma_{min},\sigma_{max}\right) d\sigma_{min} d\sigma_{max} \qquad (2.103)$$

or in terms of amplitude and mean stress

$$E[D_{a0}] = E[P]T \int_{-\infty}^{\infty}\int_{0}^{\infty} g\left(\sigma_{a0}/A_{a0}\right)^{-1/b} p\left(\sigma_a,\sigma_0\right) d\sigma_a d\sigma_0 \qquad (2.104)$$

where $p(\sigma_a, \sigma_0)$ is the joint PDF of stress amplitude and mean rainflow cycles, and $g(\sigma/A)$ is a function based on the chosen nonzero mean stress fatigue method (see, for example, equations (2.91) through (2.96) [189]). The problem is that there is no known closed form for the joint rainflow cycle PDF, although there are a number of approximations [34, 183, 208, 209, 257]. The joint probability density function can be estimated numerically as a histogram with cycle counting algorithms (see, for example, the rainflow matrix functions developed by the WAFO group [258]).

It is common to simplify the joint-stress PDF, working instead with the one-dimensional rainflow range PDF $p(\Delta\sigma)$. The wideband damage equation given the rainflow range $p(\Delta\sigma)$ is

$$E[D_{wb}] = E[P]\,T \int_{0}^{\infty} \left(\Delta\sigma/2A\right)^{-1/b} p(\Delta\sigma) d\Delta\sigma \qquad (2.105)$$

One approximation for $p(\Delta\sigma)$ is given by Dirlik's expression [174].

2.4.6 Rainflow matrix

The 2-D histogram of rainflow cycles calculated by WAFO functions is called a rainflow matrix (RFM). A RFM is a convenient numerical estimate of the joint PDF [189]. The RFM has minimum and maximum stress axes that can easily be related to amplitude and mean stress dimensions. Only half of the RFM is used because the minimum stress can never be greater than the maximum stress. The WAFO group has chosen to display the RFM as shown in Figure 2.7 with the minimum stress on the x-axis and maximum stress on the y-axis. The figure also has lines drawn along constant values of the stress ratio R. Constant amplitude conditions are found along diagonals of positive slope, and constant mean stress ranges are found along diagonals of negative slope.

The RFM can also be used to calculate one-dimensional histograms of peak values. The histogram of maxima is found by summing the bins in a row of the RFM; the histogram of minima can be found by summing columns. Amplitude and mean value histograms can be found by summing positive and negative diagonals respectively.

2.4.6.1 Fatigue damage from rainflow matrix [189]

The random fatigue damage equation based on the RFM 2D histogram estimate of the joint PDF is

$$D = \sum_{\sigma_{min}} \sum_{\sigma_{max}} \frac{RFM\left(\sigma_{min}, \sigma_{max}\right)}{N_f\left(\sigma_{min}, \sigma_{max}\right)} \tag{2.106}$$

where RFM(σ_{min}, σ_{min}) are the number of counts in the RFM bin with value of σ_{min} and σ_{min}. The denominator of (2.106) is determined based on a choice of fatigue equations. The estimate using the alternating stress equation (2.90) (with no mean stress effects) is

$$D_{alt} = \sum_{\sigma_{min}} \sum_{\sigma_{max}} \frac{RFM\left(\sigma_{min}, \sigma_{max}\right)}{N_{fa}\left(\sigma_a\right)} = \sum_{\sigma_{min}} \sum_{\sigma_{max}} RFM\left(\sigma_{min}, \sigma_{max}\right)\left(\sigma_a / A\right)^{-1/b} \tag{2.107}$$

The alternating stress $\sigma_a = (\sigma_{max} - \sigma_{min})/2$ varies over the RFM and is calculated for each histogram bin. The estimate using the Morrow equation (2.91) is

$$D_{mi} = \sum_{\sigma_{min}} \sum_{\sigma_{max}} RFM(\sigma_{min}, \sigma_{max}) \left[\sigma_a \Big/ A\left(1 - \frac{\sigma_0}{\sigma_f'}\right) \right]^{-1/b} \tag{2.108}$$

The mean stress $\sigma_0 = (\sigma_{max} + \sigma_{min})/2$ also varies over the RFM and is calculated for each histogram bin. An alternate form of the Morrow equation (2.92) follows this form with $\tilde{\sigma}_{fB}$ substituted for σ_f'. The damage estimate using the Walker equation (2.93) is

$$D_w = \sum_{\sigma_{min}} \sum_{\sigma_{max}} RFM(\sigma_{min}, \sigma_{max}) \left[\frac{\sigma_{max}}{A} \left(\frac{1-R}{2} \right)^{\gamma} \right]^{-1/b} \tag{2.109}$$

The R value is calculated for each histogram bin using equation (2.94). The Smith-Watson-Topper equation (2.95) follows this form with the exponent $\gamma = \frac{1}{2}$. The damage estimate using the modified Walker equation and the equivalent stress equation (2.96) from [255] is

$$D_S = \sum_{\sigma_{min}} \sum_{\sigma_{max}} \frac{RFM(\sigma_{min}, \sigma_{max})}{10\text{^}\left[A_1 + A_2 \log(\sigma_{eq} - A_4) \right]} \tag{2.110}$$

A set of functions has been developed to estimate damage given a RFM and a choice of fatigue equations (2.107) through (2.110).

2.4.7 Time to failure

The damage equation (2.97) can also be written in terms of time

$$D = \sum_{k=1}^{n} \frac{T_k}{T_{fk}} \tag{2.111}$$

where T_k are the periods and T_{fk} times to failure for load case k. This equation can be used to estimate the time to failure

$$T_{fk} = \frac{T_k}{D} \tag{2.112}$$

where the damage D, determined from equations (2.107) through (2.110), includes the integrated effects of all the cycles in the RFM for a load case of time T_k. Time to failure estimates include the effects of the shift in natural frequency, and are useful because they allow comparison of data sets with different analysis time periods.

2.5 Summary

This chapter has served as a brief review of the time and frequency domain equations that will be used throughout the remainder of this thesis to develop random response statistic relationships. Fatigue and damage equations have also been reviewed.

Probability functions have been presented, and the relationships between them have been illustrated. Probability density functions of peak stress response will be used later in this thesis to determine time to failure based on linear and nonlinear fatigue damage equations. The inverse distribution function method to determine a functional value given a predicted probability was introduced and will be used extensively to estimate linear to nonlinear functions from tabulated response histograms. These linear to nonlinear functions will be used with the PDF transform method to predict useful nonlinear PDFs of displacement and stress.

Nonlinear frequency response function estimation techniques, using the reverse-path method, have been introduced. The reverse-path method is general and will be used in novel ways to study the nonlinear displacement and strain response of experimental data in Chapter 3.

2.6 Chapter 2 figures

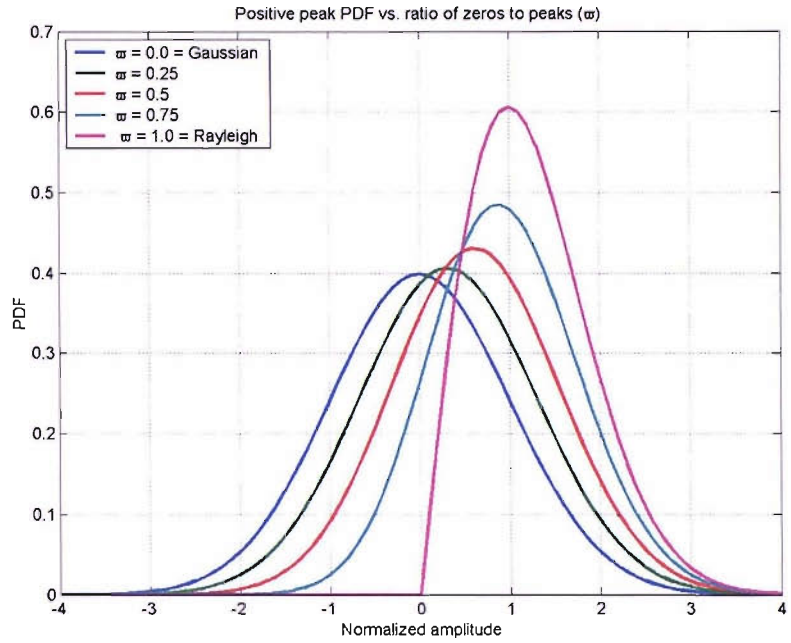

Figure 2.1. Generalized peak PDF shown for various ratios of zeros to peaks ϖ.

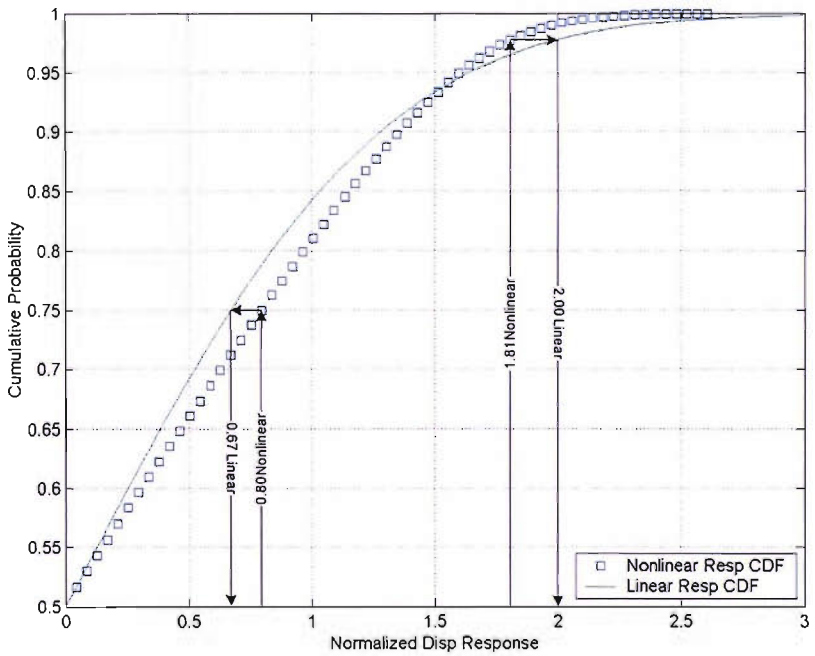

Figure 2.2. Example cumulative distribution functions showing mapping between linear and nonlinear responses with equal probability.

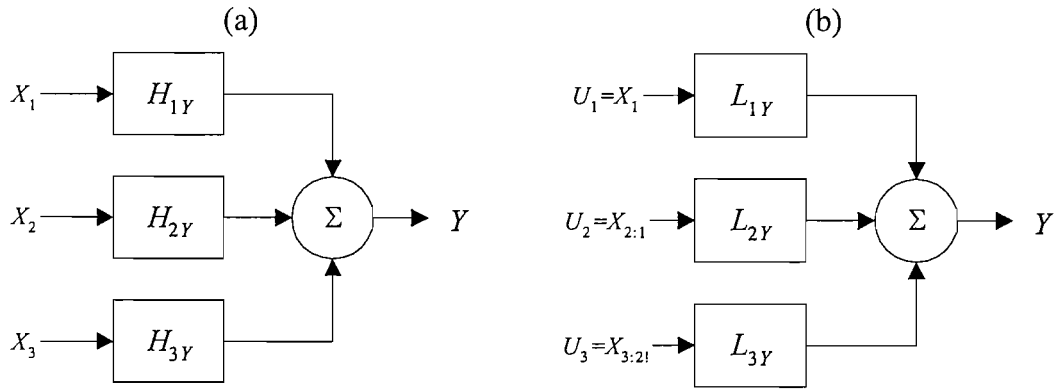

Figure 2.3. MISO system models: (a) system with possibly correlated inputs X_i and frequency response functions H_{iY}, (b) system with conditioned uncorrelated inputs U_i and frequency response functions L_{iY}.

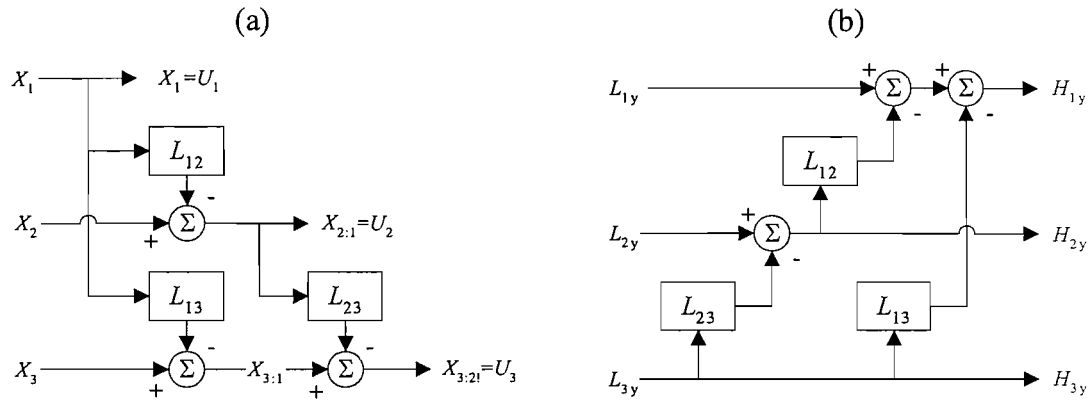

Figure 2.4. MISO system analysis flow diagrams: (a) method to condition inputs X_i forming uncorrelated inputs U_i using frequency response functions L_{ij} and (b) method to calculate frequency response functions H_{iy} given frequency response functions L_{iY}.

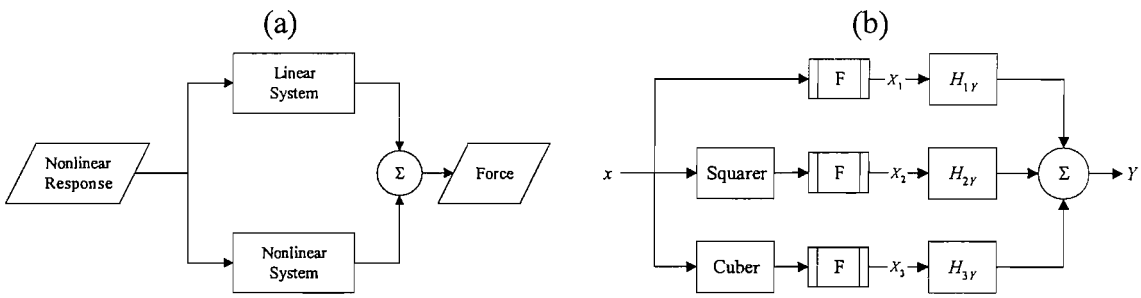

Figure 2.5. Reverse-path dynamic model: (a) Nonlinear response as "mathematical" input to MISO system, (b) nonlinear model with linear, squared, and cubed inputs.

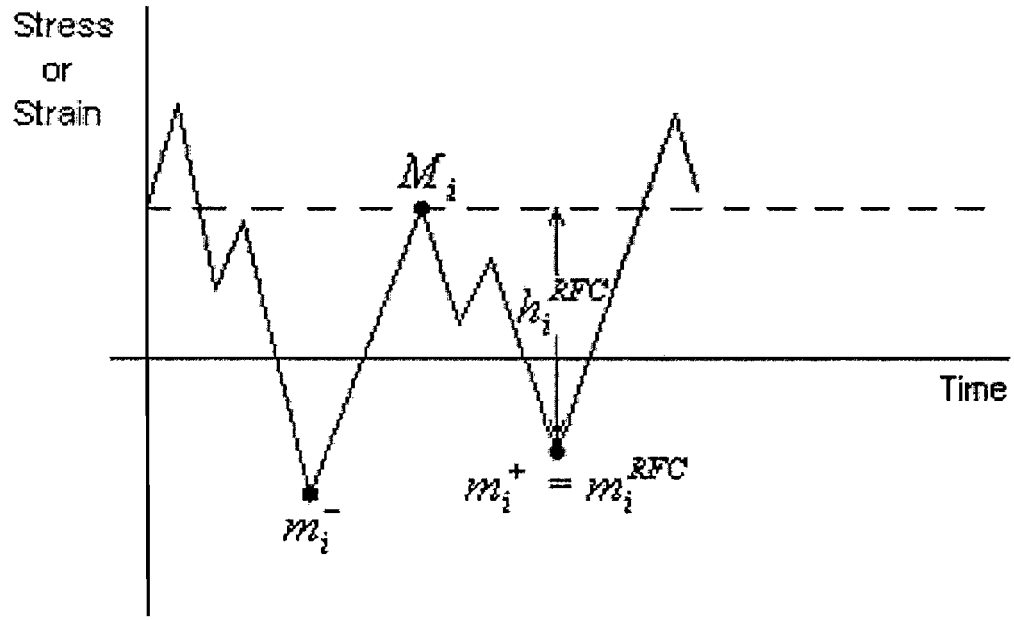

Figure 2.6. Rainflow cycle maximum (M_i) and minima (m_i) for a random time signal. The smaller of the two minima with value less than the maxima determines the range of the rainflow cycle. (From [256] Figure 1.13, derived from [165] Figure 1).

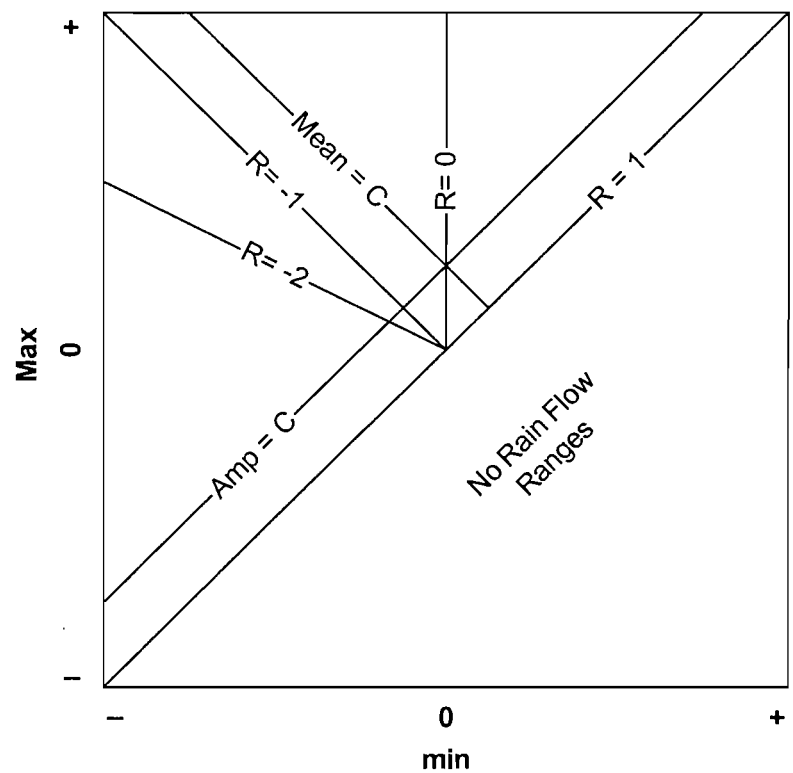

Figure 2.7 The WAFO convention for *RFM* with special stress ratio cases shown.

3 NONLINEAR EXPERIMENTAL SYSTEM ANALYSIS

This chapter discusses the analysis of experiments performed at Wright Patterson Air Force Base (WPAFB), USA. The experiments are discussed in several papers [7, 110], but it is worth briefly describing the experiments and available data here.

The experiments were designed to produce nonlinear responses for a simple physical system "to generate high-quality random response data for comparison with predictions". The original intent was to allow for validation of recent low-order nonlinear modal models, but the data has been extremely useful for this study, as a basis for examining the changes as the system response progresses from mildly to strongly nonlinear. The experiment comprised a clamped-clamped steel beam, with length = 229 mm, width = 12.7 mm and thickness = 0.79 mm. The measured time domain data included the test base shake acceleration input (g), plus displacement (in), and strain ($\mu\varepsilon$) responses at the center of the beam. Strain gages were mounted to the top and bottom surfaces of the beam. The data record length was 88 s with a sample rate of 4096 Hz. The base shake input was a flat acceleration PSD from 20 to 500 Hz with RMS values of 0.5, 1, 2, 4, 8 g. Figure 3.1 shows a picture of the experimental setup.

The nonlinear responses are studied here in both the frequency and time domains. The reverse path identification method [125] is used three different ways to determine linear and nonlinear frequency response functions. The nonlinear frequency response functions, and especially their coherence functions, provided a keen insight into a model that could best describe the response of the system in terms of the displacement and strain states. The linear frequency response functions allowed for estimates of the variance for the linear part of the random response. This proved to be useful as a basis for establishing the linear portion of the linear to nonlinear PDF transforms.

The time domain analysis concentrates on determining basic statistics (mean, variance, skew and kurtosis) plus the underlying probability density and distribution functions. The full data sets were processed to determine histograms of the input and response, which were reduced further to PDFs and CDFs. A second set of time domain analysis

concentrated on sampling the data to determine peak distributions. The peak distributions formed the basis for subsequent fatigue analysis.

Given estimates of the linear response and measured data for the nonlinear response, linear to nonlinear functions were determined using the Inverse Distribution Function (IDF) method. The linear to nonlinear functions were used with the PDF transform method to estimate nonlinear PDFs of nominal and peak response. The wideband experimental data required understanding of the interaction between rates of zero crossings and peaks and their implications to the resulting distribution functions. Work with the PDFs and histograms resulted in an expression to estimate the number of zero crossings and the ratio of zeros to peaks ϖ. Additional equations were derived to determine the value of the peak distribution function at the point of zero peak response.

The nonlinear frequency response functions were used to reconstruct time domain strain responses from the nonlinear displacement data. The linear, squared and cubic nonlinear parts of the time response helped to show their interaction as the response alternated between positive and negative cycles. Low-pass filtering of the data below the second response mode helped to further illustrate the contributions of the linear, squared and cubic terms. Polynomial coefficients were fit to the filtered data for use in ODE simulations, which are discussed in later chapters.

Fatigue life predictions were grouped into wideband and narrowband estimates. The wideband estimates used the raw data for comparison to estimates made by using linear and nonlinear frequency response functions. Narrowband fatigue estimates used the filtered data for comparison to polynomial and PDF transform estimates from the displacement data. In each case, three different fatigue life models (a baseline model and two models that included mean stress effects) were used to explore the sensitivity of the nonlinear membrane effects on life estimates.

3.1 Frequency domain analysis of wideband system

The frequency domain analysis of the WPAFB data is presented before the time domain analysis, because the majority of the nonlinear aspects of the system response are easily shown and determined in the frequency domain. The basic PSD measurements of the

response are shown first to illustrate the shift and broadening of the response. Next, much emphasis is devoted to the application of the reverse path identification technique to the test data. Several nonlinear frequency response functions help to explain the underlying nature of the nonlinear system. These frequency response functions are used later in Section 3.3.1 to estimate the strain response from nonlinear displacement inputs.

3.1.1 PSD of displacement and strain response

The PSD for the beam center displacement response is shown in Figure 3.2. Note how the response in the frequency regions of the first and second modes becomes much broader. Also note how the second and third harmonics of the natural frequencies are evident at even the lowest input level.

The PSD of average strain (average of the top and bottom strain) response is shown in Figure 3.2(a). Note the similarities and differences to the displacement PSD; the second harmonic is now much stronger, and the relative magnitude of the second strain response mode is much greater than the displacement mode, as shown in Figure 3.2(b). It is also apparent that the third harmonic of the fundamental becomes obscured by the response of the second mode at inputs above 2 g. These observations will be discussed further in the next sections.

3.1.2 Nonlinear system identification

The reverse path nonlinear system identification method proved to be useful for determining the displacement to force relationships for the WPAFB data. This is the "textbook" [125, 143] use where the nonlinear displacement and the squared and cubed version of it are used as multiple "mathematical inputs" to a system with force "mathematical response". The force was presumed to be proportional to the measured base acceleration, using a mass of 18 grams (see Section 4.1).

The reverse path identification method (introduced in Section 2.2.6) estimates the parts of the response that are correlated to the linear, squared and cubed displacement input.

The estimated linear (see Figure 3.3) and cubic (see Figure 3.4(b)) displacement to force frequency response functions (FRFs) show consistent results for all test levels, while the squared displacement FRFs (see Figure 3.4(a)) exhibit markedly different, yet stable (in the low-frequency range), results at each level. The coherence functions show that the nonlinear model was able to account for most of the response at the low 0.5 g input level (see Figure 3.5(a)), but, this nonlinear model did not fair as well at the higher input levels (see Figure 3.5(b)). It is interesting to see that at the higher level, the cubic displacement term accounted for the majority of the coherent response over the range between the first and second observed peaks in the system response. The coherence plots show that the squared terms were noticeable at the low level (perhaps caused by a "pre-buckled" condition), but they were insignificant at the highest level.

The WPAFB top surface strain gage response data was also used with the reverse path identification method to estimate strain to force FRFs. These results were not as encouraging. The FRFs for linear (Figure 3.6), squared (Figure 3.7(a)) and cubed strains (Figure 3.7(b)) are not as "clean" as the displacement to force data. The squared and cubic strain FRFs are especially noisy. A telling indication of the quality of these nonlinear FRF estimates can be seen in the coherence plots. The lowest level strain input case (shown in Figure 3.8(a)) produced respectable FRFs (and corresponding coherence estimates), but the higher levels (shown in Figure 3.8(b)) yielded poor results.

The reverse path method was then applied to the data to determine nonlinear top surface displacement to strain FRFs, where the displacement is the "mathematical input" and the strain is the response. The linear FRFs (see Figure 3.9) showed a very consistent set of results throughout the frequency range. The general "upturn" in the strain response, as displacement increased, will be discussed further in the next section. The squared (see Figure 3.10(a)) and cubed (see Figure 3.10(b)) displacement to strain FRFs show consistent trends over the entire frequency range and the coherence functions (see Figure 3.11) show that the nonlinear model can account for most of the measured response. This nonlinear displacement to strain model is arguably better than the displacement to force model (compare the coherence results in Figure 3.5 and Figure 3.11). These FRF estimates were used to establish some of the parameters for PDF transforms and the SDOF ODE models discussed in the next two chapters.

3.1.3 Linear frequency response function parameter estimation

One important outcome of this nonlinear FRF estimation process is a method to estimate the linear response of the system. The linear FRFs of displacement to force and strain to force were used to estimate the linear random response standard deviation of each input level. At first, an attempt was made to use the FRFs in their raw numerical format. This proved to be undesirable because small changes in the numerical values of the FRF estimates produced vastly different results. A parameter estimation of the multi degree of freedom (MDOF) transfer function proved to be more stable and informative.

The first step of this MDOF parameter estimation was to determine the force to displacement (and later force to strain) FRF. These were simply the reciprocal of the displacement to force FRF. The Laplace domain numerator and denominator polynomial representations of the transfer function were estimated and then converted into their equivalent roots (or poles) format. The modal roots are, assuming a viscous model for the modal damping,

$$\lambda_i = \omega_i\left(-\zeta_i \pm \sqrt{\zeta_i^2 - 1}\right) = -\omega_i\zeta_i \pm i\omega_i\sqrt{1-\zeta_i^2} \tag{3.1}$$

This was useful for determining the modal parameters of the FRF

$$\begin{aligned} \omega_i &= \sqrt{-\left[\text{real}\left(\lambda_i\right)^2 - \text{imag}\left(\lambda_i\right)^2\right]} \\ \zeta_i &= -\text{real}\left(\lambda_i\right)/\omega_i \end{aligned} \tag{3.2}$$

It was encouraging to find that the estimated parameters were comparatively consistent among the runs, as given in Table 3.1. There are two outliers: the 2 g (low ζ_1) and 8 g (large ζ_1 and higher f_{n1}) estimates. The average 1 g linear displacement response estimate σ_x, determined from the other three estimates, was 0.4293 mm. This was used as the linear response baseline for linear distribution function estimates (see Section 3.2.3).

Example FRFs and transfer function estimates are shown in Figure 3.12(a). The parameter estimates improved when the FFT frequency spacing was reduced to 0.25 Hz with a corresponding number of averages of 22. This was an interesting tradeoff; the

smaller number of averages yielded a more variable point-to-point FRF estimate, but the larger number of points and the finer frequency spacing allowed for better estimates of the modal parameters.

A typical numerical example of the force input to displacement output transfer function for the 1 g input is

$$H_{Fx} = \frac{x}{F} = \frac{41s^2 - 2.0\times10^4 s + 4.7\times10^8}{s^4 + 25s^3 + 7.1\times10^6 s^2 + 1.5\times10^7 s + 1.7\times10^{12}} \frac{\text{m}}{\text{N}} \tag{3.3}$$

The force input to strain output modal parameters were estimated in a similar fashion. The eigenvalue (modal frequency and damping) estimates (see Table 3.2) are similar to those estimated from the force input to displacement output FRFs. The force to strain graphs show strong similarities to the force to displacement graphs (compare Figure 3.12(a) and Figure 3.12(b)). Note that the second-mode strain response is proportionately higher than the displacement response. It is also interesting to note that the first-mode damping estimates based on strain tend to be about twice as large as that of the displacement estimates, while the second-mode estimates are much closer in value (see Table 3.2). A typical numerical example of the force input to strain output transfer function for the 1 g input is

$$H_{F\varepsilon} = \frac{\varepsilon}{F} = \frac{4.4\times10^6 s^2 + 4.7\times10^{10} s - 7.2\times10^{13}}{s^4 + 25s^3 + 7.1\times10^6 s^2 + 3.0\times10^7 s + 1.7\times10^{12}} \frac{\mu\varepsilon}{\text{N}} \tag{3.4}$$

Note the similarity in the denominators of this function and the displacement transfer function given in equation (3.3).

MDOF parameter estimates were then made with the displacement to strain FRFs (see for example, Figure 3.13(a)). A typical numerical example of this displacement input to strain output transfer function for the data from the 1 g input case is

$$H_{\varepsilon x} = \frac{\varepsilon}{x} = \frac{1.6\times10^5 s^2 + 7.5\times10^8 s - 1.7\times10^{12}}{s^2 + 115s + 1.1\times10^7} \frac{\mu\varepsilon}{\text{m}} \tag{3.5}$$

At first this is not informative, but considering that the ratio of transfer function equations (3.4) and (3.3) (assuming that the denominators are equal) is

$$\frac{\varepsilon}{x} = \frac{\varepsilon}{F}\frac{F}{x} = \frac{4.4\times10^{6}s^{2} + 4.7\times10^{10}s - 7.2\times10^{13}}{41s^{2} - 2.0\times10^{4}s + 4.7\times10^{8}}\frac{\mu\varepsilon}{\mathrm{m}}$$
$$\frac{\varepsilon}{x} = \frac{1.1\times10^{5}s^{2} + 1.1\times10^{9}s - 1.7\times10^{12}}{s^{2} - 493s + 1.1\times10^{7}}\frac{\mu\varepsilon}{\mathrm{m}} \tag{3.6}$$

one can recognize the similarity to equation (3.5). A plot of this transfer function estimate and the raw FRF from the reverse identification method are shown in Figure 3.13(b).

3.1.4 Flow diagrams of nonlinear strain and displacement models

The nonlinear transfer function estimation results suggest two methods for representing the nonlinear force to strain model: one based on a series connection of nonlinear displacement and strain FRFs, and a second based on a parallel connection of modal models.

The first model (see Figure 3.14) is based on the two most successful nonlinear system identification models from the previous section, namely, the displacement to force and displacement to strain nonlinear FRFs. The second model is an attempt to show how the modal models (labeled osc1 and osc2 in Figure 3.15) are linked to both the displacement and strain responses. It may be possible to refine this modal model further to allow more of the nonlinear combination of terms to be described in the "modal domain."

3.2 Time domain analysis of wideband system

The following sections cover the time domain analysis of the WPAFB data using the methods introduced in Chapter 2.

3.2.1 Basis statistics

The first step in the time domain analysis was to determine the basic and central statistical moments of the test data. The results given in Table 3.3 agree with the published values [7]. The input random acceleration statistics (subscript a) help to

confirm that it was normally distributed with near-zero mean and skew values, and kurtosis approximately equal to 3 (see Table 3.3).

The displacement data (subscript *y*) show indications of the nonlinear behavior of the system (as indicated by a kurtosis value less than 3), with additional nonzero mean and skew that will need explanation. The top and bottom strain gage data sets (subscripts *top* & *bot* respectively) (see Table 3.4) are even more complicated. If the test item were truly symmetric, as designed, the response statistics would be equal in magnitude with an opposite sign for the odd measures (mean and skew). The authors [7] discussed the results from three sets of experiments noting that an unfortunate outcome of the clamped-clamped design is its sensitivity to temperature-induced preloads. It was assumed that this data set had no preload, but the skew and nonzero mean strain measures tend to indicate that there may have been a small amount of compressive preload. The low-level tests (0.5 and 1 g inputs) showed compressive mean strains on the bottom strain gage μ_{bot} and slightly positive mean values on the top strain gage μ_{top}. This may be an indication of a small amount of static buckling as a result of a compressive preload.

The standard deviation of strain response was also different for the top and bottom strain gages. The top strain σ_{top} was always greater that the bottom strain σ_{bot}. This may be explained by differences in strain gage placement or instrumentation gain factors.

3.2.2 Histograms and response PDFs from data

The experimental data was processed further to determine histograms, PDFs, and CDFs. To begin, PDFs of the acceleration input were determined from histograms, as shown in Figure 3.16(a). This figure shows that the input appears normally distributed as intended. Displacement response PDFs (see Figure 3.16(b)) show non-normal behavior with the addition of some asymmetry that may be caused by the hypothesized pre-buckled state of the beam.

The strain response PDFs are even more non-normal. The strain response at the top surface of the beam (Figure 3.17(a)) shows nearly normal behavior at the lowest input level, while the bottom surface strain (Figure 3.17(b)) shows a highly skewed response

for the same input. It is interesting to observe that the large amplitude response points at this lowest input level tend to return to the normal PDF values. As the input increases, both the top and bottom strains tend to skew away from a normal PDF, which is due to the addition of tensile membrane effects.

The strain data was further processed to separate the bending and membrane strains. Ideally, the top and bottom strains would be symmetric such that

$$\begin{aligned} \varepsilon_{top} &= \varepsilon_{bend} + \varepsilon_{memb} \\ \varepsilon_{bot} &= -\varepsilon_{bend} + \varepsilon_{memb} \end{aligned} \tag{3.7}$$

The addition of instrument gain (k) and bias (b) errors give measured values $\hat{\varepsilon}$

$$\begin{aligned} \hat{\varepsilon}_{top} &= k_1\varepsilon_{top} + b_1 = k_1\left(\varepsilon_{bend} + \varepsilon_{memb}\right) + b_1 \\ \hat{\varepsilon}_{bot} &= k_2\varepsilon_{bot} + b_2 = k_2\left(-\varepsilon_{bend} + \varepsilon_{memb}\right) + b_2 \end{aligned} \tag{3.8}$$

Also, assume further that

$$\begin{aligned} \sigma_{\varepsilon_{top}} &= \sigma_{\varepsilon_{bot}} \\ \sigma_{\hat{\varepsilon}_{top}} &= k_1\sigma_{\varepsilon_{top}};\ \sigma_{\hat{\varepsilon}_{bot}} = k_2\sigma_{\varepsilon_{bot}} = k_2\sigma_{\varepsilon_{top}} \end{aligned} \tag{3.9}$$

and, if the first gain $k_1 = 1$

$$k_2 = \frac{\sigma_{\hat{\varepsilon}_{bot}}}{\sigma_{\hat{\varepsilon}_{top}}} \tag{3.10}$$

$$\hat{\varepsilon}_{top} = \varepsilon_{bend} + \varepsilon_{memb} + b_1$$

or

$$\frac{\hat{\varepsilon}_{bot}}{k_2} = \frac{\hat{\varepsilon}_{bot}\sigma_{\hat{\varepsilon}_{top}}}{\sigma_{\hat{\varepsilon}_{bot}}} = \left(-\varepsilon_{bend} + \varepsilon_{memb}\right) + b_3 \tag{3.11}$$

subtracting the two equations gives

$$\begin{aligned} \hat{\varepsilon}_{top} - \frac{\hat{\varepsilon}_{bot}\sigma_{\hat{\varepsilon}_{top}}}{\sigma_{\hat{\varepsilon}_{bot}}} &= 2\varepsilon_{bend} + \left(b_1 - b_3\right) \\ \varepsilon_{bend} &= \frac{1}{2}\left[\hat{\varepsilon}_{top} - \frac{\hat{\varepsilon}_{bot}\sigma_{\hat{\varepsilon}_{top}}}{\sigma_{\hat{\varepsilon}_{bot}}} - \left(b_1 - b_3\right)\right] \end{aligned} \tag{3.12}$$

Presuming that the bias errors are constant and that the bending strain has zero mean, the unbiased bending strain can be estimated by

$$\varepsilon_{bend} = \frac{1}{2}\left(\hat{\varepsilon}_{top} - \frac{\hat{\varepsilon}_{bot}\sigma_{\hat{\varepsilon}_{top}}}{\sigma_{\hat{\varepsilon}_{bot}}} - E\left[\hat{\varepsilon}_{top} - \frac{\hat{\varepsilon}_{bot}\sigma_{\hat{\varepsilon}_{top}}}{\sigma_{\hat{\varepsilon}_{bot}}} \right] \right) \tag{3.13}$$

The two equations in (3.11) can be added to form an estimate of the membrane strain.

$$\begin{aligned} \hat{\varepsilon}_{top} + \frac{\hat{\varepsilon}_{bot}\sigma_{\hat{\varepsilon}_{top}}}{\sigma_{\hat{\varepsilon}_{bot}}} &= 2\varepsilon_{mem} + (b_1 - b_3) \\ \varepsilon_{mem} &= \frac{1}{2}\left[\hat{\varepsilon}_{top} + \frac{\hat{\varepsilon}_{bot}\sigma_{\hat{\varepsilon}_{top}}}{\sigma_{\hat{\varepsilon}_{bot}}} - (b_1 - b_3) \right] \end{aligned} \tag{3.14}$$

Unfortunately, the membrane strain does not have zero mean, so the combined bias errors are not easily determined. Fortunately, the membrane strain should always be positive, allowing a graphical estimation of the combined bias errors.

Comparison of these results (Table 3.5) with the other results is of interest. The kurtosis of the bending strain estimates is nearly the same as the kurtosis of displacement (see Table 3.3). This link between the bending strain and displacement is expected and will be investigated more in the next sections. The skew of the bending strains is larger than expected (especially at low-input levels) and is thought to be due to a compressive preload-induced buckling of the beam.

The bending and membrane strain estimates were then used to determine PDFs. The bending strain PDFs (Figure 3.18(a)) are now "enforced" to be nearly symmetric, yet non-normal, while the membrane strain PDFs (Figure 3.18(b)) are almost completely positive. For comparison, a chi-squared PDF (the theoretical result for a squared normal random signal [125]) is shown with the membrane strain PDFs.

3.2.3 Linear to nonlinear function estimation using IDF method

The response PDF estimates of the nonlinear displacement determined above can be used to determine linear to nonlinear functions, using the inverse distribution function (IDF) method (see Section 2.1.3). When working with nonlinear data, it is convenient to

start with the nonlinear estimates of the distribution function determined from a histogram of the measured data. The histogram H of displacement y is (see also Section 2.1.2)

$$H[y,W] = \text{Count}\left[\left(y - \frac{W}{2}\right) \le y(t) \le \left(y + \frac{W}{2}\right)\right] \tag{3.15}$$

Note that y is the bin center and W is the bin width. The estimate of the distribution function $\hat{F}(y_i)$ from the binned data is

$$\hat{F}(y_i) = \frac{\sum_{j=1}^{i} H[y_j, W]}{N} = \hat{\rho}_i \tag{3.16}$$

where N is the total number of counts in all bins, and ρ_i is the cumulative probability at bin i. Note that it is important to define the estimate of the distribution function at the upper bound of the histogram bins:

$$\hat{y}_i = y_i + \frac{W}{2} \tag{3.17}$$

It should be stated that $\hat{F}(\hat{y}_i)$ is an unbiased estimate of $F(y)$ at $\hat{y}_i$.

Then, having estimated the nonlinear (non-normal) distribution function, at each value of ρ_i, find the linear distribution function F_{lin} with equal probability

$$\hat{F}_{nl}(\hat{y}_i) = \rho_i = F_{lin}(x_i) \tag{3.18}$$

The corresponding linear (normal) function value x_i, is determined using the IDF

$$x_i = F_{lin}^{-1}\left(F_{nl}(\hat{y}_i)\right) \tag{3.19}$$

If the linear distribution function is presumed normal, then the linear function value x can be estimated by using the inverse distribution function for a normal distribution (see equation 2.30)

$$F_{norm}^{-1}(\rho) = \sigma_x \sqrt{2}\,\mathrm{erf}^{-1}(2\rho - 1) = x \tag{3.20}$$

where erf^{-1} is the inverse error function, or, in terms of the estimated nonlinear distribution function by

$$x_i = \sigma_x \sqrt{2}\,\mathrm{erf}^{-1}\left(2F_{nl}(\hat{y}_i) - 1\right) \tag{3.21}$$

An example nonlinear (non-normal) distribution function (CDF) determined from the 8 g displacement PDF is shown in Figure 3.19(a) overlaid with a linear (normal) CDF. The IDF method can be traced graphically on Figure 3.19(b), which shows the positive response portion of the linear and nonlinear CDFs. For example, given a nonlinear normalized displacement of 0.8 σ_y, what linear displacement will have the same CDF? By inspection, the corresponding linear displacement is approximately 0.7 σ_x. Another example is 1.8 σ_y nonlinear mapping to 2.0 σ_x linear. The linear displacement response σ_x= 0.429 mm for a base acceleration input σ_a= 1 g was estimated from the linear transfer function of displacement response for the Gaussian random input (see Section 3.1.3). The linear displacement response σ_x for each test input case was determined by scaling the 1 g σ_x by the corresponding input acceleration level. Nonlinear displacement responses are given in Table 3.3.

The IDF method can be repeated at every nonlinear response CDF value. The resulting x and y pairs are shown in Figure 3.20(a). The positive pairs are shown again in Figure 3.20(b) with a log-log scale. Note that the results from each input level form a set of unique curves.

3.2.3.1 Curve fitting the linear to nonlinear functions

In previous attempts [160] a piecewise power-law was used to curve fit the RMS stress linear to nonlinear functions. Research with similar nonlinear functions [259] suggests that a polynomial function of the nonlinear response is the preferred method to curve fit "stress stiffening" data

$$\begin{aligned} h(y) &= x \\ c_1 y + c_2 y^2 + \cdots + c_n y^n &= x \end{aligned} \tag{3.22}$$

where y and x are the nonlinear and linear displacement levels respectively. Note that the polynomial is now on the left hand side of the equation (see Section 2.1.5). A third order polynomial proved to be a good fit of the linear to nonlinear response function data. These linear to nonlinear polynomial functions are used extensively in this thesis as part of the PDF transform method to predict nonlinear PDFs (see Section 2.1.5) and subsequent estimates of σ_y, kurtosis, rates of zero crossings (see Section 4.2.12) and fatigue life.

3.2.4 Response rates

The response rates (see Section 2.1.4) of the displacement and strain results were calculated using WAFO MATLAB functions [258] (which determine level crossings and response peaks). An interesting observation is that the bending strain rates of zero crossings and peaks are significantly lower than the displacement rates (see Table 3.6). Also, the ratio ϖ is not as constant for each input level. The rates for bending strain are similar to the rates of top and bottom strain (see Table 3.7), except for the highest input of 8 g. At the highest input level, the addition of the membrane strain has shifted the ratio ϖ up significantly for the top and bottom strains, while the bending strain has not increased proportionately.

3.2.5 Peak PDFs from data

Normalized peak displacement PDFs, determined from displacement RFMs (see also Section 2.4.6), are shown in Figure 3.21(a) for three of the input levels, with a linear peak PDF (determined at a ratio $\varpi = 0.967$) for comparison. The data shows strong nonlinear behavior, with increasing probability for negative-valued maxima. The peak displacement RFM for the highest input level (8 g) is also shown (Figure 3.21(b)) for comparison to other peak RFM, which will be presented later.

One major observation from the data is that the ratio ϖ was not constant for each input data set, as given in Table 3.6. This change in the ratio ϖ with the input level (and degree of nonlinearity) required a decision regarding the manner in which one proceeds with the IDF method discussed above in Section 3.2.3. The logical choices were to use

one linear CDF, based on the linear ratio ϖ, or to allow the ratio ϖ to change and, therefore, determine a corresponding linear peak CDF for each input level. Figure 3.22 shows the normalized linear and nonlinear CDFs for the data. Notice that the CDF for the nonlinear data at the highest input of 8 g crosses the zero displacement level at a cumulative probability of approximately 0.8, while the CDF for the lowest level input of 0.5 g crosses the zero displacement level at approximately 0.2. The linear peak CDFs, based on variable ratios ϖ, cross at about the same level as the nonlinear data.

A more compelling argument for a variable ratio ϖ comes when one inspects the linear to nonlinear functions determined using the IDF method. Figure 3.23(a) shows the linear to nonlinear function, based on a fixed linear peak CDF, while Figure 3.23(b) shows the function based on a variable linear peak CDF. Log-log plots of these functions are shown in Figure 3.24. In both cases the data does not all fall along one common curve. The data for the variable linear-peak CDF functions does tend to cross the zero-zero point, which is considered to be desirable when curve fitting. One could attempt to develop a family of curve-fit parameters for each input level using the fixed linear peak CDF data, but this would require that an additional constant coefficient c_0 be added to the polynomial function in equation (3.22). Instead, a single curve fit of the linear to nonlinear function data, through only the most extreme positive peak values (those above about 2 σ) from all of the input levels, was used.

$$c_1 y + c_2 y^2 + c_3 y^3 = x \tag{3.23}$$

The set of points used, and the polynomial curve fit of the data, are shown in Figure 3.24. It is promising to note that a polynomial curve fit of the same set of data points, determined from the fixed linear peak CDF, yield similar coefficients, as given in Table 3.8.

3.2.5.1 Nonlinear peak PDFs estimated with PDF transform

Using the PDF transform method (introduced in section 2.1.5), nonlinear peak PDFs were determined using this single set of coefficients. To review, the peak PDF transform for this LHS function is:

$$p_{nl\,peak}(y,\varpi) = |h'(y)|\, p_{peak}(h(y),\varpi) \tag{3.24}$$

where $h(y)$ is from equation (3.22) and p_{peak} is from equation (2.20). The PDF transform method was attempted two ways: the first using a fixed linear peak PDF based on a fixed ratio ϖ calculated using equations (2.61) and (2.53) with the 0.5 g linear transfer function estimate (see Section 3.1.3), and the second using a variable linear peak PDF based on the variable ratio ϖ (given in Table 3.6) determined for each set of test data. A goodness-of-fit test of these transformed PDFs was performed, with the results given in Table 3.9. The results are encouraging, especially for the variable linear peak PDF cases. Observe that both methods yield good fit tests at the lower input level, but, as the input increases, the transformed PDFs based on the variable linear peak PDFs continue to show good fit test values.

Comparisons of the PDF transforms are shown in Figure 3.25 for the highest test input. Notice that the nonlinear peak PDF estimate made using the fixed linear peak PDF is in error in both the low-amplitude and mid-amplitude regions. In the high-amplitude range, the estimate tends to be conservatively high, which may prove to be acceptable when determining fatigue damage.

3.2.5.2 Peak histogram relationships

An interesting finding occurs when estimating the histogram of peaks for use in the chi-squared test. When using the variable PDF transform based on the ratio of zeros to peaks ϖ_k, where k is an index for a particular input level, the histogram of peaks at that input level is simply (see also equation (3.15))

$$H[x,W]_{nl:k} = N_{p:k} W\, p_{nl:k}(x,\varpi_k) \tag{3.25}$$

When the estimate of the nonlinear peak PDF is made based on a PDF determined by an assumed ϖ_a that is different than the ϖ_k for this input level (e.g., $\varpi_a = 1$ for a linear Rayleigh PDF), the histogram of peaks can be approximated as

$$\hat{H}_{nl:k} = N_{p:k}\left(\frac{\varpi_k}{\varpi_a}\right) W\, p_{nl:a} = H_{p:a}\left(\frac{\Phi_k\left[0_x^+\right]}{\Phi_a\left[0_x^+\right]}\right) W\, p_{nl:a} \tag{3.26}$$

Figure 3.26(a) shows peak histogram estimates when this correction is made for the WPAFB data at the 8 g input level. Note how well the agreement is in the high-amplitude regions where fatigue damage is most important.

This leads to an interesting observation: Given a generalized zero-mean normal random response, the generalized histogram of positive maxima is equal to the Rayleigh histogram of maxima plus the generalized histogram of negative maxima in reverse order. An example of this relationship is shown in Figure 3.26(b).

An outcome of this observation is a method for estimating the number of zero crossings from a general peak response histogram. Let N_{p+} be the total number of positive peaks (or maxima) determined from a data set histogram by

$$N_{p^+} = \sum_{i=-\infty}^{\infty} H_{p^+}[x_i, W] \tag{3.27}$$

and the subset of these peaks that occur at negative values are

$$N_{-p^+} = \sum_{x_i=-\infty}^{0} H_{p^+}[x_i, W] \tag{3.28}$$

From the discussion above, the number of maxima with positive values

$$N_{+p^+} = \sum_{x_i>0}^{\infty} H_{p^+}[x_i, W] \tag{3.29}$$

is equal to the number of zero crossings (determined from a Rayleigh histogram (due to the fact that narrow band system has an equal number of peaks and zero crossings)) plus the number of negative value maxima

$$N_{+p^+} = N_0 + N_{-p^+} \tag{3.30}$$

Relating these to the total number of peaks from equation (3.27)

$$N_{p^+} = N_{-p^+} + N_{+p^+} \tag{3.31}$$

yields an interesting relationship

$$N_0 = N_{p^+} - 2N_{-p^+} \tag{3.32}$$

and an equation for the ratio of zeros to peaks

$$\varpi = \frac{N_0}{N_{p^+}} = 1 - \frac{2N_{-p^+}}{N_{p^+}} \tag{3.33}$$

An intuitive check for this relationship can be made for the two limiting cases of a peak distribution. When the response is ideally narrowband, the number of negative-value maxima is zero, therefore

$$\varpi_{nb} = 1 - \frac{2(0)}{N_{p^+}} = 1 \tag{3.34}$$

When the response is ideally wideband, the number of negative-value maxima is the same as the number positive-value maxima, therefore

$$\varpi_{wb} = 1 - \frac{2N_{-p^+}}{N_{-p^+} + N_{+p^+}} = 1 - \frac{2N_{-p^+}}{N_{-p^+} + N_{-p^+}} = 0 \tag{3.35}$$

These two results agree with the definitions of ϖ for narrowband and wideband responses.

Further, this relationship has been found to be useful for estimating the value at which a peak distribution function crosses zero. Starting with the generalized peak distribution function (equation (2.28))

$$\begin{aligned} F_{peak}(z,\varpi) &= 1 - Q_1(z) - \varpi \exp\left(-\frac{z^2}{2}\right)\left[1 - Q_2(z)\right] \\ Q_n(z) &= \frac{1}{2}\operatorname{erfc}\left(\frac{z}{k_n\sqrt{2}}\right) \end{aligned} \tag{3.36}$$

at $z = 0$, this reduces to

$$F_{peak}(0,\varpi) = 1 - Q_1(0) - \varpi\left[1 - Q_2(0)\right]$$
$$Q_n(0) = \frac{1}{2}\operatorname{erfc}\left(\frac{0}{k_n\sqrt{2}}\right) = \frac{1}{2} \tag{3.37}$$
$$F_{peak}(0,\varpi) = 1 - \frac{1}{2} - \frac{\varpi}{2} = \frac{1-\varpi}{2}$$

The intuitive check is, again, informative. When the response is ideally narrowband, $\varpi = 1$

$$F_{ray}(0,1) = \frac{1-\varpi_{nb}}{2} = \frac{1-1}{2} = 0 \tag{3.38}$$

When the response is ideally wideband, $\varpi = 0$

$$F_{norm}(0,0) = \frac{1-\varpi_{wb}}{2} = \frac{1-0}{2} = \frac{1}{2} \tag{3.39}$$

These two results agree with the values of Rayleigh and normal distribution functions at zero. One last substitution of equations is of interest. Observe that the distribution function at 0 can be estimated from cumulative histograms by

$$F_{peak}(0,\varpi) \approx \frac{1}{N_{p^+}} \sum_{i=-\infty}^{0} H_p\left[x_i, W\right] = \frac{N_{-p^+}}{N_{p^+}} \tag{3.40}$$

substituting equation (3.33) into equation (3.37) gives

$$F_{peak}(0,\varpi) = \frac{1 - \left(1 - \dfrac{2N_{-p^+}}{N_{p^+}}\right)}{2} = \frac{\dfrac{2N_{-p^+}}{N_{p^+}}}{2} = \frac{N_{-p^+}}{N_{p^+}} \tag{3.41}$$

which completes the discussion of the findings.

3.2.6 RFMs and peak PDFs of strain response

The bending strain data was also sampled to determine peak strain RFMs and PDFs. The RFM for this bending strain data (see for example, the 8 g input data in

Figure 3.27(a)) has many more mid-amplitude cycles distributed off the main diagonal. Peak PDFs of the bending strain are shown in Figure 3.27(b).

A typical RFM of membrane strain is shown in Figure 3.28(a) for the 2 g input case. This figure shows that the strain instrumentation bias estimate, based on equation (3.14) , may have been slightly in error. Ideally, the median minimum peak strain value would have been zero. In this case, the RFM of the data suggests that the median minimum peak strain is one bin off. Peak membrane strain PDFs determined from the RFMs are shown in Figure 3.28(b). Here, the results are compared to a linear Rayleigh PDF. Theoretically, the peak membrane strain PDF for a squared response would be infinite at zero strain. This is not strictly the case for this data, perhaps as a result of the errors in bias estimation or perhaps because of the errors based on assuming the simple model of total strain (see equation (3.7)).

The peak top and bottom strain RFMs are some of the most interesting yet investigated. The progression from a mildly to strongly nonlinear peak strain response is best studied as a series of RFMs. The top strain RFMs are shown in Figure 3.29 through Figure 3.30(b) for three input levels.

The first major observation is that the main diagonal of the RFM is bent toward the positive strain ranges. Another interesting observation is that there seems to be a minimum "mean" strain value that limits the response in the negative values of strain. One explanation of the minimum mean strain value is due to the higher frequency strain responses riding on top of a lower frequency strain response, which is limited to some minimum value (see discussion in Section and 3.3.1.2 and Figure 3.45(b)).

PDF transforms based on strain functions are discussed in Section 3.3.2.

3.3 Response estimates

The nonlinear functions estimated in the previous sections will be used next to investigate some interesting aspects of the WPAFB experimental results.

3.3.1 Time domain strain estimates from displacements using FRFs

The nonlinear FRFs estimated using the reverse MISO method can be used to estimate time domain responses with simple forward and inverse Fourier transforms, as shown in Figure 3.31. The measured nonlinear displacement time domain data is squared and cubed to form the other two inputs (after being Fourier transformed) for the three nonlinear displacement to strain FRFs. The nonlinear strain component estimates are then converted back to the time domain, using inverse Fourier transforms. The strain components are then summed (with the appropriate sign) to estimate the total strain response at the top and bottom surfaces.

Note: The Fourier transform FRF method was used here for simplicity; a digital filtering method based on the Laplace domain form of the estimated transfer functions could be used as well. This digital filtering method may be useful when working with purely theoretical data (e.g. from finite element models).

The nonlinear strain estimation method is demonstrated here with two cases: a full frequency range case and a filtered frequency range case.

3.3.1.1 Strain response estimates from nonlinear FRFs

The first method uses the raw point-by-point numerical estimates for the three FRFs of displacement to strain over the full frequency range. This set of estimates includes the effects of the second, higher frequency mode (see the linear and cubic FRFs, Figure 3.32 and Figure 3.33(b), respectively) and low-frequency variations below the bandwidth of the input (see both the squared and cubic FRFs in Figure 3.33). The real and imaginary parts of the FRFs are shown so that one can gain an understanding of the sign of each FRF.

The resulting sum of the three estimated time domain strain components compare very well with the raw top and bottom strains, as shown in Figure 3.34 for a high amplitude range, and Figure 3.35 for a low amplitude range of response. There are several interesting observations to be made from these results. Over the range of time periods where the response is greatest, the response appears to be dominated by the first mode, with some higher frequency components visible at the minima and maxima. Even more

interesting is the interaction between the squared (labeled $\mu\varepsilon$-x^2) and cubic (labeled $\mu\varepsilon$-x^3) components of the nonlinear strain. Near the maxima, the two nonlinear terms tend to cancel each other, while near the minima the two terms add, and therefore, affect the sum greatly. Also interesting is that the cubic term is out of phase with the linear term. This was not expected and has not been discussed in the literature. Over the low-amplitude range of response, the higher frequency strain is very evident, and it tends to be superimposed on the lower frequency mode. Note too that the squared and cubic nonlinear terms have much less variation, and they have a localized bias effect on the summation. These bias shifts are thought to be due to the very low frequency response of this nonlinear system below the lower cutoff frequency of the input (20 Hz). Both sets of figures also show that the top and bottom strains are clearly out of phase with each other.

As a check of the nonlinear strain theory developed here, the bottom strains were estimated from the top strain FRFs. This check used the top strain squared estimates with the negative of the linear and cubic top strain estimates for comparison to the raw bottom strain data:

$$\begin{aligned} \varepsilon_{top} &= \varepsilon_{lin} + \varepsilon_{square} + \varepsilon_{cube} \\ \varepsilon_{bot} &= -\varepsilon_{lin} + \varepsilon_{square} - \varepsilon_{cube} \end{aligned} \tag{3.42}$$

Figure 3.36(a) shows the estimates over a region of high-amplitude response. The estimates are very good for the maxima, but they consistently have larger negative amplitudes for the minima. This is also the case for the low-amplitude response range shown in Figure 3.36(b). One explanation for this is illustrated in Figure 3.37(a). Compared to the bottom strain FRF shown in Figure 3.33(b), this figure shows that, over the frequency range of 20 to 500 Hz (the input acceleration range), the top and bottom FRFs have very similar magnitudes but with a difference in sign, as expected. The low-frequency range (1 to 10 Hz) shows similar magnitudes but with the same sign; this is unexpected and may be another indication of a pre-buckled condition or of instrumentation bias errors. Another explanation could be that this range has very poor coherence and any estimates of the frequency response functions are suspect.

The questions about the low frequency contribution of the FRF estimates to the time domain strain were investigated by forming a signed average of the top and bottom FRF estimates. These estimates were edited to give the low-frequency real and imaginary values a nominal constant value, determined from the higher frequency values of the FRFs, resulting in the functions shown in Figure 3.37(b) through Figure 3.38(b). Compare these to the raw estimated FRFs in Figure 3.32 through Figure 3.33. The time domain estimates of strain based on the averaged FRFs are shown in Figure 3.39. These figures now show membrane strain (squared strain data labeled $\mu\varepsilon$-x^2) with near-zero minimum and cubic strain (labeled $\mu\varepsilon$-x^3) with near-zero mean. Compare these time domain estimates of strain to those based on raw estimated FRFs in Figure 3.34 and Figure 3.35; the differences in these results give an indication of the bias errors discussed in Section 3.2.1.

The averaged FRFs, which have a frequency spacing of 0.25 Hz determined from overlapped and averaged 4 s data blocks, were used recursively (22 times) over the full 88 s of displacement data to estimate time domain strain responses and, ultimately, rainflow matrices. These RFM results are shown in Figure 3.40 through Figure 3.43. The time domain strain estimation process based on nonlinear FRFs allows one to look at the different individual or summed components of the strain. It is encouraging to compare the bending RFM that is calculated from the time domain strain data using (3.13) in Figure 3.27 with Figure 3.43. The comparison helps to modify the understanding; what was previously described as a bending strain can more accurately be thought of as a symmetric strain. The concept of bending strain is more closely tied to a linear strain (see, for example, Figure 3.42), while the concept of a symmetric strain can include the higher-order odd harmonics that have been demonstrated to be important in the decomposition of the total nonlinear strain response. The membrane strain estimates using the averaged and edited nonlinear FRFs (see, for example, Figure 3.40(b)) compare well to the time domain estimates using (3.14) shown in Figure 3.28(a). One can argue that the estimate made from the FRF is "cleaner."

3.3.1.2 Strain response estimates from filtered nonlinear FRFs

A final set of time domain strain estimates were calculated using filtered nonlinear displacement data. This case first used a band pass filter from 20 to 120 Hz on the "input" nonlinear displacement data. As before, this time domain filtered data was squared and cubed. The linear, squared, and cubic strain FRFs were band limited to 120, 240, and 360 Hz, respectively. These frequencies were chosen based on the coherence functions for this input level, as shown in Figure 3.44(a).

The simulated responses, based on the band pass filtered nonlinear displacement inputs, show good agreement with the filtered strain response data, as shown in Figure 3.44(b) and Figure 3.45(a). The simulated response data is shown with the raw top strain data in Figure 3.45(b). This shows how the higher frequency strain from the second mode can add to the lower frequency mode, as theorized above based on observations of the rainflow matrix, which indicate a limiting minimum mean stress. The simulated response RFM in Figure 3.41(b) and Figure 3.43(b) show this minimum mean stress behavior as well.

In a manner similar to the development in Section 3.2.2, the filtered response data was used to estimate a time domain polynomial relationship between the filtered nonlinear displacement y and the filtered top and bottom strains. The polynomial model is

$$\begin{aligned} \hat{\varepsilon}_{top} &= e_1 y + e_2 y^2 + e_3 y^3 \\ \hat{\varepsilon}_{bot} &= -e_1 y + e_2 y^2 - e_3 y^3 \end{aligned} \tag{3.43}$$

The addition of instrument gain (k) and bias (b) errors give

$$\begin{aligned} \hat{\varepsilon}_{top} &= k_{top}\hat{\varepsilon}_{top} + b_{top} \\ \hat{\varepsilon}_{bot} &= k_{bot}\hat{\varepsilon}_{bot} + b_{bot} \end{aligned} \tag{3.44}$$

and, if the top gain $k_{top} = 1$ and the bottom gain is

$$k_{bot} = \frac{\sigma_{\hat{\varepsilon}_{bot}}}{\sigma_{\hat{\varepsilon}_{top}}} \tag{3.45}$$

Subtracting the top and bottom strain equations gives an equation for the symmetric strain terms

$$\hat{\varepsilon}_{dif} = \hat{\varepsilon}_{top} - \frac{\hat{\varepsilon}_{bot}\sigma_{\hat{\varepsilon}_{top}}}{\sigma_{\hat{\varepsilon}_{bot}}} = e_{dif} + 2\left(e_1 y + e_3 y^3\right) \tag{3.46}$$

while summing them gives an equation for the squared term

$$\hat{\varepsilon}_{sum} = \hat{\varepsilon}_{top} + \frac{\hat{\varepsilon}_{bot}\sigma_{\hat{\varepsilon}_{top}}}{\sigma_{\hat{\varepsilon}_{bot}}} = e_{sum} + 2e_2 y^2 \tag{3.47}$$

A least-squares polynomial fit of the filtered nonlinear displacement y to the sum and difference filtered strain data at each input level was performed with the results given in Table 3.10. The polynomial coefficients were then used to estimate the bias terms

$$\begin{aligned} b_{top} &= \hat{\varepsilon}_{top} - \widehat{\varepsilon}_{top} \\ b_{bot} &= \hat{\varepsilon}_{bot} - k_{bot}\widehat{\varepsilon}_{bot} \end{aligned} \tag{3.48}$$

Note that the polynomial coefficients are quite similar at the lower input levels, but some shift in the results is noticeable at the higher input levels. This shift is most noticeable in the cubic coefficient. These coefficients will be used as a basis for estimating stress from nonlinear displacements determined from ODE simulations that will be discussed in the next chapter.

This concludes the time and frequency domain analysis of the displacement to strain frequency response functions. The next section explores the relationship based on their PDFs.

3.3.2 Estimates of strain PDF from displacement PDF using IDF method

The success with estimating the response strain from an "input" displacement from frequency response functions suggests a similar method based on the IDF method. Can one estimate a displacement to strain function based on distribution functions of the unfiltered data? This section describes the attempts based on peak displacement to peak bending strain and peak displacement to peak membrane strain.

Compared to the peak displacement PDFs (see Figure 3.21(a)), the peak bending strain PDFs are shifted more toward a normal distribution (see Figure 3.27(b)). Also remember that the ratio ϖ is very different for the measured displacement and bending strain (see Table 3.6). The true ramification of these issues are seen when one tries to estimate nonlinear displacement to nonlinear bending strain functions using the IDF method. The resulting data (see Figure 3.46(a)) does not show a clear trend toward one common function. Especially interesting are the data points that would imply positive peak displacements for negative bending strain maxima. Figure 3.46(b) shows the data again on a log-log plot with a single best-fit linear function through the higher amplitude peak data points. This linear function was used with the PDF transform method to estimate peak bending strain PDFs from peak displacement PDFs. Figure 3.47 shows a typical peak bending strain PDF estimate. Note how poorly the estimate matches the experimental data over the whole range of response, except at the few highest response levels (in the 200 to 250 $\mu\varepsilon$ range), which correspond to the best-fit linear function.

An explanation of these poor results is based on the difference in the ratio ϖ for the displacement and strain data. The frequency response functions of displacement input to strain output showed that the relationship between the two was not constant (see, for example, Figure 3.13). Filtering the data, so that only the fist mode was observed, allowed a time domain polynomial relationship to be determined between displacement and strain (see equation (3.43)). This single degree of freedom time domain relationship will be used in Chapter 5 to predict strain based on nonlinear simulation displacement results.

The IDF method was also used to estimate the peak membrane strain PDF. A ratio ϖ was assumed to be 1, based on the standard assumption that the membrane strain is always positive, and therefore has no negative valued maxima. The nonlinear peak displacement was used as the basis for comparison to the nonlinear peak membrane strain. The peak displacement to peak membrane strain function (see Figure 3.48(a)) shows that there is a trend in the data, but as in other examples, the 8 g data does not follow the others. Given this apparent shortcoming, a squared function was fit to the data (see Figure 3.48(b)) and was used to estimate the peak membrane strain PDF.

The process of estimating the membrane strain PDF from the nonlinear displacement PDF presented two options: transform the raw peak displacement PDF data or transform the estimated peak displacement PDF. Examples of both options are shown in Figure 3.49(a) and Figure 3.49(b). Both methods show good agreement with the PDFs estimated from the measurements.

3.4 Fatigue analysis of experimental data

The fatigue analysis of the WPAFB data is separated into two sections. The first is based on the raw measured strain while the second is based on the filtered strain. These sections include estimated nonlinear responses and a baseline linear response derived from the linear transfer function estimates. Comparison of the time to failure for different fatigue life models is included (see section 2.4.7).

The material SAE 1015 (a low-carbon steel) was used for the fatigue analysis because fatigue property data for the different fatigue models (given in Table 3.11) was available (Dowling [147]). The baseline alternating stress equation assumed no mean stress effects, while the Morrow (with true fracture strength) and Walker equations included mean stress effects.

The measured and estimated strains were converted to stress by multiplying by the elastic modulus $E = 204$ GPa (assuming no Poison effect of the unmeasured perpendicular strain). The stress results are in units of MPa.

3.4.1 Wideband analysis of WPAFB data

The raw top and bottom strain data from the WPAFB experiments is compared with estimates using nonlinear frequency response functions and a baseline case using a linear frequency response function. These cases include the effects of the second response mode.

3.4.1.1 Rainflow range matrices and life estimates of raw data

The raw top and bottom strain data measurements were converted to rainflow matrices (RFMs), see Figure 3.29 and Figure 3.30. These RFMs were used to calculate rainflow damage (RFD) matrices using the three damage models (see Section 2.4.6.1). A total of 85 s of the raw data files were used to estimate the time to failure (see equation (2.112)).

For all of the raw data file cases, the time to failure was shorter for the top strain (see Table 3.12) than the bottom strain data (see Table 3.13). This is consistent with the findings in previous sections, which pointed out that the standard deviation of the bottom strain was about 0.9 times that of the top strain. The bottom strain could be scaled by this amount as an attempt to show better agreement between the top and bottom strains.

Example of rainflow damage matrices for these raw strain results are shown in Figure 3.50 through Figure 3.51.

3.4.1.2 Estimates from averaged nonlinear frequency response functions

The averaged nonlinear frequency response functions from Section 3.3.1 were used to estimate the total stress at the top surface of the beam. The nonlinear FRF estimates were based on averaged auto and cross spectra for 4 s data blocks. The RFMs for this example were determined by summing the resulting rainflow cycles from 22 nonlinear input displacement blocks, each with 3.75 s of valid data, for a total of 82.5 s. As expected, the results in Table 3.14 show that the time to failure estimates fall between the results from the raw top and bottom stresses. Typical damage matrices are shown in Figure 3.52.

The nonlinear FRF method could also allow comparison of combinations of linear and nonlinear FRFs, e.g., a linear displacement to strain FRF applied to nonlinear displacements. These are left for future research.

3.4.1.3 Baseline linear estimates

Another set of wideband damage estimates were developed based on the linear estimates of the transfer function between input acceleration and linear response top surface strain. In this case, the transfer function estimates from the 1 g data files (as described in Section 3.1.3) were used to estimate the top surface response strain. The Laplace domain polynomial representation of the transfer function allowed for a larger time record estimate of a single block of input acceleration data (64 s, in this case). Rainflow damage matrices are shown in Figure 3.53 for the minimum and maximum input level. The damage matrices (and their RFM precursors) have nearly identical shapes as one would expect for linear models; one is approximately a scaled version of the other.

Several observations are worth noting with this example. First, note that the estimates of time to failure are almost equal for the baseline and Morrow damage models at the lowest input levels (see Table 3.15). This is due to the symmetric nature of the RFM for the linear model (near-zero mean stress). This should be compared to the nonlinear results given in the previous sections. Next, note that the lowest 0.5 g input-level top surface nonlinear time to failure results (see Table 3.12) are close to the low-level linear estimates calculated here, but that the high-level linear life estimates are approximately four to five orders of magnitude shorter than the nonlinear life estimates. This is very strong motivation for performing the nonlinear analysis. Another interesting point is that the peak stresses from the highest input case are approximately at the ultimate strength limit of the material. From a pure strength standpoint, this would indicate almost certain failure.

3.5 Nonlinear wideband analysis summary

The WPAFB experiments yielded a wealth of data that was analyzed in the frequency and time domains. The reverse path nonlinear technique was shown to be very effective in identifying nonlinear models for measured data. The identified frequency response and coherence functions gave keen insight into models for both the force to nonlinear displacement response and the displacement to nonlinear strain response. Modal models of the nonlinear system response were proposed.

Time domain analysis of the data showed strong nonlinear behavior. PDFs of displacement and strain responses were developed and used with the Inverse Distribution Function (IDF) method to estimate linear to nonlinear functions. Investigations of the change in peak PDFs, as the ratio of the rates of zeros to peaks changed, yielded observations of importance. The peak PDF and the peak histogram of a generalized response (i.e., any response from narrowband to completely wideband) were shown to be composed of the sum of narrowband and wideband parts. Equations to estimate the ratio of zeros to peaks ϖ, based on the number of negative value maxima, were developed. An equation to determine the value of the distribution function at a peak value of zero, as a function of ϖ, was also developed.

Estimated nonlinear strain response based on linear, squared and cubic displacement to strain FRFs allowed clear visualization of the interactions between the linear and nonlinear terms.

Time to failure was estimated based on the raw strain measurements and several estimates of linear and nonlinear response. The time to failure estimates showed that the nonlinear results were significantly longer than the linear results, especially at the highest input level. The life estimates were also made with two damage models that included nonzero mean stresses.

Numerical simulations, performed on a nonlinear single degree of freedom system, are discussed in the next chapter. Nonlinear ordinary differential equation (ODE) simulations are used to study parameters not available from the WPAFB experimental results (i.e. velocity and acceleration response states). The effects of damping level on the nonlinear response are also investigated. Long time duration simulations are used to study the rate of convergence of basic response statistics.

3.6 Chapter 3 Tables

Table 3.1. Multi-mode linear displacement response for force input parameter estimation from WPAFB data.

Run	f_{n1} Hz	ζ_1	f_{n2} Hz	ζ_2	Est Linear σ_x mm	Est Linear 1g σ_x mm
0.5 g	78.9	0.23%	416.	0.52%	0.213	0.429
1 g	78.3	0.14%	416.	0.46%	0.447	0.452
2 g	78.4	0.064%	420.	0.38%	0.927	0.472
4 g	79.0	0.26%	438.	0.076%	1.582	0.404
8 g	83.9	0.51%	443.	0.031%	2.469	0.312

Table 3.2. Multi-mode linear top surface strain response for force input parameter estimation from WPAFB data.

Run	f_{n1} Hz	ζ_1	f_{n2} Hz	ζ_2	Est Linear σ_ε ($\mu\varepsilon$)	Est Linear 1g σ_ε ($\mu\varepsilon$)
0.5 g	79.2	0.42%	416.	0.49%	23.8	48.1
1 g	78.3	0.37%	416.	0.41%	48.9	49.5
2 g	78.0	0.16%	417.	0.28%	150	76.4
4 g	100	0.91%	430.	0.027%	241	61.8
8 g	108	2.8%	442.	0.078%	420	53.6

Table 3.3. Input acceleration and displacement response statistics from WPAFB data.

Input	σ_a g	μ_a mg	ι_a	κ_a	σ_y mm	μ_y μm	ι_y	κ_y
0.5 g	0.495	1.9	0.2%	3.0	0.183	−0.12	10%	2.9
1 g	0.989	15	5%	2.9	0.292	0.005	11%	2.8
2 g	1.97	5.7	1%	3.0	0.488	−0.025	8%	2.5
4 g	3.91	5.4	1%	2.9	0.777	−0.001	4%	2.2
8 g	7.85	4.1	2%	3.1	1.087	−0.064	3%	2.1

Table 3.4. Top and bottom surface strain response statistics from WPAFB data.

Input	σ_{top} με	μ_{top} με	ι_{top}	κ_{top}	σ_{bot} με	μ_{bot} με	ι_{bot}	κ_{bot}
0.5 g	26.6	1	27%	2.8	23.0	−6.8	−45%	2.6
1 g	42.8	1.2	36%	2.8	37.7	−3.0	31%	2.9
2 g	70.5	4.6	64%	2.7	64.3	7.1	94%	3.1
4 g	111	18	103%	2.9	104	27	130%	3.2
8 g	157	45	129%	3.3	148	56	145%	3.4

Table 3.5. Bending and membrane strain response statistics from WPAFB data.

Input	σ_{bend} με	μ_{bend} με	ι_{bend}	κ_{bend}	σ_{mem} με	μ_{mem} με	ι_{mem}	κ_{mem}
0.5 g	26.5	0.021	−13%	2.8	2.04	2.02	211%	5.9
1 g	42.5	−0.002	−14%	2.7	5.00	4.16	239%	7.4
2 g	69.4	0.004	−9%	2.4	12.4	11.6	214%	5.7
4 g	107	0.002	−4%	2.1	28.7	28.0	198%	4.7
8 g	148	0.011	−2%	2.2	50.8	45.0	198%	4.7

Table 3.6. Rates of displacement and bending strain zero crossing and peaks for WPAFB data.

Input	$\Phi\left[0_x^+\right]$ Hz	$\Phi\left[P_x^+\right]$ Hz	ϖ_x	$\Phi\left[0_{bend}^+\right]$ Hz	$\Phi\left[P_{bend}^+\right]$ Hz	ϖ_{bend}
0.5 g	81.4	84.2	0.967	103	218	0.471
1 g	83.8	87.2	0.961	110	258	0.428
2 g	92.0	102	0.903	137	318	0.431
4 g	109	122	0.890	165	367	0.450
8 g	132	152	0.865	209	430	0.485

Table 3.7. Rates of top and bottom surface strain response zero crossing and peaks for WPAFB data.

Input	$\Phi\left[0^{+}_{top}\right]$ Hz	$\Phi\left[P^{+}_{top}\right]$ Hz	ϖ_{top}	$\Phi\left[0^{+}_{bot}\right]$ Hz	$\Phi\left[P^{+}_{bot}\right]$ Hz	ϖ_{bot}
0.5 g	98.5	203	0.484	96.6	236	0.408
1 g	106	244	0.433	111	274	0.406
2 g	133	311	0.426	141	328	0.430
4 g	165	360	0.457	179	369	0.485
8 g	250	421	0.591	270	425	0.634

Table 3.8. Polynomial coefficients for linear to nonlinear curve fit of WPAFB peak displacement data.

	c_1 mm/mm	c_2 mm/mm^2	c_3 mm/mm^3
Fixed ϖ_x CDF	0.90	0.51	0.29
Variable ϖ_x CDF	0.95	0.36	0.33

Table 3.9. Goodness-of-fit peak PDF comparison for WPAFB data.

Input	Bin Center Range	DOF	PDF: X^2
0.5 g	$-0.17 < \sigma < 3.18$	30	Fixed PDF: 126.
1 g	$-0.17 < \sigma < 3.25$	30	Fixed PDF: 457
2 g	$-0.15 < \sigma < 2.86$	30	Fixed PDF: 1255
4 g	$-0.13 < \sigma < 2.53$	30	Fixed PDF: 1507
8 g	$-0.13 < \sigma < 2.44$	30	Fixed PDF: 3309
0.5 g	$-0.17 < \sigma < 3.18$	30	Variable PDF: 121
1 g	$-0.17 < \sigma < 3.25$	30	Variable PDF: 423
2 g	$-0.15 < \sigma < 2.86$	30	Variable PDF: 295
4 g	$-0.13 < \sigma < 2.53$	30	Variable PDF: 186
8 g	$-0.13 < \sigma < 2.44$	30	Variable PDF: 389

Table 3.10. Filtered strain response parameter estimation from WPAFB data.

Input	f_{filt} Hz	e_1 $\mu\varepsilon$/mm	e_2 $\mu\varepsilon$/mm^2	e_3 $\mu\varepsilon$/mm^3	b_{top} $\mu\varepsilon$	b_{bot} $\mu\varepsilon$	k_2
0.5 g	100	−143	41.5	15.5	−0.36	−9.29	0.856
1 g	110	−144	42.9	15.4	−2.48	−7.12	0.877
2 g	120	−143	41.7	14.8	−4.66	−2.45	0.901
4 g	160	−141	40.0	12.0	−5.82	5.10	0.934
8 g	220	−137	36.7	9.4	1.57	15.6	0.944

Table 3.11. Material properties for nonlinear total stress damage evaluation.

Fatigue Equation	Material Properties (MPa)
Baseline Alternating Stress	$\sigma'_f = 801, b = -0.113$
Morrow, reduced fracture strength	$\sigma'_f = 801, \tilde{\sigma}_{fB} = 726, b = -0.113$
Walker	$\sigma'_f = 799, \gamma = 0.713, b = -0.114$

Table 3.12. Time to failure estimates for raw top strain measurements from WPAFB data.

Run	Baseline (s)	Morrow (s)	Walker (s)
0.5 g	1.55×10^{14}	1.52×10^{14}	8.93×10^{13}
1 g	2.27×10^{12}	2.17×10^{12}	1.20×10^{12}
2 g	3.77×10^{10}	3.42×10^{10}	1.73×10^{10}
4 g	1.40×10^{9}	8.64×10^{8}	4.14×10^{8}
8 g	1.86×10^{7}	1.28×10^{7}	7.18×10^{6}

Table 3.13. Time to failure estimates for raw bottom strain measurements from WPAFB data.

Run	Baseline (s)	Morrow (s)	Walker (s)
0.5 g	5.21×10^{14}	5.17×10^{14}	3.30×10^{14}
1 g	5.91×10^{12}	5.62×10^{12}	2.81×10^{12}
2 g	7.63×10^{10}	6.78×10^{10}	3.03×10^{10}
4 g	1.87×10^{9}	1.52×10^{9}	6.61×10^{8}
8 g	2.90×10^{7}	1.96×10^{7}	1.40×10^{7}

Table 3.14. Time to failure estimates for averaged nonlinear frequency response functions of WPAFB data.

Run	Baseline (s)	Morrow (s)	Walker (s)
0.5 g	3.17×10^{14}	3.11×10^{14}	1.72×10^{14}
1 g	3.78×10^{12}	3.59×10^{12}	1.82×10^{12}
2 g	5.56×10^{10}	4.96×10^{10}	2.29×10^{10}
4 g	1.32×10^{9}	1.11×10^{9}	5.27×10^{8}
8 g	1.89×10^{7}	1.38×10^{7}	8.06×10^{6}

Table 3.15. Time to failure estimates for linear top strain response from input acceleration WPAFB data.

Run	Baseline (s)	Morrow (s)	Walker (s)
0.5 g	1.1683×10^{14}	1.1680×10^{14}	8.44e13
1 g	6.4175×10^{11}	6.4168×10^{11}	4.84×10^{11}
2 g	1.644×10^{9}	1.642×10^{9}	1.30×10^{9}
4 g	5.48×10^{5}	5.47×10^{5}	4.70×10^{5}
8 g	5.82×10^{2}	5.74×10^{2}	5.31×10^{2}

3.7 Chapter 3 Figures

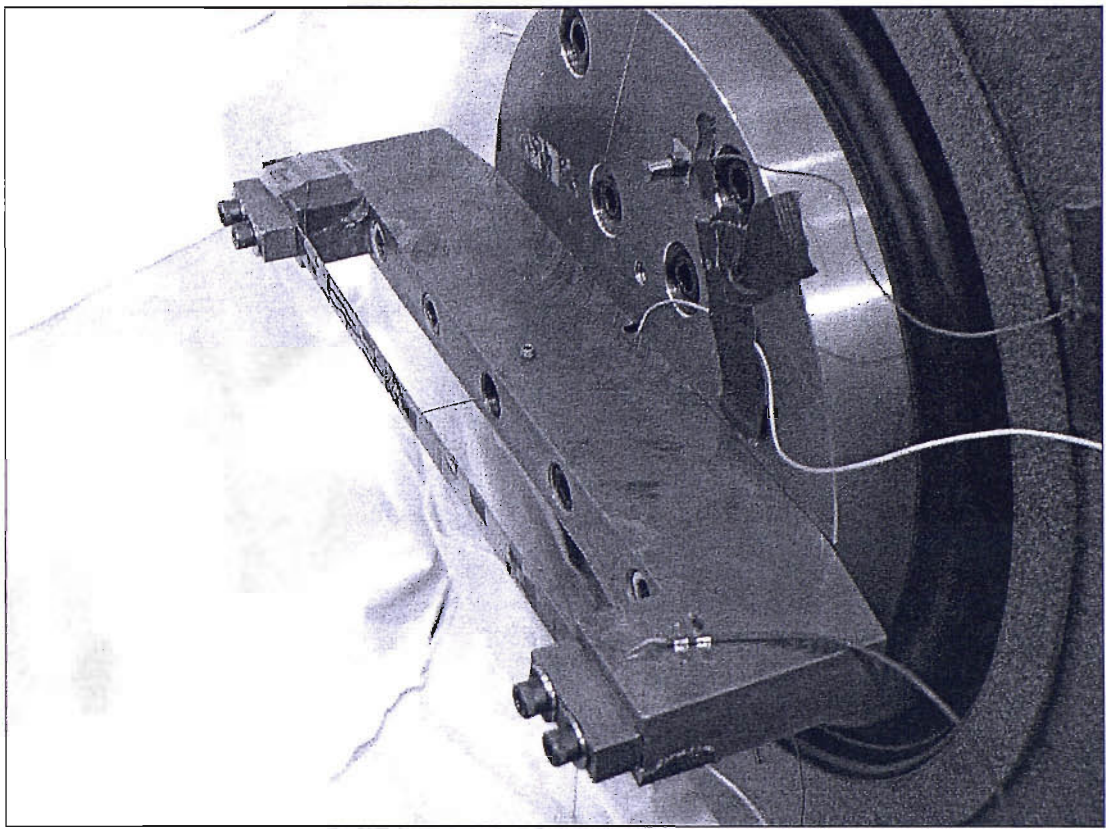

Figure 3.1. Vibration experiment at WPAFB, showing clamped-clamped beam, fixture, strain gages, differential variable reluctance displacement transducer, base input accelerometer, thermocouples and electrodynamic shaker (from [7], Figure 1).

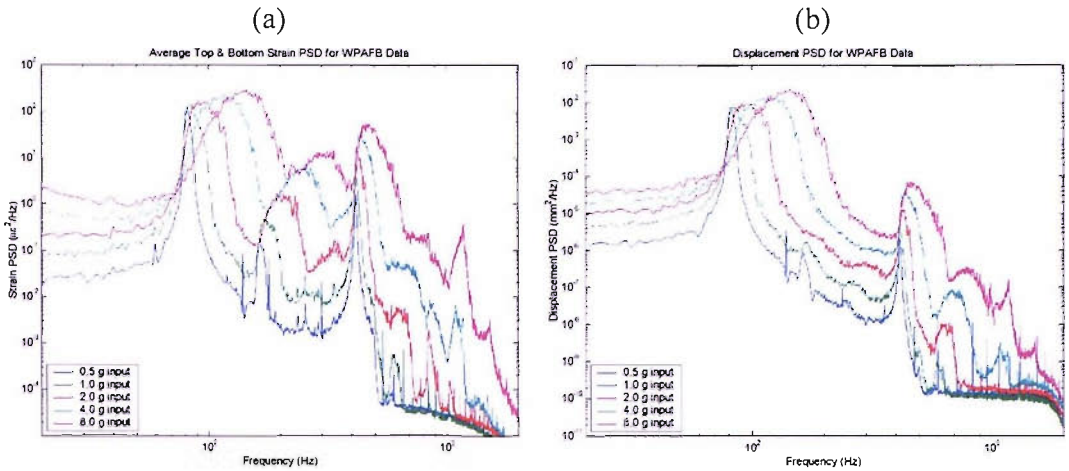

Figure 3.2. PSD responses determined from WPAFB input = (0.5, 1, 2, 4, 8) g data: (a) averaged (top and bottom) strain and (b) displacement.

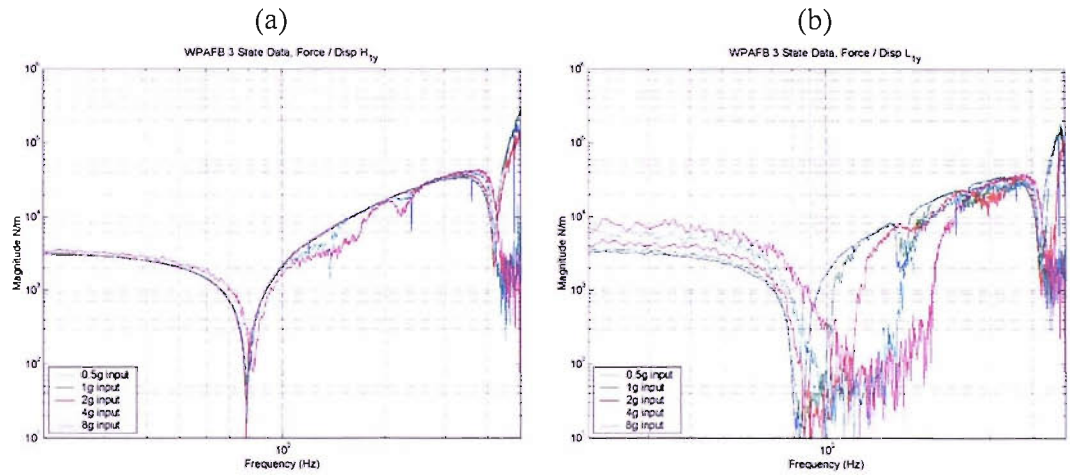

Figure 3.3. Displacement input to force output frequency response functions determined from WPAFB input = (0.5, 1, 2, 4, 8) g data: (a) uncorrelated displacement input to force output and (b) correlated displacement input to force output.

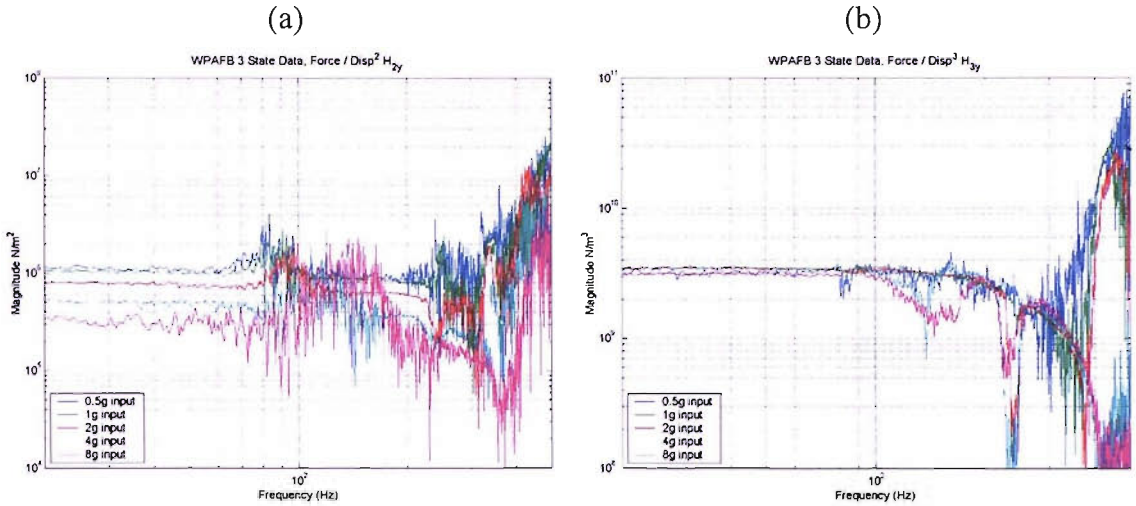

Figure 3.4. Nonlinear displacement input to force output frequency response functions determined from WPAFB input = (0.5, 1, 2, 4, 8) g data: (a) uncorrelated squared displacement input and (b) uncorrelated cubed displacement input.

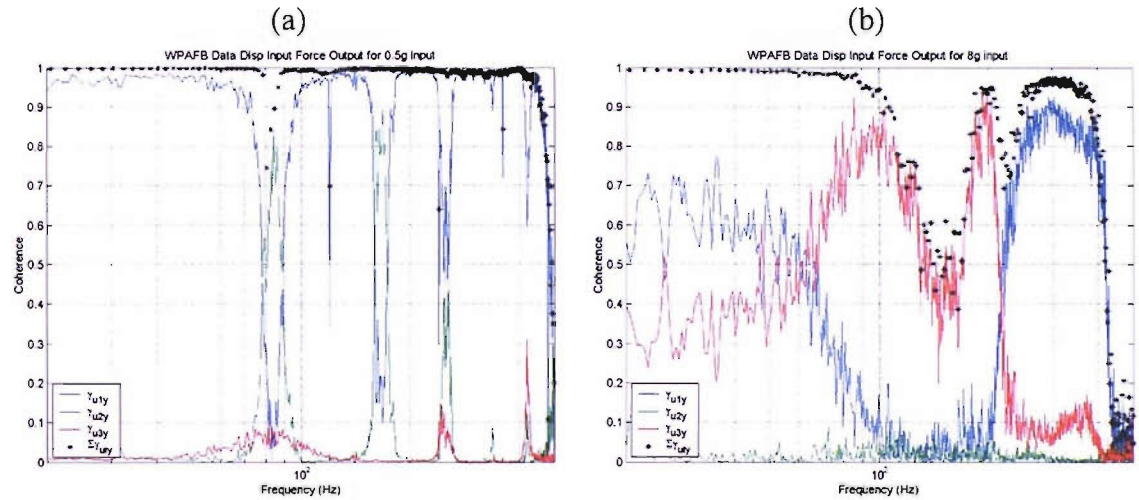

Figure 3.5. Coherence functions for displacement input to force output frequency response functions determined from WPAFB data: (a) input = 0.5 g and (b) input = 8 g.

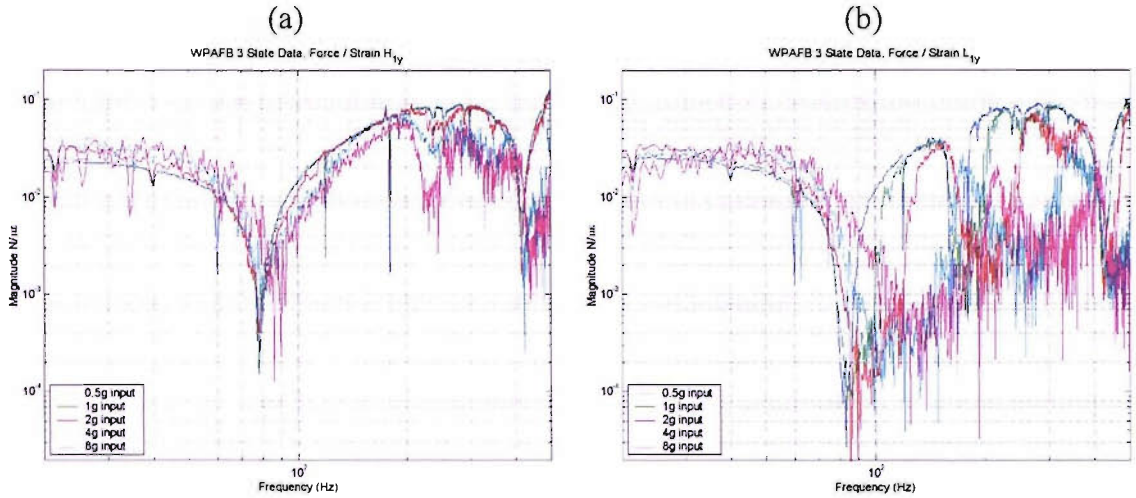

Figure 3.6. Top surface strain input to force output frequency response functions determined from WPAFB input = (0.5, 1, 2, 4, 8) g data: (a) uncorrelated top surface strain input to force output and (b) correlated top surface strain input to force output.

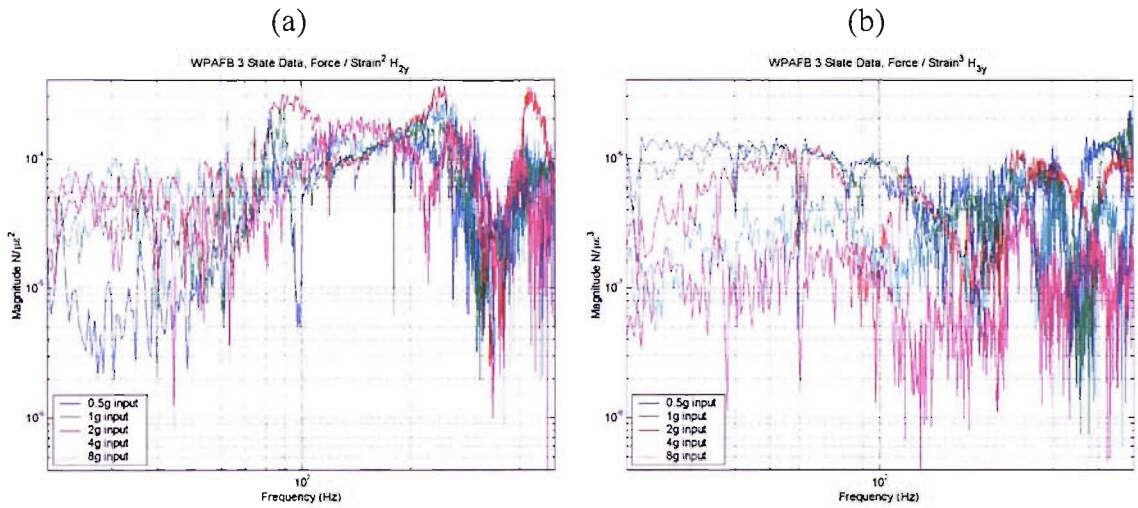

Figure 3.7. Nonlinear top surface strain input to force output frequency response functions determined from WPAFB input = (0.5, 1, 2, 4, 8) g data: (a) squared top surface strain input and (b) cubed top surface strain input.

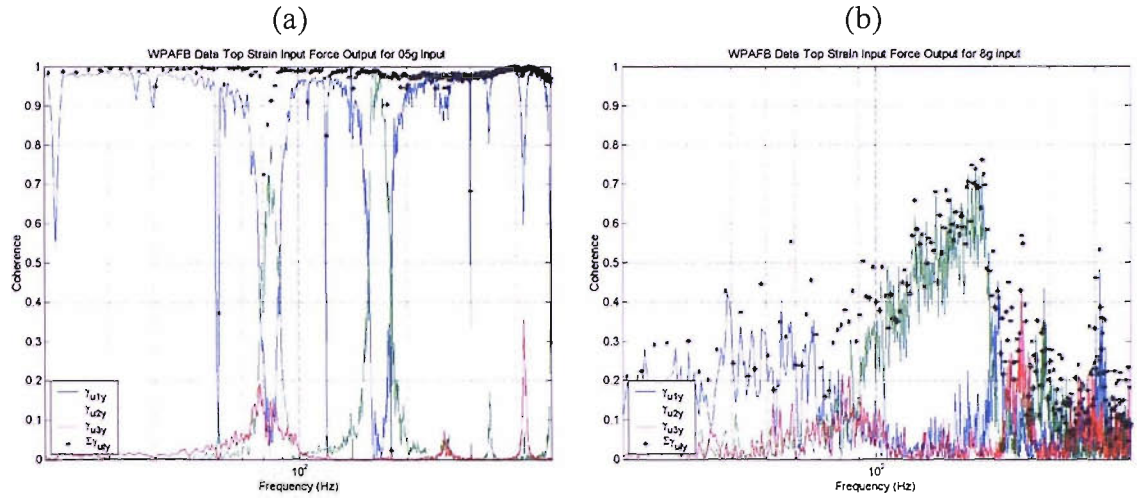

Figure 3.8. Coherence functions for top surface strain input to force output frequency response functions determined from WPAFB data: (a) input = 0.5 g and (b) input = 8 g.

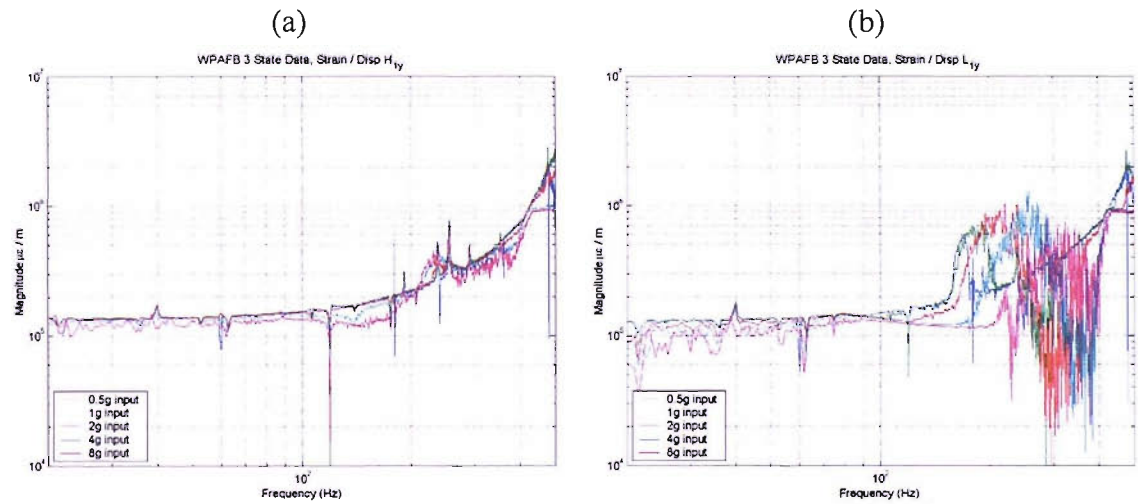

Figure 3.9. Displacement input to top surface strain output frequency response functions determined from WPAFB input = (0.5, 1, 2, 4, 8) g data: (a) uncorrelated displacement input and (b) correlated displacement input.

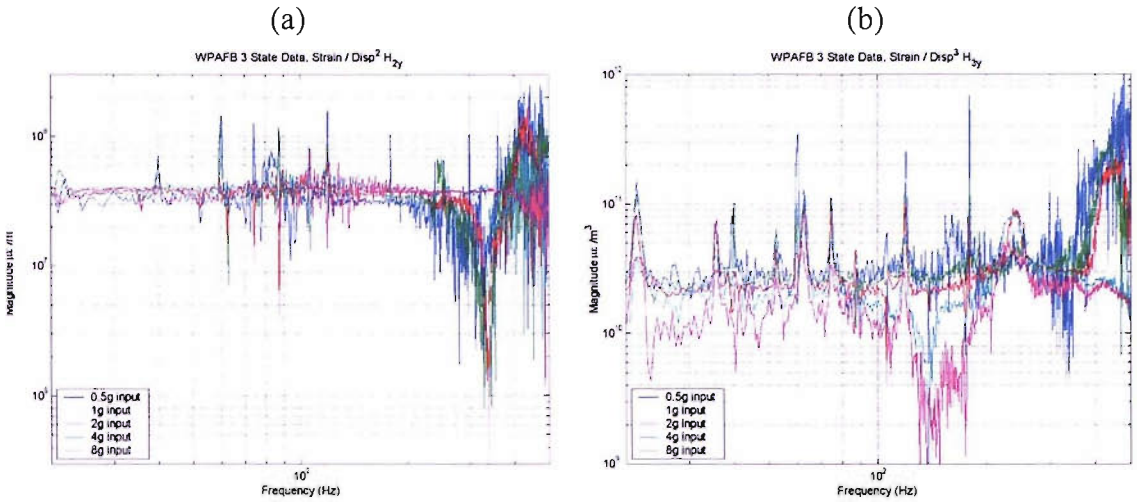

Figure 3.10. Nonlinear displacement input to force output frequency response functions determined from WPAFB input = (0.5, 1, 2, 4, 8) g data: (a) squared displacement input and (b) cubed displacement input.

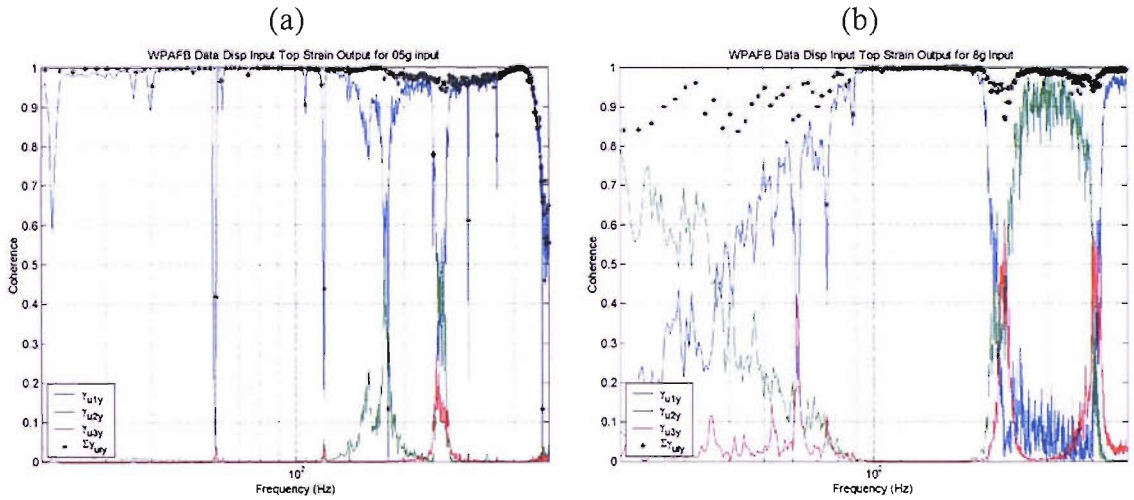

Figure 3.11. Coherence functions for displacement input to top surface strain output frequency response functions determined from WPAFB data: (a) input = 0.5 g and (b) input = 8 g.

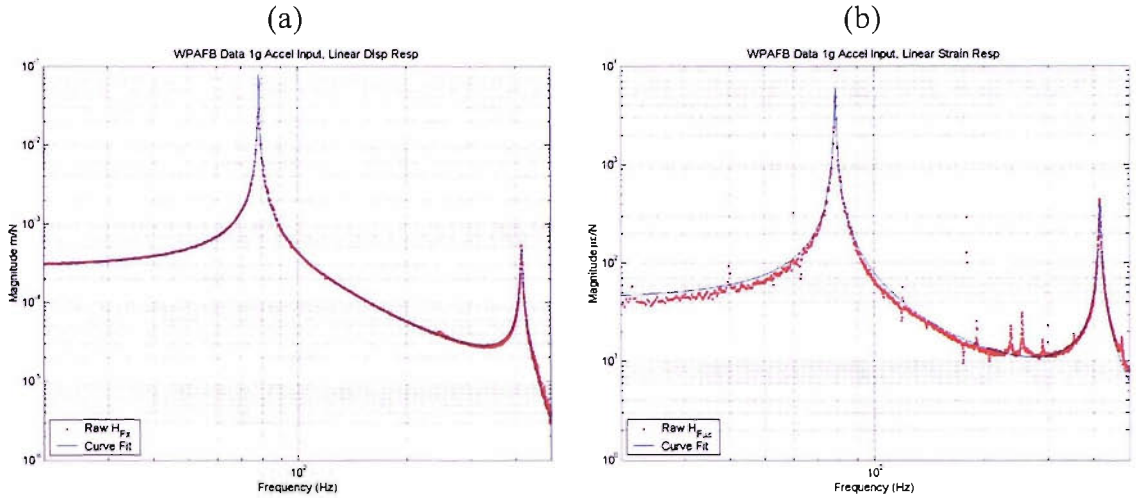

Figure 3.12. Estimated force input transfer functions from WPAFB input = 1 g data: (a) linear displacement response and (b) linear top surface strain response.

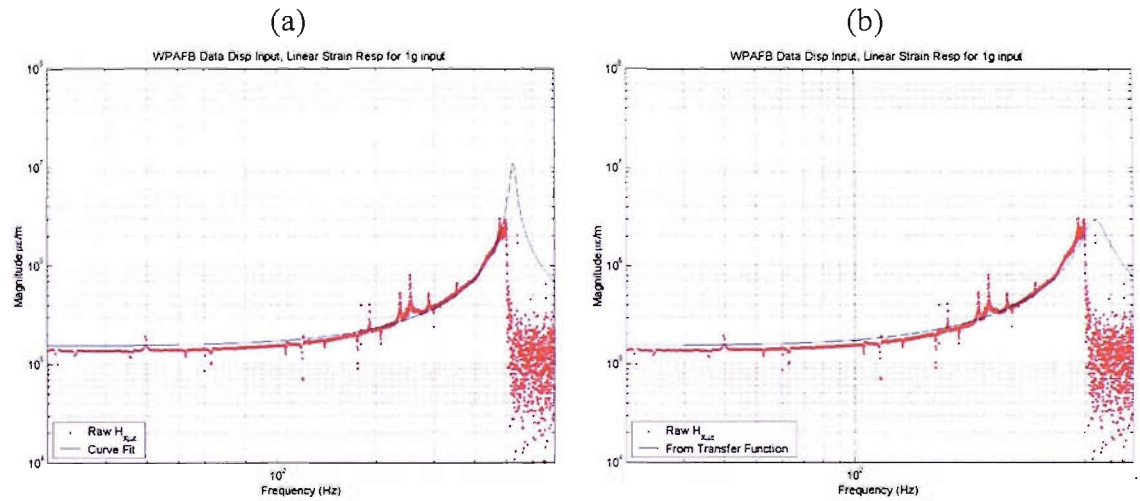

Figure 3.13. Estimated displacement input, linear top strain output transfer functions for WPAFB input = 1 g data: (a) MDOF parameter estimate from raw strain to displacement data and (b) estimate from product of strain to force and force to displacement transfer functions.

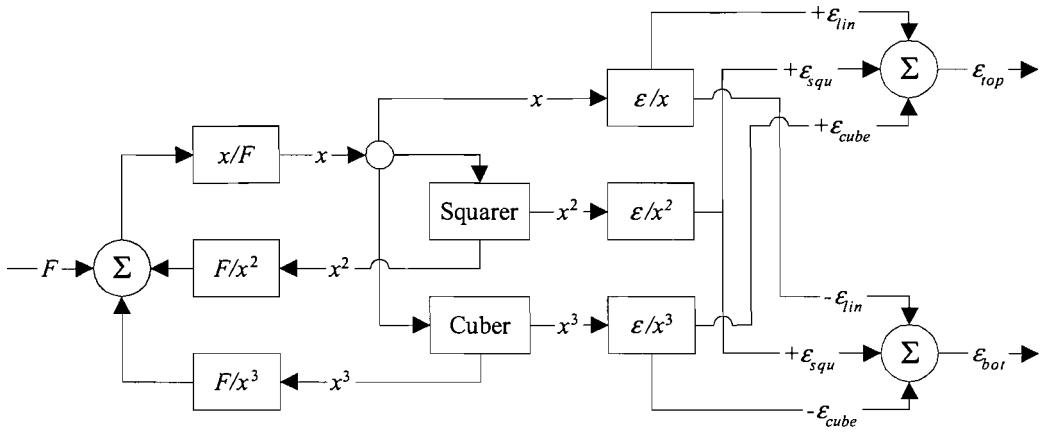

Figure 3.14. Flow diagram of nonlinear clamped-clamped beam model with series connection of displacement and strain functions.

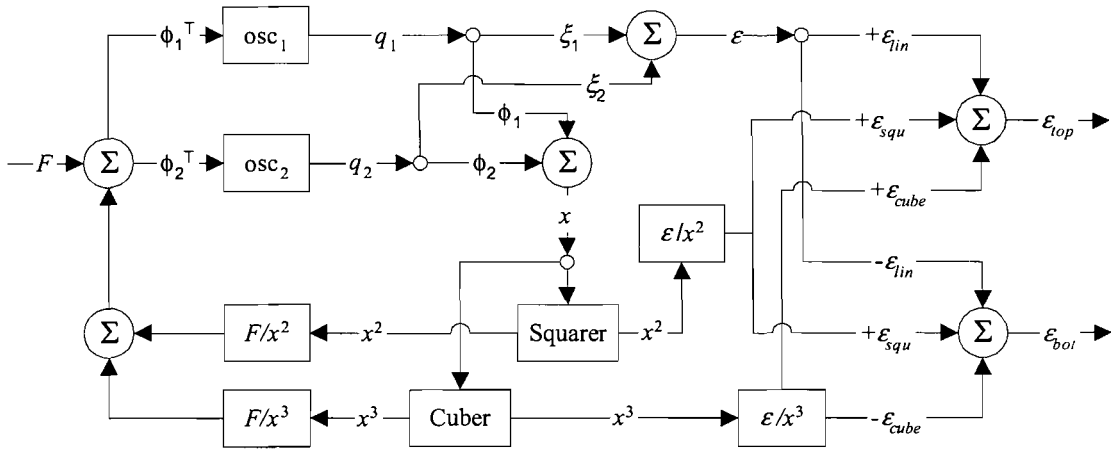

Figure 3.15. Flow diagram of nonlinear clamped-clamped beam model with modal superposition for displacement and strain functions.

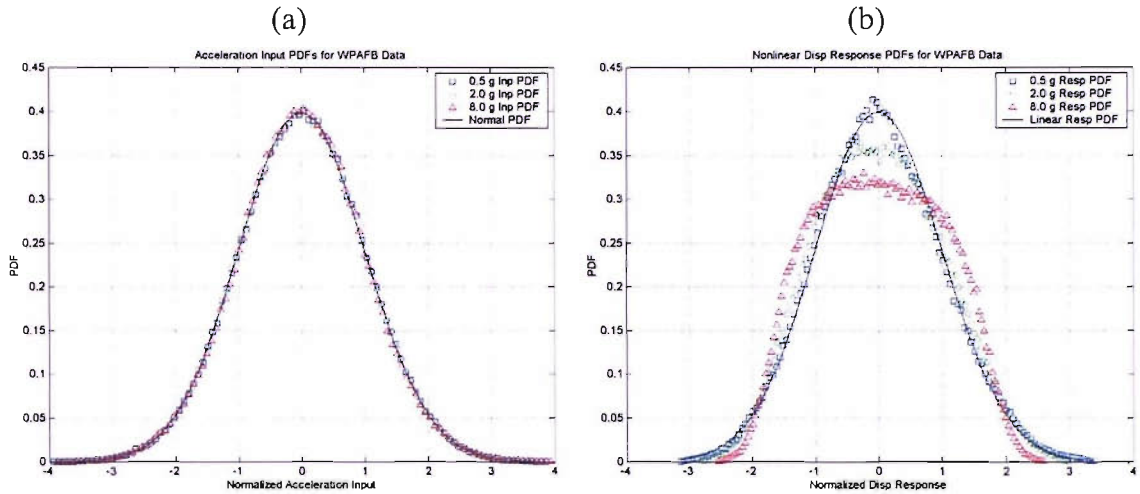

Figure 3.16. Normalized PDFs from WPAFB input = (0.5, 2, 8) g data: (a) input acceleration: σ_a = (0.495, 1.97, 7.85) g and (b) beam center displacement response: σ_y = (0.183, 0.488, 1.087) mm.

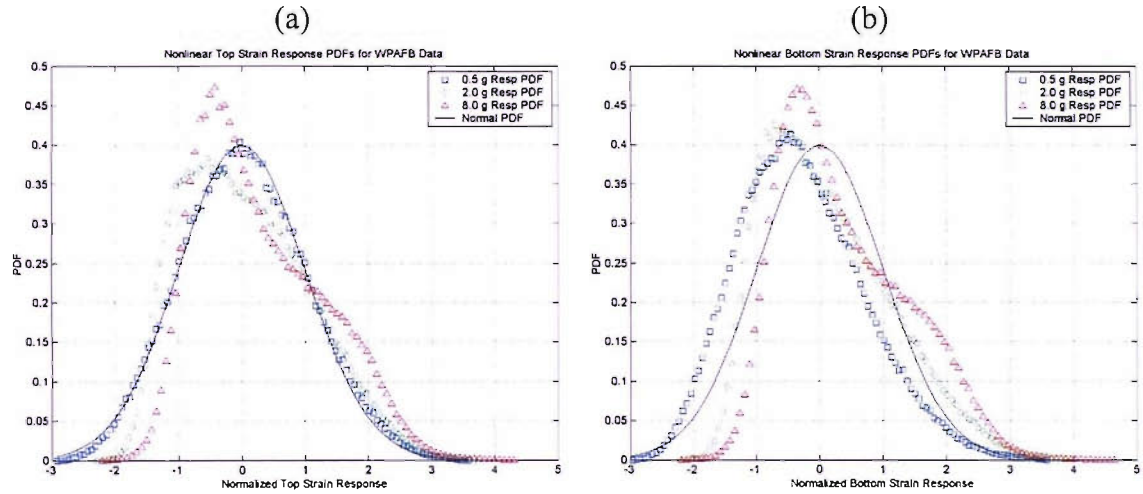

Figure 3.17. Normalized PDFs from WPAFB input = (0.5, 2, 8) g strain response data at center of beam: (a) top surface: σ_{top} = (26.6, 70.5, 157) $\mu\varepsilon$ and (b) bottom surface: σ_{bot} = (23.0, 64.3, 148) $\mu\varepsilon$.

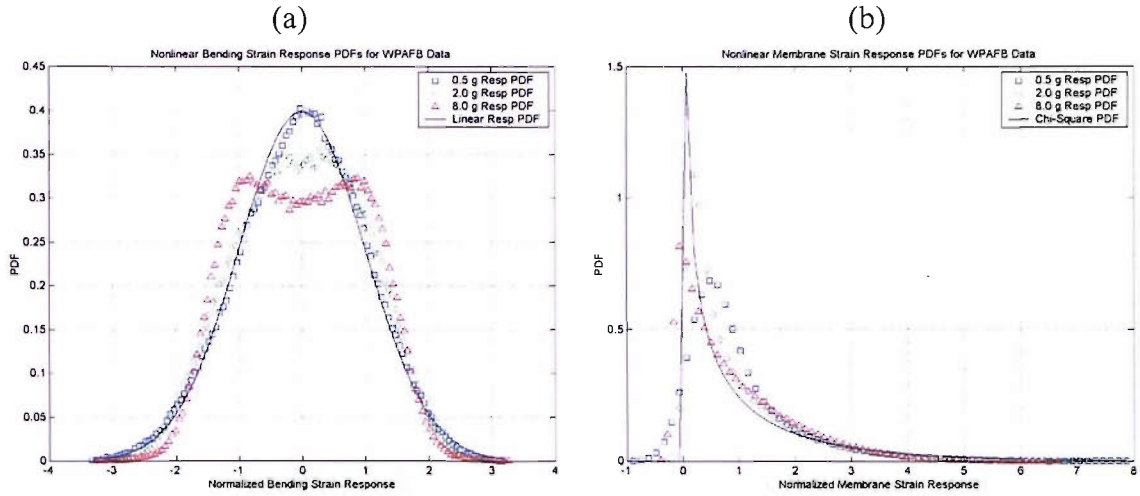

Figure 3.18. Normalized PDFs from estimated strain at center of beam for WPAFB input = (0.5, 2, 8) g data: (a) bending strain: σ_{bend} = (26.5, 69.4, 148) $\mu\varepsilon$ and (b) membrane strain σ_{mem} = (2.04, 12.4, 50.8) $\mu\varepsilon$, with chi-squared (DOF = 1) PDF.

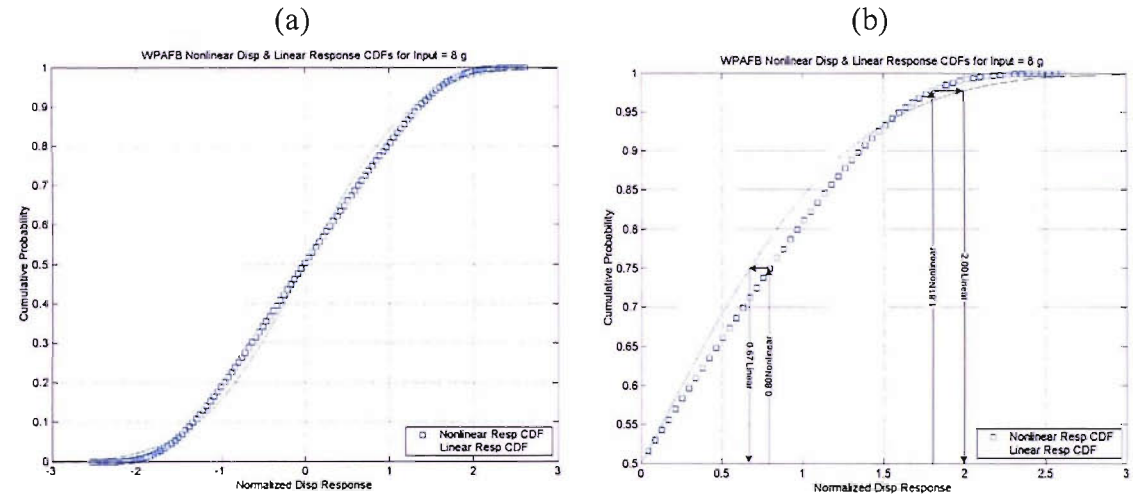

Figure 3.19 Normalized cumulative distribution functions for WPAFB input = 8 g displacement data overlaid with normal CDFs: σ_y = 1.087 mm (a) full data range and (b) positive response range showing linear to nonlinear mappings based on IDF method.

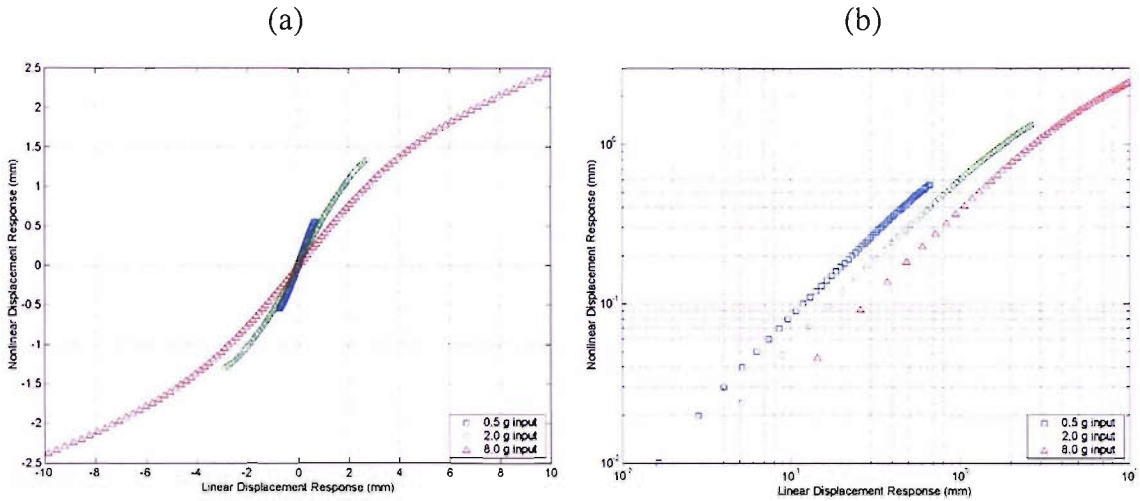

Figure 3.20. Linear to nonlinear displacement response functions from WPAFB input = (0.5, 2, 8) g data: (a) full range linear to nonlinear displacement functions and (b) log-log plot of positive valued linear to nonlinear displacement functions.

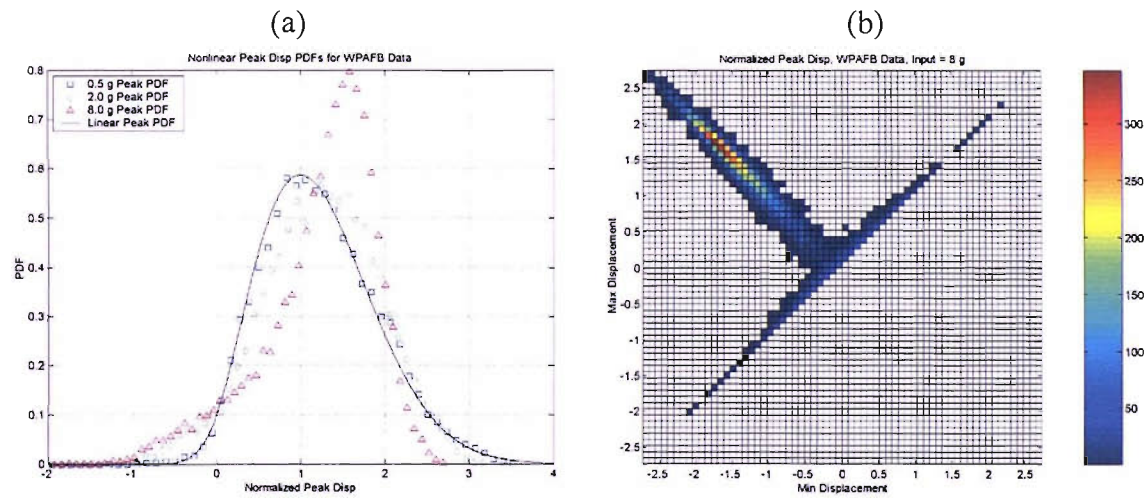

Figure 3.21. Normalized WPAFB data: (a) normalized nonlinear peak displacement PDFs and linear peak PDF: σ_y = (0.183, 0.488, 1.087) mm for input = (0.5, 2, 8) g, and (b) normalized peak displacement RFM for input = 8 g: σ_y = 1.087 mm.

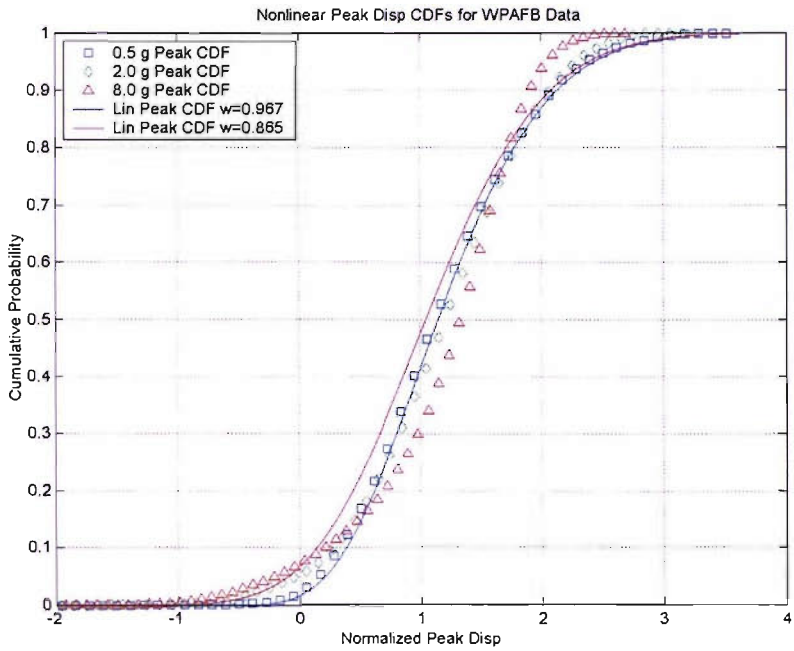

Figure 3.22. Normalized nonlinear peak displacement CDFs and linear peak CDFs at ratio $\varpi = 0.967$ and 0.865 for WPAFB input = (0.5, 2, 8) g data: σ_y = (0.183, 0.488, 1.087) mm.

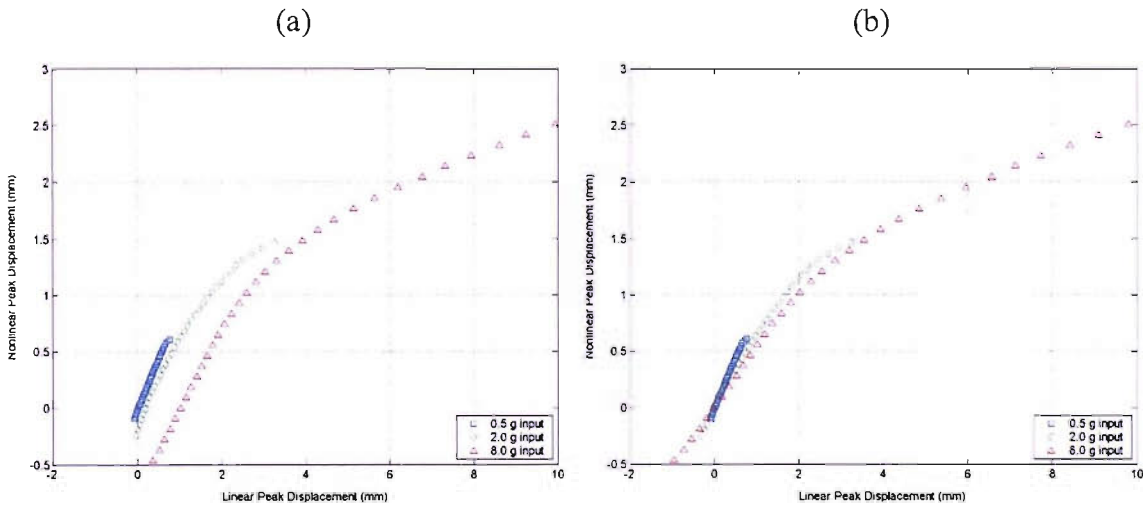

Figure 3.23. Linear to nonlinear peak displacement functions for WPAFB input = (0.5, 2, 8) g data: (a) Fixed ratio linear peak CDF and (b) variable ratio linear peak CDF.

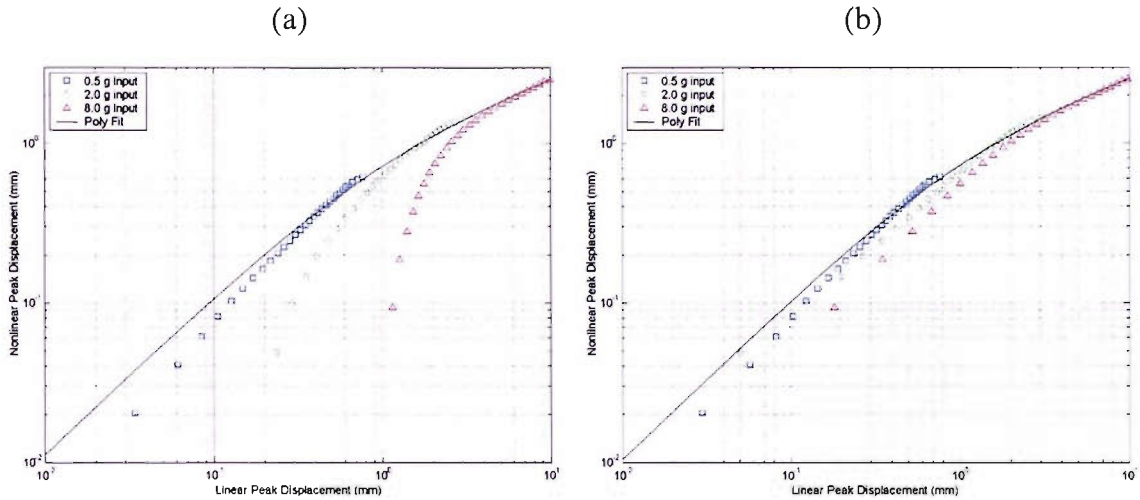

Figure 3.24. Log-log plot of linear to nonlinear peak displacement functions for WPAFB input = (0.5, 2, 8) g data: (a) fixed ratio linear peak CDF and (b) variable ratio linear peak CDF.

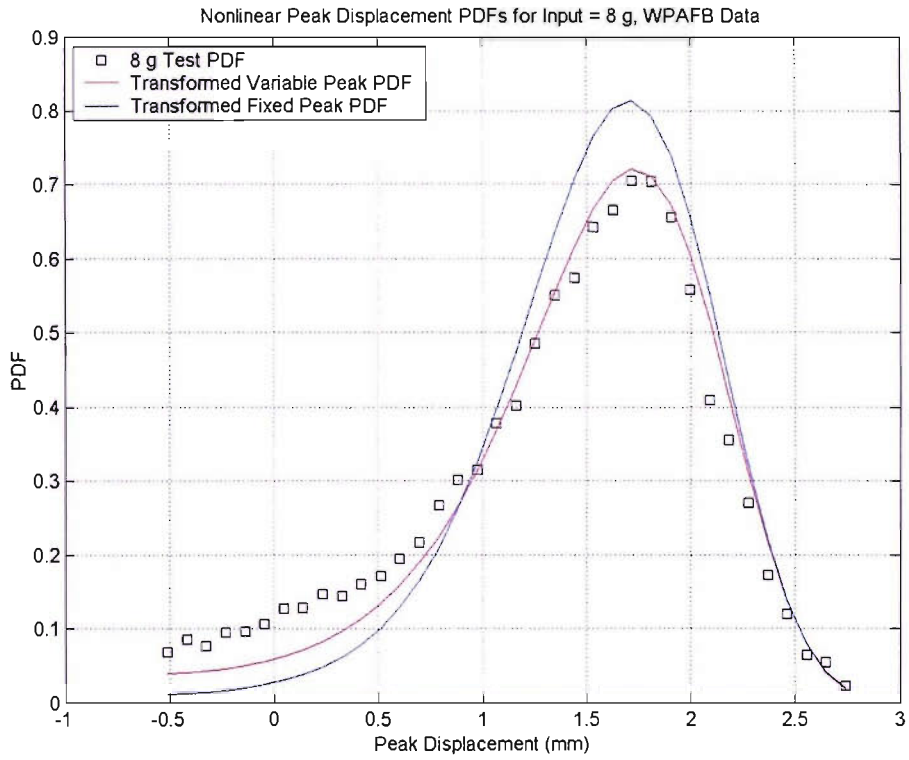

Figure 3.25. Nonlinear peak displacement PDF estimates from variable and fixed PDF transform methods for WPAFB input = 8 g data.

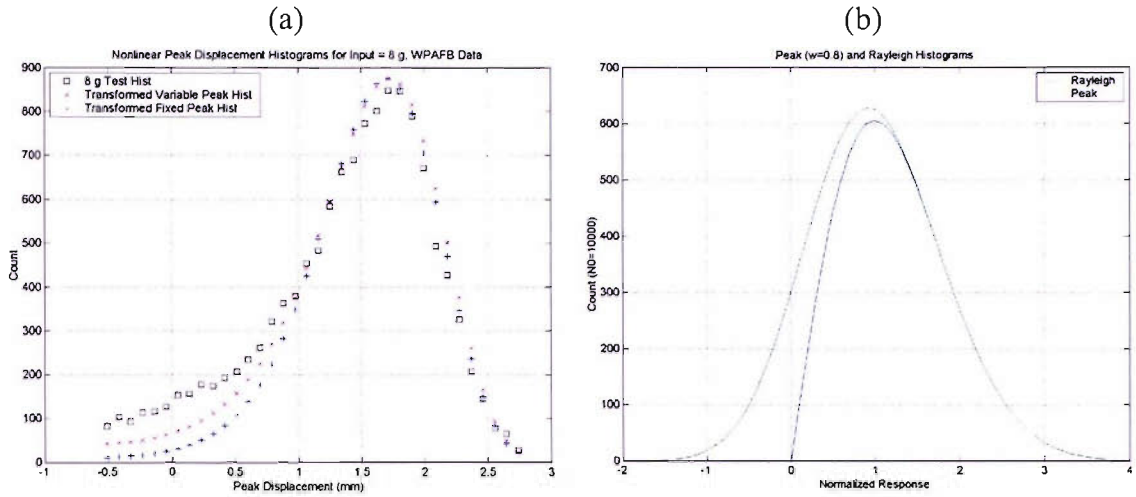

Figure 3.26. Nonlinear peak displacement histogram estimates: (a) histogram from variable and fixed PDF transform methods from WPAFB input = 8 g data and (b) Rayleigh and peak response histograms for linear system, $\varpi = 0.8$.

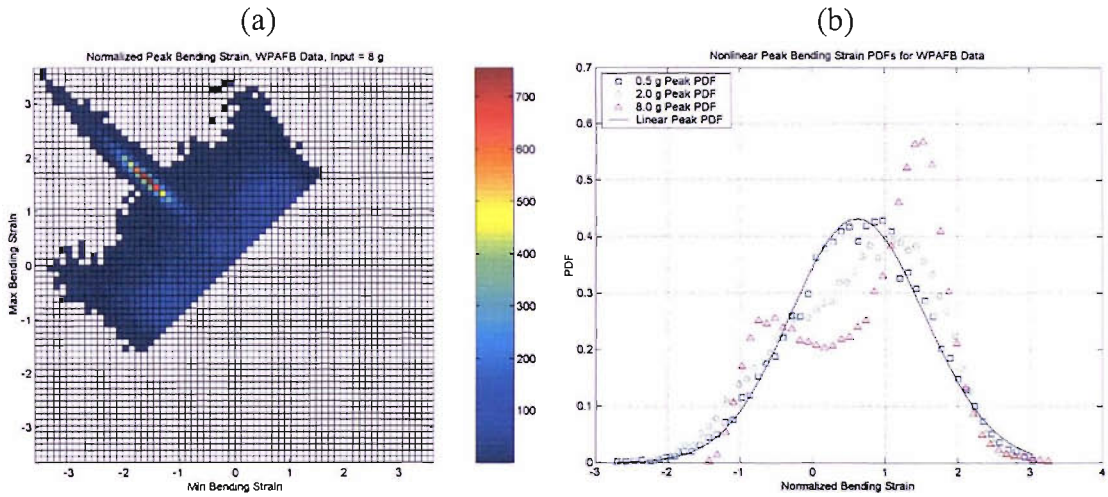

Figure 3.27. Normalized peak bending strain results from WPAFB data: (a) RFM for input = 8 g, $\sigma_{bend} = 148\ \mu\varepsilon$ and (b) nonlinear peak bending strain PDFs and linear peak PDF with $\varpi = 0.471$, $\sigma_{bend} = (26.5, 69.4, 148)\ \mu\varepsilon$ for input = (0.5, 2, 8) g.

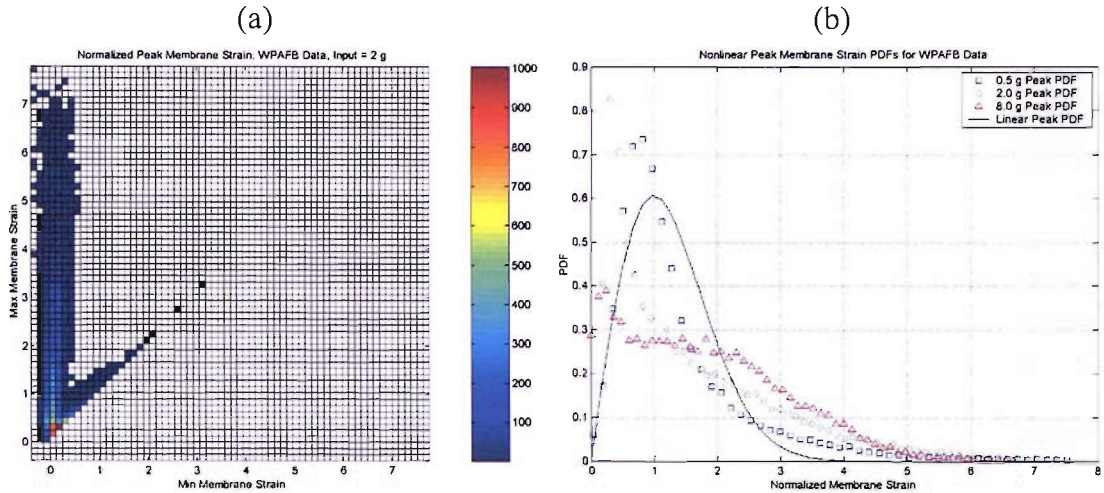

Figure 3.28. Normalized peak membrane strain results from WPAFB data: (a) normalized RFM of membrane strain for input = 2 g, σ_{mem} = 12.4 $\mu\varepsilon$ and (b) normalized peak membrane strain PDFs and Rayleigh PDF, σ_{mem} = (2.04, 12.4, 50.8) $\mu\varepsilon$ for input = (0.5, 2, 8) g.

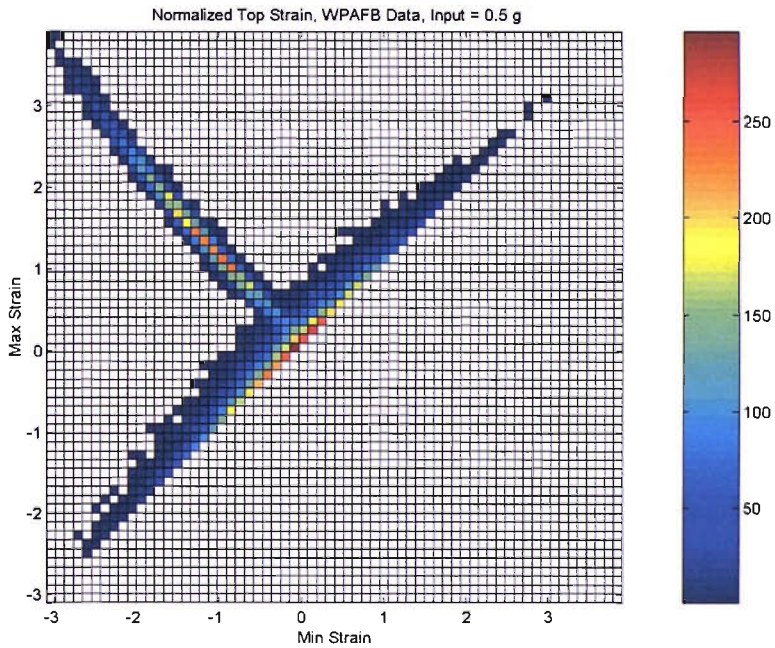

Figure 3.29. Normalized top surface strain RFM for raw WPAFB input = 0.5 g data, σ_{top} = 26.6 $\mu\varepsilon$.

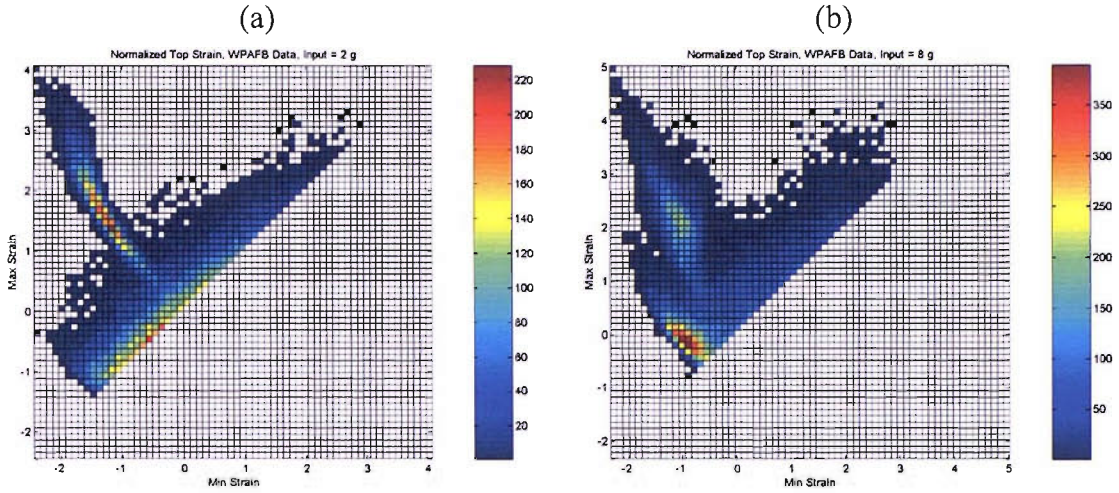

Figure 3.30. Normalized top surface strain RFM for raw WPAFB data: (a) input = 2 g, σ_{top} = 70.5 $\mu\varepsilon$ and (b) input = 8 g, σ_{top} = 157 $\mu\varepsilon$.

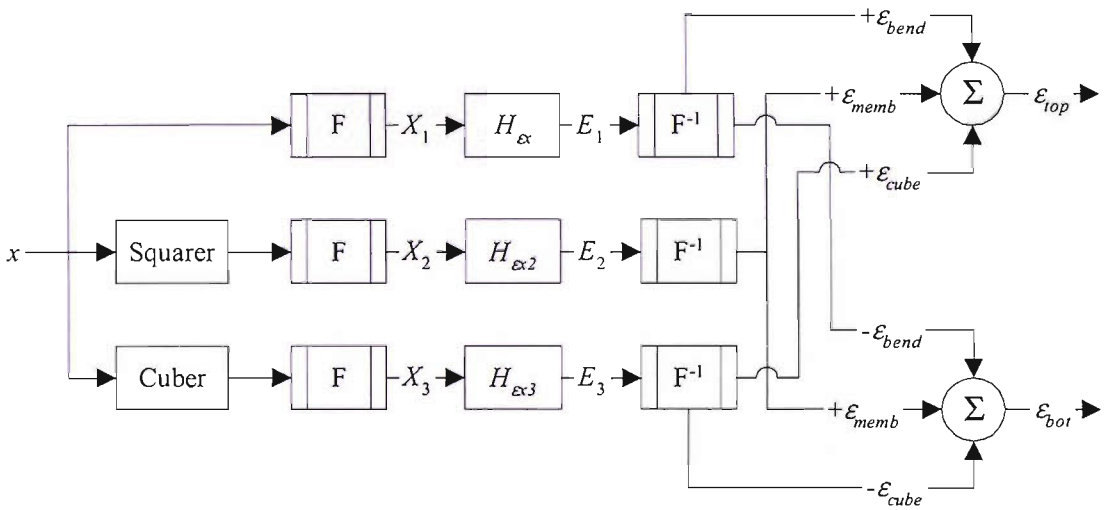

Figure 3.31. Flow diagram for estimating top and bottom strains from frequency response functions using Fourier and inverse Fourier transforms.

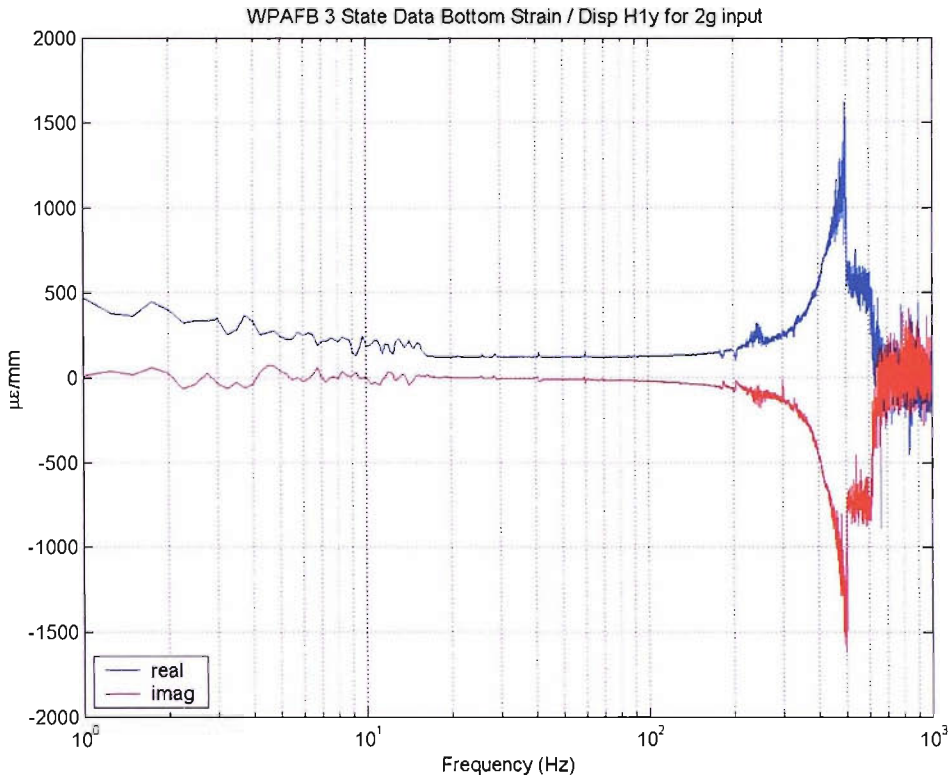

Figure 3.32. Linear estimate of displacement to bottom strain frequency response function determined from WPAFB input = 2 g data.

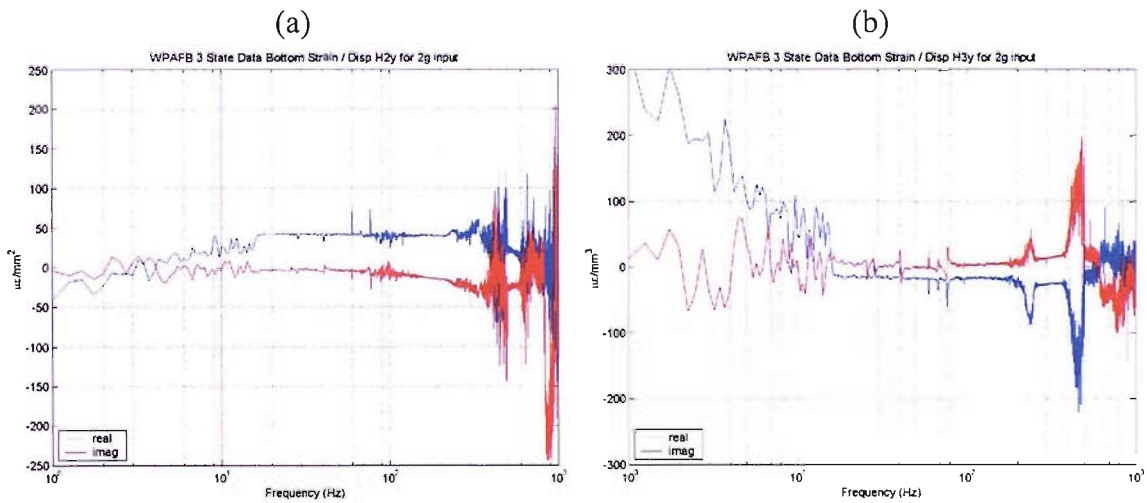

Figure 3.33. Estimates of displacement to bottom strain frequency response function determined from WPAFB input = 2 g data: (a) displacement squared input and (b) displacement cubed input.

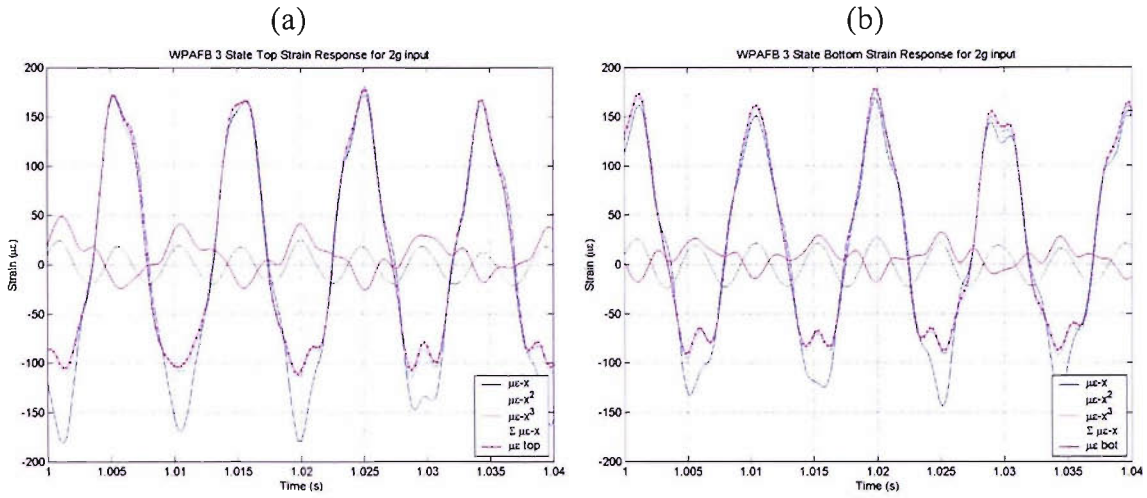

Figure 3.34. High amplitude time domain strain response estimates from full frequency range FRFs and raw strain WPAFB input = 2 g data: (a) top strain response estimates and (b) bottom strain response estimates.

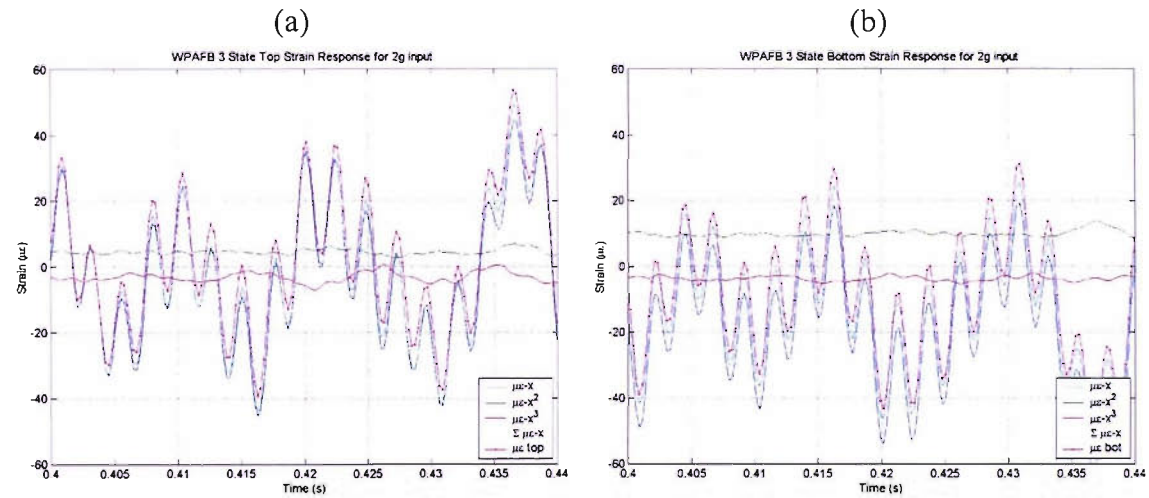

Figure 3.35. Low amplitude time domain strain response estimates from full frequency range FRFs and raw strain WPAFB input = 2 g data: (a) top strain response estimates and (b) bottom strain response estimates.

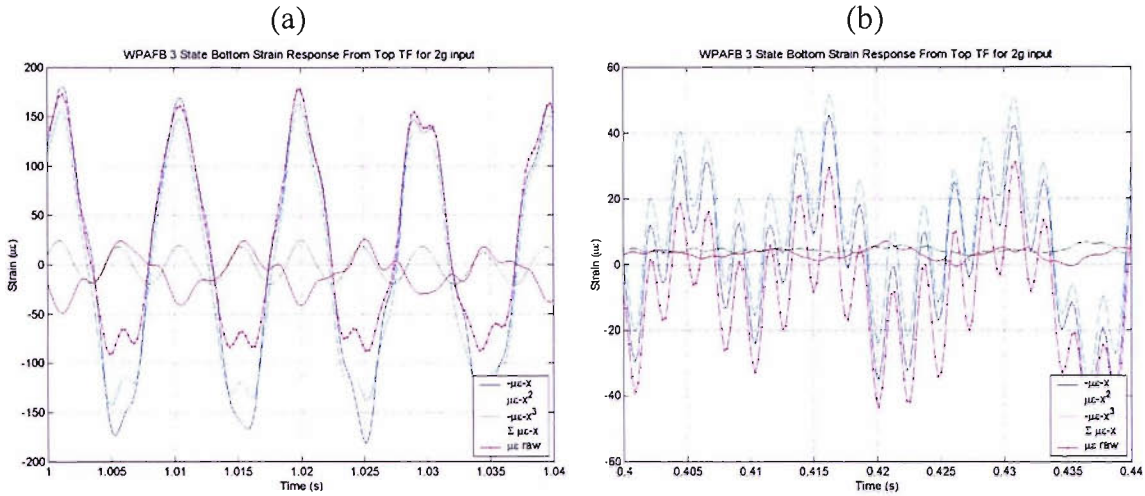

Figure 3.36. Time domain bottom strain response estimates from full frequency range top strain FRFs and raw bottom strain WPAFB input = 2 g data: (a) high amplitude bottom strain estimates and (b) low amplitude bottom strain estimates.

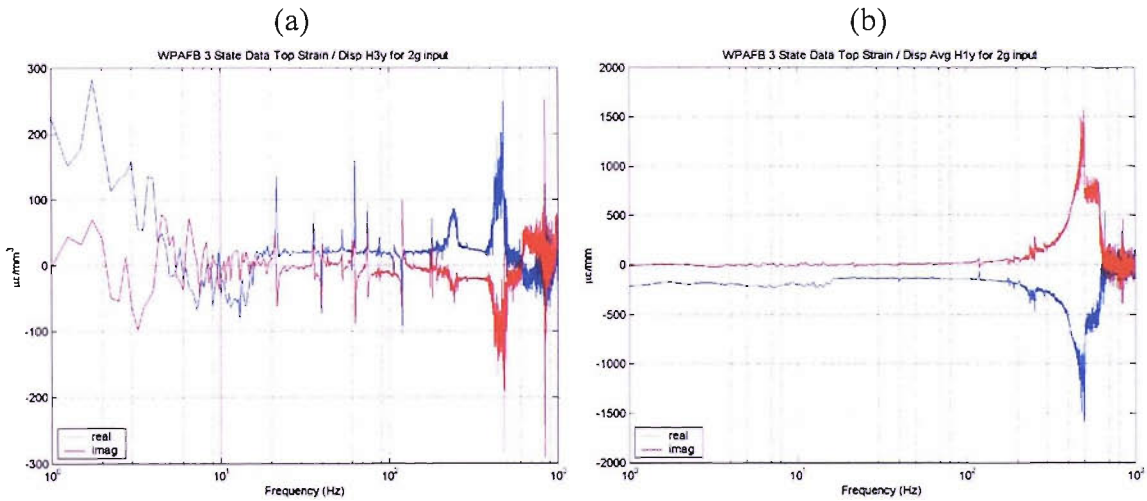

Figure 3.37. Displacement to top strain frequency response function determined from WPAFB input = 2 g data: (a) raw strain to displacement cubed input FRF and (b) averaged strain to linear displacement functions with constant low frequency values.

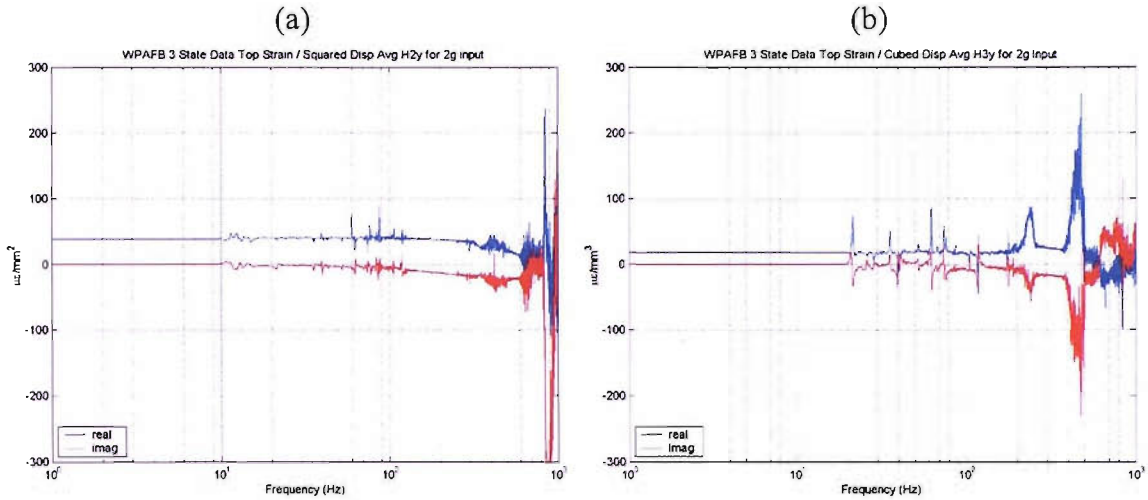

Figure 3.38. Displacement to strain averaged frequency response functions with constant low frequency values determined from WPAFB input = 2 g data: (a) strain to displacement squared functions and (b) strain to displacement cubed functions.

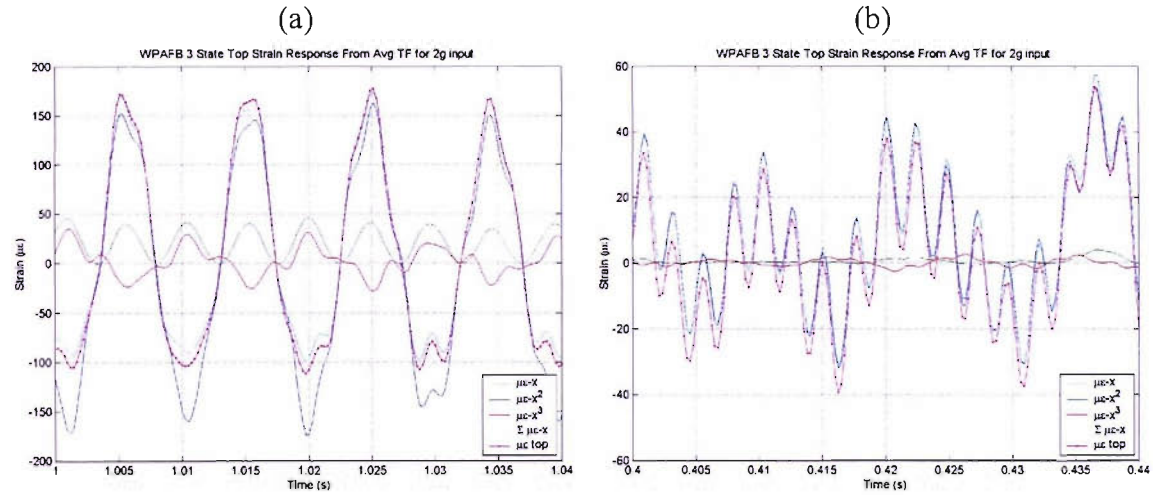

Figure 3.39. Time domain bottom strain response estimates from averaged frequency response functions of top strain and raw strain WPAFB input = 2 g data: (a) high amplitude top strain estimates and (b) low amplitude top strain estimates.

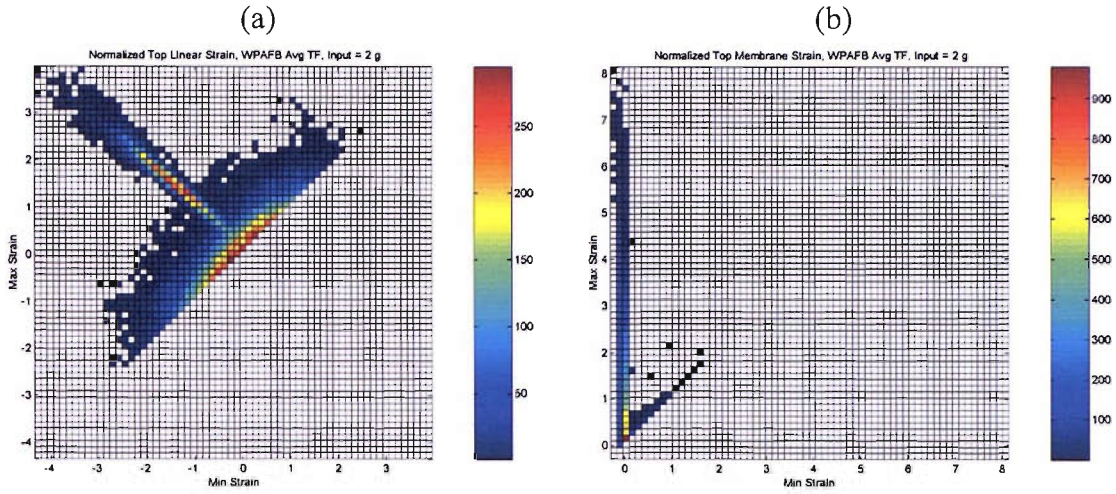

Figure 3.40. Normalized top surface RFM estimates from averaged frequency response functions for WPAFB input = 2 g data: (a) linear strain RFM estimates, $\sigma_{lin} = 71.8\ \mu\varepsilon$ and (b) membrane strain RFM estimates, $\sigma_{mem} = 11.5\ \mu\varepsilon$.

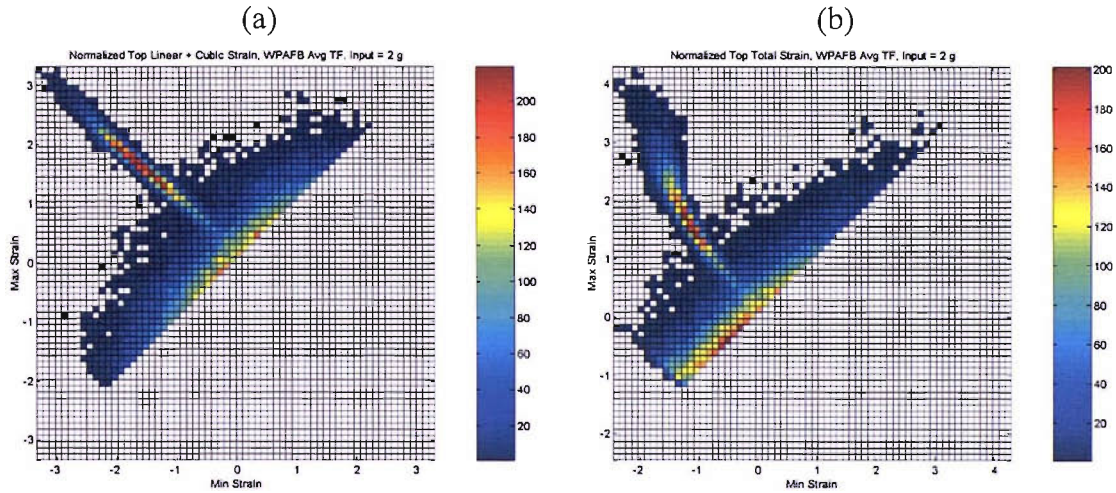

Figure 3.41. Normalized top surface RFM estimates from averaged frequency response functions for WPAFB input = 2 g data: (a) linear plus cubic strain RFM estimates, $\sigma_{lin+cube} = 66.4\ \mu\varepsilon$, and (b) total strain RFM estimates, $\sigma_{total} = 66.9\ \mu\varepsilon$.

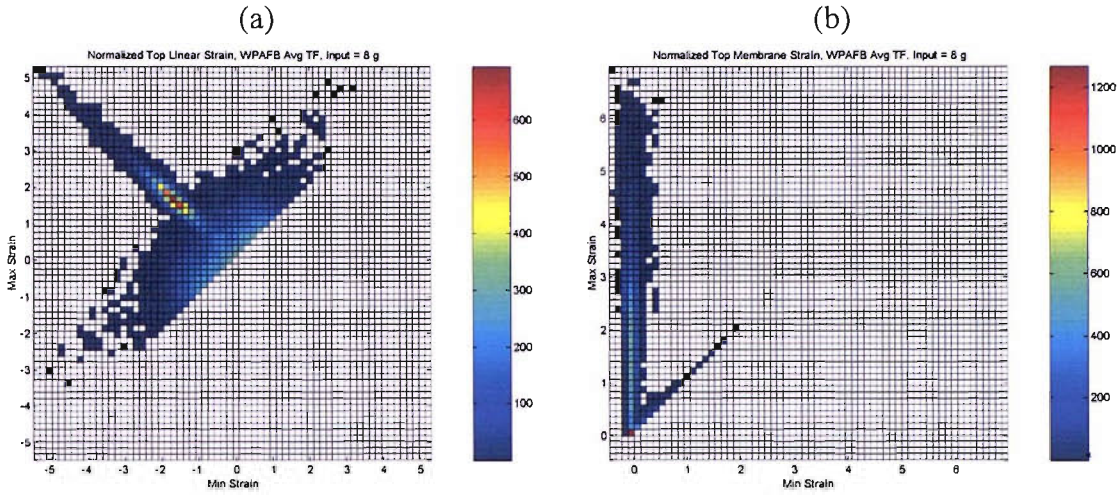

Figure 3.42. Normalized top surface RFM estimates from averaged frequency response functions for WPAFB input = 8 g data: (a) linear strain RFM estimates, σ_{lin} = 151 $\mu\varepsilon$ and (b) membrane strain RFM estimates, σ_{mem} = 45.3 $\mu\varepsilon$.

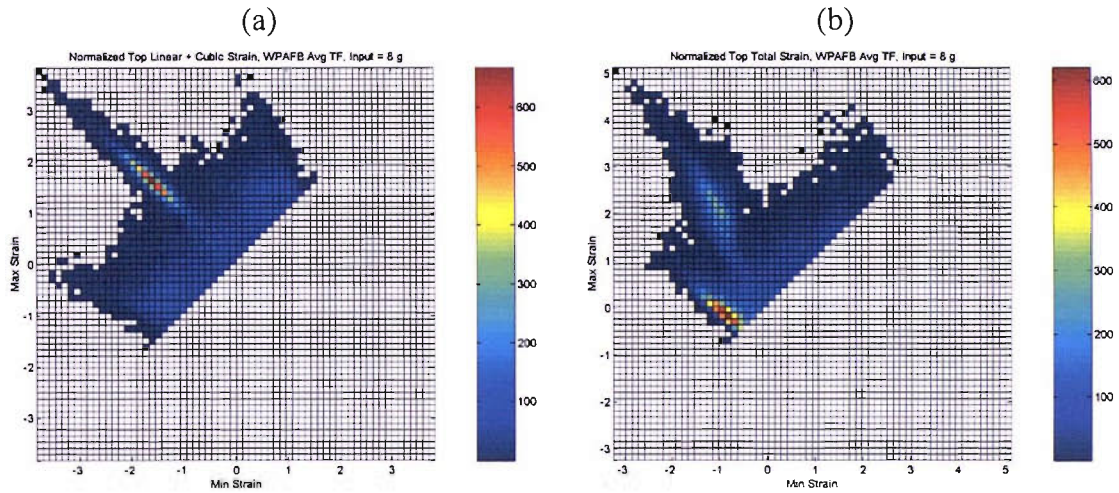

Figure 3.43. Normalized top surface RFM estimates from averaged frequency response functions for WPAFB input = 8 g data: (a) linear plus cubic strain RFM estimates, $\sigma_{lin+cube}$ = 144 $\mu\varepsilon$, and (b) total strain RFM estimates, σ_{total} = 150 $\mu\varepsilon$.

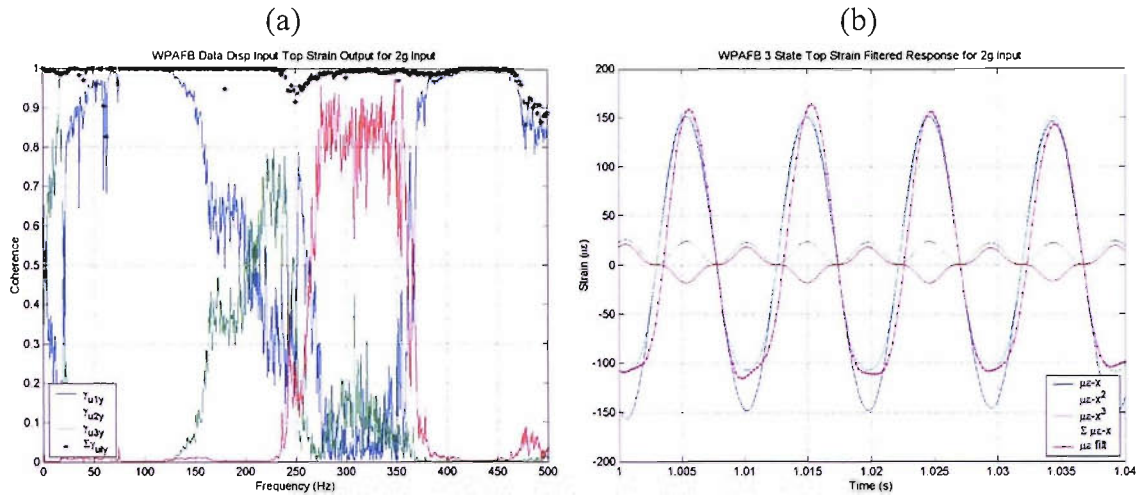

Figure 3.44 Surface strain results from WPAFB input = 2 g data: (a) Coherence functions for displacement input to top strain output frequency response functions and (b) high amplitude top strain time domain response estimates from filtered and averaged frequency response functions, compared to filtered strain data.

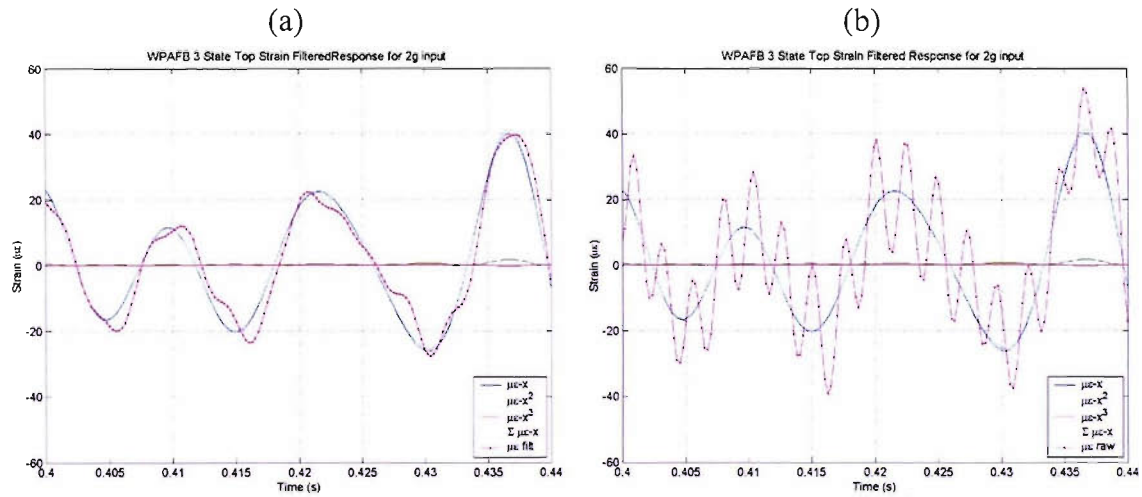

Figure 3.45.Time domain bottom strain low amplitude response estimates from filtered and averaged frequency response functions from WPAFB input = 2 g data: (a) top strain estimates with filtered strain data, and (b) top strain estimates with raw strain data.

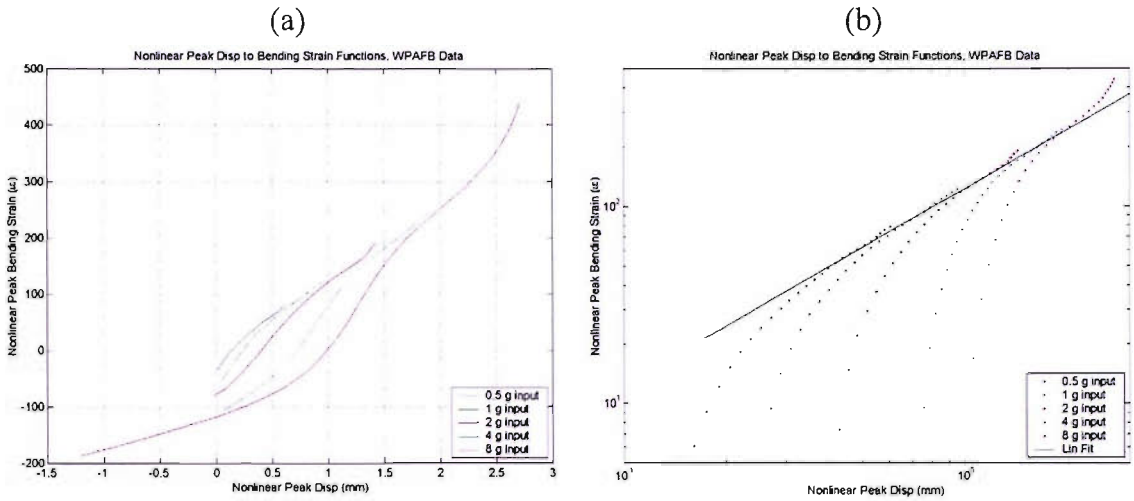

Figure 3.46. Nonlinear peak displacement to nonlinear peak bending strain functions from WPAFB input = (0.5, 1, 2, 4, 8) g data. (a) Linear plot of function and (b) log-log plot of function.

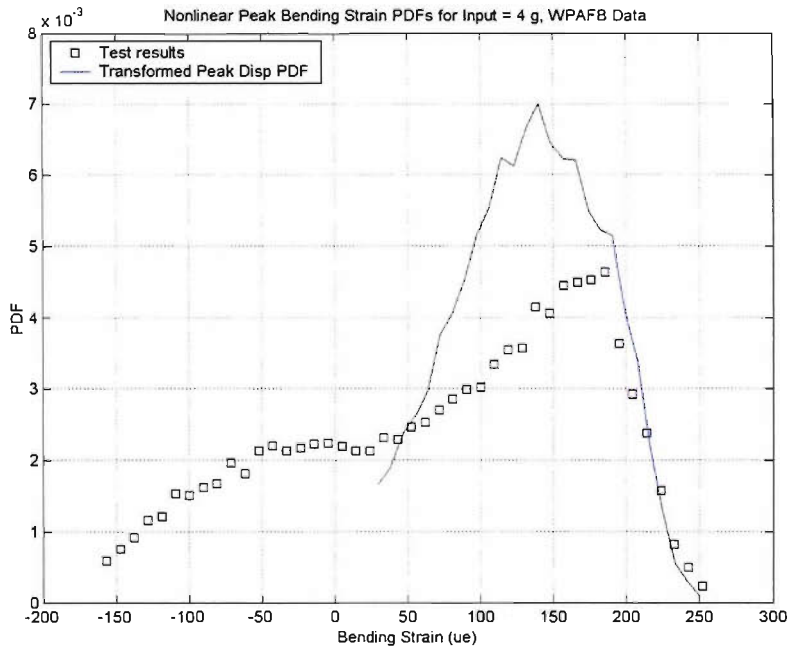

Figure 3.47. Peak bending strain PDF estimated from peak displacement PDF from WPAFB input = 4 g data.

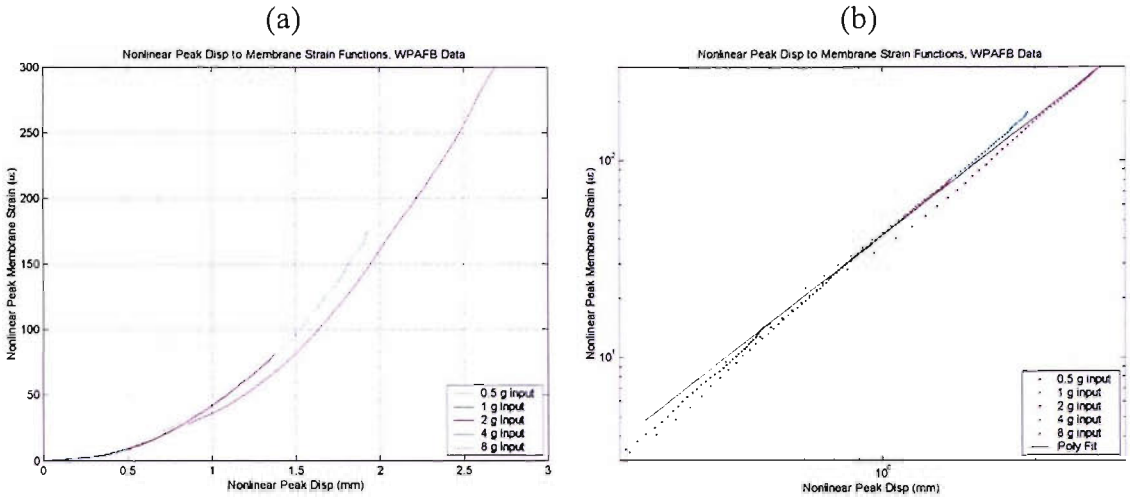

Figure 3.48. Nonlinear peak displacement to nonlinear peak membrane strain functions from WPAFB input = (0.5, 1, 2, 4, 8) g data. (a) Linear plot of function and (b) log-log plot of function.

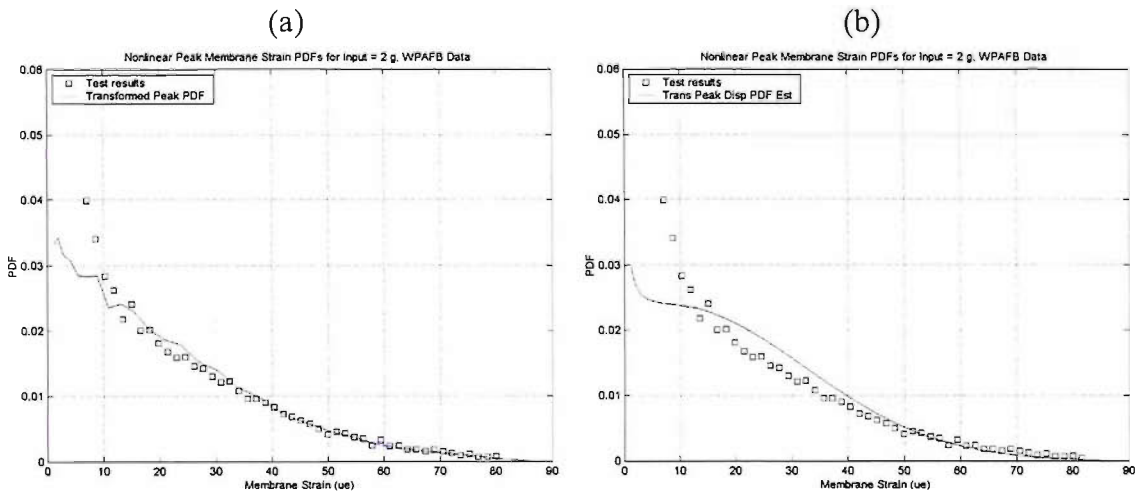

Figure 3.49. Peak membrane strain PDF estimate from WPAFB input = 2 g data. (a) Estimate from raw peak displacement PDF and (b) estimate from estimate peak displacement PDF.

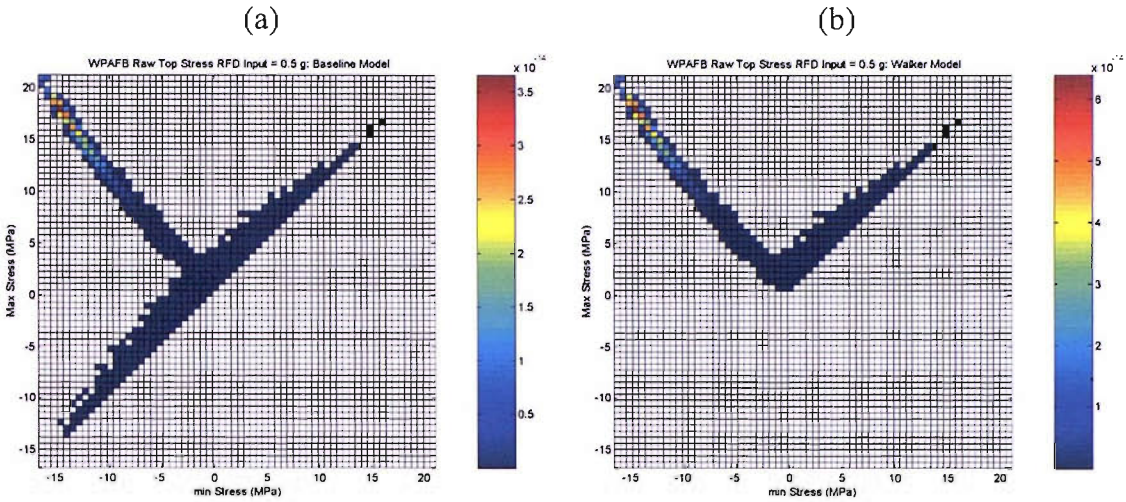

Figure 3.50. Rainflow damage matrices for raw top surface stress estimates from WPAFB input = 0.5 g data: (a) damage for baseline equation and (b) damage for Walker equation.

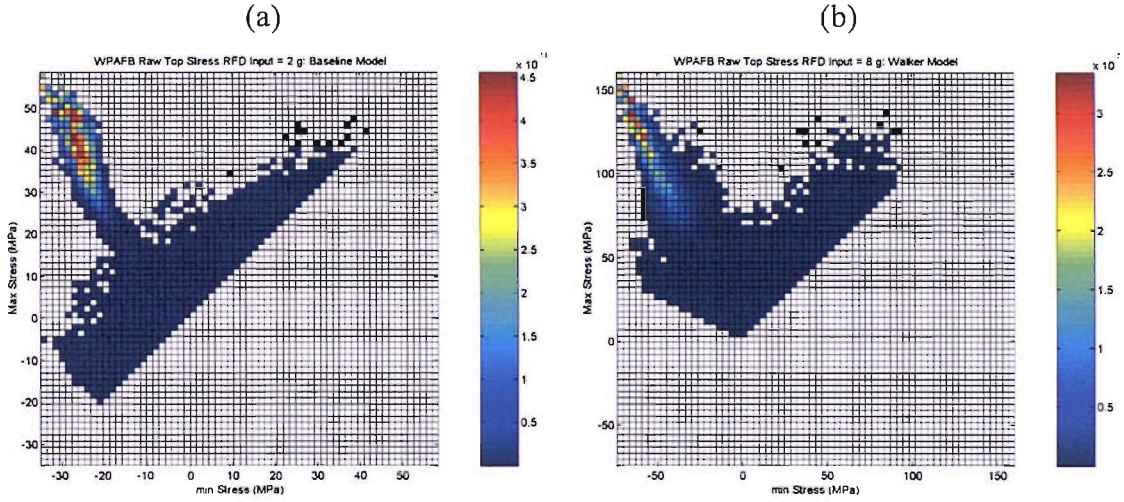

Figure 3.51. Rainflow damage matrices for raw top surface stress estimates from WPAFB data: (a) damage for baseline equation from input = 2 g data and (b) damage for Walker equation from input = 8 g data.

(a) (b)

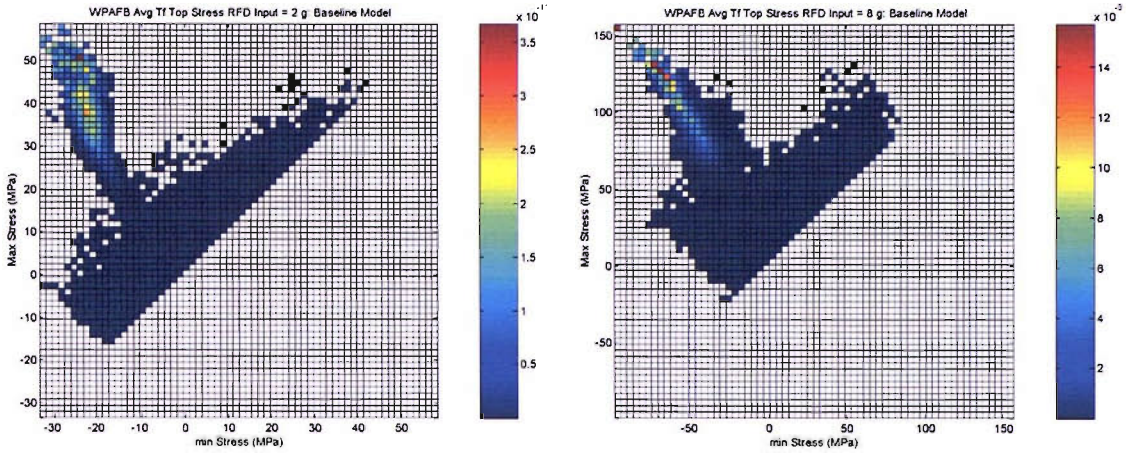

Figure 3.52. Rainflow damage matrices for top surface stress estimates using averaged frequency response functions from WPAFB data: (a) damage for baseline equation from input = 2 g data and (b) damage for baseline equation from input = 8 g data.

(a) (b)

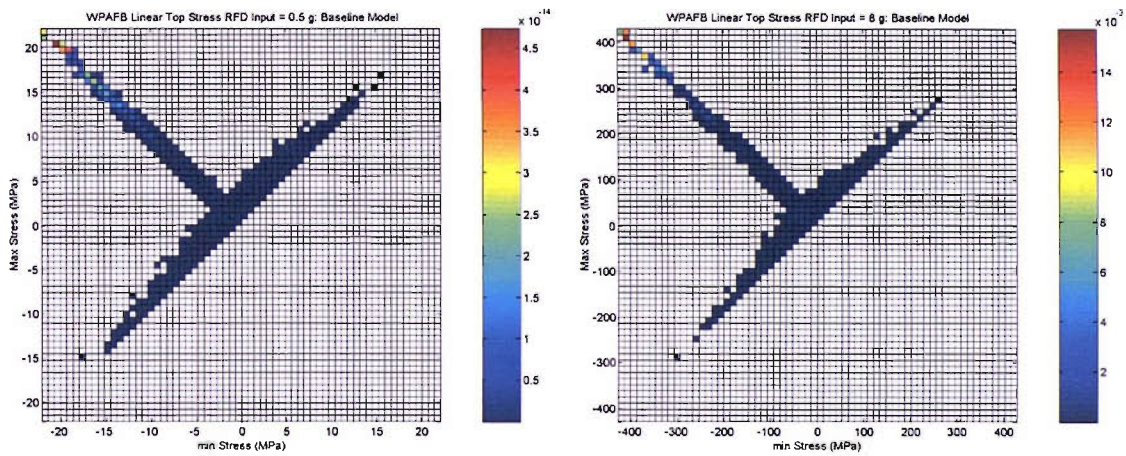

Figure 3.53. Rainflow damage matrices for top surface stress estimates using linear frequency response function from WPAFB data: (a) damage for baseline equation from input = 0.5 g data and (b) damage for baseline equation from input = 8 g data.

4 TIME & FREQUENCY DOMAIN ANALYSIS OF NONLINEAR NARROWBAND SIMULATIONS

This chapter will describe the ordinary differential equation (ODE) simulations that were performed on baseline linear and nonlinear single degree of freedom models, and the subsequent time and frequency domain post processing of these results. The ODE models developed in this chapter are based on the WPAFB experiments discussed in the previous chapter. The ODE simulations were performed so that large samples of nonlinear random data could be generated with various model input arguments and output states. Each simulation run yielded 256 s of response data and the simulations were repeated 20 times with different random input files.

The simulation outputs represented displacement and velocity response states for Gaussian broadband input. Further processing of these states yielded the acceleration response. Basic statistical estimates of the responses were determined for each simulation run and cumulatively over the set of 20 simulations. The results showed that the nonlinear displacement had a kurtosis less than 3, the velocity had a kurtosis approximately equal to 3 and the acceleration had a kurtosis greater than 3. The rate of convergence for the linear and nonlinear models was studied as well as the random errors in each statistical estimate.

Histograms and subsequent PDFs of the response data were generated to investigate the change in the functions as the results progressed from normal to nonlinear. Linear to nonlinear functions were estimated using the Inverse Distribution Function (IDF) method. The linear to nonlinear functions were then used to estimate the nonlinear PDFs using the PDF transform method. A chi-squared Goodness-of-fit test of the resulting PDFs was used to quantitatively evaluate the transformed PDFs. The test showed that the velocity response could be considered "nearly" normal. This result and the nonlinear response functions were used to develop an expression for the nonlinear change in the expected rate of zero crossings.

Peak histograms and PDFs were determined by sampling the data to find the minima and maxima. The peak PDFs were then used with the IDF method to estimate linear to

nonlinear peak response functions. Estimates of the nonlinear peak PDFs were then generated using the PDF transform method. The nonlinear peak displacement PDFs will be used in chapter 5, with further nonlinear PDF transforms, to study the change in fatigue life as the system progresses from linear to nonlinear.

A flow diagram of the overall simulation process is shown in Figure 4.1. The diagram shows the section numbers where each part of the flow will be described in further detail.

4.1 Differential equation simulation method

The nonlinear ODE models are based on the classic Duffing oscillator [2] with cubic stiffness and linear system parameters based on a lumped parameter model of the clamped-clamped geometry that was tested at WPAFB (see chapter 3). Once the displacement and velocity results were determined, the state derivatives (namely velocity and acceleration) were calculated. Linear models were also run to determine baseline results to compare with the nonlinear data.

The simulations were run for five different base shake input acceleration levels (0.5, 1, 2, 4 and 8 g RMS to match the WPAFB experiments) and three different viscous damping values ($\zeta = 0.01$, 0.003, and 0.001) which span the range of first mode damping values estimated in Chapter 3 (see Table 3.1). The results for each time domain input simulation were saved for further time and frequency domain analysis.

4.1.1.1 Random Time Domain Input

The ODE simulations required calculation of random time domain input data for use by each of the models. A flat random base shake acceleration input from 20 to 500 Hz was used, consistent with the WPAFB experiments. The input data were created by determining an equivalent Fourier Transform of the PSD spectrum magnitude with random phase angles for each frequency point (see section 2.2.3). The Fourier Transform was zero padded above the maximum input frequency to 32 768 Hz (approximately 64 times the maximum input frequency of 500 Hz) to ensure a smooth time history that could be linearly interpolated while running the ODE. A 256 s time

record, with a corresponding 0.004 Hz frequency spacing was used. The Inverse Fourier Transform of this spectrum yielded time domain records, with 8.4 million data points. This process was repeated 20 times with a new seed for the random number generator.

4.1.1.2 Nonlinear state space model

The model parameters were determined based on static properties of the clamped-clamped beam

$$\begin{aligned} I = bh^3/12 \quad A = bh \quad m = \rho lA \\ k_1 = 384EI/l^3 \quad k_3 = 10EA/l^3 \end{aligned} \tag{4.1}$$

where width b = 12.7 mm, thickness h = 0.79 mm, length l = 229 mm, elastic modulus E = 204.8 GPa and density ρ = 7867 kg/m^3. The stiffness k_1 is evaluated at the center of an ideal clamped-clamped beam, and the cubic stiffness k_3 is from equation (1.4) with an additional calibration factor of 10. Note, these values yield a natural frequency f_n = 69.21 Hz, which is slightly less than that estimated in Section 3.1.3.

The second order ODE simulations were based on the Duffing equation including viscous damping

$$m\ddot{x} + c\dot{x} + k_1 x + k_3 x^3 = F(t) = F \tag{4.2}$$

this was reduced to a standard first order two state ODE

$$\begin{aligned} z_1 = x;\ \dot{z}_1 = \dot{x} \\ z_2 = \dot{x};\ \dot{z}_2 = \ddot{x} = \frac{F - cz_2 + k_1 z_1 + k_3 z_1^3}{m} \end{aligned} \tag{4.3}$$

This SDOF system can also be written in mass normalized modal form

$$\begin{aligned} z_1 = x;\ \dot{z}_1 = \dot{x} \\ z_2 = \dot{x};\ \dot{z}_2 = \ddot{x} = \alpha - 2\zeta\omega_n z_2 - \omega_n^2 z_1 - \omega_{nl}^2 z_1^3 \end{aligned} \tag{4.4}$$

where

$$\alpha = \frac{F}{m};\ 2\zeta\omega_n = \frac{c}{m};\ \omega_n = \sqrt{\frac{k_1}{m}};\ \omega_{nl} = \sqrt{\frac{k_3}{m}} \tag{4.5}$$

and where α can be thought of as an inertial load, or the base acceleration. The differential equations can also be written using the state space (SS) form. The basic form of the continuous time SS equations is

$$\dot{z} = Az + Bu \tag{4.6}$$

where the vectors u are inputs and z are states. The linear SS model based on equation (4.4) above (with $u = \alpha = F/m$) is

$$\begin{bmatrix} \dot{z}_1 \\ \dot{z}_2 \end{bmatrix} = \begin{bmatrix} 0 & 1 \\ -\omega_n^2 & -2\zeta\omega_n \end{bmatrix} \begin{bmatrix} z_1 \\ z_2 \end{bmatrix} + \begin{bmatrix} 0 \\ 1 \end{bmatrix} u \tag{4.7}$$

A simple extension of the SS form includes the addition of cubic states such that

$$\dot{z} = Az + A_3 z^3 + Bu \tag{4.8}$$

where

$$A_3 = \begin{bmatrix} 0 & 0 \\ -\omega_{nl}^2 & 0 \end{bmatrix} \quad z^3 = \begin{bmatrix} z_1^3 \\ z_2^3 \end{bmatrix} \tag{4.9}$$

The Matlab ODE45 solver was used to determine the response states (displacement and velocity) based on numerical integration. Once the response states are estimated, the response rates (or state derivatives), namely the velocity and acceleration, can be determined by simple matrix algebra using equation (4.8).

4.1.1.3 Differential equation solver parameters

An output sample rate of 4096 Hz (with a Nyquist frequency of 2048 Hz) was used to capture third order harmonic response of the system where the input was limited to 500 Hz. Investigations described below (section 4.2.1.2) showed that the default ODE solver parameters needed to be modified for the simulations with the least damping ($\zeta = 0.001$). The default value for relative tolerance needed to be improved from 1×10^{-3} to 1×10^{-4} to give acceptable convergent results.

It should be stated that the solutions of the Duffing differential equations are not unique (i.e. two response conditions can be stable near resonance [1]). The method of using random input tends to "average" the non-unique solution (e.g. as opposed to a sinusoidal sweep that would experience a response "jump" near resonance). The problem with the random excitation is that small changes in the simulation solver parameters can yield different response results especially as the simulation times become longer. At first investigation these differences were of concern, but once they were understood, they were accepted as an underlying characteristic of the non-unique nonlinear response. The solution to this problem was to run multiple simulations with different random input vectors, followed by post processing to average the results. The assumption is that although there are differences between individual simulation responses one can still obtain convergence on the underlying statistical quantities.

4.1.2 Linear baseline simulations

Baseline linear results were determined for each time domain input and for each of the model damping values. A check was performed on the ODE solver over the 5 input levels to confirm that the solver returned consistent results at each input level for the linear model. Subsequent simulations were run with a 1 g RMS forcing function; the linear response was scaled by the 5 input values for comparison to the nonlinear results.

4.2 Time domain analysis of narrow band simulations

The next step in the analysis was to determine time domain statistics of the data. These statistics were then subsequently used to estimate PDFs, CDFs and IDFs for each family of simulations. Curve fits of the nonlinear functions were used with the PDF transform method to estimate PDFs for nonlinear displacement and acceleration.

4.2.1 Initial transient response

Differential equation solutions always contain a transient and a steady state solution. This nonlinear ODE simulation is no different and requires additional time (as described below) for the initial "start up" transient to decay.

4.2.1.1 Logarithmic decrement

The Logarithmic Decrement was used to estimate the time period required for an unknown ODE solution to reach a stable solution. The Logarithmic Decrement δ [260, 261] is defined for a viscously damped linear SDOF system as

$$\delta = \ln \frac{x_1}{x_2} = \zeta \omega_n T \tag{4.10}$$

where x_1 and x_2 are the values of the maxima for successive cycles.

The time period T_φ required for a free vibration transient response x to decay by a factor of φ is

$$T_\varphi = \frac{\ln \varphi}{\zeta \omega_n} = \frac{\ln \varphi}{\zeta 2\pi f_n} \tag{4.11}$$

For example, if it is desired to have the transient response decay by a factor φ equal to 1000, for a system with $\zeta = 0.01$ and $f_n = 70$ Hz

$$T_{1000} = \frac{\ln(1000)}{(0.01)2\pi(70)} = 1.57 \text{ s}$$

For the same system with $\zeta = 0.001$

$$T_{1000} = \frac{\ln(1000)}{(0.001)2\pi(70)} = 15.7 \text{ s}$$

4.2.1.2 Nonlinear free decay

To inspect the decay times, nonlinear ODE simulations were run for each of the damping values for a range of initial conditions. Zero initial displacement and various initial positive velocities were investigated. Figure 4.2(a) shows an example of the first few cycles of the nonlinear transient response for an initial velocity of 10 m/s and $\zeta = 0.003$.

Decay curves were produced by finding the maximum response (and time of occurrence) for each cycle. Another method using Hilbert transforms was also investigated, but it tended to produce decay curves with more noise (especially for strongly nonlinear responses), see Figure 4.2(b). Further investigation revealed that reducing the default ODE relative tolerance from 1×10^{-3} to 1×10^{-4} improved the behavior of the ODE solver for the lightly damped cases.

Typical plots of the decay of the system using $\zeta = 0.001$ are shown in Figure 4.3(a) and (b) for displacement and velocity. The plots were normalized so that time on the x axis is divided by T_{1000} and response on the y axis is divided by the peak value from the first cycle. (Note: this normalization was chosen instead of the initial conditions because the initial displacement is zero). If one sets a transient decay criterion to 1/1000 of the initial response then these plots show that one would need to wait approximately $1.2\times T_{1000}$.

4.2.2 Statistical errors in basic estimates of nonlinear results

Section 2.3 gives the time and number of samples required for estimating basic statistical properties (with a given level of uncertainty (for both bias and random errors)) for linear systems subjected to normal Gaussian inputs. This system is not linear; the following sections will describe the investigation into how the estimated results and their errors vary as the sampled time increases.

A function determined the basic and running sum statistics for each model damping value. The minimum and maximum results were also determined for subsequent histogram determination as discussed in section 4.2.3.

Applying the notation from section 2.1.1, i.e. $\hat{\phi}$ is an estimate of ϕ, μ_ϕ is the mean value of ϕ, σ_ϕ is the standard deviation of ϕ and $\varepsilon[\phi]$ is the normalized RMS error of ϕ. The ODE simulation results were analyzed for each 256 s file (with initial transient decay time removed) producing estimates $\hat{\phi}_k$ for each file and as a running sum $\underline{\hat{\phi}_k}$ of each estimate. The running sum technique used the formula

$$\underline{\hat{\phi}}_k = \frac{k-1}{k}\underline{\hat{\phi}}_{k-1} + \frac{1}{k}\hat{\phi}_k, 2 \le k < n \tag{4.12}$$

to determine the best estimate after k blocks of data. Where no closed form estimate for ϕ exists, $\phi = \underline{\hat{\phi}}_{20}$ will be assumed.

4.2.2.1 Mean

The results of the simulations are expected to have zero mean values for the displacement, velocity and acceleration, i.e.

$$\mu_x = \mu_v = \mu_a = 0 \tag{4.13}$$

The normalized bias error estimate of the mean has been modified for this case to be

$$\varepsilon_b\left[\hat{\mu}_0\right] = \frac{E\left[\hat{\mu}_0\right] - 0}{\underline{\hat{\sigma}}_{20}} = \frac{E\left[\hat{\mu}_0\right]}{\underline{\hat{\sigma}}_{20}} \tag{4.14}$$

where $\underline{\hat{\sigma}}_{20}$ is the estimate of σ determined from the total simulated time history.

Figure 4.4(a) shows the normalized bias error estimates of the mean displacement and velocity for $\zeta = 0.01$ for the linear model. Estimates of the normalized bias error for the nonlinear simulations tended to be larger than the errors from the linear model (as shown for example in Figure 4.4(b) for $\zeta = 0.01$). This is a preliminary indication of the nonlinear effects on the rate of convergence of results.

4.2.2.2 Standard deviation

The standard deviation estimates for the ODE simulations are given in Table 4.1 for the linear model and Table 4.3 for the nonlinear models after averaging 20 blocks of data. As a check, the standard deviation values were calculated (see Table 4.2) based on the theoretical estimate for a SDOF system with a flat spectral input [154]

$$\sigma_x^2 = \frac{\pi S_{FF}(\omega_n)}{kc} = \frac{\pi S_{FF}(\omega_n)}{2\zeta m^2 \omega_n^3}$$
$$\sigma_v^2 = \frac{\pi S_{FF}(\omega_n)}{mc} = \frac{\pi S_{FF}(\omega_n)}{2\zeta m^2 \omega_n} \qquad (4.15)$$
$$\sigma_a^2 = \frac{\pi G_{aa}(f_n) f_n}{4\zeta}$$

where $S_{FF}(\omega_n)$ is the two-sided spectrum of force (with units N^2/(rad/s)) at the natural frequency ω_n and $G_{aa}(f_n)$ is the one-sided spectrum of acceleration (with units g^2/Hz) at the natural frequency f_n. The check is the best for displacements and for the lightest damping cases.

The normalized standard deviation of each of the block estimates of σ for the sample of 20 blocks are given in Table 4.4 for the linear models and in Table 4.5 for the nonlinear models based on

$$\frac{\sigma[\hat{\sigma}]}{\underline{\hat{\sigma}}_{20}} = \frac{\sqrt{E(\hat{\sigma} - \underline{\hat{\sigma}}_{20})^2}}{\underline{\hat{\sigma}}_{20}} \qquad (4.16)$$

The results show that the linear models produce a common RMS error for each response state for a given value of damping, but in each case the RMS error in the nonlinear response estimates is increased for the derivative responses. Also interesting is that the RMS errors for displacement and velocity tend to decrease as the input increases for the $\zeta = 0.001$ model. This is an unexpected result and may be due to the increase in the statistical bandwidth B_s of the nonlinear response (see equation (2.81)). The PSD of the linear and nonlinear results are given later (Section 4.3.1), but the bandwidth B_s, given in Table 4.6 and Table 4.7, will be used to estimate the RMS error of the σ estimates here.

The statistical bandwidth is used as a parameter in a relationship for the normalized random error of σ as a function of the sample time (see [248] equation (8.47))

$$\varepsilon_r[\hat{\sigma}] = \frac{1}{2\sqrt{B_s T}} \qquad (4.17)$$

The normalized random error estimate of σ for the first k blocks of the 20 data blocks is defined to be

$$\varepsilon_r\left[\hat{\sigma}_k\right] = \frac{\sqrt{\left(\hat{\underline{\sigma}}_k - \hat{\underline{\sigma}}_{20}\right)^2}}{\hat{\underline{\sigma}}_{20}} \tag{4.18}$$

Typical plots of normalized random error for the linear model are shown in Figure 4.5(a) and Figure 4.5(b). Both examples show that equation (4.17) gives a good estimate of the upper bound of the random error, and that the models with more damping ($\zeta = 0.01$) tend to have less variation in the estimates than the models with less damping ($\zeta = 0.001$).

The random error estimates of σ are shown for the nonlinear model in Figure 4.6(a) and (b) for $\zeta = 0.01$ and $\zeta = 0.001$ respectively. At the lowest input level, when $\zeta = 0.01$, the random error estimates of σ_x tend to be near the linear estimates, but as the model becomes more nonlinear, the random error of σ tends to increase. Also, the theoretical random error based on the statistical bandwidth given in equation (4.17) clearly underestimates the measured random error. The random error estimates of nonlinear acceleration σ_a are much worse than expected.

These observations reinforce the need for very large sample sizes for producing basic statistical estimates of the nonlinear response. The use of the statistical bandwidth estimated from nonlinear PSDs is not advised as a method to estimate the random errors in σ calculations. Inspection of Table 4.6 shows that B_s determined from the linear response tends to decrease as the damping decreases and increases for derivative responses. Table 4.7 also shows that B_s increases for the nonlinear derivative responses, but B_s decreases and then increases as the damping decreases. It is hypothesized that the harmonic distortions, seen in the high frequencies of the nonlinear response, significantly affect these calculations. Other researchers have also identified the need for large sample sizes when working with nonlinear random data [262].

4.2.3 Histograms and PDFs from ODE data

Another function was used to determine histograms, PDFs and central moments of the PDFs. The number of histogram bins was chosen to be 128 (64 for the positive values and 64 for the negative) with minimum and maximum limits determined from the complete set of 20 data files. The maximum response measured was typically around 4 σ; This yielded bin spacing (W) of approximately $\sigma/16$ which is considered an acceptable comprise for minimizing both bias and random errors in the PDF estimates (See section 2.3.2).

The resulting PDFs presented were determined based on the full set of data for each of the damping and input levels. The PDF estimates for a typical baseline linear model ($\zeta = 0.001$) are shown in Figure 4.7(a); the response PDFs appear normal for all linear models.

A Chi-Squared Goodness-of-Fit test of the PDFs was used to test the normality of the results using

$$X^2 = \sum_{i=1}^{K} \frac{(f_i - F_i)^2}{F_i} \tag{4.19}$$

where f_i is the observed frequency of the simulation histogram and F_i is the expected frequency of a histogram based on a normal PDF. K is the degree of freedom for the Goodness-of-Fit test; for these results a conservative value of $K = 120$ was used based on a number of histogram bins of 128. The region of acceptance of the one-sided test is

$$X^2 \leq \chi^2_{n;a} \tag{4.20}$$

where the value of $\chi^2_{n;a}$ is available from standard statistical tables (e.g. Table A.3 from [248]) for an acceptance region of 1-α. For example, if one desired an acceptance region of 90% (i.e. stating a hypothesis that a histogram or PDF from a normal distribution would have a goodness-of-fit test value less than $\chi^2_{n;0.1}$ for 90% of the trials) for $K = 120$, $\chi^2_{120;0.1} = 140.23$. Table 4.8 gives the results of the goodness-of-fit test for

the linear models. The hypothesis test of normality can easily be accepted at the 90% ($\alpha = 0.1$) level of significance for the displacement and velocity results.

Figure 4.7(b) shows typical displacement response PDFs estimated from the $\zeta = 0.001$ nonlinear simulations. These clearly show the non-normal response behavior for the nonlinear displacement, especially as the input increases and the damping is reduced.

Figure 4.8(a) shows a set of velocity response PDFs estimated from the nonlinear simulations. Unlike the nonlinear displacement, this data seems to follow the Normal PDF in most regions, except for a slight increase around zero velocity, especially for the $\zeta = 0.001$ model at high input levels. The Chi-Squared Goodness-of-Fit test on the nonlinear velocity response PDFs shows that data from the two lower levels would pass a 90 % acceptance normality test at $\chi^2_{120;0.1} = 140.23$, while a larger 99 % acceptance test at $\chi^2_{120;0.01} = 158.95$ would allow the 8 g response data to pass the normality hypothesis as well.

Figure 4.8(b) shows a typical set of acceleration response PDFs estimated from the $\zeta = 0.01$ nonlinear simulations. Unlike the nonlinear displacement results, this acceleration data shows response PDFs with increased tails and center values.

4.2.3.1 Moments of the response PDFs

As described in section 2.1.1, the standard deviation, skew and kurtosis can be determined by calculating the higher order moments of a PDF. As a check, standard deviation results calculated from the second moment of the PDFs determined above were compared with the results determined in Section 4.2.2.2. The comparison had normalized bias differences on the order of -1×10^{-4}. The kurtosis results presented here were calculated based on the fourth moment of the PDFs.

As with the other statistical measures of the linear model response, the linear kurtosis estimates were virtually identical for the displacement and velocity response calculations for a given value of damping (see Table 4.10). Figure 4.9 shows typical kurtosis results for the $\zeta = 0.001$ linear model, which are all close to the theoretical value of 3.

The displacement kurtosis for the nonlinear $\zeta = 0.01$ model is shown in Figure 4.10(a). The velocity kurtosis is shown in Figure 4.10(b) for $\zeta = 0.01$. These plots show that the velocity kurtosis seems to converge in both cases to a value of approximately 3, but the nonlinear displacement results have kurtosis values less than 3. The kurtosis estimates from the nonlinear model responses are given in Table 4.11. The acceleration kurtosis is much greater than 3, especially at the highest input levels. It is also interesting to note that the normalized random error in the kurtosis estimates is highest for the acceleration results.

4.2.4 Peak response matrices and PDF from data

Peak response estimates for the response data were generated using Rain Flow Matrices (RFM) (as discussed in Section 2.4.6). A typical normalized displacement RFM is shown in Figure 4.11(a). Figure 4.11(b) shows the normalized minimum and maximum peak displacement histograms for this RFM. Note that the two histograms are almost mirror images of each other. The histogram of minima can be averaged with the histogram of maxima to form a single estimate of the peak PDF, when the functions can be presumed symmetric.

4.2.5 Response zero crossing and peak rates

The rates of zero crossings and peaks are very important for peak response and fatigue analysis (see Section 2.1.4). Table 4.12 gives the rates of positive slope zero displacement and velocity crossings as well as the rates of positive displacement peaks (maxima) for the nonlinear simulations. Also tabulated are the ratios of displacement zeros to peaks ϖ_x. One observation from the results is that the ratio ϖ_x tends to decrease as the system becomes more nonlinear. This trend was also noted with the WPAFB data (see Table 3.6).

The corresponding rates of zero crossings and peaks were also determined for the acceleration (see Table 4.13). These results show some trends that were not observed with the peak displacement results. Table 4.13 shows that like the displacement results, the rates of zero crossings tends to increase as the input increases, but the change in the rate of peaks is not as clearly defined. The lower damping model shows that the rate of

peaks actually decreases as the input increases. An explanation of this can be hypothesized with the aid of Figure 4.26 which shows the acceleration PSD. At the lowest input level of 0.5 g, there is a significant "plateau" of acceleration response (from about 100 to 500 Hz) that tends to generate a large number of peaks. As the input level increases, the system becomes stiffer thereby reducing the "plateau" relative to the fixed upper frequency of 500 Hz. It is interesting to see that the $\zeta = 0.001$ model results show a decrease in the rate of acceleration peaks for the first two input levels, but then the trend reverses and the rates of peaks starts to increase again.

The ratio of acceleration zeros to peaks shows a clear decrease for all conditions. The reversal in the trend of peaks for the $\zeta = 0.001$ model is countered by the continual rise in rates of zero crossings to yield rate ratios ϖ_a that always increase.

Perhaps an even more convincing argument comes from examination of the time domain data. The strong nonlinearity in the acceleration at high inputs tends to make the peaks very pointed (see Figure 4.12(b)) masking the effect of the higher frequency response that can "ride on top" of fundamental response cycles of the linear acceleration at low inputs (see Figure 4.12(a)). The strongly nonlinear response looks very "narrow band" in the time domain as the values of ϖ_a indicate.

4.2.6 Displacement response peak PDFs

The peak displacement PDFs were calculated from displacement RFM. Figure 4.13(a) shows a comparison of a PDF determined for the linear $\zeta = 0.001$ model and a Rayleigh PDF. Note that the ratio of zero to peaks for this model was 1 to four significant digits. Figure 4.13(b) shows a comparison of a PDF determined from the $\zeta = 0.01$ data, with the Rayleigh and generalized peak PDFs. The ratio of zero to peaks for this model was 0.993. Modified goodness-of-fit tests,

$$X^2 = \sum_{i=1}^{K} \frac{(f_i - F_i)^2}{f_i} \tag{4.21}$$

where f_i is the observed frequency of the simulation histogram and F_i is the expected frequency of the histogram (based on a Rayleigh and the generalized Peak PDF), were

computed. The observed frequency f_i was used here to avoid a division by zero for negative amplitude bins when performing the test with the Rayleigh PDF. The results are given in Table 4.14 for various bin center ranges. Although the data in Figure 4.13(a) looks to closely match the Rayleigh PDF, this hypothesis cannot be accepted based on a Chi-Squared criterion at the lowest α level of significance (see Table 4.15) for either bin center range calculated.

The data from Figure 4.13(b) requires a bit more discussion. This data begins to show the existence of maxima at negative values (even at a ratio of zeros to peaks of 0.993). The Rayleigh PDF has a value of zero for negative maxima. The goodness-of-fit test was modified to allow the calculation of test statistic for both the Rayleigh and generalized peak PDF as given in Table 4.14. Over the wide range of bins that included negative maxima, both tests yield results that will reject the hypothesis, although the peak PDF result is much closer to being accepted. The hypothesis can be accepted at the $\alpha = 0.10$ level of significance for the peak PDF and at the $\alpha = 0.01$ level for a Rayleigh PDF over the higher amplitude positive bin range. Based on these findings, a Rayleigh PDF will only be assumed for the lowest damping SDOF cases while the generalized peak PDF will be used for all other calculations. The peak displacement PDFs were then determined for the nonlinear results. Figure 4.14(a) and (b) show the corresponding peak displacement PDFs determined for $\zeta = 0.001$ and $\zeta = 0.01$ respectively. Again it is interesting to note the negative maxima for the $\zeta = 0.01$ model.

4.2.7 Response velocity peak PDFs

Given that the response velocity was nearly normal, the peak velocity is assumed to follow the peak response predicted for a Gaussian (normal) signal (i.e. a generalized peak PDF); Figure 4.15(a) shows that this is a reasonable assumption.

4.2.8 Response acceleration peak PDFs

An example nonlinear acceleration peak PDFs is shown in Figure 4.15(b). Here the peak PDFs show negative maxima at the lowest input levels, but only positive maxima at the highest input. Note the increase in the normalized value of the acceleration

response tails that reach a value of approximately 10 σ. Again, time domain data shown in Figure 4.12 helps to explain the peak PDF results.

4.2.9 Linear to nonlinear functions based on inverse distribution function

The inverse distribution function (IDF) method was used in Chapter 3 to estimate linear to nonlinear functions for the wideband experimental data. The linear to nonlinear functions generated for displacement response (based on the assumed Gaussian distribution) resulted in a unique set of functions for each input level. On the other hand, the peak displacement linear to nonlinear functions, for the wideband data, tended to fall along one common curve at the large amplitude response. This trend was especially noticeable when one assumed a linear peak distribution with the same ratio ϖ as the measured nonlinear peak data (see Section 3.2.5). The behavior of the linear to nonlinear functions for the SDOF Duffing model is presented next.

4.2.9.1 Linear to nonlinear function of displacement response

Histograms of the nonlinear displacement (see Section 4.2.3) were used to generate linear to nonlinear functions as described in Section 3.2.3, fit with polynomial functions

$$d_{i,1}y + d_{i,2}y^2 + d_{i,3}y^3 = x \tag{4.22}$$

where $d_{i,j}$ are the displacement coefficients for the input i and the polynomial power j (see Table 4.16). The linear to nonlinear functions from this nonlinear model are similar to those from Chapter 3 (compare Figure 3.19(b) with Figure 4.17(b)). This polynomial model will be used in Section 4.2.12 to estimate rates of zero crossings of nonlinear displacement. One additional observation here is that the standard deviation results from the linear and nonlinear simulations (see Table 4.1 and Table 4.3) fall just below the corresponding response curve (see Figure 4.16(b)).

4.2.9.2 Linear to nonlinear function of peak displacement

The findings from Section 3.2.5 suggest an IDF method for determining the linear to nonlinear function peak displacement based on a variable ratio ϖ_x linear peak PDF. The

nonlinear displacement data again shows a change in the ratio ϖ_x with input level and damping (see Table 4.12). For these reasons, the linear to nonlinear peak functions determined here will use the variable ratio peak PDFs with the IDF method.

Figure 4.17 shows two sets of data points for the linear to nonlinear peak functions for the SDOF simulations. This data now shows one common trend for all input levels. In fact, when the data from the models with damping are plotted on one graph (see Figure 4.18(a)), it suggests that the underlying relationship is based on the Duffing parameters α and γ from Equation (1.5) and not the damping level ζ.

As before, a polynomial curve fit, of the form

$$c_1 y + c_2 y^2 + c_3 y^3 = x \tag{4.23}$$

was used to determine peak displacement coefficients (see Table 4.17). It is interesting to compare these coefficients with the normal displacement function results in Table 4.16. The displacement $d_{i,1}$ linear slope term is increasing as the input increases and the $d_{i,3}$ term for the highest input level is approaching the peak c_3 term.

Given that these linear to nonlinear peak functions are so consistent across the inputs and damping values, it is worth comparing them to the results obtained for the normal displacement IDF problem from Section 4.2.9.1. Figure 4.18(b) shows the normal displacement data again, but now with the linear to nonlinear peak displacement function polynomial fit shown for comparison. It is worth observing that the peak displacement function seems to be a limiting function for the normal displacement functions. This is due to the fact that the peak response and the peak value of the data are the same at high amplitudes. Hence the normal displacement function is tangent to the peak displacement function in these regions.

4.2.9.3 Linear to nonlinear function of peak acceleration

The IDF method was applied to the acceleration results yielding typical linear to nonlinear peak acceleration functions as shown in Figure 4.19. These curves are different than the linear to nonlinear peak displacement functions in that they show a nonlinear increase as the linear response increases. This behavior is hypothesized to be

due to a balancing of the differential equation which describes the relationship between the various states of the response, i.e., if the input force is normal, the summation of the displacement, velocity and acceleration terms need to be also normal. It has been shown that the velocity is nearly normal, and that the displacement shows a nonlinear decrease in response as the linear response increases (see, for example, Figure 4.18). The acceleration is therefore hypothesized to show a nonlinear increase in response to balance the displacement decrease.

This increasing nonlinear response lends itself to a "right hand" nonlinear polynomial model like

$$\begin{aligned} \alpha &= g(a) \\ \alpha &= \kappa_1 a + \kappa_2 a^2 + \cdots + \kappa_n a^n \end{aligned} \tag{4.24}$$

where α is the nonlinear acceleration. As before, the positive peak values (maxima) were used to produce the cubic polynomial curve fit coefficients. Figure 4.19 also shows the third order polynomial curve fit determined from each data set. The peak acceleration linear to nonlinear functions show a few more data points that do not follow one main trend (compared to the peak displacement functions (see Figure 4.18)). This is similar to what was observed with the experimental peak displacement data (see Figure 3.23(b)).

4.2.10 Nonlinear peak displacement PDFs from PDF transforms

The PDF transfer function for the linear to nonlinear peak displacement polynomial function determined from the IDF method is

$$p_{nl\,peak}(y,\varpi) = \left| dx/dy \right| p_{peak}(x,\varpi) \tag{4.25}$$

Instead of trying to solve this equation in closed form, the numerical result can be easily determined by first estimating the linear peak "bin center" values using

$$\hat{x} = c_1 y + c_2 y^2 + c_3 y^3 \tag{4.26}$$

where now, the y values should be based on the nonlinear histogram bin centers. The derivative of equation (4.23) for the third order polynomial is

$$dx/dy = c_1 + 2c_2 y + 3c_3 y^2 \tag{4.27}$$

Substituting equations (4.27), and (4.26) into (4.25) yields

$$p_{nl\,peak}(y,\varpi) = \left|c_1 + 2c_2 y + 3c_3 y^2\right| p_{peak}(\hat{x},\varpi) \tag{4.28}$$

The generalized peak PDF p_{peak} is given in equation (2.20). In use, one would evaluate the generalized peak PDF at the estimated linear peak bin center values (from equation (4.26)) and then simply multiply by the derivative (using equation (4.27)) to estimate the nonlinear peak PDF given in equation (4.28). Results from two peak displacement PDF transforms are shown in Figure 4.20.

Having estimated the nonlinear peak PDF, the goodness-of-fit of these transforms can be evaluated as before. The results of this evaluation are given in Table 4.18 and Table 4.19 for the transformed Rayleigh and general peak PDFs respectively. The magnitude of the test results shows that a strict statistical hypothesis statement cannot be made, but the results can still be used to make some observations.

First, the PDF transforms for the $\zeta = 0.01$ model results are a better fit to the simulation data than the transforms for the $\zeta = 0.001$ model. Secondly, the PDF transforms tend to be best at the lowest and highest levels of response. Remember that these were the data cases that were used to estimate the polynomial coefficients for the linear to nonlinear peak displacement functions.

4.2.11 Nonlinear peak acceleration PDFs from PDF transforms

Nonlinear PDF estimates based on the linear to nonlinear acceleration response functions use the PDF transform equation based on the right hand side linear to nonlinear function given in equation (4.24)

$$p_{nl\,peak}(\alpha,\varpi) = \frac{p_{peak}(a,\varpi)}{\left|d\alpha/da\right|} \tag{4.29}$$

Here again, the ratio ϖ_a is determined at each input level and used with the linear peak PDF. Figure 4.21(a) and (b) shows typical peak PDF transform for the $\zeta = 0.01$ and $\zeta = 0.001$ models compared with the PDF determined from the min and max histograms calculated from a peak acceleration RFM. These results are not as good as those determined for transformed displacement functions, but, they are still encouraging, especially in the high PDF, low response amplitude regions. Figure 4.22 shows the same data as Figure 4.21, but this time with a logarithmic PDF; these results show very good agreement in the low PDF, high response amplitude regions.

4.2.12 Estimating rates of zero crossings from nonlinear amplitude PDFs

Section 5.5.1 of [248] derives the expected number of zero crossings per unit time for stationary random data with any joint probability density function. This derivation will be used here to estimate the rates of zero crossings for the nonlinear displacement results.

Let $p_{x,v}(x,v)$ represent the joint probability density function of displacement and velocity when $x(t) = x, v(t) = \dot{x}(t) = v$. The number of zero up and down crossings per unit time is given by

$$E[0_x] = \int_{-\infty}^{\infty} |v| \, p_{x,v}(0,v) \, dv \tag{4.30}$$

Assume also that the displacement and velocity are statistically independent, i.e. $p_{x,v}(x,v) = p_x(x)\, p_v(v)$ [4, 248]. From the findings in Section 4.2.3, the velocity PDF is assumed to be "nearly" normal

$$p_{norm}(v) = \frac{1}{\sigma_v \sqrt{2\pi}} \exp\left(\frac{-v^2}{2\sigma_v^2}\right) \tag{4.31}$$

and the nonlinear displacement PDF is estimated using a PDF transform [125, 160, 263] by

$$p_{nl\,norm}(x) = \frac{\left(d_{i,1} + 2d_{i,2}x + 3d_{i,3}x^2\right)}{\sigma_x\sqrt{2\pi}} \exp\left(\frac{-\left(d_{i,1}x + d_{i,2}x^2 + d_{i,3}x^3\right)^2}{2\sigma_x^2}\right) \tag{4.32}$$

where the coefficients $d_{i,j}$ were determined for each input level i (see equation (4.22)). At $x = 0$,

$$p_{nl\,norm}(0) = \frac{d_{i,1}}{\sigma_x\sqrt{2\pi}} \tag{4.33}$$

and

$$E_{nl}[0_x] = \frac{d_{i,1}}{2\pi\sigma_x\sigma_v}\int_{-\infty}^{\infty}|v|\exp\left(\frac{-v^2}{2\sigma_v^2}\right)dv = \frac{d_{i,1}\sigma_v}{\pi\sigma_x} \tag{4.34}$$

If one would prefer only the number of up crossings (or positive slope zero crossings), then:

$$E_{nl}\left[0_x^+\right] = \frac{d_{i,1}\sigma_v}{2\pi\sigma_x} \tag{4.35}$$

The nonlinear estimates of $E_{nl}\left[0_x^+\right]$ for the (0.5, 2, 8) g input levels using equation (4.35) and the $d_{i,1}$ coefficients are given in Table 4.20. Although these results slightly underestimate the expected rates determined by counting the raw displacement zero level crossings (repeated from Table 4.12 column labeled $\Phi\left[0_x^+\right]$), they validate the usefulness of equation (4.35).

4.3 Frequency domain analysis of narrow band simulations

The frequency domain analysis of the linear baseline and nonlinear results is presented to augment the extensive time domain analysis present in the previous section and to form a basis for comparison. Also presented are reverse path nonlinear identification results.

4.3.1 PSD and expected rates

Figure 4.23(a) and (b) show the PSD of displacement and velocity respectively from the linear model. The sample size chosen for these PSD estimates was 16 s which resulted in a frequency resolution Δf of 0.0625 Hz. The PSD estimates were made using a Hamming window, 50% overlap and a sample rate of 4096 Hz resulting in 65 536 points for the FFT and 32 769 frequency domain points (including $f = 0$ and $f = f_{nyq}$). The Δf of 0.0625 Hz was chosen as a compromise between number of averages and frequency resolution (see Section 2.5 for further discussion of errors in basic estimates of random processes). The standard deviations and expected response rates determined from these baseline PSDs (see section 2.2.2) for the linear models are given in Table 4.21.

Figure 4.24(a) through Figure 4.25(b) show the PSD of displacement and velocity respectively from the nonlinear models. The standard deviations and expected response rates determined from the PSDs (and the assumption that the underlying data is Gaussian) for the nonlinear models are given in Table 4.22. Compared to the rates calculated by level crossings given in Table 4.12, it is clear that the standard spectral moment method of determining response rates is in error for nonlinear systems. On the other hand, the estimates of σ (or the zero moment of the PSD) differ by approximately 0.1%.

4.3.2 Reverse path nonlinear system identification

The reverse path identification method was used in Chapter 3 to identify nonlinear frequency domain trends in the experimental data. The technique is used again here as an additional illustration which shows how the system parameters from equation (4.2) can be determined.

The first set of frequency response functions presented are L_{1y} and H_{1y} (see Figure 4.27(a) and (b) for $\zeta = 0.01$, and Figure 4.30(a) and (b) for $\zeta = 0.001$). These functions are the reciprocal of the normal displacement / force frequency response functions, but as described in the text [125], they can be used to estimate the modal parameters. The value of H_{1y} at $f = 0$ Hz equals the static stiffness k_1 (approximately 3.5

kN/m) and the frequency where $|H_{1y}|$ is a minimum is approximately equal to the natural frequency. Inspection of the plots (for both damping levels) shows that this is the case. Note that while H_{1y} stays constant for each input level (the curves of these overlay each other quite well), L_{1y} diverges from the "linear" result as the model becomes more nonlinear.

The frequency response functions of H_{3y} are shown in Figure 4.28(b) for $\zeta = 0.01$, and Figure 4.31(b) for $\zeta = 0.001$. These functions should theoretically equal the nonlinear stiffness parameter k_3 that operates on the cubic power of the response at all frequencies. Inspection of the results shows very good agreement with the original model value (approximately 1.8 GN/m^3) and that the estimates become better as the problem becomes more nonlinear. It is believed that this is true as the difference between H_{1y} and L_{1y} becomes greater (allowing better numerical resolution between small values).

A distinguishing measure of the nonlinearity of the mathematical input displacements are the coherence functions between the uncorrelated inputs U_i and the mathematical output force. Figure 4.29(a) and (b) show the coherence functions for the 0.5 and 8 g simulations with $\zeta = 0.01$, while Figure 4.32(a) and (b) show the same when $\zeta = 0.001$. In each plot the coherence functions are labeled following the notation from equation (2.74). Figure 4.29(a) shows that the response is almost completely correlated with only U_1 whilst at the other extreme, Figure 4.32(b) shows that the response is strongly correlated with the cubic term U_3 over most of the frequency range. It is also reassuring that the four plots of the total summed coherence $\Sigma\gamma_{uiy}$ are nearly 1 over the whole frequency range.

4.4 Nonlinear simulation summary

The linear and nonlinear Duffing simulations, based on the clamped-clamped beam experiments from WPAFB, were run so that large data sets could be used to show trends in the nonlinear response. The major findings of this chapter can be summarized as:

The standard deviation and kurtosis for the nonlinear random response converge much more slowly than the corresponding linear random response quantities. The response

displacement kurtosis tended to be less than 3 and the response acceleration kurtosis tended to be greater than 3, whilst the response velocity kurtosis tended to equal 3 for the Duffing model studied. The distribution for the velocity response tended to be normal for the nonlinear models.

Random errors in nonlinear standard deviation estimates, based on the statistical bandwidth of the frequency domain PSD response, are much greater than what would be estimated with linear random theory. The harmonic distortion of the displacement, velocity and acceleration response states can be significant enough to cause an estimate of the statistical bandwidth to be even greater than the bandwidth of the input load.

Linear to nonlinear displacement functions determined from the ODE results, using the inverse distribution function method, appear similar to those estimated from the WPAFB displacement data. The linear peak to nonlinear peak functions all tended to follow one main trend, even over wide ranges of input amplitude and damping values. The linear to nonlinear peak functions determined using an assumed generalized linear peak distribution function, with a ratio of zeros to peaks determined from the nonlinear data, produced the best goodness-of-fit agreements. The linear to nonlinear peak displacement response functions appear to form an upper bound (or limiting case) of the linear to nonlinear normal displacement response functions. A novel use of the linear to nonlinear normal displacement function was developed to estimate the rate of zero crossings for the nonlinear response. The estimated rates agree well with those determined by counting level crossings.

The reverse path identification process was used again in this chapter to demonstrate its behavior with simulated nonlinear Duffing model data. The method accurately estimated the Duffing model linear and nonlinear parameters.

4.5 Chapter 4 Tables

Table 4.1. Linear ODE baseline standard deviation results after averaging 20 blocks of data.

Input, Damping	σ_x mm	σ_v m/s	σ_a g (a/9.81 m/s^2)	T_{block} s
1 g, $\zeta = 0.01$	0.1742	0.0755	3.512	250
1 g, $\zeta = 0.003$	0.3183	0.1384	6.222	245
1 g, $\zeta = 0.001$	0.5512	0.2397	10.68	235

Table 4.2. Linear model standard deviation estimates from closed form equations.

Input, Damping	σ_x mm	σ_v m/s	σ_a g (a/9.81 m/s^2)
1 g, $\zeta = 0.01$	0.1746	0.0759	3.365
1 g, $\zeta = 0.003$	0.3187	0.1386	6.144
1 g, $\zeta = 0.001$	0.5512	0.2401	10.64

Table 4.3. Nonlinear ODE standard deviation results after averaging 20 blocks of data.

Input, Damping	σ_y mm	σ_v m/s	σ_a g (a/9.81 m/s^2)
0.5 g, $\zeta = 0.01$	0.0866	0.0379	1.764
2 g, $\zeta = 0.01$	0.3256	0.1519	7.534
8 g, $\zeta = 0.01$	0.9582	0.6081	42.50
0.5 g, $\zeta = 0.003$	0.1562	0.0692	3.164
2 g, $\zeta = 0.003$	0.5390	0.2758	14.81
8 g, $\zeta = 0.003$	1.405	1.114	99.06
0.5 g, $\zeta = 0.001$	0.2668	0.1219	5.714
2 g, $\zeta = 0.001$	0.8244	0.4881	30.95
8 g, $\zeta = 0.001$	1.939	1.946	223.5

Table 4.4. Normalized standard deviation estimates of block σ results from 20 blocks of linear ODE simulation data.

Damping	$\frac{\sigma[\hat{\sigma}_x]}{\sigma_x}$	$\frac{\sigma[\hat{\sigma}_v]}{\sigma_v}$	$\frac{\sigma[\hat{\sigma}_a]}{\sigma_a}$
$\zeta = 0.01$	0.2 %	0.2 %	0.2 %
$\zeta = 0.003$	0.4 %	0.4 %	0.4 %
$\zeta = 0.001$	0.8 %	0.8 %	0.8 %

Table 4.5. Normalized standard deviation estimates of block σ results from 20 blocks of nonlinear ODE simulation data.

Input, Damping	$\frac{\sigma[\hat{\sigma}_y]}{\sigma_y}$	$\frac{\sigma[\hat{\sigma}_v]}{\sigma_v}$	$\frac{\sigma[\hat{\sigma}_a]}{\sigma_a}$
0.5 g, $\zeta = 0.01$	0.3 %	0.3 %	0.3%
2 g, $\zeta = 0.01$	1.1 %	1.2 %	1.3%
8 g, $\zeta = 0.01$	1.1 %	1.6 %	2.1%
0.5 g, $\zeta = 0.003$	2.0%	2.1%	2.1%
2 g, $\zeta = 0.003$	2.2%	3.0%	3.8%
8 g, $\zeta = 0.003$	2.2%	3.6%	5.2%
0.5 g, $\zeta = 0.001$	4.5 %	4.8 %	5.2%
2 g, $\zeta = 0.001$	3.3 %	4.5 %	5.8%
8 g, $\zeta = 0.001$	3.1 %	3.9 %	6.3%

Table 4.6. Statistical bandwidth estimates from 20 blocks of linear ODE simulation data.

Damping	B_{sx} Hz	B_{sv} Hz	B_{sa} Hz
$\zeta = 0.01$	68.8	69.1	81.9
$\zeta = 0.003$	21.2	21.2	22.3
$\zeta = 0.001$	7.21	7.21	7.34

Table 4.7. Statistical bandwidth estimates from 20 blocks of nonlinear ODE simulation data.

Input, Damping	B_{sy} Hz	B_{sv} Hz	B_{sa} Hz
0.5 g, $\zeta = 0.01$	71.4	71.7	84.9
2 g, $\zeta = 0.01$	190	196	234
8 g, $\zeta = 0.01$	820	853	1011
0.5 g, $\zeta = 0.003$	51.1	51.6	54.9
2 g, $\zeta = 0.003$	358	380	425
8 g, $\zeta = 0.003$	1278	1285	1461
0.5 g, $\zeta = 0.001$	110	114	120
2 g, $\zeta = 0.001$	662	696	769
8 g, $\zeta = 0.001$	1811	1780	2059

Table 4.8. Linear ODE baseline chi-square goodness-of-fit test results for displacement and velocity response normality

Damping	X_x^2	X_v^2
$\zeta = 0.01$	19.02	19.67
$\zeta = 0.001$	39.03	39.09

Table 4.9. Nonlinear ODE chi-square goodness-of-fit test results for velocity response normality

Input, Damping	X_v^2
0.5 g, $\zeta = 0.01$	25.69
2 g, $\zeta = 0.01$	16.29
8 g, $\zeta = 0.01$	36.84
0.5 g, $\zeta = 0.001$	102.57
2 g, $\zeta = 0.001$	137.45
8 g, $\zeta = 0.001$	154.51

Table 4.10. Kurtosis and normalized random error estimates of kurtosis for results from 20 blocks of linear ODE simulation data.

Input, Damping	κ_x	κ_v	$\frac{\sigma[\hat{\kappa}_x]}{\kappa_x}$	$\frac{\sigma[\hat{\kappa}_v]}{\kappa_v}$
1 g, $\zeta = 0.01$	2.997	2.996	2.1 %	2.1 %
1 g, $\zeta = 0.003$	3.017	3.017	4.3 %	4.3 %
1 g, $\zeta = 0.001$	3.015	3.014	5.1 %	5.1 %

Table 4.11. Kurtosis and normalized random error estimates of kurtosis for results from 20 blocks of nonlinear ODE simulation data.

Input, Damping	κ_y	κ_v	κ_α	$\frac{\sigma[\hat{\kappa}_y]}{\kappa_y}$	$\frac{\sigma[\hat{\kappa}_v]}{\kappa_v}$	$\frac{\sigma[\hat{\kappa}_\alpha]}{\kappa_\alpha}$
0.5 g, $\zeta = 0.01$	2.97	2.98	3.04	1.8 %	1.4 %	1.4 %
2 g, $\zeta = 0.01$	2.80	3.01	3.81	1.3 %	2.0 %	3.5 %
8 g, $\zeta = 0.01$	2.44	3.02	7.27	0.8 %	1.9 %	5.4 %
0.5 g, $\zeta = 0.003$	2.93	2.99	3.20	2.7 %	2.9 %	3.3 %
2 g, $\zeta = 0.003$	2.62	2.98	5.07	2.2 %	3.4 %	7.2 %
8 g, $\zeta = 0.003$	2.34	3.00	8.78	1.2 %	3.6 %	9.5 %
0.5 g, $\zeta = 0.001$	2.85	3.00	3.60	3.6 %	4.3 %	6.2 %
2 g, $\zeta = 0.001$	2.49	3.02	6.86	3.8 %	7.3 %	14.4 %
8 g, $\zeta = 0.001$	2.28	2.98	9.44	2.9 %	7.1 %	13.0 %

Table 4.12. Rates and ratios of positive zero level crossings and peaks for displacement and velocity results from 20 blocks of data.

Input, Damping	$\Phi\left[0_x^+\right]$ Hz	$\Phi\left[0_v^+\right]$ Hz	$\Phi\left[P_x^+\right]$ Hz	ϖ_x
0.5 g, $\zeta = 0.01$	69.5	72.4	69.9	0.9949
2 g, $\zeta = 0.01$	72.0	75.0	72.5	0.9931
8 g, $\zeta = 0.01$	89.5	93.0	91.5	0.9899
0.5 g, $\zeta = 0.003$	69.9	70.8	69.9	0.9996
2 g, $\zeta = 0.003$	76.3	77.3	76.4	0.9989
8 g, $\zeta = 0.003$	107.8	109.1	108.1	0.9976
0.5 g, $\zeta = 0.001$	71.1	71.4	71.0	1.0000
2 g, $\zeta = 0.001$	84.7	85.0	84.8	0.9999
8 g, $\zeta = 0.001$	133.2	133.7	133.3	0.9994

Table 4.13. Rates and ratios of positive zero level crossings and peaks for acceleration results from 20 blocks of data.

Input, Damping	$\Phi\left[0_a^+\right]$ Hz	$\Phi\left[P_a^+\right]$ Hz	ϖ_a
0.5 g, $\zeta = 0.01$	110	242	0.46
2 g, $\zeta = 0.01$	113	217	0.53
8 g, $\zeta = 0.01$	132	155	0.84
0.5 g, $\zeta = 0.003$	71	151	0.47
2 g, $\zeta = 0.003$	77	122	0.63
8 g, $\zeta = 0.003$	109	128	0.85
0.5 g, $\zeta = 0.001$	77	96	0.79
1 g, $\zeta = 0.001$	81	91	0.89
2 g, $\zeta = 0.001$	91	95	0.96
4 g, $\zeta = 0.001$	110	110	0.99
8 g, $\zeta = 0.001$	141	141	1.00

Table 4.14. Goodness-of-fit peak PDF comparison for linear ODE simulation results.

Damping	Bin Center Range	DOF	PDF: X^2
$\zeta = 0.001$	$0.08 < \sigma < 4.55$	27	Ray: 70.8
$\zeta = 0.001$	$1.16 < \sigma < 4.55$	20	Ray: 48.7
$\zeta = 0.01$	$-0.41 < \sigma < 4.81$	30	Ray: 1023, Peak: 72.9
$\zeta = 0.01$	$1.22 < \sigma < 4.81$	20	Ray: 33.3, Peak: 26.6

Table 4.15. Chi-square percentage points used for goodness-of-fit testing.

DOF	$\alpha = 0.10$	$\alpha = 0.01$	$\alpha = 0.005$
20	28.41	37.57	40.00
27	36.74	46.96	49.64
30	40.26	50.89	53.67

Table 4.16. Displacement response polynomial coefficients $d_{i,j}$ (input i and polynomial power j) for linear to nonlinear function determined using inverse distribution method.

Input, Damping	$d_{i,1}$ mm/mm	$d_{i,2}$ mm/mm^2	$d_{i,3}$ mm/mm^3
0.5 g, $\zeta = 0.01$	0.9927	0.1357	-0.1990
2 g, $\zeta = 0.01$	1.0341	0.0224	0.0842
8 g, $\zeta = 0.01$	1.2742	0.0374	0.0559
0.5 g, $\zeta = 0.001$	1.0331	-0.1094	0.2155
2 g, $\zeta = 0.001$	1.1982	0.0213	0.0648
8 g, $\zeta = 0.001$	1.9023	0.0111	0.0385

Table 4.17. Peak displacement polynomial coefficients for linear to nonlinear function determined using inverse distribution method.

Damping	c_1 mm/mm	c_2 mm/mm^2	c_3 mm/mm^3
$\zeta = 0.01$	0.9628	0.1010	0.0565
$\zeta = 0.003$	0.9668	0.1213	0.0497
$\zeta = 0.001$	0.9328	0.1563	0.0405

Table 4.18. Goodness-of-fit results for transformed Rayleigh PDF for nonlinear ODE simulation peak displacement results.

Input, Damping	Bin Center Range	DOF	Transformed Rayleigh PDF: X^2
0.5 g, $\zeta = 0.001$	$0.066 < \sigma < 3.88$	27	1102
1 g, $\zeta = 0.001$	$0.063 < \sigma < 3.69$	27	1470
2 g, $\zeta = 0.001$	$0.055 < \sigma < 3.23$	27	1270
4 g, $\zeta = 0.001$	$0.051 < \sigma < 3.03$	27	409
8 g, $\zeta = 0.001$	$0.050 < \sigma < 2.97$	27	720

Table 4.19. Goodness-of-fit results for transformed general peak PDF for nonlinear ODE simulation peak displacement results.

Input, Damping	Bin Center Range	DOF	Transformed General Peak PDF: X^2
0.5 g, $\zeta = 0.01$	$-0.40 < \sigma < 4.67$	30	118
1 g, $\zeta = 0.01$	$-0.39 < \sigma < 4.54$	30	184
2 g, $\zeta = 0.01$	$-0.34 < \sigma < 4.03$	30	560
4 g, $\zeta = 0.01$	$-0.32 < \sigma < 3.74$	30	466
8 g, $\zeta = 0.01$	$-0.31 < \sigma < 3.59$	30	492

Table 4.20. Rates of positive zero displacement level crossings based on PDF transforms $E\left[0_x^+\right]$ and simulations $\Phi\left[0_x^+\right]$.

Input, Damping	$E\left[0_x^+\right]$ Hz	$\Phi\left[0_x^+\right]$ Hz
0.5 g, $\zeta = 0.01$	69.1	69.5
2 g, $\zeta = 0.01$	71.9	72.0
8 g, $\zeta = 0.01$	89.3	89.5
0.5 g, $\zeta = 0.001$	71.1	71.1
2 g, $\zeta = 0.001$	83.6	84.7
8 g, $\zeta = 0.001$	132.8	133.2

Table 4.21. Response displacement standard deviation and rate results from baseline linear ODE simulations determined from PSD estimates.

Input, Damping	σ_x mm	$E\left[0_x^+\right]$ Hz	$E\left[P_x^+\right]$ Hz	$E\left[0_x^+\right]/E\left[P_x^+\right]$
1 g, $\zeta = 0.01$	0.176	69.29	72.39	0.9571
1 g, $\zeta = 0.001$	0.550	69.23	69.73	0.9927

Table 4.22. Response displacement standard deviation and rate results from nonlinear ODE simulations determined from PSD estimates.

Input, Damping	σ_x mm	$E\left[0_x^+\right]$ Hz	$E\left[P_x^+\right]$ Hz	$E\left[0_x^+\right]/E\left[P_x^+\right]$
0.5 g, $\zeta = 0.01$	0.0869	69.68	72.80	0.9571
2 g, $\zeta = 0.01$	0.326	74.28	77.53	0.9580
8 g, $\zeta = 0.01$	0.958	100.99	109.12	0.9255
0.5 g, $\zeta = 0.001$	0.267	72.70	73.34	0.9912
2 g, $\zeta = 0.001$	0.824	94.31	99.11	0.9516
8 g, $\zeta = 0.001$	1.939	159.73	179.32	0.8908

4.6 Chapter 4 Figures

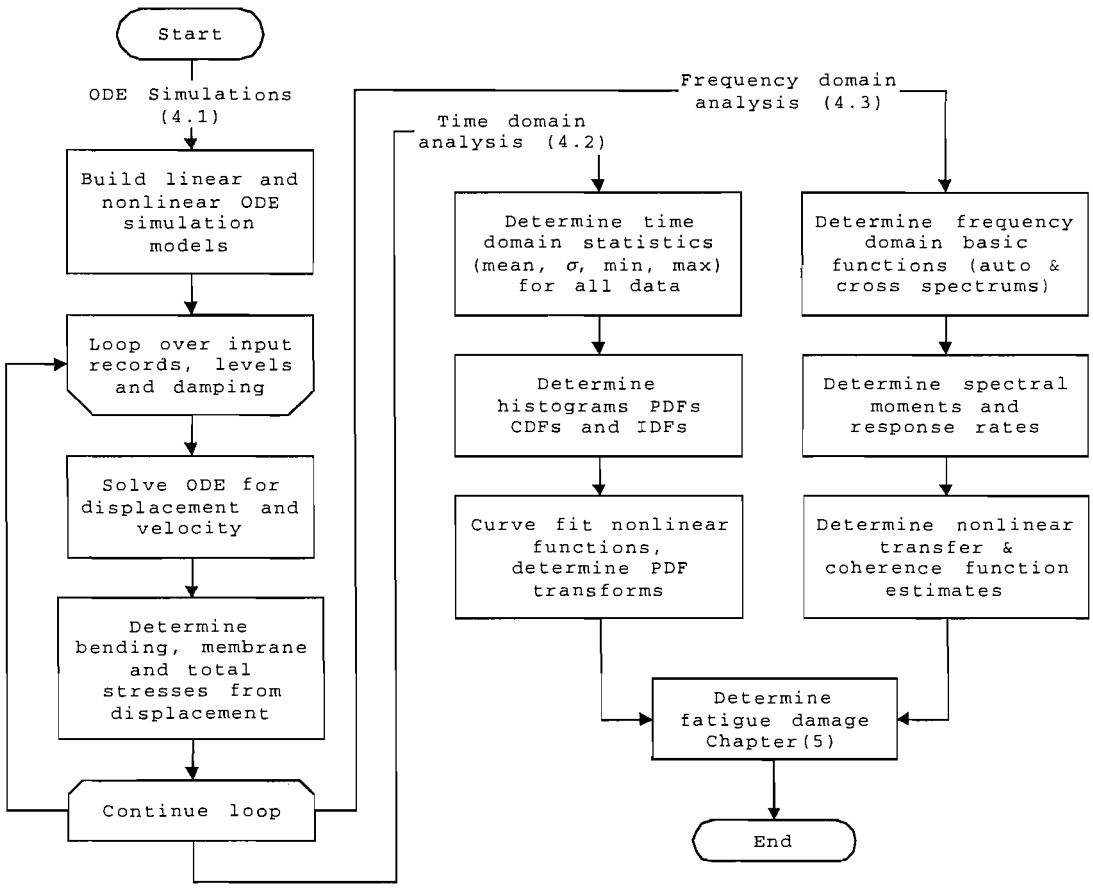

Figure 4.1. Simulation and analysis flow diagram for nonlinear ODE models

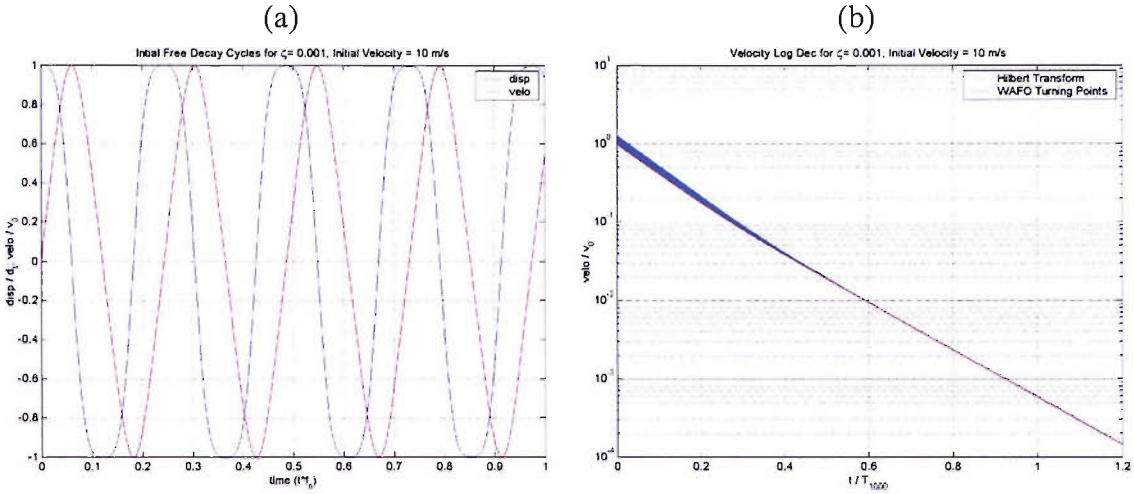

Figure 4.2. Initial free decay response for nonlinear Duffing $\zeta = 0.001$ model, initial velocity = 10 m / s. (a) Normalized initial displacement and velocity for 1 linear response period and (b) nonlinear free vibration velocity decay computed with WAFO turning points and Hilbert Transform methods.

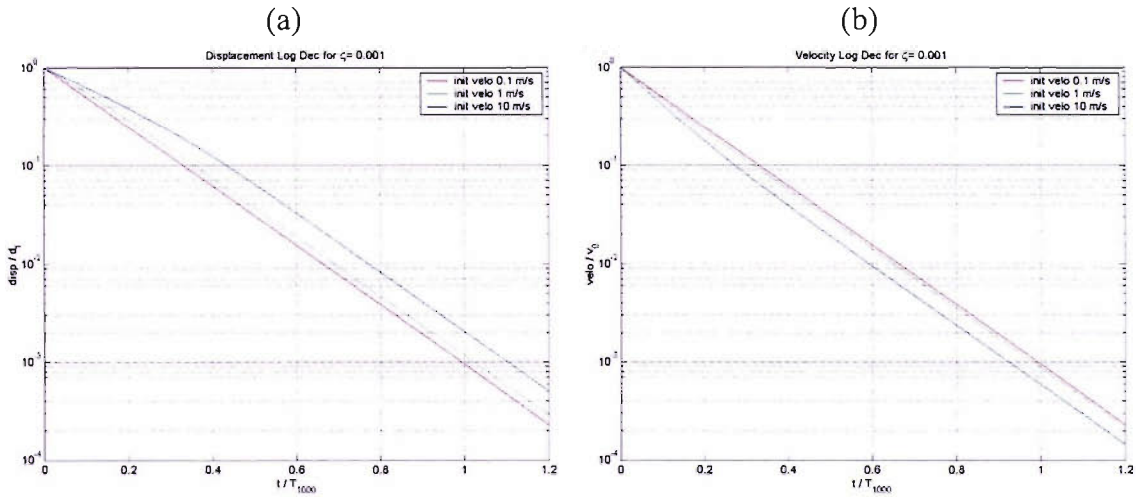

Figure 4.3. Normalized nonlinear free vibration decay for initial velocities (0.1, 1 10) m / s and $\zeta = 0.001$ model with ODE relative error = 1×10^{-4}: (a) displacement and (b) velocity.

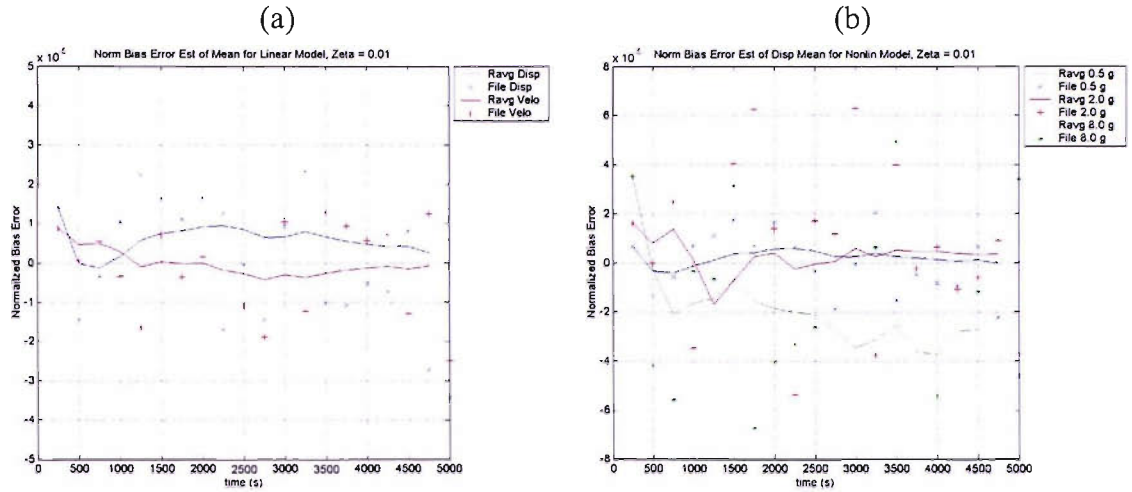

Figure 4.4. Normalized bias error estimate of: (a) displacement and velocity mean from baseline linear $\zeta = 0.01$ model input = 1 g data, and (b) displacement mean for nonlinear $\zeta = 0.01$ model input = (0.5, 2, 8) g data. Legend: Ravg = running average of displacement, File = results from each simulation file.

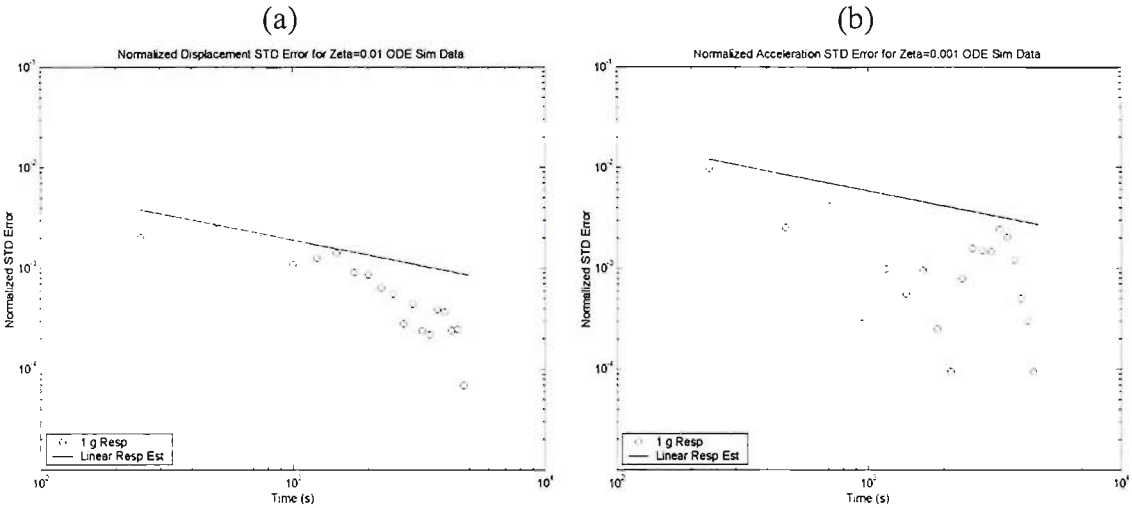

Figure 4.5. Normalized random error estimates of standard deviation from linear model input = 1 g data: (a) $\zeta = 0.01$ model displacement data, $\sigma_x = 0.174$ mm, and (b) $\zeta = 0.001$ model acceleration data, $\sigma_a = 10.7$ g.

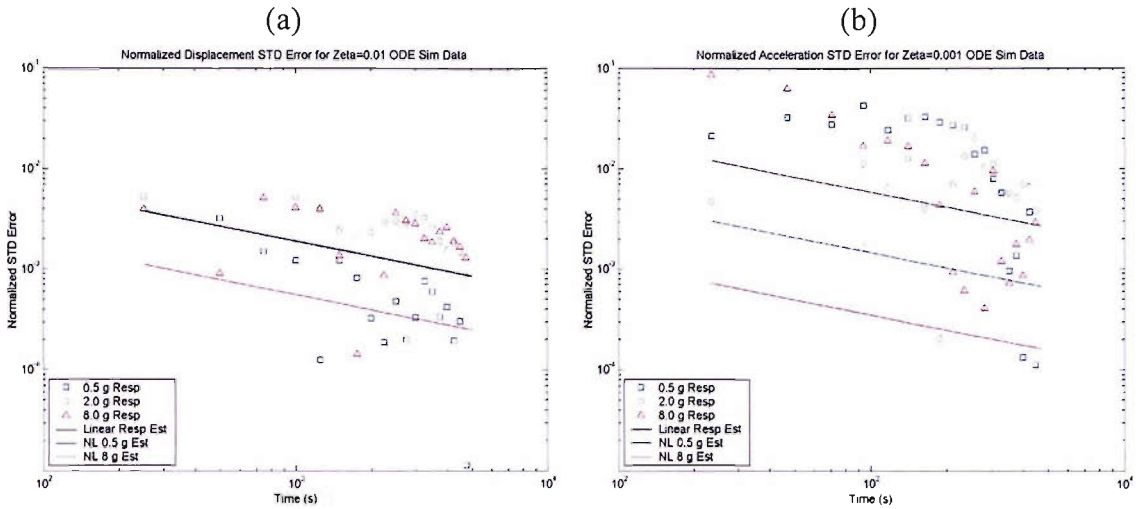

Figure 4.6. Normalized random error estimates of standard deviation from nonlinear model input = (0.5, 2, 8) g data: (a) $\zeta = 0.01$ model displacement data, $\sigma_y = (0.087, 0.326, 0.958)$ mm, and (b) $\zeta = 0.001$ model acceleration data, $\sigma_\alpha = (5.71, 31.0, 224)$ g.

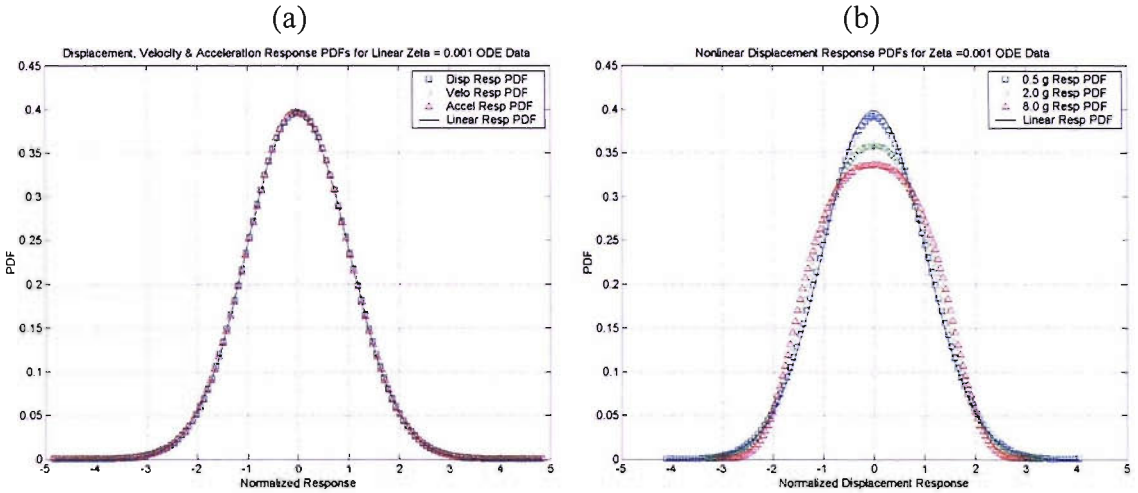

Figure 4.7. Normalized response PDFs determined from ODE simulations: (a) linear $\zeta = 0.001$ model input = 1 g data displacement, velocity & acceleration PDFs, $\sigma_x = 0.551$ mm, $\sigma_v = 0.240$ m/s, $\sigma_a = 10.7$ g and (b) nonlinear $\zeta = 0.001$ model input = (0.5, 2, 8) g data displacement PDFs, $\sigma_y = (0.267, 0.824, 1.94)$ mm.

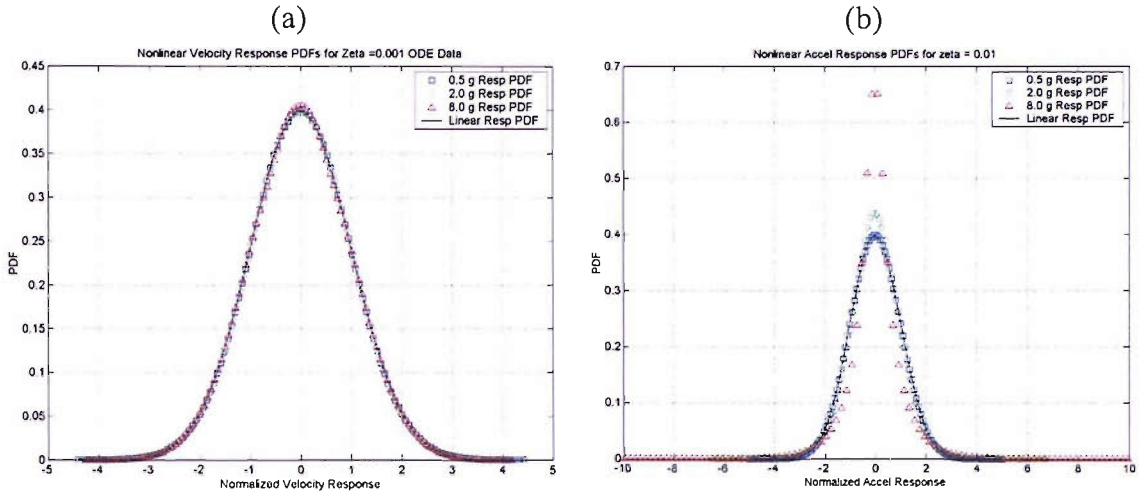

Figure 4.8. Normalized response PDFs determined from nonlinear ODE simulation input = (0.5, 2, 8) g data: (a) $\zeta = 0.001$ model velocity PDFs, σ_v = (0.122, 0.488, 1.95) m/s, and (b) $\zeta = 0.01$ model acceleration PDFs, σ_a = (1.76, 7.53, 42.5) g.

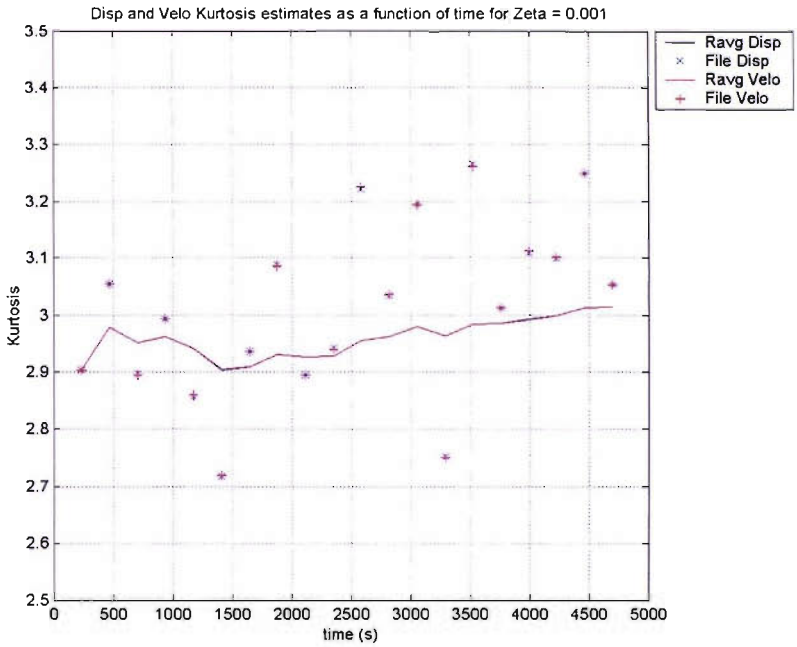

Figure 4.9. Displacement and velocity kurtosis from linear $\zeta = 0.001$ model input = 1 g data, displayed as running averages and individual file results.

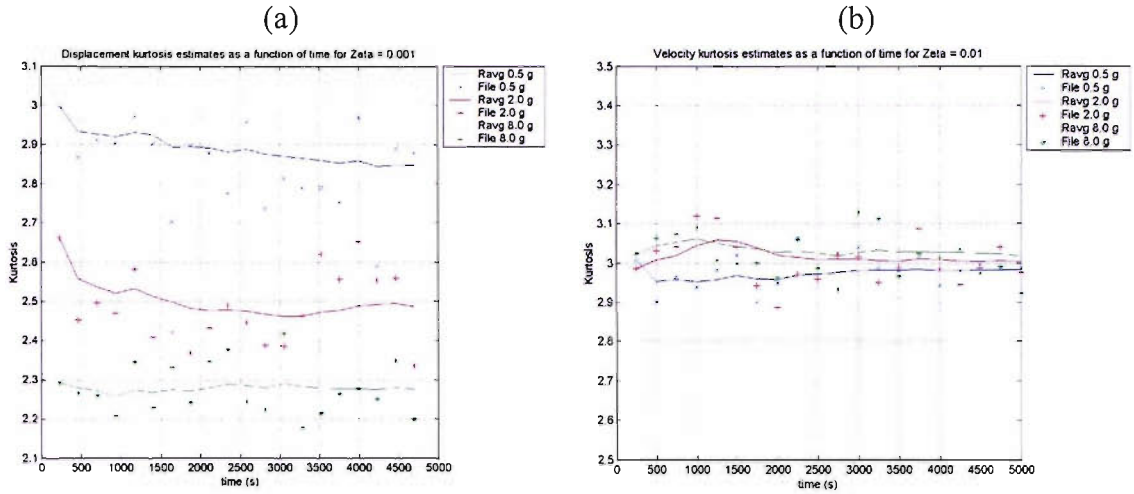

Figure 4.10. Kurtosis values from nonlinear model simulations displayed as running averages and individual file results for input = (0.5, 2, 8) g data: (a) displacement kurtosis for $\zeta = 0.001$ model and (b) velocity kurtosis for $\zeta = 0.01$ model.

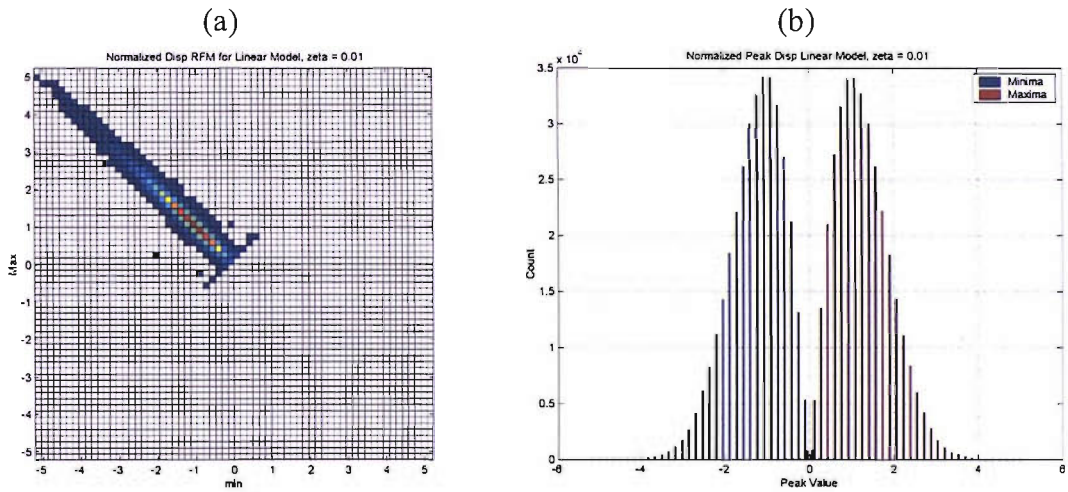

Figure 4.11. Normalized displacement ($\sigma_x = 0.174$ mm) results from linear $\zeta = 0.01$ model input = 1 g data: (a) RFM and (b) minimum and maximum peak displacement histogram.

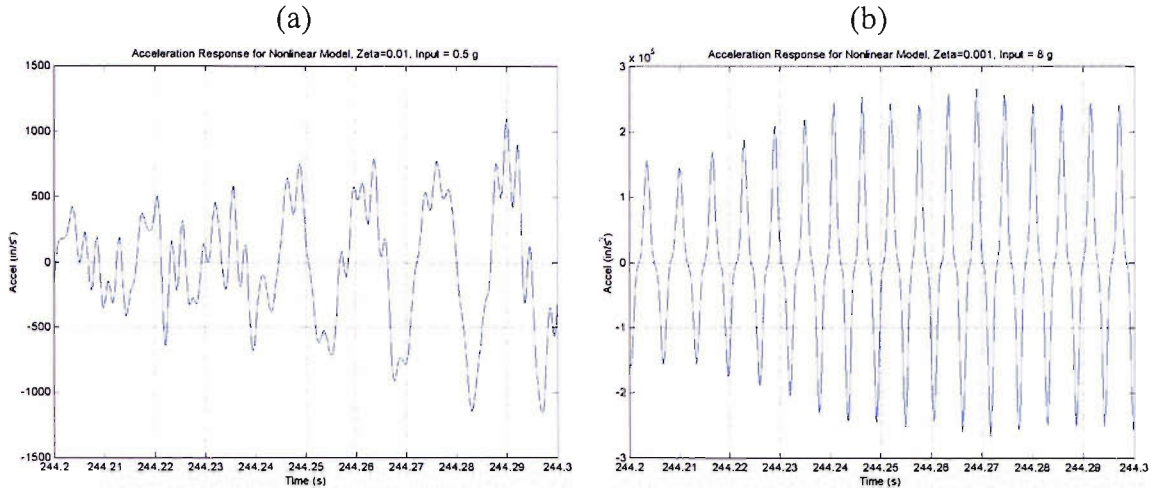

Figure 4.12. Acceleration response from nonlinear ODE simulations: (a) $\zeta = 0.01$ model, input = 0.5 g and (b) model $\zeta = 0.001$, input = 8 g.

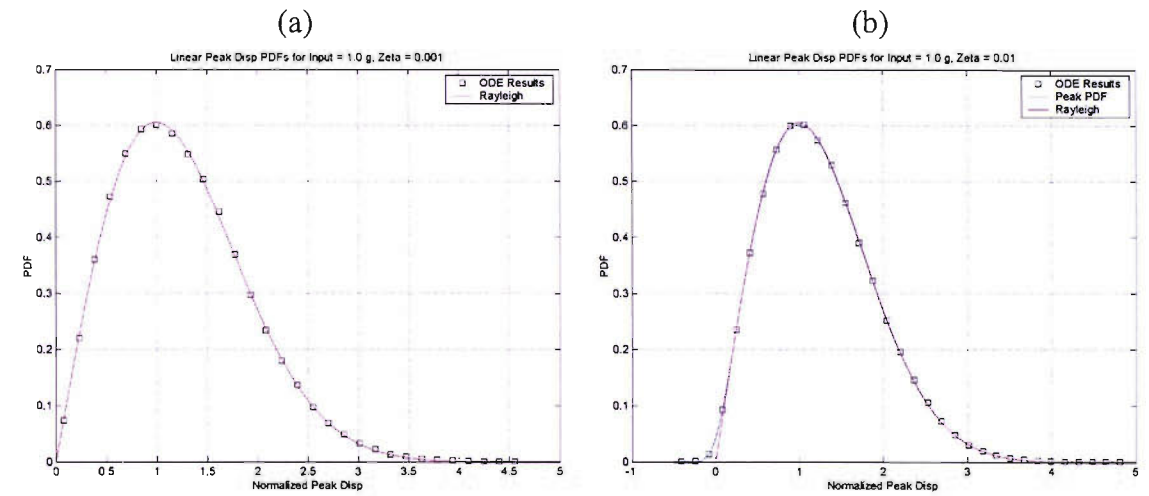

Figure 4.13. Normalized peak displacement PDFs for linear ODE simulations for input = 1 g: (a) raw peak PDF for $\zeta = 0.001$ model ($\sigma_x = 0.551$ mm) and Rayleigh PDF and (b) raw peak PDF for $\zeta = 0.01$ model ($\sigma_x = 0.174$ mm), Rayleigh PDF and Peak PDF.

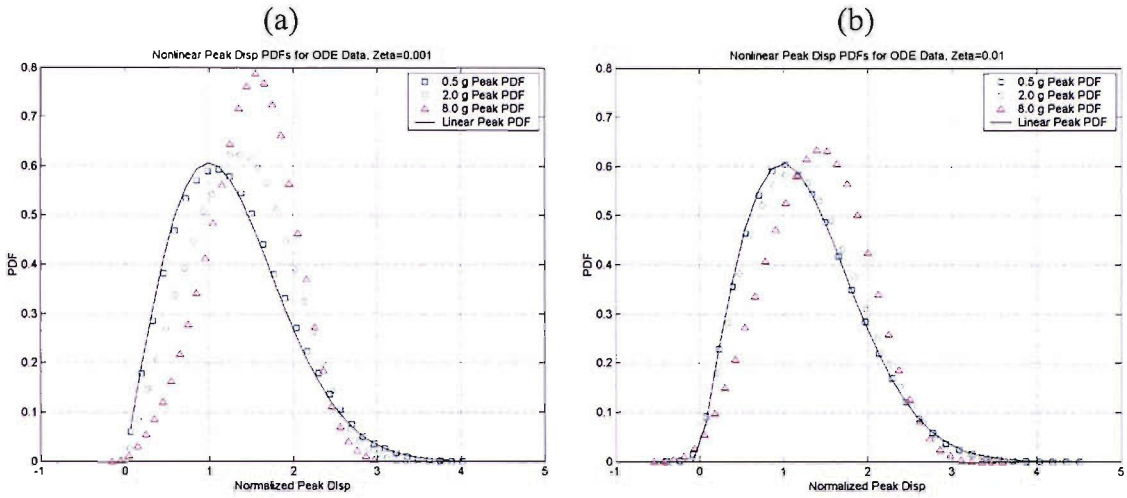

Figure 4.14. Normalized peak displacement PDFs from nonlinear ODE simulation input = (0.5, 2, 8) g data: (a) $\zeta = 0.001$ model, σ_y = (0.267, 0.824, 1.94) mm and (b) $\zeta = 0.01$ model, σ_y = (0.087, 0.326, 0.958) mm.

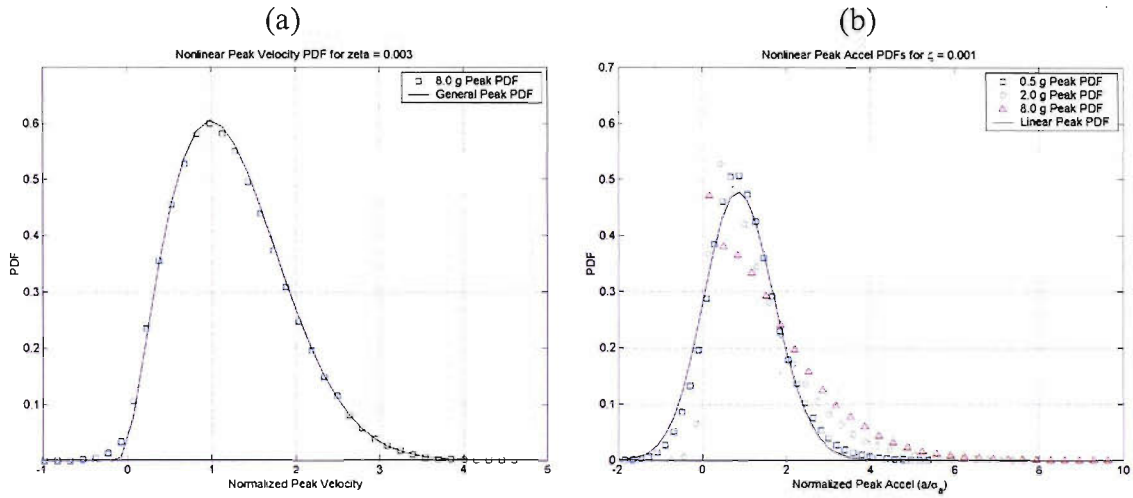

Figure 4.15. Normalized peak PDFs from nonlinear ODE simulations: (a) peak velocity (σ_v = 1.11 m/s) for $\zeta = 0.003$ model input = 8 g data and (b) peak acceleration (σ_a = (1.76, 7.53, 42.5) g) for $\zeta = 0.001$ model input = (0.5, 2, 8) g data.

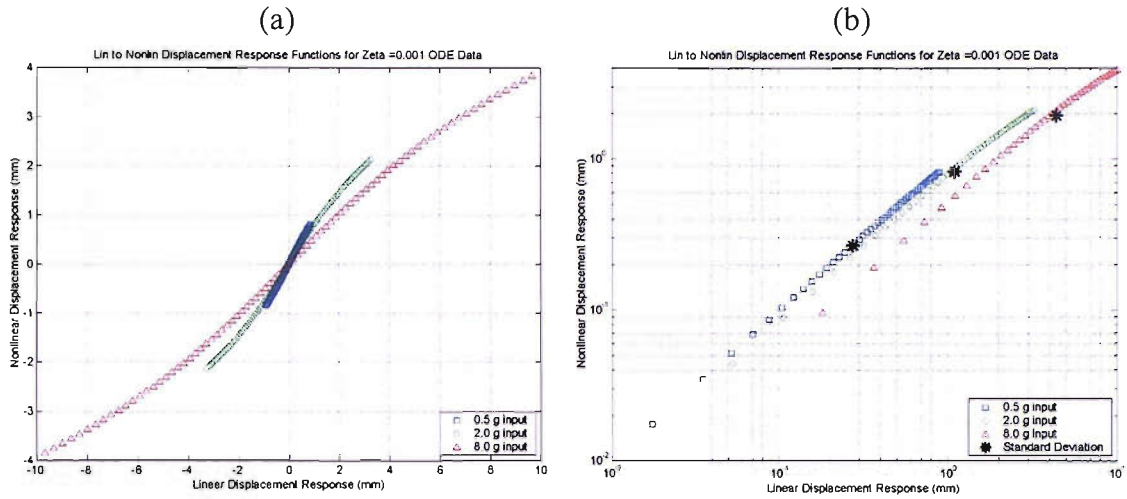

Figure 4.16. Linear to nonlinear normal displacement functions from $\zeta = 0.001$ model input = (0.5, 2, 8) g data: (a) linear graph over positive and negative ranges and (b) logarithmic graph over positive ranges, with standard deviation points displayed.

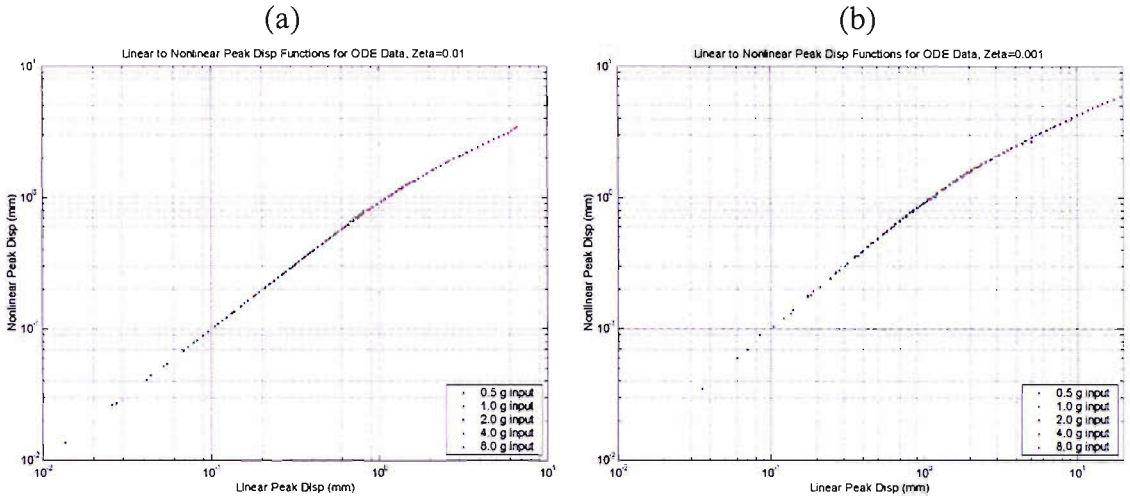

Figure 4.17. Linear to nonlinear peak displacement functions from input = (0.5, 1, 2, 4, 8) g data: (a) for $\zeta = 0.01$ model and (b) $\zeta = 0.001$ model.

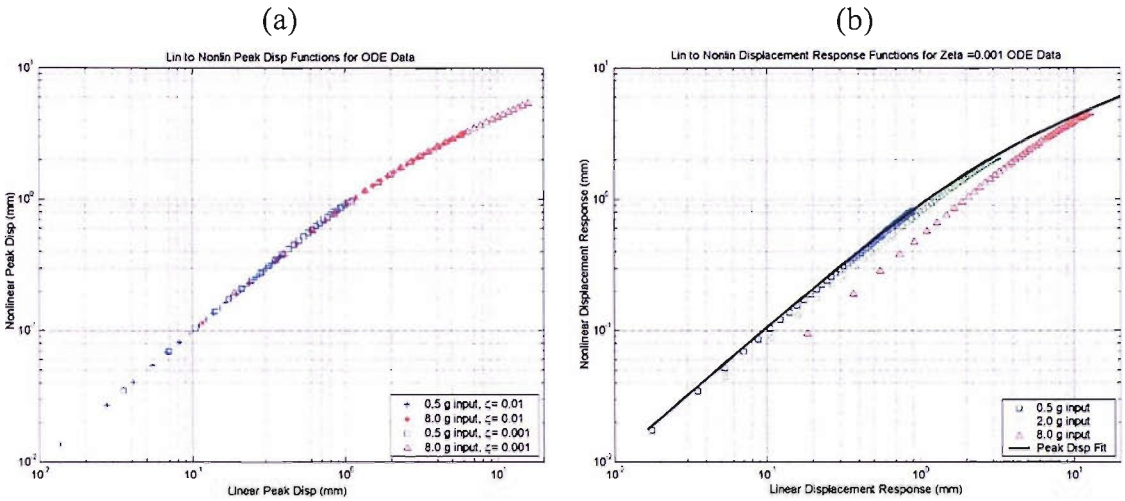

Figure 4.18. Linear and nonlinear displacement functions: (a) peak functions from $\zeta = 0.01$ and $\zeta = 0.001$ models input = (0.5, 8) g data and (b) displacement response and peak functions from $\zeta = 0.001$ model input = (0.5, 2, 8) g data.

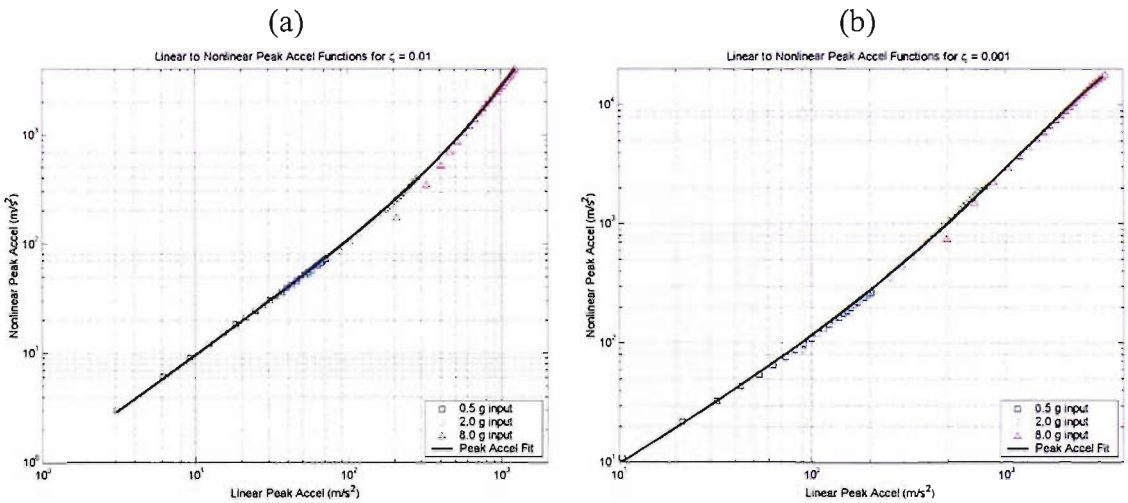

Figure 4.19. Linear to nonlinear peak acceleration functions from input = (0.5, 2, 8) g data: (a) for $\zeta = 0.01$ model and (b) $\zeta = 0.001$ model.

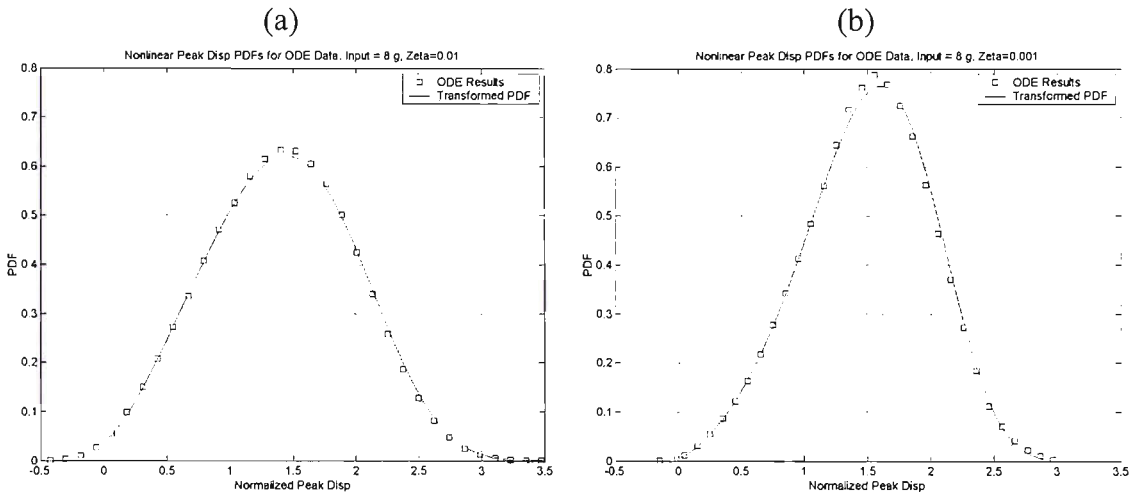

Figure 4.20. Nonlinear peak displacement PDF estimates and ODE results from input = 8 g data: (a) $\zeta = 0.01$ model and (b) $\zeta = 0.001$ model.

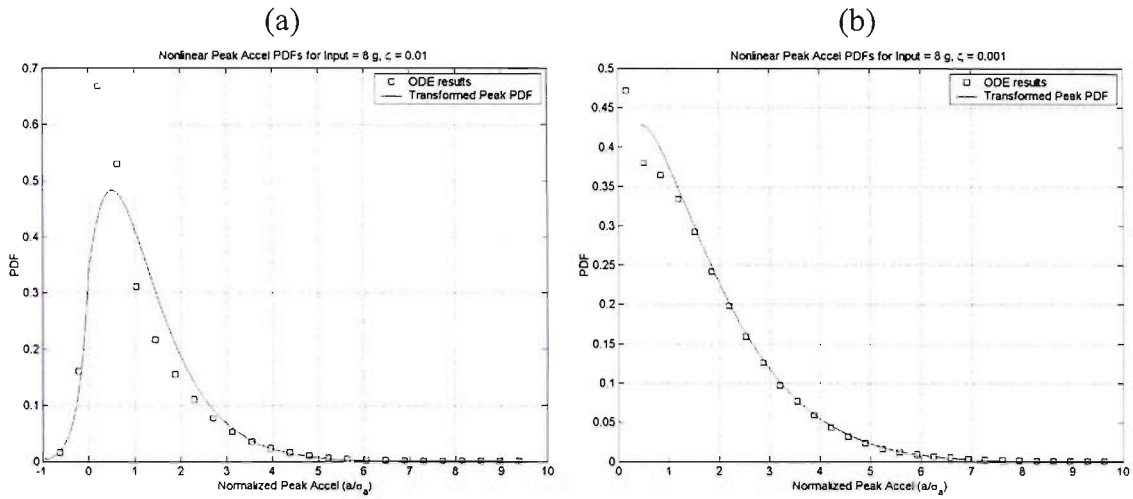

Figure 4.21. Nonlinear peak acceleration PDF estimates and ODE results from input = 8 g data: (a) $\zeta = 0.01$ model and (b) $\zeta = 0.001$ model.

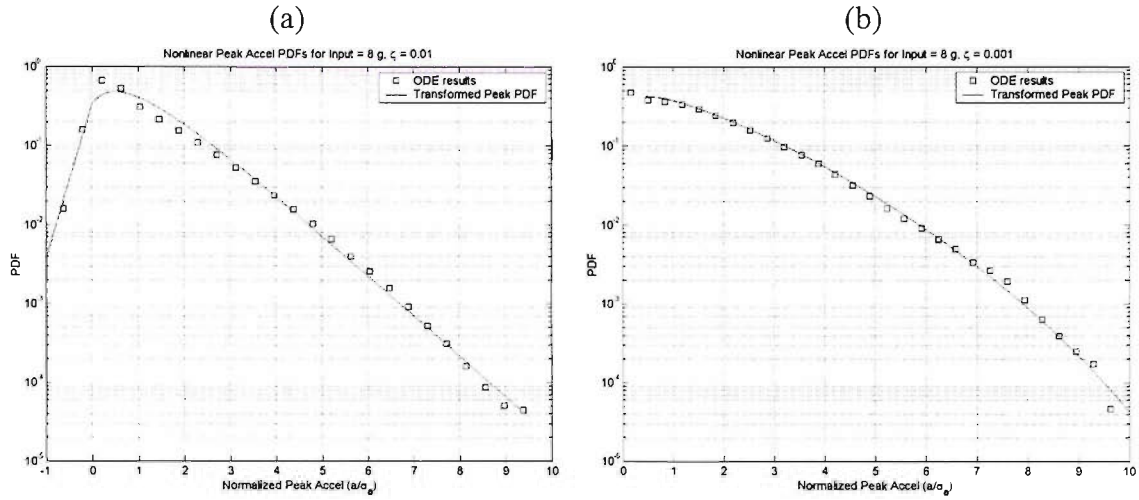

Figure 4.22. Nonlinear peak acceleration logarithmic PDF estimates and ODE results from input = 8 g data: (a) $\zeta = 0.01$ model and (b) $\zeta = 0.001$ model.

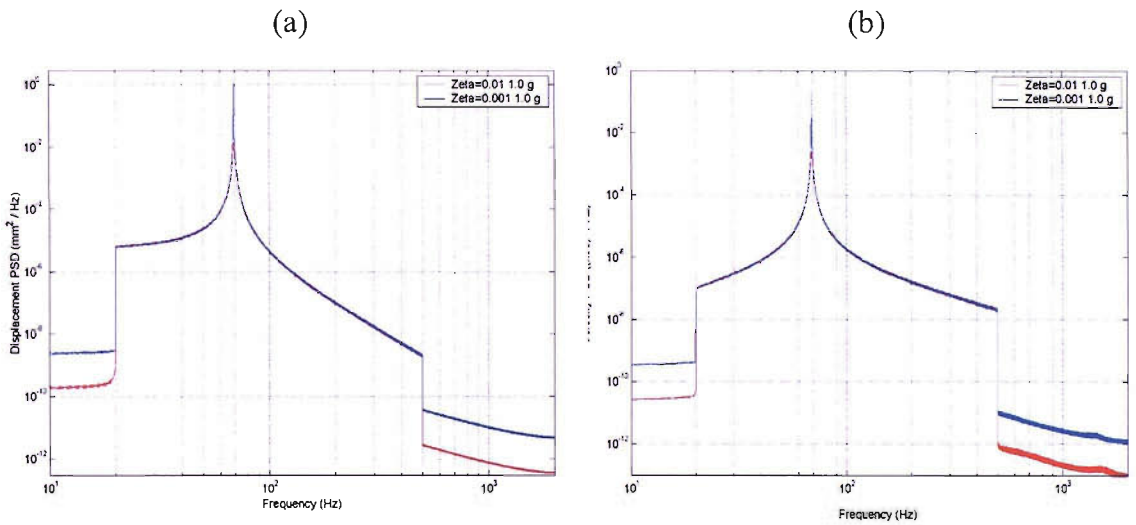

Figure 4.23. Response PSDs from linear ODE simulations for $\zeta = 0.01$and 0.001 model input = 1 g data: (a) displacement PSDs and (b) velocity PSDs.

(a) (b)

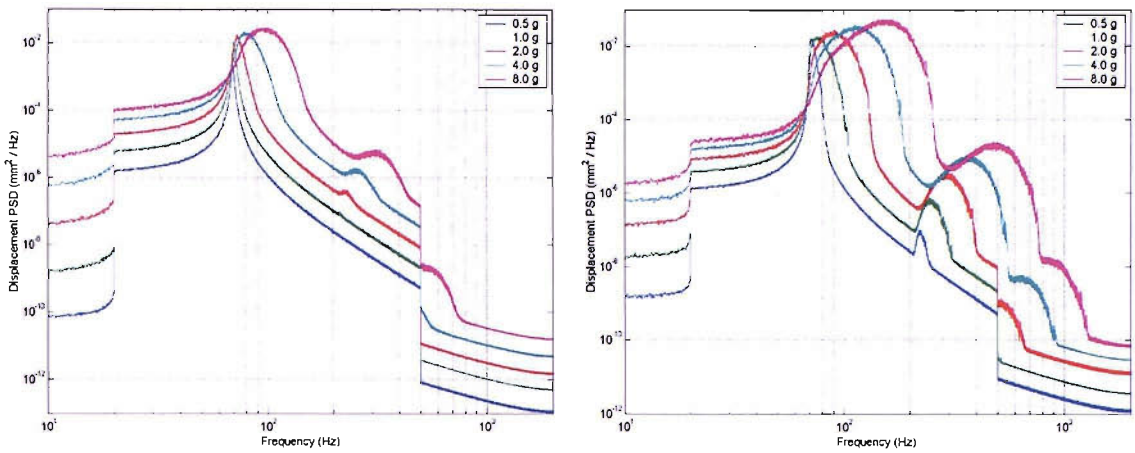

Figure 4.24. Displacement PSDs from nonlinear ODE simulations for input = (0.5, 1, 2, 4, 8) g data: (a) $\zeta = 0.01$ model and (b) $\zeta = 0.001$ model.

(a) (b)

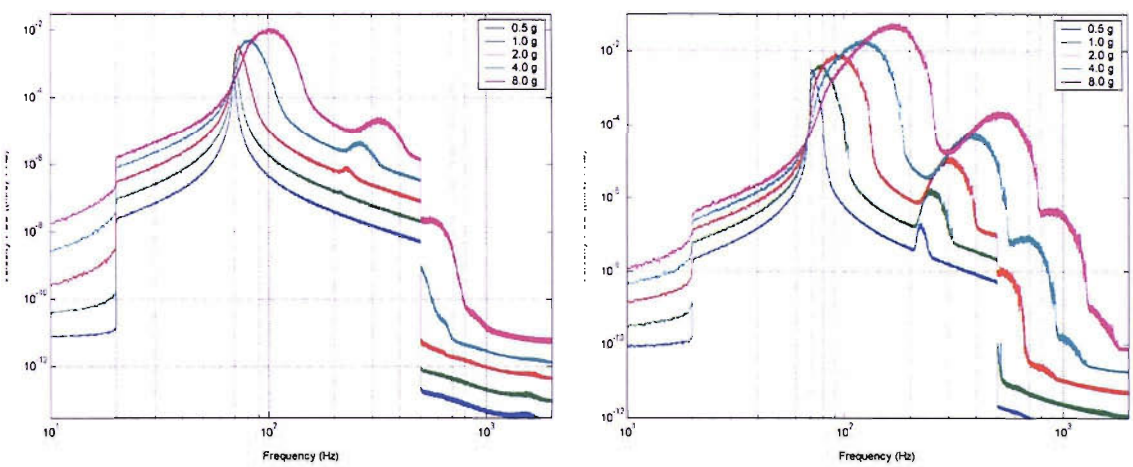

Figure 4.25. Velocity PSDs from nonlinear ODE simulations for input = (0.5, 1, 2, 4, 8) g data: (a) $\zeta = 0.01$ model and (b) $\zeta = 0.001$ model.

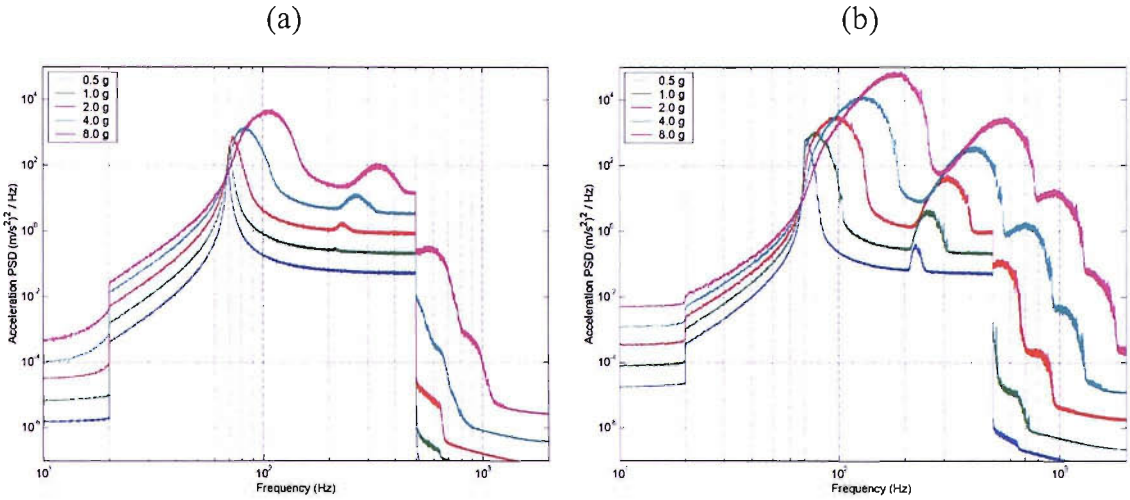

Figure 4.26 Acceleration PSDs from nonlinear ODE simulations for input = (0.5, 1, 2, 4, 8) g data: (a) $\zeta = 0.01$ model and (b) $\zeta = 0.001$ model.

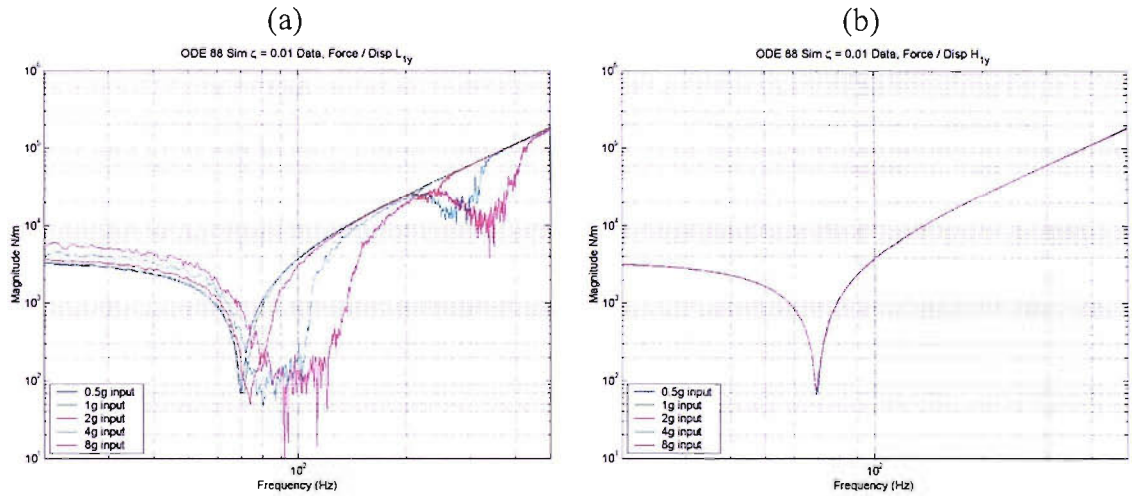

Figure 4.27 Displacement input to force output frequency response functions determined from 88 s of nonlinear ODE simulation results, $\zeta = 0.01$ model input = (0.5, 1, 2, 4, 8) g data: (a) correlated displacement input and (b) uncorrelated displacement input.

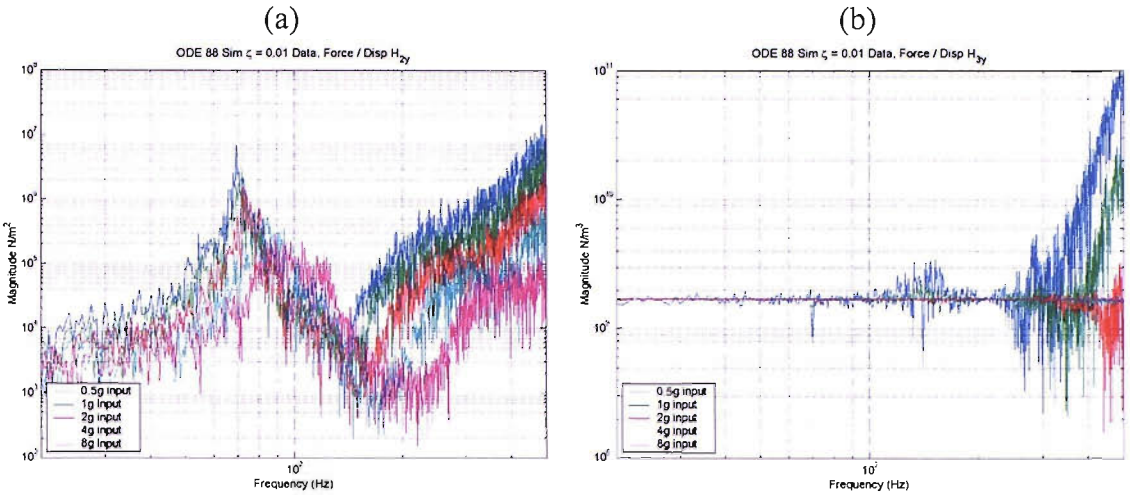

Figure 4.28. Nonlinear displacement input to force output frequency response functions determined from 88 s of nonlinear ODE simulation results, $\zeta = 0.01$ model input = (0.5, 1, 2, 4, 8) g data: (a) uncorrelated squared displacement input and (b) uncorrelated cubed displacement input.

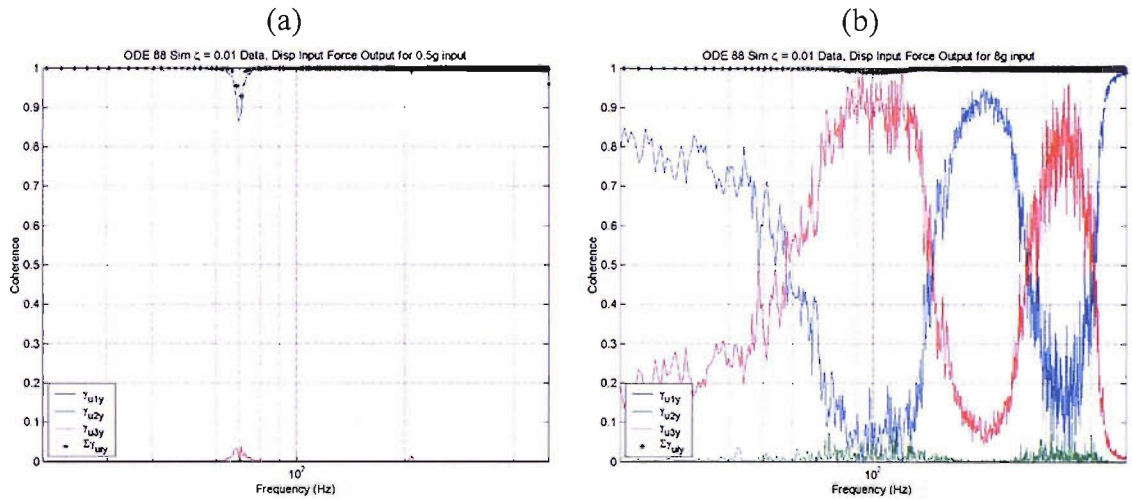

Figure 4.29. Displacement input to force output coherence functions determined from 88 s of nonlinear ODE simulation results, $\zeta = 0.01$ model data: (a) input = 0.5 g and (b) input = 8 g. Legend: γ_{u1y}= coherence of linear uncorrelated displacement to force, γ_{u2y} = coherence of squared uncorrelated displacement to force, γ_{u3y} = coherence of cubed uncorrelated displacement to force, $\Sigma\gamma_{uiy}$ = summed coherences.

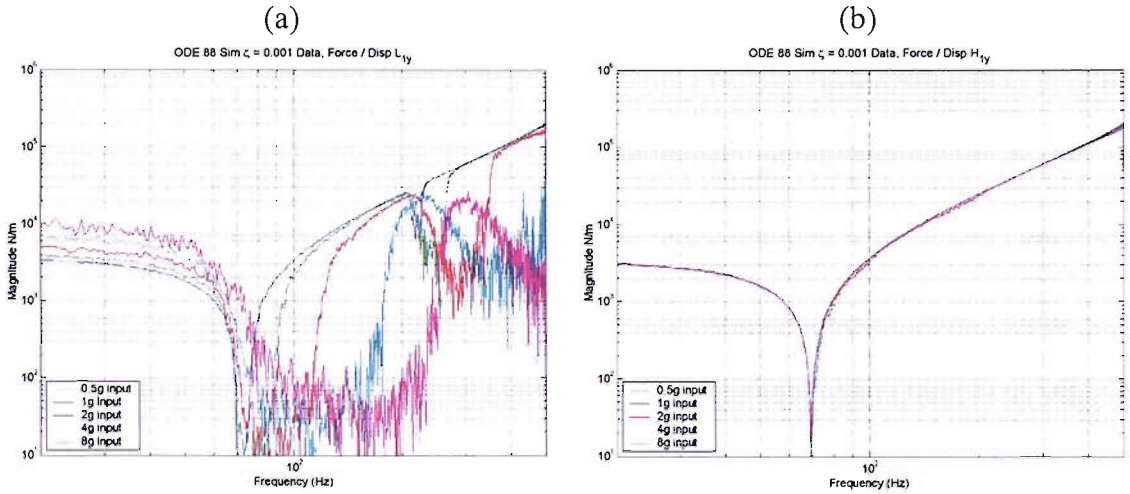

Figure 4.30 Displacement input to force output frequency response functions determined from 88 s of nonlinear ODE simulation results, $\zeta = 0.001$ model input = (0.5, 1, 2, 4, 8) g data: (a) correlated displacement input and (b) uncorrelated displacement input.

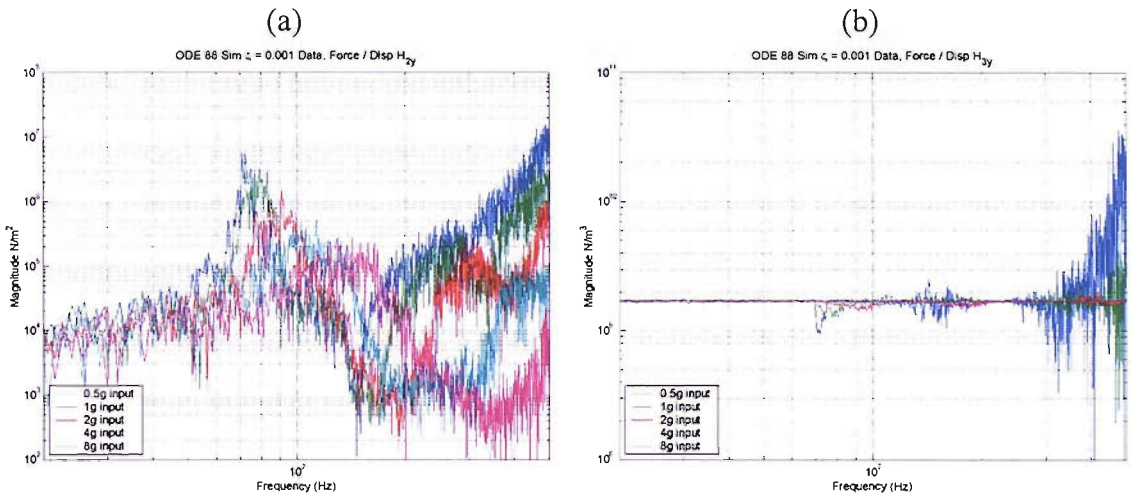

Figure 4.31 Nonlinear displacement input to force output frequency response functions determined from 88 s of nonlinear ODE simulation results, $\zeta = 0.001$ model input = (0.5, 1, 2, 4, 8) g data: (a) uncorrelated squared displacement input and (b) uncorrelated cubed displacement input.

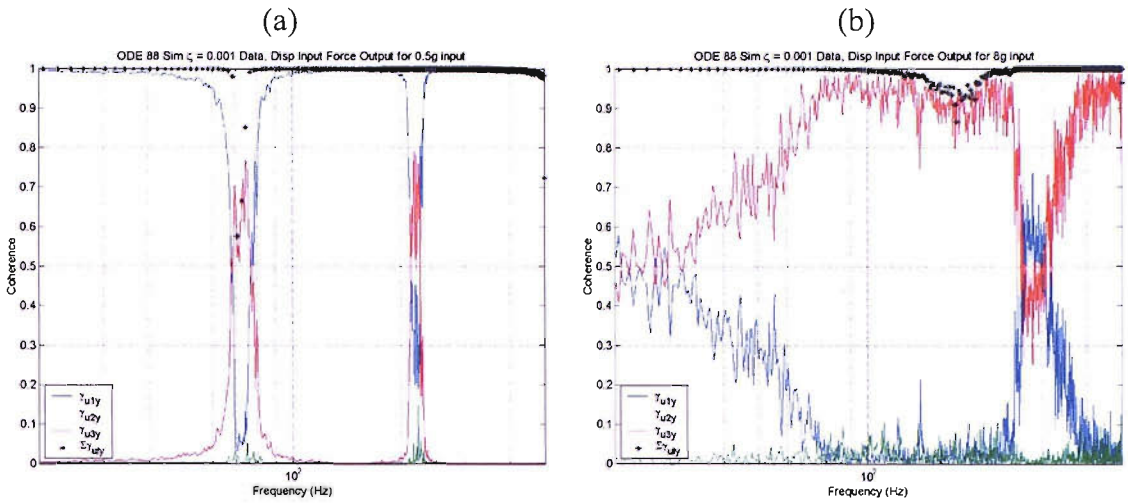

Figure 4.32 Coherence function functions for 88 s of nonlinear ODE simulation results, $\zeta = 0.001$ model data: (a) input = 0.5 g and (b) input = 8 g. Legend: γ_{u1y}= coherence of linear uncorrelated displacement to force, γ_{u2y} = coherence of squared uncorrelated displacement to force, γ_{u3y} = coherence of cubed uncorrelated displacement to force, $\Sigma\gamma_{uiy}$ = summed coherences.

5 FATIGUE ANALYSIS OF NONLINEAR NARROWBAND SIMULATIONS

This chapter will discuss stress and fatigue damage analysis of the linear and nonlinear ODE model results. The goal of this chapter is to demonstrate that time to failure estimates based on peak stress response probability density functions can be determined with novel and efficient PDF transforms.

Displacement time history files (discussed in Chapter 4) are processed with linear first-order and cubic third-order displacement to strain relationships to show how the nonlinearities affect the results. The properties of the linear and nonlinear displacement to strain equations were determined from measured values from the WPAFB experiments (discussed in Chapter 3). Once the strains were determined, the stress was estimated based on a simple stress strain relationship with the elastic modulus.

The stress time histories were sampled to determine peak stresses, which resulted in Rainflow Matrices (RFM). The RFM were processed to determine fatigue damage and time to failure, assuming the use of a steel SAE1015 material (as in Chapter 3). The damage calculations were performed for a baseline damage equation with no mean stress effects and with two additional equations that included mean stress effects have been considered.

First, baseline linear ODE models are used for comparison to the subsequent nonlinear model damage calculations. Next, an intermediate set of calculations was performed on the nonlinear displacement results using just the linear part of the displacement to strain relationship. A final set of calculations was performed on the total nonlinear stress matrices. Histograms were calculated for the minimum and maximum peak stress values to be used for comparison to the PDF transform results.

The time domain stress response simulations were augmented with estimates of the rainflow matrices determined with the PDF transform method. The PDF transforms started with the peak displacement PDFs and estimated the peak stress PDFs based on the linear and nonlinear displacement to strain relationships. The nonlinear PDF transform expression yielded a complication, which was due to the addition of a second

mapping of displacement to strain that occurs with the addition of the squared membrane stress term. The nonlinear peak stress PDFs were converted to histograms for use in damage calculations. These time to failure results compared well to the time domain simulations and the measured data from the WPAFB experiments.

5.1 Stress response calculation

Several authors [16, 206] suggest that the bending, membrane, and total strain stress response can be estimated with a simple quadratic function of the nonlinear displacement y (see equation (1.8)) with the form

$$\begin{aligned} \varepsilon_{bend} &= C_1 y \\ \varepsilon_{memb} &= C_2 y^2 \\ \sigma_{total} &= E\left(\varepsilon_{bend} + \varepsilon_{memb}\right) \end{aligned} \tag{5.1}$$

This equation captures the simple relationship between bending and membrane strain and stress, and introduces local minima in the displacement to total strain function, as shown in Figure 5.1, which adds a second mapping of strain to nonlinear displacement.

The results from the WPAFB experiments (see Chapter 3) suggest a more complex form of the function

$$\begin{aligned} \varepsilon_{lin} &= H_{y1\varepsilon}(f)\, y \\ \varepsilon_{square} &= H_{y2\varepsilon}(f)\, y^2 \\ \varepsilon_{cube} &= H_{y3\varepsilon}(f)\, y^3 \\ \sigma_{total} &= E\left(\varepsilon_{lin} + \varepsilon_{square} + \varepsilon_{cube}\right) \end{aligned} \tag{5.2}$$

where $H_{y1\varepsilon}$, $H_{y2\varepsilon}$ and $H_{y3\varepsilon}$ are the multi-mode frequency response functions of the linear, squared, and cubic nonlinear displacement input to strain response. The filtered input and response analysis in Chapter 3 determined a set of constants for these functions. These constants (e_1, e_2, and e_3) were simplified and modified slightly for use in this chapter (see Table 5.1). The strain relationship for this cubic system is now

$$\varepsilon = e_1 y + e_2 y^2 + e_3 y^3 \tag{5.3}$$

The addition of the cubed term requires further care with regard to estimating nonlinear strain (and stress). The new cubic equation has the possibility of local maxima that are not considered real and must be avoided in the simulations. The parameter e_3 is chosen to ensure that the local maxima did not occur within the range of data from the ODE simulation. The local minimum and maximum values for the cubic equation occur when the derivative equals zero, i.e.

$$d\varepsilon/dy = e_1 + 2e_2 y + 3e_3 y^2 = 0 \tag{5.4}$$

This has two solutions

$$y = \frac{-e_2 \pm \sqrt{e_2^2 - 3e_2 e_3}}{e_1} \tag{5.5}$$

Substituting theses roots into equation (5.3) gives the value of strain at the minimum and maximum. The numerical values for the roots are given in Table 5.2. Figure 5.1(b) shows an example cubic function that will be used in the following analysis. To illustrate their interaction, typical time domain plots of the linear, squared, cubic, and total strains are shown in Figure 5.2. Note that the total strain reaches a minimum at approximately -100 με; this corresponds to the minima of the cubic displacement to strain function shown in Figure 5.1(b). For comparison, the same function with the cubic term omitted is shown in Figure 5.1(a); the addition of the cubic term tends to make the positive displacement region more linear and the negative displacement region more nonlinear.

Stress responses were determined using equation (5.6) (which includes a stress concentration factor $K = 1.1$, that is used to increase the stress locally to compare with fatigue calculations in Chapter 3) for the entire set of model results.

$$\sigma_{ode} = K\sigma_{total} \tag{5.6}$$

The analysis of the linear and nonlinear stresses from the ODE simulations is discussed next. The results from the $\zeta = 0.003$ model will be used because it is closest to the measured damping from the WPAFB experiments. The SAE 1015 steel material with

elastic modulus $E = 204$ GPa, and the three sets of fatigue parameters are used again in this chapter.

5.1.1 Linear ODE baseline model rainflow matrix and damage

The normalized RFM for 4900 s of the baseline linear $\zeta = 0.003$ model is shown in Figure 5.3. The plot shows that the main response is along the R=-1 (zero mean) diagonal of the RFM. The RFM can then be integrated or summed along the minimum and maximum stress axes to form histograms, as shown in Figure 5.4(a). Both histograms show a classic Rayleigh shape. Note that the histogram of minima is a "mirror image" of the histogram of maxima. Figure 5.4(b) shows that the peak PDF determined from the histogram of maxima is in excellent agreement with a Rayleigh distribution.

The stress standard deviation σ_σ and time to failure results for the linear ODE baseline model are given in Table 3.15. Note that at the highest 8 g input level, the predicted times to failure are less than the total of 4900 s of data used to generate the RFM and RFD results. This would imply a high probability of fatigue failure if the linear assumption were true. A typical RFD matrix for the scaled linear baseline ODE results is shown in Figure 5.5(a).

One important observation from this plot is that there are a few stress cycles that occur at stresses above the ultimate strength of 415 MPa for this material. This would indicate that the material could also fail as a result of a peak stress at some time within the 4900 s of simulation. There are also many cycles that occur above the yield strength of 228 MPa. These observations require further investigation.

5.1.2 Nonlinear ODE model linear rainflow matrix and damage

A preliminary step toward the total nonlinear fatigue analysis is to analyze the fatigue damage for the linear part of stress, which is determined from the nonlinear displacement. This set of results includes the nonlinear change in the peak displacement PDF, the nonlinear change in the stress standard deviation and the shift in the rate of

zero crossings and peaks. This linear model does not include any effects of the membrane or cubic displacement to stress terms.

The stress standard deviation and time to failure results for the nonlinear displacement with linear stress model are given in Table 5.4. Compare this with the linear results in Table 3.15; the estimated time to failure increases dramatically as the system response becomes more nonlinear. At the maximum input, the nonlinear estimate is approximately four orders of magnitude longer than the linear estimate.

An important observation from these linear stress model results is that the time to failure is about the same for the three damage equations. This is an expected result; the baseline damage model has a zero mean stress assumption.

5.1.3 Nonlinear ODE model membrane stress rainflow matrix

An example of the quadratic membrane stress RFM, determined from the nonlinear ODE results, is shown in Figure 5.6(a) for the 2 g input load. The figure is normalized by the standard deviation of the membrane stress. It shows that membrane stress is always positive with all stress cycles (except for two outliers) having a minimum stress of zero.

5.1.4 Nonlinear ODE model total stress rainflow matrix and damage

The total stress RFM shows the truly nonlinear nature of the predicted stress response. This model now includes all of the nonlinear effects that are assumed to be present in this analysis. Figure 5.6(b) through Figure 5.7(b) show the normalized total stress RFM for the nonlinear model from the lowest 0.5 g input through to the highest 8 g input. The addition of the squared and cubic displacement to strain terms causes the RFM to curve away from the main RFM diagonal. This indicates the existence of a significant mean stress term in the rainflow cycles. The RFM above 2 g shows the increase in the number of rainflow cycles that have a minimum stress of approximately -20 MPa.

Normalized histograms of stress peak minima and maxima are shown for each input level in Figure 5.8(a) through Figure 5.9(b). These histograms were normalized by the

absolute value of the minimum stress at each level (see Table 5.2) to clarify the asymptotic nature of the peak response. At the lowest input level, the shape of the histograms of minima and maxima appear approximately Rayleigh, but as the input increases and the response becomes more nonlinear, the shapes change dramatically. It is also interesting to observe that at the relatively low 1 g input level, some positive stress maxima start to appear near $\sigma_{peak} / |\sigma_{min}| = -1$ (see Figure 5.8(b)). As the input level increases, the number of stress minima near $\sigma_{peak} / |\sigma_{min}| = -1$ increases dramatically. The vertical scale in these graphs is linear to illustrate the dramatic increase in low amplitude cycles.

The normalized nonlinear bending stress damage results presented in this section show the departure of the nonlinear damage from the linear cases presented in the previous sections. Figure 5.10(a) through

Figure 5.11 show the RFD matrices for the total stress model using the Morrow damage equation. One important observation is that the damage is concentrated near the high stress cycles with very little contribution from the plentiful low-amplitude cycles near the minimum peak stress asymptote.

Another important observation is that the time to failure estimates (see Table 5.5) now show a marked reduction when using the Morrow and Walker damage equations, which include mean stresses. These examples help to illustrate the importance of using a fatigue model that includes mean stress effects when working with structures that exhibit nonlinear stress responses.

5.2 Nonlinear PDFs and life estimates

This section extends the PDF transforms of nonlinear displacement to strain that was introduced for use with the raw multi degree of freedom WPAFB data in section 3.3.2. The work in this section is based on single degree of freedom models that now have the same rates of displacements and bending strains.

5.2.1 PDF estimate for nonlinear total stress

The PDF transform method is used to estimate the nonlinear peak total stress PDF from nonlinear peak displacement PDFs. In this case, the nonlinear peak displacement to peak total stress function was determined based on single mode nonlinear parameter estimates of the WPAFB data (discussed in Section 3.3.1.2)

$$\begin{aligned} \sigma &= g(y) \\ \sigma &= KE\left(e_1 y + e_2 y^2 + e_3 y^3\right) \end{aligned} \tag{5.7}$$

where σ is the nonlinear peak total stress and y is the nonlinear peak displacement. The parameters K, E, and the coefficients e_i are given in Section 5.1. This is the standard form of the nonlinear function with the polynomial on the right hand side of the equation.

The PDF transfer function for this nonlinear peak displacement to peak stress function is

$$p_{nl\,peak}(\sigma) = \frac{p_{nl\,peak}(y)}{\left|d\sigma/dy\right|} \tag{5.8}$$

where $p_{nl\,peak}$ are the nonlinear PDFs of peak stress and displacement. The absolute value of the derivative of (5.7) is

$$\left|d\sigma/dy\right| = \left|e_1 + 2e_2 y + 3e_3 y^2\right| \tag{5.9}$$

The derivative has two roots

$$y = \frac{-e_2 \pm \sqrt{e_2^2 - 3e_2 e_3}}{e_1} \tag{5.10}$$

The range of results was limited such that only one root (the minimum) was observed (see discussion in Section 5.1).

The second step in this development was to make a further assumption that each positive displacement peak is followed immediately by a negative displacement

minimum with the same magnitude. Another way of thinking of this is that each point on a positive peak displacement PDF maps to a complete cycle with amplitude equal to the positive peak value. This is considered fair, based on the standard assumption that a narrowband response (single degree of freedom model) has one positive peak for each positive zero crossing (see Figure 5.2 for example time data). The displacement cycle assumption now lets one calculate the PDF for min and max stresses based on the total stress in equation (5.7). Theories that extend this single mode stress model to multi mode stress models [170, 172] may be useful for further research.

At this point, it is helpful to observe how the displacement maps to total stress with an example. Figure 5.12(a) shows six cycles of an increasing displacement function, and Figure 5.12(b) shows the corresponding total stress based on equation (5.7). The first three cycles behave "normally," but the final three cycles show that the stress function now contains two cycles for one displacement cycle. First, define a primary cycle that has a stress maxima mapping to the positive displacement maxima, and a stress minima mapping to the displacement minima. This one-to-one mapping works for displacement cycles up to the value determined by equation (5.10). Note that the standard PDF transfer function (4.29) is asymptotic at this point. The primary cycles have a minimum at the zero slope of the total stress function. Also, define a secondary cycle that has a minimum stress at this same minimum and a maximum stress at the point mapping to the negative minimum of the displacement cycle.

The total stress PDF can be determined numerically as follows. First, define a range of nonlinear peak displacement values y at a convenient spacing

$$\begin{aligned} -4\sigma_y \le y \le 4\sigma_y \\ dy = 0.01\sigma_y \end{aligned} \tag{5.11}$$

corresponding to the positive peak displacement range observed in the nonlinear ODE simulation. Determine the PDF of nonlinear positive displacement peaks $p_{nl\,peak}(y)$ based on a PDF transform

$$p_{nl\,peak}(y) = |dx/dy|\, p_{peak}(x) \tag{5.12}$$

of linear peak displacement PDF ($p_{peak}(x)$) with the values of x and the derivative dx/dy of the nonlinear functions (see Chapter 4, Section 4.2.9.2)

$$\begin{aligned} x &= h(y),\ y \in [0,\infty) \\ x &= c_1 y + c_2 y^2 + c_3 y^3 \\ dx/dy &= c_1 + 2c_2 y + 3c_3 y^2 \end{aligned} \tag{5.13}$$

determined numerically from the positive values of y chosen above from equation (5.11). Also, determine a second nonlinear displacement PDF of negative minima using the same PDF, but now assigned at the negative values of y

$$\begin{aligned} x &= h(y),\ y \in (-\infty,0) \\ x &= c_1 y - c_2 y^2 + c_3 y^3 \\ dx/dy &= c_1 - 2c_2 y + 3c_3 y^2 \end{aligned} \tag{5.14}$$

Figure 5.13 is an example of this process for data from the 8 g simulation, $\zeta = 0.003$. Now, given the PDFs of nonlinear peak displacement from equation (5.12), numerically evaluate the PDF transfer function in equation (4.29) using the derivative from equation (5.9) and the values of y from equation (5.8) to yield the nonlinear peak stress PDF. At the lower levels of input, the mapping of displacement to stress is one to one, as shown in Figure 5.14(a). At higher input levels, the secondary cycles start to occur, resulting in additional cycles. There are now two possibilities for generating stress maxima and minima. Figure 5.14(b) gives an example of this result. Note that the total stress PDF has an asymptote at –19.67 MPa.

Figure 5.14(b), shows a PDF of primary maxima and secondary maxima. These functions can be plotted in a form like the WAFO RFM as shown in Figure 5.15. A visual comparison of the PDF transform results (see Figure 5.15(a)), and the RFM of the ODE data (see Figure 5.15(b)) is very encouraging.

These functions are not strictly PDFs anymore, because the "one-to-two" mapping of stress results in an integrated area greater than one. The correct peak total stress PDF has to be normalized by the sum of the primary and secondary contributions. The normalization can be determined as discussed below.

One complication of this numerical PDF transform method is that the total stress functions determined from equation (5.7) have uneven spacing. The resulting nonlinear, unevenly spaced PDFs of primary and secondary stress cycles can be interpolated at evenly spaced points and normalized by the sum of the two functions. Another method is to generate histograms of the primary and secondary cycles and simply sum the two to get an overall histogram of total cycles. This method was used to generate histograms for comparison to those determined from the ODE simulations of total stress (see Section 5.1.4).

Peak stress histograms of minima and maxima are shown in Figure 5.16. Note that the histograms are shown on a logarithmic scale in order to allow for better observation of the results near the tails of the histograms. These figures show that the histogram results determined by PDF transform compare very well with the rainflow histograms determined from the time domain data of total stress. An intermediate result of this work is the estimation of the number of stress peak cycles for the 4900 s of simulated data (see Table 5.6). An alternative way to present this could be to estimate the rates of primary, secondary and total peaks.

5.2.2 Damage estimates for PDF transform method

Having estimated the PDFs and histograms of nonlinear peak total stress, the next step in the analysis is to determine time to failure for the transformed displacement results. In this case, damage estimates were determined directly from the primary and secondary histograms of peak total stress minima and maxima (the RFM were not calculated). Damage calculations were also made using only the primary histograms of peak total stress minima and maxima. The calculations based on only the primary cycles were equal to the combined damage of primary and secondary cycles up to the fifth significant digit or more. The primary cycle results are given in Table 5.7. These compare very favorably with the time to failure results from the ODE stress simulations in Table 5.5.

5.3 Nonlinear narrowband simulation summary

This chapter was devoted to the fatigue analysis of the narrowband ODE simulations discussed in Chapter 4. Linear baseline and nonlinear time domain stress responses were processed to determine rainflow matrices of stress peaks. Time to failure estimates were made with three damage equations.

A method to estimate nonlinear peak total stress PDFs was developed. The PDFs were determined by first estimating the nonlinear peak displacement PDFs (from linear peak PDFs) and then by determining the nonlinear peak total stress PDFs (from the nonlinear peak displacement PDFs). The PDF transform results were used to estimate time to failure, which compared well to the time domain cycle counting estimates. Primary stress cycles were shown to account for the bulk of the fatigue damage.

The change in time to failure, based on each fatigue equation assumption, is illustrated in Figure 5.17 for the assumed SAE1015 material and the results tabulated in this chapter. The graphs show that the linear model can estimate lives over 100 times shorter at the maximum input level, while the nonlinear model without mean stress effects can estimate lives about 10 times longer.

When one considers nonlinear structural effects, the ODE simulations have demonstrated that there can be a potential improvement in the fatigue lives of structures (compared to linear estimates), but there are potential simplifications that could overestimate the improvement. It is highly recommended to use fatigue equations that include mean stress effects (e.g. the Walker or Morrow equations) when working with nonlinear structures.

This chapter has demonstrated that the PDF transform method can be successfully used to estimate peak stress joint PDFs for single degree of freedom systems. The added complication of the one-to-two mapping of displacement cycles to stress cycles has been included in a straightforward and efficient solution technique.

5.4 Chapter 5 Tables

Table 5.1. Nonlinear displacement to bottom strain parameters for ODE simulations.

Input	e_1 με/mm	e_2 με/mm^2	e_3 με/mm^3
0.5 g	141.7	40.3	-15.26
1 g	141.7	40.3	-15.26
2 g	141.7	40.3	-14.65
4 g	141.7	40.3	-10.37
8 g	141.7	40.3	-6.10

Table 5.2. Nonlinear displacement to bottom strain and stress minimum and maximum for ODE simulations.

Input	y_{min} mm	y_{max} mm	ε_{min} με	σ_{min} MPa
0.5 g	-1.087	2.848	-86.85	-19.49
1 g	-1.087	2.848	-86.85	-19.49
2 g	-1.100	2.934	-87.65	-19.67
4 g	-1.201	3.791	-94.12	-21.12
8 g	-1.347	5.749	-102.9	-23.09

Table 5.3. Time to failure estimates for linear ODE baseline model data.

Input	σ_σ MPa	σ_{max} MPa	Baseline (s)	Morrow (s)	Walker (s)
0.5 g	5.06	26.63	1.9452×10^{14}	1.9450×10^{14}	1.4058×10^{14}
1 g	10.12	53.25	4.217×10^{11}	4.216×10^{11}	3.216×10^{11}
2 g	20.24	106.5	9.141×10^{8}	9.138×10^{8}	7.357×10^{8}
4 g	40.24	213.0	1.982×10^{6}	1.980×10^{6}	1.683×10^{6}
8 g	80.96	426.0	4.296×10^{3}	4.285×10^{3}	3.850×10^{3}

Table 5.4. Time to failure estimates for nonlinear ODE displacement, linear stress model data.

Input	σ_σ (MPa)	σ_{max} MPa	Baseline (s)	Morrow (s)	Walker (s)
0.5 g	4.97	23.15	6.55×10^{15}	6.55×10^{15}	4.69×10^{15}
1 g	9.59	41.67	1.12×10^{13}	1.12×10^{13}	8.49×10^{12}
2 g	17.14	66.84	2.38×10^{11}	2.38×10^{11}	1.85×10^{11}
4 g	28.74	102.9	1.90×10^{9}	1.90×10^{9}	1.54×10^{9}
8 g	44.67	149.5	2.43×10^{7}	2.43×10^{7}	2.03×10^{7}

Table 5.5. Time to failure estimates for nonlinear ODE displacement, total nonlinear stress model data.

Input	σ_σ MPa	σ_0 MPa	σ_{max} MPa	Baseline (s)	Morrow (s)	Walker (s)
0.5 g	4.94	0.22	26.62	3.45×10^{14}	3.36×10^{14}	1.78×10^{14}
1 g	9.40	0.82	49.50	2.02×10^{12}	1.86×10^{12}	8.41×10^{11}
2 g	16.17	2.63	76.28	3.97×10^{10}	3.28×10^{10}	1.24×10^{10}
4 g	26.24	7.39	118.7	6.75×10^{8}	4.52×10^{8}	1.65×10^{8}
8 g	41.71	17.84	207.1	7.27×10^{6}	3.20×10^{6}	1.51×10^{6}

Table 5.6. Number of stress cycles from transformed nonlinear displacement PDF compared to stress model ODE data.

Input	Primary cycles	Secondary cycles	Total cycles	ODE Stress cycles
0.5 g	342 492	0	342 492	342 550
1 g	350 811	135	350 946	350 977
2 g	374 394	50 992	425 386	393 897
4 g	429 342	231 359	660 701	590 007
8 g	529 485	431 135	960 620	890 603

Table 5.7. Time to failure estimates for transformed nonlinear displacement PDF primary cycle data.

Input	Baseline (s)	Morrow (s)	Walker (s)
0.5 g	3.72×10^{14}	3.63×10^{14}	1.93×10^{14}
1 g	2.40×10^{12}	2.23×10^{12}	1.02×10^{12}
2 g	4.11×10^{10}	3.40×10^{10}	1.28×10^{10}
4 g	6.80×10^{8}	4.54×10^{8}	1.67×10^{8}
8 g	7.03×10^{6}	3.09×10^{6}	1.46×10^{6}

5.5 Chapter 5 Figures

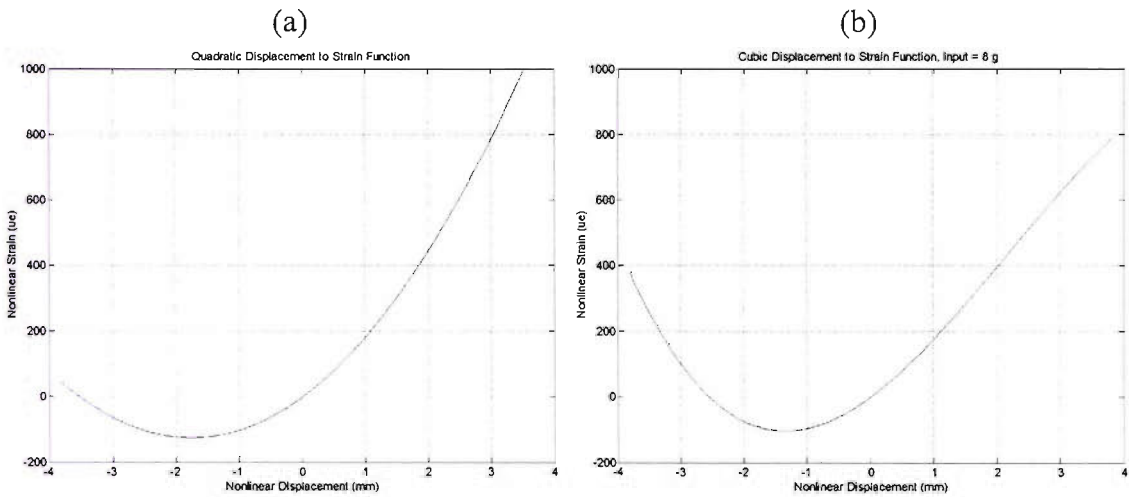

Figure 5.1. Nonlinear displacement to nonlinear strain functions: (a) quadratic function and (b) cubic function for 8 g parameters.

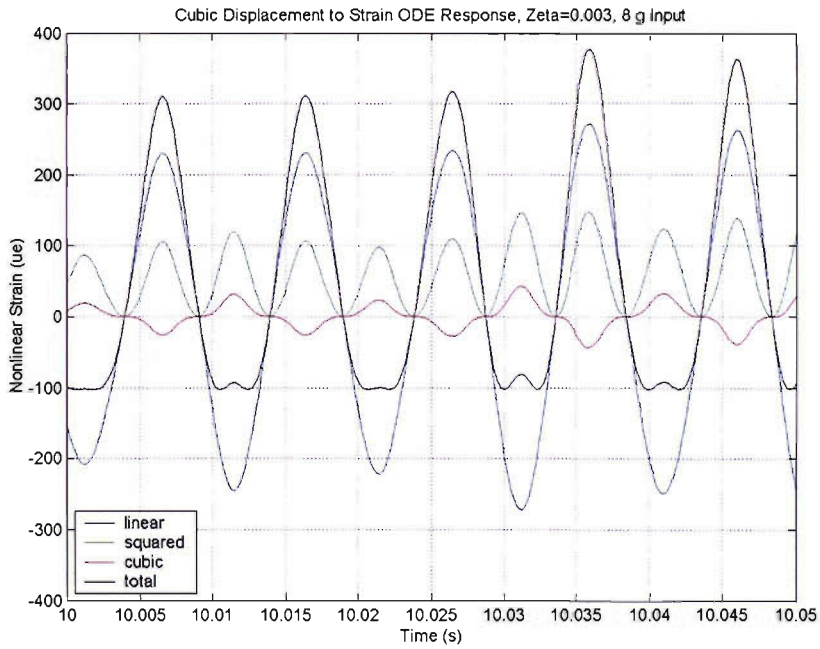

Figure 5.2. Time domain linear, squared, cubic and total strains for nonlinear ODE simulations: $\zeta = 0.003$ model, input = 8 g.

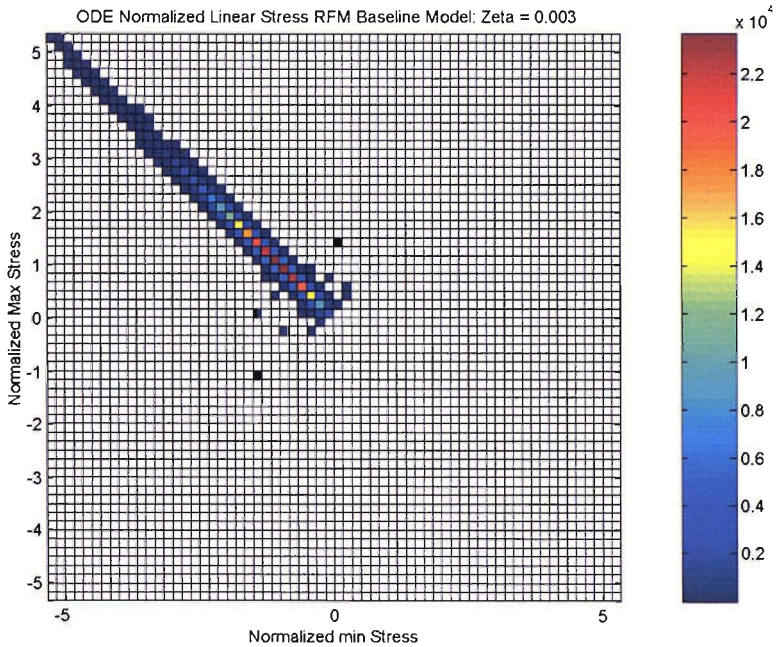

Figure 5.3. Normalized bending stress rainflow matrix for linear ODE simulation: $\zeta = 0.003$ model, input = 1.0 g data, $\sigma_\sigma = 10.12$ MPa.

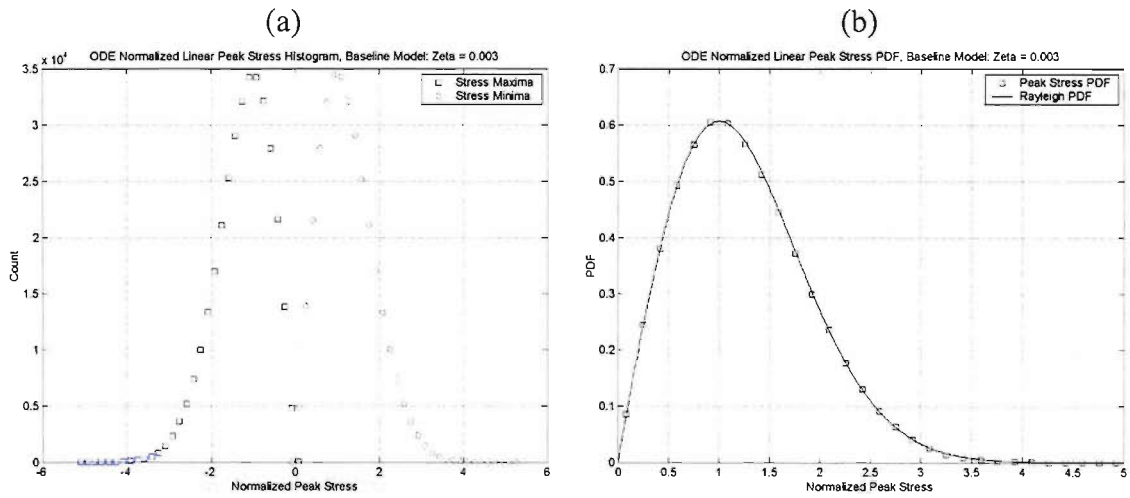

Figure 5.4. Normalized peak stress data from for linear ODE simulation, $\zeta = 0.003$ model, input = 1.0 g data $\sigma_\sigma = 10.12$ MPa: (a) Minimum (symbol = □) and maximum (symbol = ◇) stress histograms and (b) peak stress PDF from data (symbol = □) and Rayleigh PDF (line).

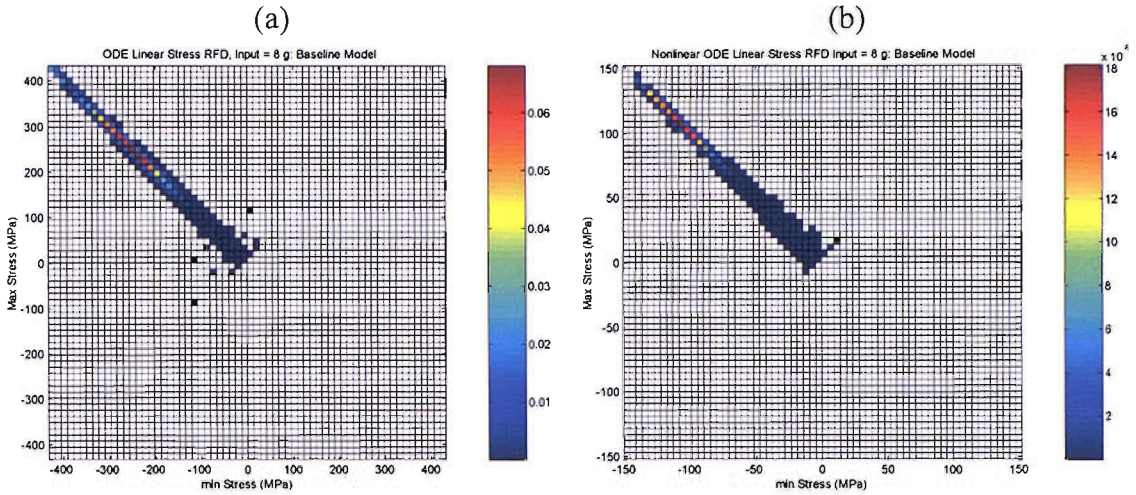

Figure 5.5. Rainflow damage matrices for ODE simulations, $\zeta = 0.003$ model input = 8 g. (a) Linear displacement transformed with linear stress function, σ_σ = 80.96 MPa and (b) nonlinear displacement transformed with linear stress function σ_σ = 44.67 MPa.

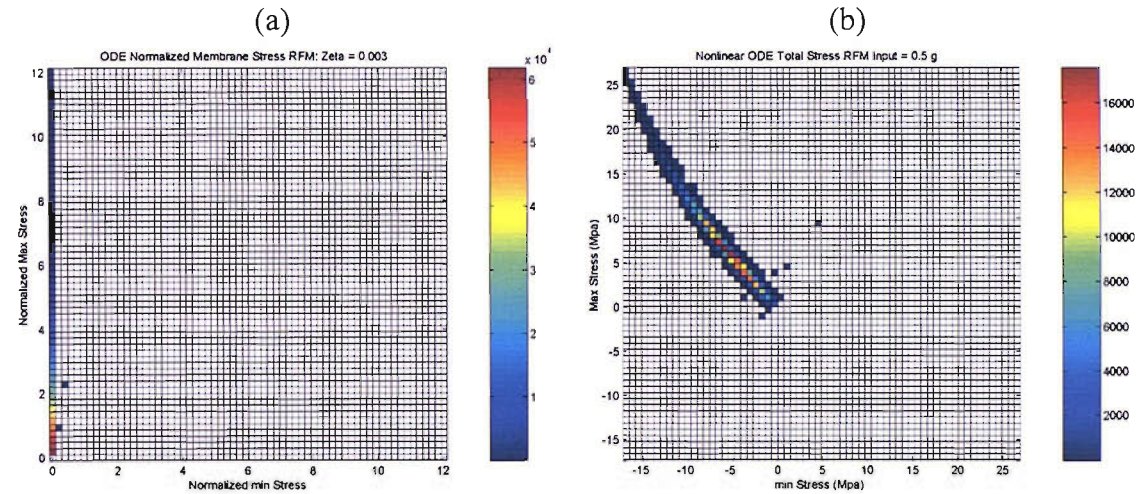

Figure 5.6. (a) Normalized membrane stress rainflow matrix for nonlinear ODE simulation: $\zeta = 0.003$ model, input = 2.0 g, $\sigma_\sigma = 3.35$ MPa. (b) Total stress rainflow matrix for nonlinear ODE simulation: $\zeta = 0.003$ model, input = 0.5 g, $\sigma_\sigma = 4.94$ MPa.

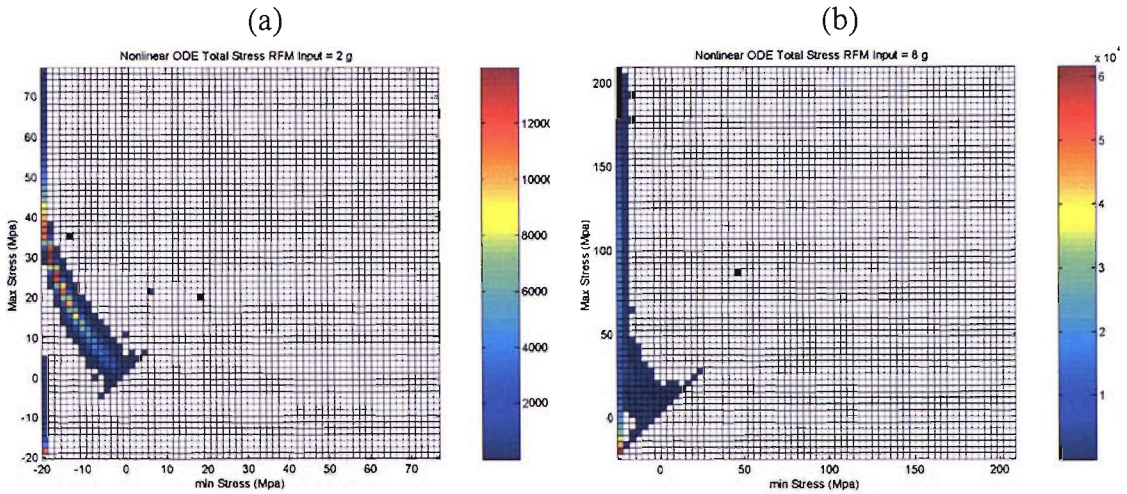

Figure 5.7. Total stress rainflow matrix for nonlinear ODE simulation $\zeta = 0.003$ model: (a) input = 2.0 g, $\sigma_\sigma = 16.17$ MPa and (b) input = 8.0 g, $\sigma_\sigma = 41.71$ MPa.

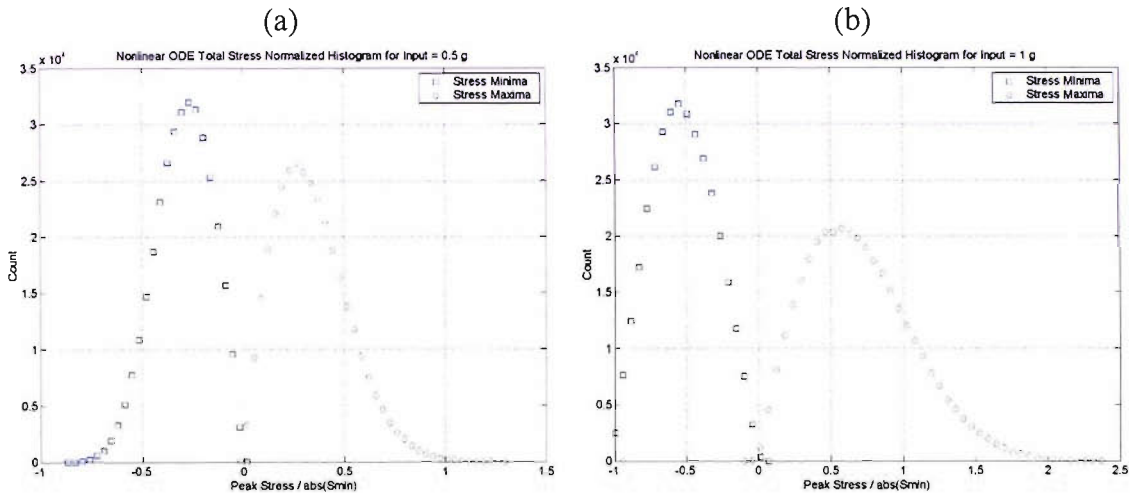

Figure 5.8. Total stress rainflow minima and maxima histograms for nonlinear ODE simulation, $\zeta = 0.003$ model: (a) input = 0.5 g, $\sigma_{min} = 19.49$ MPa, $\sigma_\sigma = 4.94$ MPa and (b) input = 1.0 g, $\sigma_{min} = 19.49$ MPa, $\sigma_\sigma = 9.40$ MPa.

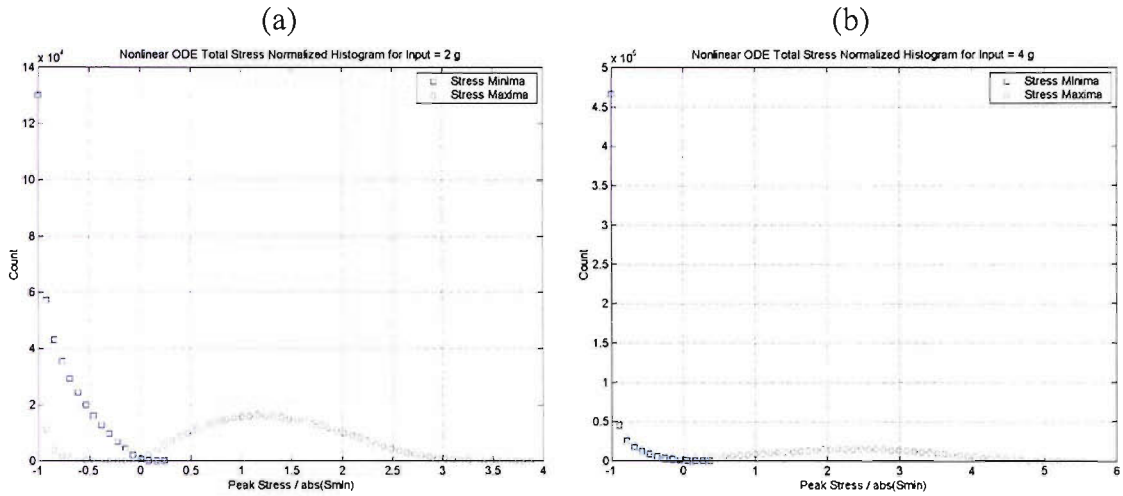

Figure 5.9. Total stress rainflow minima and maxima histograms for nonlinear ODE simulation $\zeta = 0.003$ model: (a) input = 2.0 g, σ_{min} = 19.67 MPa, σ_{σ} = 16.17 MPa and (b) input = 4.0 g, σ_{min} = 21.12 MPa, σ_{σ} = 26.24 MPa.

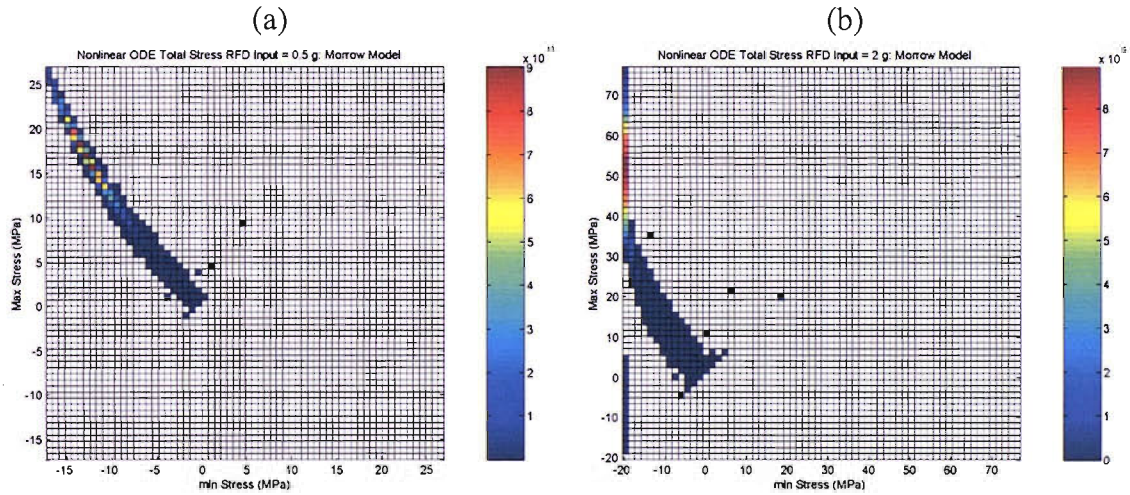

Figure 5.10. Total stress rainflow damage matrix, morrow damage equation, for nonlinear ODE simulation $\zeta = 0.003$ model: (a) input = 0.5 g, σ_{σ} = 4.94 MPa and (b) input = 2.0 g, σ_{σ} = 16.17 MPa.

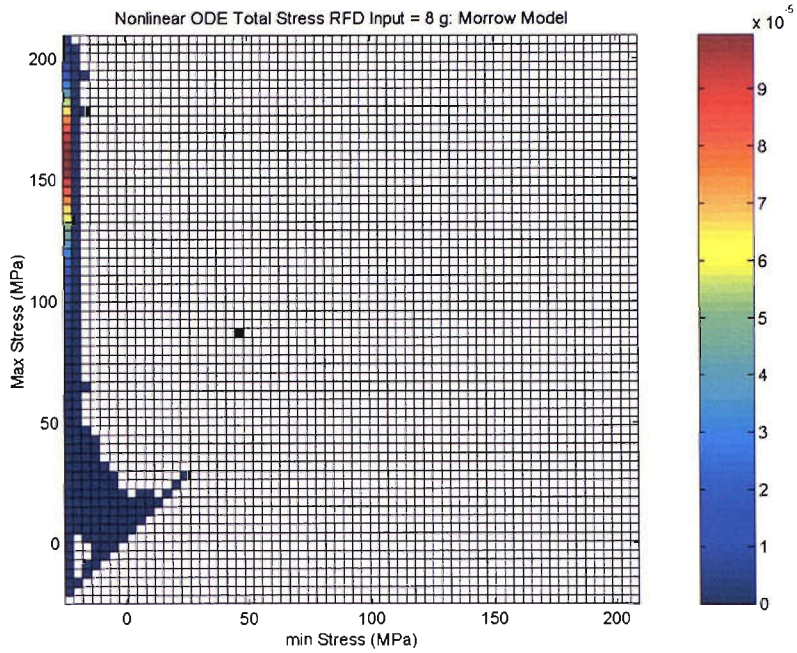

Figure 5.11. Total stress rainflow damage matrix for nonlinear ODE simulation: $\zeta = 0.003$ model, input = 8.0 g, $\sigma_\sigma = 41.71$ MPa, morrow damage equation.

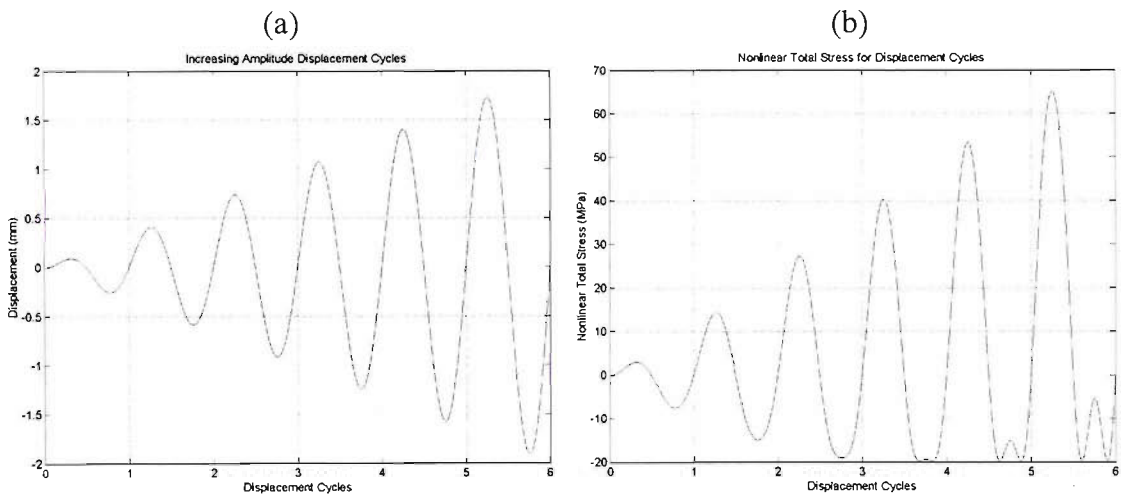

Figure 5.12. (a) Six cycles of an increasing displacement function. (b) Total stress determined from displacement.

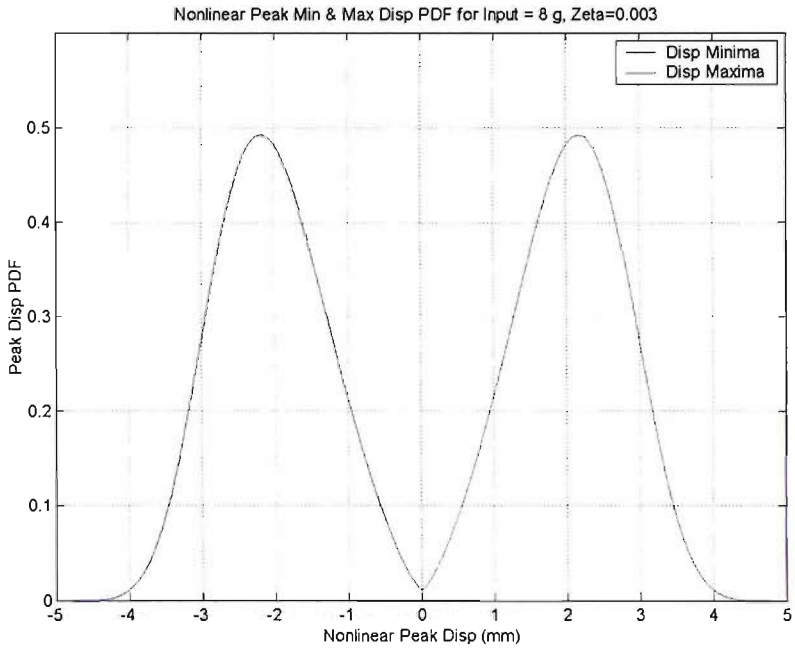

Figure 5.13. Nonlinear positive maxima and negative minima displacement PDFs for $\zeta = 0.003$ model, input = 8 g simulation.

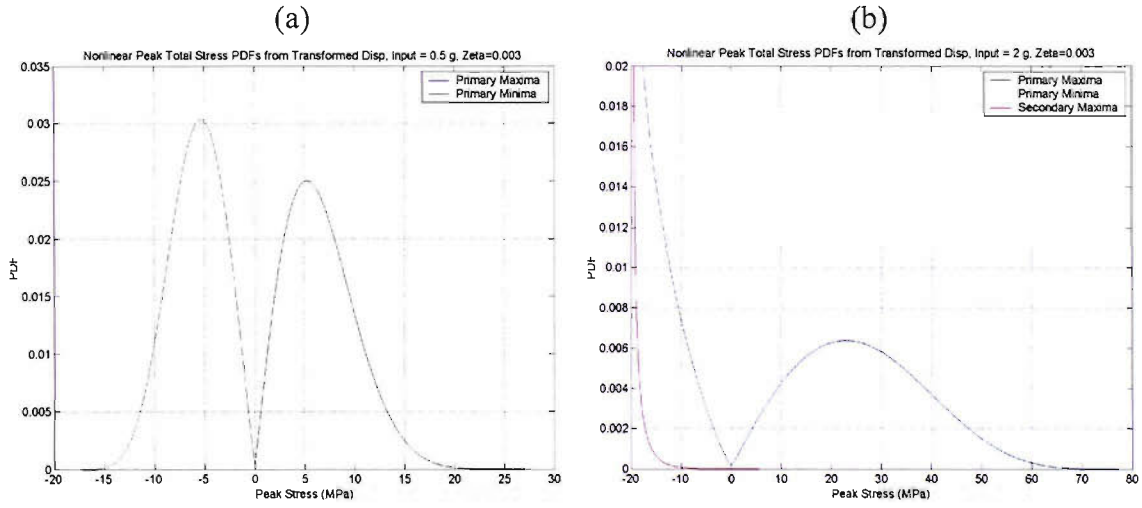

Figure 5.14. Peak total stress PDF determined from transformed positive and negative displacement PDFs for $\zeta = 0.003$ model (a) input = 0.5 g simulation and (b) input = 2 g simulation.

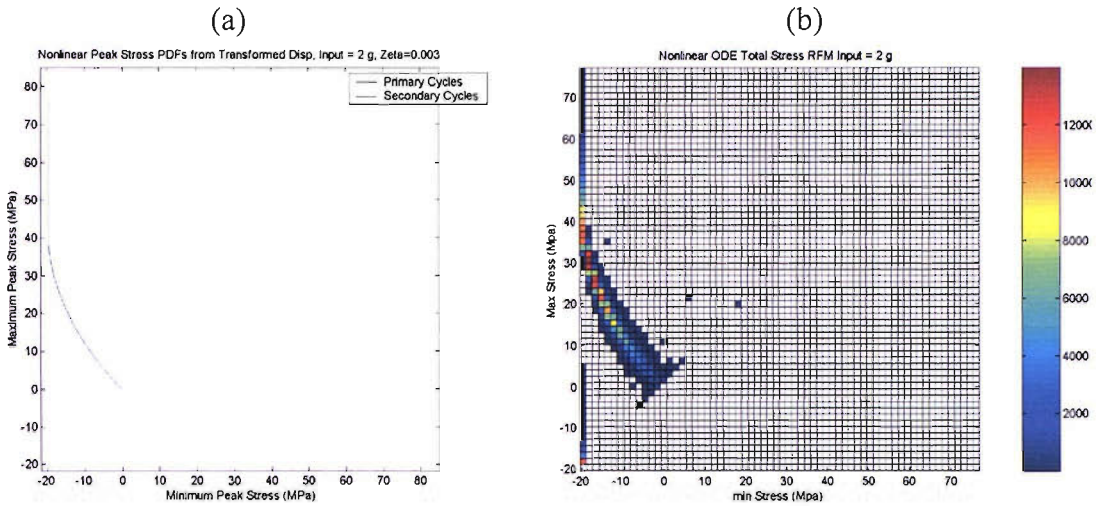

Figure 5.15. Stress results from $\zeta = 0.003$ model input = 2 g nonlinear ODE simulation. (a) Nonlinear total stress primary and secondary ranges from displacement PDFs. (b) Total stress rain flow matrix.

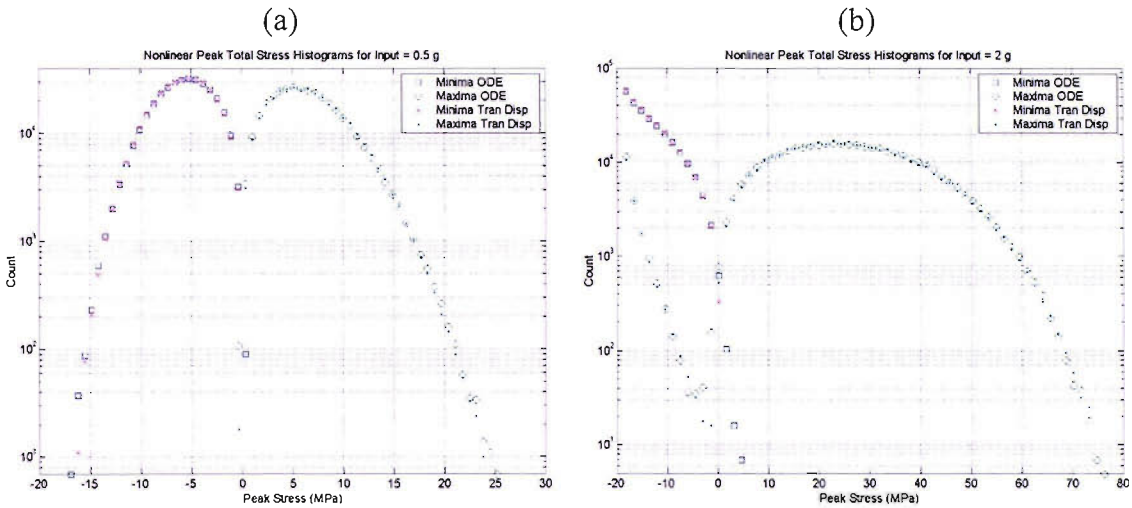

Figure 5.16. Nonlinear peak stress histograms of minima and maxima from nonlinear ODE simulation and transformed displacement PDFs for $\zeta = 0.003$ model: (a) input=0.5 g, (b) input=2 g.

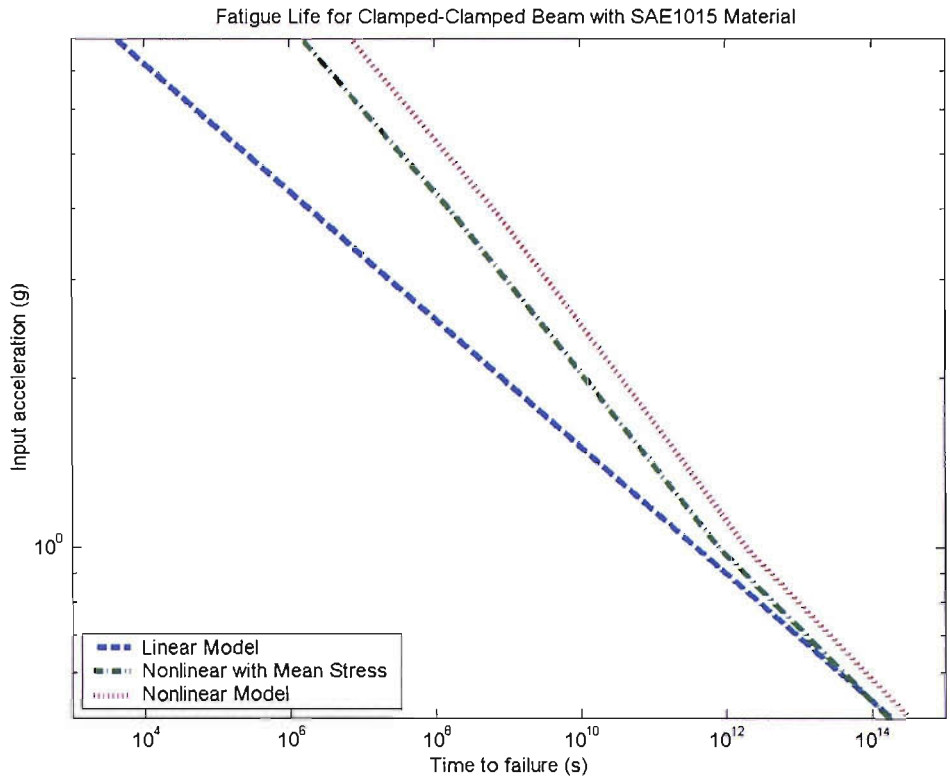

Figure 5.17. Fatigue life estimates for the clamped-clamped ODE simulation $\zeta = 0.003$ model data based on linear and nonlinear damage equations with SAE1015 material properties.

6 CONCLUSIONS

6.1 Summary

The primary focus of this thesis has been to develop original approaches to assist in the estimation of time to fatigue failure for nonlinear structures when subjected to random loading. Experimental data from a set of nonlinear random vibration tests has been analyzed in the time and frequency domains, yielding useful observations about the measured displacement and strain responses. Additional complementary numerical simulations were performed to augment the experimental findings. Throughout this thesis, straightforward and accepted engineering analysis methods were used to identify trends in the data and to help explain the physics of the problem. Graphical representations and tabulated results from the analysis have lead to improved understanding of the nature of the nonlinear random fatigue problem. Specific contributions in the area of the experimental and analytical studies are now briefly described.

6.1.1 Experimental studies

The WPAFB experimental data yielded a wealth of nonlinear random multi-mode response data that was analyzed in both the frequency and time domains. The reverse path nonlinear transfer function method was shown to be very effective in identifying nonlinear models for measured data. Transfer functions for both the force to nonlinear displacement response and the displacement to nonlinear strain response were shown to be consistent even though the raw displacement and strain data showed strong nonlinear responses that changed over the five input level. Multi path nonlinear frequency domain transfer functions were also shown to be useful for reconstructing the linear, squared and cubic parts of the time domain strain response. The linear transfer function estimates were subsequently used to approximate linear random displacement and strain responses. Modal models of the nonlinear system response were proposed based on the identified transfer and coherence functions.

6.1.2 Numerical studies

The linear and nonlinear Duffing simulations, based on the clamped-clamped beam experiments, were developed and executed so that large data sets could be used to show trends in the nonlinear response. The major findings of this work can be summarized as follows:

The standard deviation and kurtosis for the nonlinear random response converge much more slowly than the corresponding linear random response quantities. The response displacement kurtosis tended to be less than 3 and the response acceleration kurtosis tended to be greater than 3, whilst the response velocity kurtosis tended to equal 3 for the Duffing model studied. The velocity response distribution tended to be normal for the nonlinear models.

Random errors in nonlinear standard deviation estimates, based on the statistical bandwidth of the frequency domain PSD response, are much greater than what would be estimated with linear random theory. The harmonic distortion of the displacement, velocity and acceleration response states can be significant enough to cause an estimate of the statistical bandwidth to be even greater than the bandwidth of the input spectrum.

Linear to nonlinear displacement functions determined from the ODE results, using the inverse distribution function method, appear similar to those estimated directly from the experimental displacement data. The linear peak to nonlinear peak functions all tended to follow one main trend, even over wide ranges of input amplitude and damping values. The linear to nonlinear peak functions determined using an assumed generalized linear peak distribution function, with a ratio of zeros to peaks determined from the nonlinear data, produced the best goodness-of-fit agreements. The linear to nonlinear peak displacement response functions appear to form an upper bound (or limiting case) of the linear to nonlinear normal displacement response functions. A novel use of the linear to nonlinear normal displacement function was developed to estimate the rate of zero crossings for the nonlinear response. The estimated rates agree well with those determined by counting level crossings.

The reverse path identification process was used again to demonstrate its potential with simulated nonlinear Duffing model data. The method accurately estimated the Duffing model linear and nonlinear frequency domain parameters.

6.1.3 Major fatigue findings

Time to failure was estimated based on the raw strain measurements and several estimates of linear and nonlinear strain response based on the estimated nonlinear frequency response functions. The time to failure estimates, using rainflow matrices of stress peaks, showed that the nonlinear results were significantly longer than the linear results, especially at the highest input level. The life estimates were also made with two damage models that included nonzero mean stresses.

A method to estimate nonlinear peak total stress PDFs was developed. The PDFs were determined by first estimating the nonlinear peak displacement PDFs (from linear peak PDFs) and then by determining the nonlinear peak total stress PDFs (from the nonlinear peak displacement PDFs). The added complication of the one-to-two mapping of displacement cycles to stress cycles has been included in a straightforward and efficient solution technique. The PDF transform results were used to estimate time to failure, which compared well to the time domain cycle counting estimates. Primary stress cycles were shown to account for the bulk of the fatigue damage.

When one considers nonlinear structural effects, there can be a potential improvement in the fatigue lives of structures (compared to linear estimates), but there are potential simplifications that could overestimate the improvement. It is highly recommended to use fatigue equations that include mean stress effects (e.g. the Walker or Morrow equations) when working with nonlinear structures.

Several significant observations can be summarized for the major changes in fatigue life for a nonlinear stiffening structure:

An increase in response rate produces a linear increase in damage.

The addition of nonlinear tensile membrane stress can yield an increase in damage.

The change in the peak response PDF shape can result in a decrease in damage.

The decrease in the response standard deviation yields an exponential decrease in damage.

6.1.4 Intermediate results of interest

Time domain analysis of the experimental data showed strong nonlinear behavior. PDFs of displacement and strain responses were determined for use with the Inverse Distribution Function (IDF) method to estimate linear to nonlinear random functions. These random functions are a unique way to show trends in the nonlinear response.

The random functions also formed the basis for nonlinear PDF transforms. Basic polynomial curve fits of the linear to nonlinear functions were used to estimate normal random and peak random PDFs of the nonlinear displacement, acceleration and strain.

Investigations of the change in peak PDFs, as the ratio of the rates of zeros to peaks changed, yielded observations of importance. The peak PDF and the peak histogram of a generalized response (i.e., any response from narrowband to completely wideband) were shown to be composed of the sum of narrowband and wideband parts. Equations to estimate the ratio of zeros to peaks ϖ, based on the number of negative value maxima, were developed. An equation to determine the value of the distribution function at a peak value of zero, as a function of ϖ, was also developed.

6.2 Areas for future research

This study has developed and introduced numerous analysis techniques that, when used together, have helped to explain the behavior of nonlinear structures. Whilst performing

this work, some additional avenues of research have been identified that may be of interest. They can be divided into experimental and theoretical research investigations.

6.2.1 Experimental studies

The predicted time to failure for nonlinear random responses has been based on established sinusoidal fatigue and cumulative damage principles. Although some experimental studies of random fatigue have been performed, it would be very interesting to study the basic problem of linear random fatigue more thoroughly. Additional random fatigue tests with controlled positive and negative mean stresses, which could build from the baseline linear random tests, would be a useful exercise. Full nonlinear random fatigue tests for stress stiffening and stress softening systems would help illuminate the underlying physical and stochastic nature of this topic.

Baseline linear random fatigue tests, under controlled conditions, would be a very interesting research project. The standard assumption of linear cumulative damage could be validated or challenged. Ideally, these baseline linear random fatigue tests would induce narrow band stresses that could be used for comparison to random fatigue equations based on a Rayleigh stress peak distribution. Additional attention to the high and low cycle regions would be of further interest. In the low cycle region, the probability of occurrence of peak loads above the elastic limit of the material might point to a revised random fatigue model that would include elastic and plastic terms. On the other hand, the high cycle region could be used to study the existence of a random endurance limit as compared to a sinusoidal endurance limit. This high cycle random fatigue study would be of interest to engineers working with high frequency mechanisms (e.g. MEMS) or structures that require very long service lives. Further basic research into the change in the random response as the test item nears failure would be of interest to those working in the area of structural safety monitoring. Perhaps a change in the response probability density function might be an indicator of the onset of failure.

An extension of these basic linear random fatigue experiments would be to add tensile and compressive stresses. Tensile mean stresses are known to reduce fatigue life while compressive stresses have been shown to increase life in metallic materials. Controlled

experiments with various magnitudes of positive and negative mean stress would help to validate the extension of sinusoidal mean stress equations for random fatigue. This research could be applied to a range on engineering problems, notably civil engineering applications that have preload due to gravity or pre-stress (e.g. pre-stressed concrete structures, subjected to random wave loads). The random mean stress fatigue problem is also a concern in aerospace applications where thermal loads can cause expansion or contraction resulting in significant mean stresses.

Multimode linear random fatigue tests would be another logical extension of the baseline linear narrowband fatigue tests. Further validation of rainflow cycle methods for random fatigue would be useful. A combined investigation that also included validated mean stress random fatigue models would be ideal.

Ultimately, combining basic linear random fatigue testing with nonlinear random fatigue testing would allow validation of the theories developed herein. Flat beam or plate fatigue tests, like the clamped-clamped beam experiments at WPAFB, could be run long enough to induce fatigue failure. Careful control of the test fixture and environment should be used to limit (or enhance) the effects of thermally induced preload. An alternate configuration with curved geometry would be useful for studying the stress softening response case where times to failure are expected to be less than predicted by linear theory. The curvature experiments may be less sensitive to thermal effects which would cause change in geometry but not significant change in preload.

All of these experimental tests could benefit from careful specimen design, additional instrumentation and large sample sizes. Adding holes or reduced section areas can yield higher strains and stresses that should allow fatigue failure at reasonable test durations and input levels. These stress concentrations could be strategically placed to study single and multimode fatigue response. Strain gage instrumentation around these high stress locations would be useful for further numerical post processing. Additional displacement and acceleration transducers would assist correlation of the time and frequency domain analysis of the test results. Temperature sensors for tests with nonlinear structures would help identify possible temperature induced loads. Simple sample designs that could be inexpensively fabricated would allow affordable tests of larger sample sizes. A common design that could be used for linear, mean stress, multi

mode and nonlinear test variations would help the researchers focus on the basic physics of the problem.

6.2.2 Theoretical research

Continued theoretical work in the area of linear and nonlinear random structural response is recommended. Ideally this theoretical research could be combined with experimental data to further the understanding of the physical problem.

Further research into the link between multi degree of freedom linear frequency domain response models (i.e. modal or frequency response function models) and the two-dimensional rainflow matrix would help validate the empirical models that have been developed to date. A rainflow model based on the physics of a linear structure and the nature of the random load would be a great advance.

This thesis concentrated on simple one-dimensional probability functions of displacement and strain. An interesting extension of this was the nonlinear PDF transformation of nonlinear displacement to nonlinear strain. The resulting total strain distributions were best shown as skewed results on a rainflow matrix. More complicated two-dimensional nonlinear PDF transforms of multi degree of freedom rainflow matrices could be an important extension of the methods presented herein.

Nonlinear reduced order "modal" domain analysis methods are being developed to help reduce the computationally expensive cost of analyzing practical engineering structures. Further research with the reverse path nonlinear frequency domain identification methods may help scientists develop more accurate nonlinear modal models. Although the "three path" linear, square and cubic reverse path method used in this thesis was successful, other nonlinear basis functions may have more physical meaning. The nonlinear models of force to displacement to strain developed in this thesis are a logical starting point for continued nonlinear modal research. The nonlinear frequency domain displacement to strain relationships are particularly novel and may help with the development of improved nonlinear modal models.

The link between PDFs of displacement, velocity and acceleration for nonlinear response may also help with nonlinear vibration analysis techniques. This study

demonstrated that the change in the displacement and acceleration PDFs were related; as the system became more nonlinear, the displacement PDF became skewed such that the kurtosis became less than 3, whilst the acceleration PDF was skewed in an opposite fashion such that the kurtosis became greater than 3. A through understanding of this interaction may be helpful for a reverse path simulation using Fourier transforms of simulated time domain responses.

6.3 Closing remarks

Overall there is still much to be done, but it is believed that the work presented is a significant step in improving the understanding and development of techniques suitable for the fatigue and random response analysis of structures in their nonlinear response regime.

REFERENCES

1 Timoshenko, S. P. and Young, D. H., *Vibration Problems in Engineering*, 3rd ed. D. Van Nostrand, Princeton, NJ, 1955.

2 Duffing, G., Erzwungene Schwingungen bei veränderlicher Eigenfrequenz und ihre technisch Bedeutung. *Sammlung Vieweg Heft 41/42, Vieweg, Braunschweig*, 1918.

3 Timoshenko, S. P. and Woinowsky-Krieger, S., *Theory of Plates and Shells*, 2nd ed. McGraw-Hill, New York, NY, 1959.

4 Lin, Y. K., *Probabilistic Theory of Structural Dynamics*. McGraw-Hill, New York, 1967.

5 Bennouna, M. M. and White, R. G., Effects of large vibration amplitudes on the fundamental mode shape of a clamped-clamped uniform beam. *Journal of Sound and Vibration*, vol. 96, pp. 309-331, 1984.

6 Benamar, R., Bennouna, M. M. K., and White, R. G., Effects of large vibration amplitudes on the mode shapes and natural frequencies of thin elastic structures Part I. Simply supported and clamped-clamped beams. *Journal of Sound and Vibration*, vol. 149, pp. 179-195, 1991.

7 Gordon, R. W., Hollkamp, J. J., and Spottswood, S. M., Nonlinear response of a clamped-clamped beam to random base excitation, *Eighth International Conference on Recent Advances in Structural Dynamics*, Southampton, UK, 2003.

8 Ribeiro, P., Second harmonic and the validity of Duffing's equation for vibration of beams with large displacements. *Computers and Structures*, vol. 79, pp. 107-117, 2001.

9 Ribeiro, P. and Manoach, E., The effect of temperature on the large amplitude vibrations of curved beams. *Journal of Sound and Vibration*, vol. 285, pp. 1093-1107, 2005.

10 Marur, S. R., Advances in nonlinear vibration analysis of structures. Part I. Beams. *Sadhana*, vol. 26, pp. 243-249, 2001.

11 Przekop, A., Azzouz, M. S., Guo, X., Mei, C., and Azrar, L., Multimode large amplitude free vibration of shallow shells considering inplane inertia, *AIAA/ ASME/ ASCE/ AHS/ ASC Structures, Structural Dynamics and Materials Conference*, 2003.

12 Przekop, A., Guo, X., Azzouz, M. S., and Mei, C., Reinvestigation of nonlinear random response of shallow shells using finite element modal formulation, *AIAA/ ASME/ ASCE/ AHS/ ASC Structures, Structural Dynamics and Materials Conference*, 2004.

13 van der Pol, B., A theory of the amplitude of free and forced triode vibrations. *Radio Review*, vol. 1, pp. 701–710, 754–762, 1920.

14 Guckenheimer, J., Hoffman, K., and Weckesser, W., The forced van der Pol equation I: The slow flow and its bifurcations. *SIAM Journal on Applied Dynamical Systems*, vol. 2, 2003.

15 Bold, K., Edwards, C., Hoffman, K., Guckenheimer, J., Oliva, R., Guharay, S., Hubbard, J., and Weckesser, W., The forced van der Pol equation II: Canards in the reduced system. *SIAM Journal on Applied Dynamical Systems*, vol. 2, pp. 570-608, 2003.

16 Lin, Y. K., Probability distributions of stress peaks in linear and nonlinear structures. *AIAA JOURNAL*, vol. 1, pp. 1133-1138, 1963.

17 BS-7544:1991, Method for graphical presentation of the complex modulus of damping materials, in *Damping materials — Graphical presentation of the complex modulus*, ISO-10112:1991, Ed. London, UK: British Standards Institution, pp. 14, 1991.

18 Gurley, K. R., Kareem, A., and Tognarelli, M. A., Simulation of a class of non-normal random processes. *International Journal of Non-Linear Mechanics*, vol. 31, pp. 601-617, 1996.

19 Fitzwater, L. M. and Winterstein, S. R., Predicting design wind turbine loads from limited data: Comparing random process and random peak models. *Journal of Solar Energy Engineering*, vol. 123, pp. 364-371, 2001.

20 Rychlik, I., Johannesson, P., and Leadbetter, M. R., Modelling and statistical analysis of ocean-wave data using transformed Gaussian processes. *Marine Structures*, vol. 10, pp. 13-44, 1997.

21 Naess, A. and Pisano, A. A., Frequency domain analysis of dynamic response of drag dominated offshore structures. *Applied Ocean Research*, vol. 19, pp. 251-262, 1997.

22 Lindgren, G., Wave analysis by Slepian models. *Probabilistic Engineering Mechanics*, vol. 15, pp. 49-57, 2000.

23 Podgórski, K., Rychlik, I., and Machado, U., Exact distributions for apparent waves in irregular seas. *Ocean Engineering*, vol. 27, pp. 979-1016, 2000.

24 Machado, U. B. and Rychlik, I., Wave statistics in nonlinear random sea 2002:15, Centre for Mathematical Sciences, Lund University, Lund, SE, 2002.

25 Elfouhaily, T., Joelson, M., Guignard, S., Branger, H., Thompson, D. R., Chapron, B., and Vandemark, D., Analysis of random nonlinear water waves: The Stokes - Woodward technique. *Comptes Rendus - Mecanique*, vol. 331, pp. 189-196, 2003.

26 Machado, U. B., Probability density functions for non-linear random waves and responses. *Ocean Engineering*, vol. 30, pp. 1027-1050, 2003.

27 Zheng, X. Y. and Liaw, C. Y., Non-linear frequency-domain analysis of jack-up platforms. *International Journal of Non-Linear Mechanics*, vol. 39, pp. 1519-1534, 2004.

28 Steinwolf, A. and Rizzi, S. A., Non-Gaussian PDF modeling of turbulent boundary layer fluctuating pressure excitation, *Eighth International Conference on Recent Advances in Structural Dynamics*, Southampton, UK, 2003.

29 Ahn, B. K., Graham, W. R., and Rizzi, S. A., Modelling unsteady wall pressures beneath turbulent boundary layers, *10th AIAA / CEAS Aeroacoustics Conference*, 2004.

30 Varvani-Farahani, A. and Alighanbari, H., Material cyclic behaviour of panels at supersonic speeds. *Journal of Materials Processing Technology*, vol. 152, pp. 84-90, 2004.

31 Radu, A. G., Yang, B., Kim, K., and Mignolet, M. P., Prediction of the dynamic response and fatigue life of panels subjected to thermo-acoustic loading, *AIAA/ ASME/ ASCE/ AHS/ ASC Structures, Structural Dynamics and Materials Conference*, 2004.

32 Rizzi, S. A. and Przekop, A., The effect of basis selection on thermal-acoustic random response prediction using nonlinear modal simulation, *AIAA/ ASME/ ASCE/ AHS/ ASC Structures, Structural Dynamics and Materials Conference*, 2004.

33 Tovo, R., On the fatigue reliability evaluation of structural components under service loading. *International Journal of Fatigue*, vol. 23, pp. 587-598, 2001.

34 Benasciutti, D. and Tovo, R., Cycle distribution and fatigue damage assessment in broad-band non-Gaussian random processes. *Probabilistic Engineering Mechanics*, vol. 20, pp. 115-127, 2005.

35 Steinwolf, A. and Ibrahim, R. A., Numerical and experimental studies of linear systems subjected to non-Gaussian random excitations. *Probabilistic Engineering Mechanics*, vol. 14, pp. 289-299, 1999.

36 Steinwolf, A., Ferguson, N. S., and White, R. G., Variations in steepness of the probability density function of beam random vibration. *European Journal of Mechanics And Solids*, vol. 19, pp. 319-341, 2000.

37 Wu, C. and Cai, G. Q., Effects of excitation probability distribution on system responses. *International Journal of Non-Linear Mechanics*, vol. 39, pp. 1463-1472, 2004.

38 Smallwood, D. O., Generation of partially coherent stationary time histories with non-Gaussian distributions, *67th Shock and Vibration Symposium*, 1996.

39 Smallwood, D. O., Generation of time histories with a specified auto spectral density, skewness, and kurtosis. *Proceedings of the Institute of Environmental Sciences - IES*, pp. 304-309, 1996.

40 Smallwood, D. O., Generation of time histories with a specified auto spectral density and probability density function SAND-96-1385C, Sandia National Laboratories, 1996.

41 Steinwolf, A., Approximation and simulation of probability distributions with a variable kurtosis value. *Computational Statistics and Data Analysis*, vol. 21, pp. 163-180, 1996.

42 Smallwood, D. O., Generation of stationary non-Gaussian time histories with a specified cross-spectral density. *Shock and Vibration*, vol. 4, pp. 361-377, 1997.

43 Kelvin, On graphic solution of dynamical problems. *Philos. Mag.*, vol. 34, 1892.

44 Hamel, G., Ueber erzwungene Schingungen bei endlischen Amplituden. *Math. Ann.*, vol. 86, pp. 1-13, 1922.

45 Mawhin, J., Seventy-five years of global analysis around the forced pendulum equation, *Conference on Differential Equations and Their Applications - EQUADIFF 9*, Masaryk University, Brno, CZ, 1997.

46 Cai, G. Q. and Lin, Y. K., Exact and approximate solutions for randomly excited MDOF non-linear systems. *International Journal of Non-Linear Mechanics*, vol. 31, pp. 647-655, 1996.

47 Cai, G. Q. and Lin, Y. K., Response spectral densities of strongly nonlinear systems under random excitation. *Probabilistic Engineering Mechanics*, vol. 12, pp. 41-47, 1997.

48 Cai, G. Q. and Lin, Y. K., Random vibration of strongly nonlinear systems. *Nonlinear Dynamics*, vol. 24, pp. 3-15, 2001.

49 El Kadiri, M., Benamar, R., and White, R. G., Improvement of the semi-analytical method, for determining the geometrically non-linear response of thin straight structures. Part I: Application to clamped-clamped and simply supported-clamped beams. *Journal of Sound and Vibration*, vol. 249, pp. 263-305, 2002.

50 El Bikri, K., Benamar, R., and Bennouna, M., Geometrically non-linear free vibrations of clamped simply supported rectangular plates. Part I: The effects of large vibration amplitudes on the fundamental mode shape. *Computers and Structures*, vol. 81, pp. 2029-2043, 2003.

51 El Bikri, K., Benamar, R., and Bennouna, M., The effect of large vibration amplitudes on the mode shapes and natural frequencies of isotropic CCSSSS rectangular plates, *Eighth International Conference on Recent Advances in Structural Dynamics*, Southampton, UK, 2003.

52 To, C. W. S., Stabilization of two-degrees-of-freedom nonlinear random systems by the statistical nonlinearization technique, *Eighth International Conference on Recent Advances in Structural Dynamics*, Southampton, UK, 2003.

53 Cai, G. Q., Non-linear systems of multiple degrees of freedom under both additive and multiplicative random excitations. *Journal of Sound and Vibration*, vol. 278, pp. 889-901, 2004.

54 Cai, G. Q. and Wu, C., Modeling of bounded stochastic processes. *Probabilistic Engineering Mechanics*, vol. 19, pp. 197-203, 2004.

55 To, C. W. S., A statistical nonlinearization technique for multi-degrees of freedom nonlinear systems under white noise excitations. *Journal of Sound and Vibration*, vol. 286, pp. 69-79, 2005.

56 Michaelov, G., Sarkani, S., and Lutes, L. D., Spectral characteristics of nonstationary random processes - A critical review. *Structural Safety*, vol. 21, pp. 223-244, 1999.

57 Michaelov, G., Sarkani, S., and Lutes, L. D., Spectral characteristics of nonstationary random processes - Response of a simple oscillator. *Structural Safety*, vol. 21, pp. 245-267, 1999.

58 Michaelov, G., Lutes, L. D., and Sarkani, S., Extreme value of response to nonstationary excitation. *Journal of Engineering Mechanics*, vol. 127, pp. 352-363, 2001.

59 Naess, A., Chaos and nonlinear stochastic dynamics. *Probabilistic Engineering Mechanics*, vol. 15, pp. 37-47, 2000.

60 Lucor, D. and Karniadakis, G. E., Adaptive generalized polynomial chaos for nonlinear random oscillators. *SIAM Journal of Scientific Computing*, vol. 26, pp. 720-735, 2005.

61 Rice, S. O., Mathematical analysis of random noise. *Bell Syst. Tech. J.*, vol. 23, pp. 282-332, 1944.

62 Crandall, S. H., Zero Crossings, Peaks, and Other Statistical Measures of Random Responses. *Journal of the Acoustical Society of America*, vol. 35, pp. 1693-1699, 1963.

63 Lyon, R. H., On the vibration statistics of randomly excited hard-spring oscillator. *Journal of the Acoustical Society of America*, vol. 32, pp. 716-719, 1960.

64 Lyon, R. H., On the vibration statistics of randomly excited hard-spring oscillator, II. *Journal of the Acoustical Society of America*, vol. 33, pp. 1395-1403, 1961.

65 Caughey, T. K., Derivation and application of the Fokker-Planck equation to discrete nonlinear dynamic systems subjected to white noise random excitation. *Journal of the Acoustical Society of America*, vol. 35, pp. 1683-1692, 1963.

66 Roberts, J. B., First passage time for oscillators with non-linear restoring forces. *Journal of Sound and Vibration*, vol. 56, pp. 71-86, 1978.

67 Leadbetter, M. R., On high level exceedance modeling and tail inference. *Journal of Statistical Planning and Inference*, vol. 45, pp. 247-260, 1995.

68 Winterstein, S. R. and Torhaug, R., Extreme jack-up response: Simulation and nonlinear analysis methods. *Journal of Offshore Mechanics and Arctic Engineering*, vol. 118, pp. 103-108, 1996.

69 Er, G. K., Crossing rate analysis with a non-Gaussian closure method for nonlinear stochastic systems. *Nonlinear Dynamics*, vol. 14, pp. 279-291, 1997.

70 Nakamoto, M., Minamihara, H., and Ohta, M., Evaluation on the peak value distribution using level crossings for non-Gaussian-type random signals with wide frequency band. *Electronics and Communications in Japan, Part III: Fundamental Electronic Science (English translation of Denshi Tsushin Gakkai Ronbunshi)*, vol. 83, pp. 20-31, 2000.

71 Naess, A., Crossing rate statistics of quadratic transformations of Gaussian processes. *Probabilistic Engineering Mechanics*, vol. 16, pp. 209-217, 2001.

72 Pandey, M. D., Extreme quantile estimation using order statistics with minimum cross-entropy principle. *Probabilistic Engineering Mechanics*, vol. 16, pp. 31-42, 2001.

73 Leadbetter, M. R. and Spaniolo, G. V., On statistics at level crossings by a stationary process. *Statistica Neerlandica*, vol. 56, pp. 152-164, 2002.

74 Winterstein, S. R., Nonlinear vibration models for extremes and fatigue. *Journal of Engineering Mechanics*, vol. 114, pp. 1772-1790, 1988.

75 Winterstein, S. R. and Lange, C. H., Moment-based probability models for wind engineering applications, *ASCE Engineering Mechanics Conference*, 1995.

76 Winterstein, S. R. and Kashef, T., Moment-based load and response models with wind engineering applications. *Journal of Solar Energy Engineering*, vol. 122, pp. 122-128, 2000.

77 Ochi, M. K. and Ahn, K., Probability distribution applicable to non-Gaussian random processes. *Probabilistic Engineering Mechanics*, vol. 9, pp. 255-264, 1994.

78 Mohr, G. and Ditlevsen, O., Partial summations of stationary sequences of non-Gaussian random variables. *Probabilistic Engineering Mechanics*, vol. 11, pp. 25-30, 1996.

79 Ochi, M. K., Probability distributions of peaks and troughs of non-Gaussian random processes. *Probabilistic Engineering Mechanics*, vol. 13, pp. 291-298, 1998.

80 Mohr, G., Higher moments of weighted integrals of non-Gaussian fields. *Probabilistic Engineering Mechanics*, vol. 14, pp. 137-140, 1999.

81 Er, G. K., An Improved Closure Method for Analysis of Nonlinear Stochastic Systems. *Nonlinear Dynamics*, vol. 17, pp. 285-297, 1998.

82 Er, G. K., A consistent method for the solution to reduced FPK equation in statistical mechanics. *Physica A: Statistical Mechanics and its Applications*, vol. 262, pp. 118-128, 1999.

83 Er, G. K., Exponential closure method for some randomly excited non-linear systems. *International Journal of Non-Linear Mechanics*, vol. 35, pp. 69-78, 2000.

84 Caughey, T. K., Response of a nonlinear string to random loading. *Journal of Applied Mechanics*, vol. 26, pp. 341-344, 1959.

85 Caughey, T. K., Response of van der Pol oscillator to random excitation. *Journal of Applied Mechanics*, vol. 26, pp. 345-348, 1959.

86 Caughey, T. K., Equivalent linearization techniques. *Journal of the Acoustical Society of America*, vol. 35, pp. 1706-1711, 1963.

87 Pradlwarter, H. J., Schuëller, G. I., and Chen, X. W., Consideration of non-Gaussian response properties by use of stochastic equivalent linearization, *Third International Conference on Recent Advances in Structural Dynamics*, Southampton, UK, 1988.

88 Muravyov, A. A., Turner, T. L., Robinson, J. H., and Rizzi, S. A., New stochastic equivalent linearization implementation for prediction of geometrically nonlinear vibrations, *AIAA / ASME / ASCE / AHS / ASC Structures, Structural Dynamics and Materials Conference*, 1999.

89 Rizzi, S. A. and Muravyov, A., Comparison of nonlinear random response using equivalent linearization and numerical simulation, *Seventh International Conference on Recent Advances In Structural Dynamics*, Southampton, UK, 2000.

90 Rizzi, S. A. and Muravyov, A. A., Equivalent linearization of geometrically nonlinear random vibrations using commercial finite element codes NASA/TP-2002-211761, 2002-07-01, 2002.

91 Muravyov, A. A. and Rizzi, S. A., Determination of nonlinear stiffness with application to random vibration of geometrically nonlinear structures. *Computers and Structures*, vol. 81, pp. 1513-1523, 2003.

92 Proppe, C., Pradlwarter, H. J., and Schuëller, G. I., Equivalent linearization and Monte Carlo simulation in stochastic dynamics. *Probabilistic Engineering Mechanics*, vol. 18, pp. 1-15, 2003.

93 Rizzi, S. A., On the use of equivalent linearization for high-cycle fatigue analysis of geometrically nonlinear structures, *Eighth International Conference on Recent Advances in Structural Dynamics*, Southampton, UK, 2003.

94 Crandall, S. H., On using non-Gaussian distributions to perform statistical linearization. *International Journal of Non-Linear Mechanics*, vol. 39, pp. 1395-1406, 2004.

95 Naess, A., Prediction of extreme response of nonlinear structures by extended stochastic linearization. *Probabilistic Engineering Mechanics*, vol. 10, pp. 153-160, 1995.

96 Polidori, D. C. and Beck, J. L., Approximate solutions for non-linear random vibration problems. *Probabilistic Engineering Mechanics*, vol. 11, pp. 179-185, 1996.

97 Polidori, D. C., Beck, J. L., and Papadimitriou, C., New stationary PDF approximation for non-linear oscillators. *International Journal of Non-Linear Mechanics*, vol. 35, pp. 657-673, 2000.

98 Elishakoff, I. and Colajanni, P., Stochastic linearization critically re-examined. *Chaos, Solitons and Fractals*, vol. 8, pp. 1957-1972, 1997.

99 Crandall, S. H., Is stochastic equivalent linearization a subtly flawed procedure? *Probabilistic Engineering Mechanics*, vol. 16, pp. 169-176, 2001.

100 Papadimitriou, C. and Lutes, L. D., Stochastic cumulant analysis of MDOF systems with polynomial-type nonlinearities. *Probabilistic Engineering Mechanics*, vol. 11, pp. 1-13, 1996.

101 Lutes, L. D. and Papadimitriou, C., Direct derivation of response moment and cumulant equations for non-linear stochastic problems. *International Journal of Non-Linear Mechanics*, vol. 35, pp. 817-835, 2000.

102 Miles, R. N., An approximate solution for the spectral response of Duffing's oscillator with random input. *Journal of Sound and Vibration*, vol. 132, pp. 43-49, 1989.

103 Miles, R. N., Spectral response of a bilinear oscillator. *Journal of Sound and Vibration*, vol. 163, pp. 319-326, 1993.

104 Soize, C., Stochastic linearization method with random parameters for SDOF nonlinear dynamical systems: prediction and identification procedures. *Probabilistic Engineering Mechanics*, vol. 10, pp. 143-152, 1995.

105 Soize, C., Nonparametric model of random uncertainties for reduced matrix models in structural dynamics. *Probabilistic Engineering Mechanics*, vol. 15, pp. 277-294, 2000.

106 Bellizzi, S. and Bouc, R., Spectral response of asymmetrical random oscillators. *Probabilistic Engineering Mechanics*, vol. 11, pp. 51-59, 1996.

107 Bellizzi, S. and Bouc, R., Analysis of multi-degree of freedom strongly non-linear mechanical systems with random input. Part I: non-linear modes and stochastic averaging. *Probabilistic Engineering Mechanics*, vol. 14, pp. 229-244, 1999.

108 Bellizzi, S. and Bouc, R., Analysis of multi-degree of freedom strongly non-linear mechanical systems with random input. Part II: equivalent linear system with random matrices and power spectral density matrix. *Probabilistic Engineering Mechanics*, vol. 14, pp. 245-256, 1999.

109 McEwan, M. I., Wright, J. R., Cooper, J. E., and Leung, A. Y. T., A combined modal/finite element analysis technique for the dynamic response of a non-linear beam to harmonic excitation. *Journal of Sound and Vibration*, vol. 243, pp. 601-624, 2001.

110 Hollkamp, J. J., Gordon, R. W., and Spottswood, S. M., Nonlinear sonic fatigue response prediction from finite element modal models: A comparison with experiments, *AIAA/ ASME/ ASCE/ AHS/ ASC Structures, Structural Dynamics and Materials Conference*, 2003.

111 Mignolet, M. P. and Radu, A. G., Validation of reduced order modeling for the prediction of the response and fatigue life of panels subjected to thermo-acoustic effects, *Eighth International Conference on Recent Advances in Structural Dynamics*, 2003.

112 Przekop, A. and Rizzi, S. A., Reduced order methods for prediction of thermal-acoustic fatigue, *7th International Conference on Computational Structures Technology*, 2004.

113 Hollkamp, J. J., Gordon, R. W., and Spottswood, S. M., Nonlinear modal models for sonic fatigue response prediction: a comparison of methods. *Journal of Sound and Vibration*, vol. 284, pp. 1145-1163, 2005.

114 Rizzi, S. A. and Przekop, A., The effect of basis selection on static and random acoustic response prediction using a nonlinear modal simulation NASA/TP-2005-213943, 2005-12-01, 2005.

115 Moon, B., Lee, C. T., Kang, B. S., and Kim, B. S., Statistical random response analysis and reliability design of structure system with non-linearity. *Mechanical Systems and Signal Processing*, vol. 19, pp. 1135-1151, 2005.

116 Middleton, D., *An Introduction to Statistical Communication Theory*. IEEE Press, Piscataway, NJ USA, 1996.

117 Davenport, W. B. and Root, W. L., *An Introduction to the Theory of Random Signals and Noise*. Wiley-IEEE Press, New York, 1987.

118 Adams, D. E. and Allemang, R. J., Survey of nonlinear detection and identification techniques for experimental vibrations, *International Conference on Noise and Vibration Engineering - ISMA*, Leuven, BE, 1998.

119 Adams, D. E. and Allemang, R. J., Characterization of nonlinear vibrating systems using internal feedback and frequency response modulation. *Journal of Vibration and Acoustics*, vol. 121, pp. 495-500, 1999.

120 Adams, D. E. and Allemang, R. J., Demonstration of multiple degree of freedom nonlinear system identification using time and frequency domain methods, *International Modal Analysis Conference - IMAC*, 1999.

121 Adams, D. E. and Allemang, R. J., A new derivation of the frequency response function matrix for vibrating non-linear systems. *Journal of Sound and Vibration*, vol. 227, pp. 1083-1108, 1999.

122 Adams, D. E. and Allemang, R. J., Spatial method of characterizing nonlinearities in multiple degree of freedom vibrating systems, *the International Modal Analysis Conference - IMAC*, 1999.

123 Adams, D. E. and Allemang, R. J., New spatial MDOF characterization and identification techniques for nonlinear systems, *the International Modal Analysis Conference - IMAC*, 2000.

124 Adams, D. E. and Allemang, R. J., Subtleties in experimental nonlinear structural dynamics, *Conference on Nonlinear Vibration, Stability, and Structural Dynamics*, 2000.

125 Bendat, J. S., *Nonlinear Systems Techniques and Applications*. John Wiley & Sons, New York, NY, 1998.

126 Richards, C. M. and Singh, R., Identification of multi-degree-of-freedom non-linear systems under random excitations by the "reverse path" spectral method. *Journal of Sound and Vibration*, vol. 213, pp. 673-707, 1998.

127 Richards, C. M. and Singh, R., Feasibility of identifying non-linear vibratory systems consisting of unknown polynomial forms. *Journal of Sound and Vibration*, vol. 220, pp. 413-450, 1999.

128 Richards, C. M. and Singh, R., Comparison of two non-linear system identification approaches derived from `reverse path' spectral analysis. *Journal of Sound and Vibration*, vol. 237, pp. 361-376, 2000.

129 Kerschen, G., Golinval, J. C., and Worden, K., Theoretical and experimental identification of a non-linear beam. *Journal of Sound and Vibration*, vol. 244, pp. 597-613, 2001.

130 Lenaerts, V., Kerschen, G., and Golinval, J. C., Identification of a continuous structure with a geometrical non-linearity. Part II: Proper orthogonal decomposition. *Journal of Sound and Vibration*, vol. 262, pp. 907-919, 2003.

131 Kerschen, G., Lenaerts, V., and Golinval, J. C., Identification of a continuous structure with a geometrical non-linearity. Part I: Conditioned reverse path method. *Journal of Sound and Vibration*, vol. 262, pp. 889-906, 2003.

132 Benini, G., Cooper, J. E., and Wright, J. R., Quantification of aircraft non-linearities from flight flutter test data, *the International Conference on Noise and Vibration Engineering - ISMA*, Leuven, BE, 2004.

133 Cauberghe, B., Guillaume, P., and Verboven, P., Frequency Response Functions based Parameter Identification from short data sequences, *Eighth International Conference on Recent Advances in Structural Dynamics*, Southampton, UK, 2003.

134 Cauberghe, B., Guillaume, P., Verboven, P., and Parloo, E., Identification of modal parameters including unmeasured forces and transient effects. *Journal of Sound and Vibration*, vol. 265, pp. 609-625, 2003.

135 Fasana, A., Garibaldi, L., and Marchesiello, S., Performances analysis of frequency domain nonlinear identification techniques, *International Conference on Noise and Vibration Engineering - ISMA*, Leuven, BE, 2004.

136 Vazquez Feijoo, J. A., Worden, K., and Stanway, R., System identification using associated linear equations. *Mechanical Systems and Signal Processing*, vol. 18, pp. 431-455, 2004.

137 Gloth, G. and Göge, D., Handling of non-linear structural characteristics in ground vibration testing, *the International Conference on Noise and Vibration Engineering - ISMA*, Leuven, BE, 2004.

138 Pacheco, R. P. and Steffen Jr, V., On the identification of non-linear mechanical systems using orthogonal functions. *International Journal of Non-Linear Mechanics*, vol. 39, pp. 1147-1159, 2004.

139 Platten, M. F., Wright, J. R., and Cooper, J. E., Identification of a continuous structure with discrete non-linear components using an extended modal model, *International Conference on Noise and Vibration Engineering - ISMA*, Leuven, BE, 2004.

140 Haroon, M., Adams, D. E., Luk, Y. W., and Ferri, A. A., A time and frequency domain approach for identifying nonlinear mechanical system models in the absence of an input measurement. *Journal of Sound and Vibration*, vol. 283, pp. 1137-1155, 2005.

141 Peifer, M., Timmer, J., and Voss, H. U., Non-parametric identification of non-linear oscillating systems. *Journal of Sound and Vibration*, vol. 267, pp. 1157-1167, 2003.

142 Rüdinger, F. and Krenk, S., Identification of nonlinear oscillator with parametric white noise excitation. *Nonlinear Dynamics*, vol. 36, pp. 379-403, 2004.

143 Bendat, J. S. and Piersol, A. G., *Engineering applications of correlation and spectral analysis*, 2nd ed. John Wiley & Sons, New York, NY, 1993.

144 Wöhler, A., Test to determine the forces acting on railway carriage axels and capacity of resistence of the axle. *Engineering*, vol. 11, pp. 199, 1871.

145 Basquin, O. H., The exponential law of endurance tests. *Proceedings of the ASTM*, vol. 10, pp. 625-630, 1910.

146 Goodman, J., Mechanics Applied to Engineering. London, UK, Longmans, Green and Co., pp. 631-636, 1919.

147 Dowling, N. E., Mean stress effects in stress-life and strain-life fatigue, *Fatigue 2004: Second SAE Brasil International Conference on Fatigue*, São Paulo, BR, 2004.

148 Fatemi, A., Plaseied, A., Khosrovaneh, A. K., and Tanner, D., Application of bi-linear log-log S-N model to strain-controlled fatigue data of aluminum alloys and its effect on life predictions. *International Journal of Fatigue*, vol. 27, pp. 1040-1050, 2005.

149 Kihl, D. P. and Sarkani, S., Mean stress effects in fatigue of welded steel joints. *Probabilistic Engineering Mechanics*, vol. 14, pp. 97-104, 1999.

150 Kim, W. D., Lee, H. J., Kim, J. Y., and Koh, S. K., Fatigue life estimation of an engine rubber mount. *International Journal of Fatigue*, vol. 26, pp. 553-560, 2004.

151 Palmgren, A. Z., Die Lebensdauer von Kugellagern. *Zeitschriyt des Vereines der Deutschen Ingenioeren*, vol. 68, pp. 339-341, 1924.

152 Miner, M. A., Cumulative damage in fatigue. *Journal of Applied Mechanics*, vol. 12, 1945.

153 Miles, J. W., On structural fatigue under random loading. *Journal of the Aeronautical Sciences*, vol. 21, pp. 753-762, 1954.

154 Newland, D. E., *An introduction to random vibrations and spectral analysis*. Longman Group Limited, London, UK, 1975.

155 Lalanne, C., *Fatigue Damage - Mechanical Vibration and Shock Series*, Vol IV, Hermes Sci Publ, Paris. Distributed in USA by Taylor & Francis Publ, New York, NY. 2002.

156 Lambert, R. G., Analysis of fatigue under random vibration. *The Shock and Vibration Bulletin*, pp. 55-71, 1976.

157 Lambert, R. G., Fatigue life prediction for various random stress peak distributions. *The Shock and Vibration Bulletin*, pp. 1-10, 1982.

158 Sarkani, S., Kihl, D. P., and Beach, J. E., Fatigue of welded joints under narrowband non-Gaussian loadings. *Probabilistic Engineering Mechanics*, vol. 9, pp. 179-190, 1994.

159 Lambert, R. G., Fatigue and time-compression methodologies for power-law non-linear systems, *Annual Technical Meeting - Institute of Environmental Sciences*, 1995.

160 Sweitzer, K. A., Veltri, M., Kerr, S. C., and Bishop, N. W. M., A preliminary application of the PDF transfer function to fatigue calculations for nonlinear systems, *Eighth International Conference on Recent Advances in Structural Dynamics*, Southampton, UK, 2003.

161 Matsuishi, M. and Endo, T., Fatigue of metals subjected to varying stress. *Japan Society of Mechanical Engineers*, 1968.

162 Dowling, N. E., Fatigue failure predictions for complicated stress-strain histories. *Journal of Materials*, vol. 7, pp. 71-87, 1972.

163 Rychlik, I., A new definition of the rainflow cycle counting method. *International Journal of Fatigue*, vol. 9, pp. 119-121, 1987.

164 Lindgren, G. and Rychlik, I., Rain Flow Cycle Distributions for Fatigue Life Prediction under Gaussian Load Processes. *Fatigue & Fracture of Engineering Materials & Structures*, vol. 10, pp. 251-260, 1987.

165 Rychlik, I., Extremes, rainflow cycles and damage functionals in continuous random processes. *Stochastic Processes and Their Applications*, vol. 63, pp. 97-116, 1996.

166 Bishop, N. W. M., *The use of frequency domain parameters to predict structural fatigue*. Ph.D. thesis, University of Warwick, UK, 1988.

167 Bishop, N. W. M. and Sherratt, F., Theoretical solution for the estimation of 'rainflow' ranges from power spectral density data. *Fatigue and Fracture of Engineering Materials and Structures*, vol. 13, pp. 311-326, 1990.

168 Lambert, R. G., Fatigue analysis of multi-degree-of-freedom systems under random vibration. *The Shock and Vibration Bulletin*, 1977.

169 Wolfe, H. F. and White, R. G., The development and evaluation of a new multimodal acoustic fatigue damage model, *International Conference on Recent Advances in Structural Dynamics*, Southampton, UK, 1997.

170 Nagode, M. and Fajdiga, M., A general multi-modal probability density function suitable for the rainflow ranges of stationary random processes. *International Journal of Fatigue*, vol. 20, pp. 211-223, 1998.

171 Wolfe, H. F., Wentz, K. R., Camden, M. P., and Simmons, L. W., Development and evaluation of a new multimodal acoustic fatigue damage model: Effects of multimodal frequency, *AIAA/ ASME/ ASCE/ AHS/ ASC Structures, Structural Dynamics and Materials Conference*, 1998.

172 Tovo, R., Damage-based evaluation of probability density distribution for rain-flow ranges from random processes. *International Journal of Fatigue*, vol. 22, pp. 425-429, 2000.

173 Fu, T. T. and Cebon, D., Predicting fatigue lives for bi-modal stress spectral densities. *International Journal of Fatigue*, vol. 22, pp. 11-21, 2000.

174 Dirlik, T., *Application of Computers in Fatigue Analysis*. Ph.D. thesis, University of Warwick, UK, 1985.

175 Bishop, N. W. M. and Sherratt, F., Fatigue life prediction from power spectral density data. *Environmental Engineering*, vol. 2, pp. 11-29, 1989.

176 Petrucci, G. and Zuccarello, B., On the estimation of the fatigue cycle distribution from spectral density data. *Proceedings of the Institution of Mechanical Engineers, Part C: Journal of Mechanical Engineering*, vol. 213, pp. 819-831, 1999.

177 Petrucci, G., Di Paola, M., and Zuccarello, B., On the characterization of dynamic properties of random processes by spectral parameters. *Journal of Applied Mechanics*, vol. 67, pp. 519-526, 2000.

178 Tovo, R., Cycle distribution and fatigue damage under broad-band random loading. *International Journal of Fatigue*, vol. 24, pp. 1137-1147, 2002.

179 Sweitzer, K. A., Bishop, N. W. M., and Genberg, V. L., Efficient computation of spectral moments for determination of random response statistics, *International Conference on Noise and Vibration Engineering - ISMA*, Leuven, BE, 2004.

180 Zhao, W. and Baker, M. J., On the probability density function of rainflow stress range for stationary Gaussian processes. *International Journal of Fatigue*, vol. 14, pp. 121-135, 1992.

181 Bouyssy, V., Naboishikov, S. M., and Rackwitz, R., Comparison of analytical counting methods for Gaussian processes. *Structural Safety*, vol. 12, pp. 35-57, 1993.

182 Braccesi, C., Cianetti, F., Lori, G., and Pioli, D., Fatigue behaviour analysis of mechanical components subject to random bimodal stress process: Frequency domain approach. *International Journal of Fatigue*, vol. 27, pp. 335-345, 2005.

183 Petrucci, G. and Zuccarello, B., Fatigue life prediction under wide band random loading. *Fatigue and Fracture of Engineering Materials and Structures*, vol. 27, pp. 1183-1195, 2004.

184 Benasciutti, D. and Tovo, R., Spectral methods for lifetime prediction under wide-band stationary random processes. *International Journal of Fatigue*, vol. 27, pp. 867-877, 2005.

185 Klemenc, J. and Fajdiga, M., Description of statistical dependencies of parameters of random load states (dependency of random load parameters). *International Journal of Fatigue*, vol. 22, pp. 357-367, 2000.

186 Klemenc, J. and Fajdiga, M., An improvement to the methods for estimating the statistical dependencies of the parameters of random load states. *International Journal of Fatigue*, vol. 26, pp. 141-154, 2004.

187 Klemenc, J. and Fajdiga, M., Prediction of loading spectra under diverse operating conditions by a localised basis function neural network. *International Journal of Fatigue*, vol. 27, pp. 555-568, 2005.

188 Rychlik, I., Lindgren, G., and Lin, Y. K., Markov based correlations of damage cycles in Gaussian and non-Gaussian loads. *Probabilistic Engineering Mechanics*, vol. 10, pp. 103-115, 1995.

189 Sweitzer, K. A. and Ferguson, N. S., Mean Stress Effects on Random Fatigue of Nonlinear Structures, *Twelfth International Congress on Sound and Vibration*, Lisbon, PT, 2005.

190 Olagnon, M., Practical computation of statistical properties of rainflow counts. *Fatigue*, vol. 16, pp. 306-314, 1994.

191 Johannesson, P., Rainflow cycles for switching processes with Markov structure. *Probability in the Engineering and Informational Sciences*, vol. 12, pp. 143-175, 1998.

192 Johannesson, P., On rainflow cycles and the distribution of the number of interval crossings by a Markov chain. *Probabilistic Engineering Mechanics*, vol. 17, pp. 123-130, 2002.

193 Ekberg, A., Random multiaxial fatigue – 13 annotated references 1991-1998 Department of Solid Mechanics, Chalmers University of Technology, Göteborg, SE, 1998.

194 Carpinteri, A., Spagnoli, A., and Vantadori, S., A multiaxial fatigue criterion for random loading. *Fatigue and Fracture of Engineering Materials and Structures*, vol. 26, pp. 515-522, 2003.

195 Pitoiset, X. and Preumont, A., Spectral methods for multiaxial random fatigue analysis of metallic structures. *International Journal of Fatigue*, vol. 22, pp. 541-550, 2000.

196 Pitoiset, X., Rychlik, I., and Preumont, A., Spectral methods to estimate local multiaxial fatigue failure for structures undergoing random vibrations. *Fatigue & Fracture of Engineering Materials & Structures*, vol. 24, pp. 715-727, 2001.

197 Bonte, M. H. A., De Boer, A., and Liebregts, R., Prediction of mechanical fatigue caused by multiple random excitations, *Proceedings of the 2004 International Conference on Noise and Vibration Engineering, ISMA*, 2004.

198 Mixon, J. S. and Roussos, L. A., Acoustic fatigue: Overview of activities at NASA Langley NASA TM-89143, Langley Research Center, Hampton, VA USA, 1987.

199 Clarkson, B. L., Review of sonic fatigue technology NASA CR-4587, April NASA Langley Research Center, Hampton, VA USA, 1994.

200 Bao, W. Z., Estimating and Increasing the Fatigue Lives of Nonlinear Structures under Random Excitations. Ph.D. thesis, SUNY Binghamton, NY USA, 1994.

201 Kihl, D. P., Sarkani, S., and Beach, J. E., Stochastic fatigue damage accumulation under broadband loadings. *International Journal of Fatigue*, vol. 17, pp. 321-329, 1995.

202 Sarkani, S., Michaelov, G., Kihl, D. P., and Beach, J. E., Fatigue of welded steel joints under wideband loadings. *Probabilistic Engineering Mechanics*, vol. 11, pp. 221-227, 1996.

203 Sun, J. Q., Bao, W., and Miles, R. N., Fatigue life prediction of nonlinear plates under random excitations. *Journal of Vibration and Acoustics*, vol. 120, pp. 353-360, 1998.

204 Sun, J. Q., Wang, X., and Bergman, L. A., Fatigue analysis of non-linear structures with von Mises Stress. *Journal of Sound and Vibration*, vol. 245, pp. 947-952, 2001.

205 Blevins, R. D., Non-Gaussian narrow-band random fatigue. *Journal of Applied Mechanics*, vol. 69, pp. 317-324, 2002.

206 Yang, B., Mignolet, M. P., and Spottswood, S. M., Modeling of damage accumulation for Duffing-type systems under severe random excitations. *Probabilistic Engineering Mechanics*, vol. 19, pp. 185-194, 2004.

207 Yu, L., Das, P. K., and Barltrop, N. D. P., A new look at the effect of bandwidth and non-normality on fatigue damage. *Fatigue and Fracture of Engineering Materials and Structures*, vol. 27, pp. 51-58, 2004.

208 Wang, X. and Sun, J. Q., Effect of skewness on fatigue life with mean stress correction. *Journal of Sound and Vibration*, vol. 282, pp. 1231-1237, 2005.

209 Wang, X. and Sun, J. Q., Multi-stage regression fatigue analysis of non-Gaussian stress processes. *Journal of Sound and Vibration*, vol. 280, pp. 455-465, 2005.

210 Newman Jr, J. C., The merging of fatigue and fracture mechanics concepts: A historical perspective. *Progress in Aerospace Sciences*, vol. 34, pp. 347-390, 1998.

211 Doliński, K. and Colombi, P., Fatigue lifetime under stochastic loading with random overloading pulse trains. *Computer Methods in Applied Mechanics and Engineering*, vol. 168, pp. 221-241, 1998.

212 Harter, J. A., Comparison of contemporary FCG life prediction tools. *International Journal of Fatigue*, vol. 21, 1999.

213 Lei, Y. and Zhu, W. Q., Fatigue crack growth in degrading elastic components of nonlinear structural systems under random loading. *International Journal of Solids and Structures*, vol. 37, pp. 649-667, 1999.

214 Shang, D. G. and Yao, W. X., A nonlinear damage cumulative model for uniaxial fatigue. *International Journal of Fatigue*, vol. 21, pp. 187-194, 1999.

215 Ray, A. and Patankar, R., Fatigue crack growth under variable-amplitude loading: Part I - Model formulation in state-space setting. *Applied Mathematical Modelling*, vol. 25, pp. 979-994, 2001.

216 Ray, A. and Patankar, R., Fatigue crack growth under variable-amplitude loading: Part II - Code development and model validation. *Applied Mathematical Modelling*, vol. 25, pp. 995-1013, 2001.

217 Moreno, B., Zapatero, J., and Domínguez, J., An experimental analysis of fatigue crack growth under random loading. *International Journal of Fatigue*, vol. 25, pp. 597-608, 2003.

218 Zapatero, J., Moreno, B., González-Herrera, A., and Domínguez, J., Numerical and experimental analysis of fatigue crack growth under random loading. *International Journal of Fatigue*, vol. 27, pp. 878-890, 2005.

219 Fatemi, A. and Yang, L., Cumulative fatigue damage and life prediction theories: A survey of the state of the art for homogeneous materials. *International Journal of Fatigue*, vol. 20, pp. 9-34, 1998.

220 Halford, G. R., Cumulative fatigue damage modeling - Crack nucleation and early growth. *International Journal of Fatigue*, vol. 19, 1997.

221 Wu, W. F., Liou, H. Y., and Tse, H. C., Estimation of fatigue damage and fatigue life of components under random loading. *International Journal of Pressure Vessels and Piping*, vol. 72, pp. 243-249, 1997.

222 Liou, H. Y., Wu, W. F., and Shin, C. S., Modified model for the estimation of fatigue life derived from random vibration theory. *Probabilistic Engineering Mechanics*, vol. 14, pp. 281-288, 1999.

223 Altus, E., Fatigue, fractals, and a modified miner's rule. *Journal of Applied Mechanics*, vol. 58, pp. 37-42, 1991.

224 Altus, E., Nonlinear differential equation for fatigue damage evolution, using a micromechanical model. *Mechanics of Materials*, vol. 34, pp. 257-266, 2002.

225 Wu, W. F. and Ni, C. C., A study of stochastic fatigue crack growth modeling through experimental data. *Probabilistic Engineering Mechanics*, vol. 18, pp. 107-118, 2003.

226 Košút, J., Quadratic damage rule in random loading case. *Fatigue and Fracture of Engineering Materials and Structures*, vol. 27, pp. 679-700, 2004.

227 Varvani-Farahani, A., Sharma, M., and Kianoush, M. R., Fatigue damage analysis and life assessment under variable amplitude loading conditions. *Materials Science and Engineering A*, vol. 403, pp. 42-47, 2005.

228 Weibull, W., A statistical theory of the strength of materials. *Ingeniörsvetenskapsakademiens*, vol. 151, 1939.

229 Weibull, W., A statistical representation of fatigue failures in solids, *The Royal Institute Of Technology*, Stockholm, SE, 1949.

230 Weibull, W., The probability of failure of a system subjected to the joint effect of cyclic loading and randomly distributed discrete load peaks AFMLTR-77-169, 1977.

231 Lambert, R. G., Fatigue life prediction for simultaneous stress and strength variances under random vibration. *Shock and Vibration Bulletin*, pp. 169-176, 1980.

232 Nagode, M. and Fajdiga, M., On a new method for prediction of the scatter of loading spectra. *International Journal of Fatigue*, vol. 20, pp. 271-277, 1998.

233 Nagode, M., Klemenc, J., and Fajdiga, M., Parametric modelling and scatter prediction of rainflow matrices. *International Journal of Fatigue*, vol. 23, pp. 525-532, 2001.

234 Varvani-Farahani, A., Kianoush, M. R., and Sharma, M., Fatigue failure assessment of engineering components under service loading conditions. *Materials & Design*, vol. In Press, Corrected Proof, 2005.

235 Xiong, J. J. and Shenoi, R. A., A reliability-based data treatment system for actual load history. *Fatigue and Fracture of Engineering Materials and Structures*, vol. 28, pp. 875-889, 2005.

236 Tang, J. and Zhao, J., Practical approach for predicting fatigue reliability under random cyclic loading. *Reliability Engineering and System Safety*, vol. 50, pp. 7-15, 1995.

237 Liao, M., Shi, G., and Xiong, Y., Analytical methodology for predicting fatigue life distribution of fuselage splices. *International Journal of Fatigue*, vol. 23, 2001.

238 Elishakoff, I., Stochasticity and safety factors: Part 1. Random actual stress and deterministic yield stress. *Chaos, Solitons and Fractals*, vol. 23, pp. 321-331, 2005.

239 Schijve, J., Statistical distribution functions and fatigue of structures. *International Journal of Fatigue*, vol. 27, pp. 1031-1039, 2005.

240 Wang, X. and Sun, J. Q., Structural fatigue life prediction with system uncertainties. *Journal of Sound and Vibration*, vol. 257, pp. 977-984, 2002.

241 Wang, X. and Sun, J. Q., Random fatigue of a higher order sandwich beam with parameter uncertainties. *Journal of Sound and Vibration*, vol. 260, pp. 349-356, 2003.

242 Ghiocel, D. M. and Rieger, N. F., Probabilistic high cycle fatigue life prediction for gas turbine engine blades, *AIAA/ ASME/ ASCE/ AHS/ ASC Structures, Structural Dynamics and Materials Conference*, 1999.

243 Ghiocel, D. M., Generalized response surface modeling for stochastic mechanics problems, *5th Annual FAA/ Air Force/ NASA/ Navy Workshop on the Application of Probabilistic Methods to Gas Turbine Engines*, Westlake, OH USA, 2001.

244 Kamiński, M., On probabilistic fatigue models for composite materials. *International Journal of Fatigue*, vol. 24, pp. 477-495, 2002.

245 Ghiocel, D. M., Advances in computational risk predictions for complex, large-size applications, *AIAA/ASME/ASCE/AHS/ASC Structures, Structural Dynamics and Materials Conference*, 2005.

246 Ghiocel, D. M. and Wang, L., Computational advances in reliability assessment of aircraft structures under corrosion-fatigue damage, *AIAA/ASME/ASCE/AHS/ASC Structures, Structural Dynamics and Materials Conference*, 2005.

247 Rice, S. O., Mathematical analysis of random noise, in *Selected Papers on Noise and Stochastic Processes*, Wax, N., Ed., Dover, New York, NY, 1954.

248 Bendat, J. S. and Piersol, A. G., *Random Data: Analysis and Measurement Procedures*, 3rd ed. John Wiley & Sons, New York, NY, 2000.

249 Zwillinger, D., *Standard Mathematical Tables and Formulae*, 30th ed. CRC Press, Boca Raton, FL, USA, 1996.

250 Papoulis, A. and Pillai, S. U., *Probability, Random Variables and Stochastic Processes*, 4th ed. McGraw-Hill, New York, NY, 2002.

251 Matlab documentation, The Mathworks Inc, Natick, MA, USA, 2006.

252 Lutes, L. D., Sarkani, S., Kihl, D. P., and Beach, J. E., Optimal S-N testing for variable-amplitude fatigue applications. *Journal of Structural Engineering*, vol. 129, pp. 829-837, 2003.

253 Lutes, L. D., Sarkani, S., Kihl, D. P., and Beach, J. E., Optimal S/N fatigue testing for stochastic service loads. *Journal of Structural Engineering*, vol. 131, pp. 1611-1619, 2005.

254 Smith, K. N., Watson, P., and Topper, T. H., Stress- strain function for the fatigue of metals. *Journal of Materials*, vol. 5, pp. 767-778, 1970.

255 DOT/FAA/AR-MMPDS-01, Metallic Materials Properties Development and Standardization. Springfield, VA, USA: National Technical Information Service (NTIS), 2003.

256 Przekop, A., Nonlinear response and fatigue estimation of aerospace curved surface panels to acoustic and thermal loads. Ph. D. thesis, Old Dominion University, Norfolk, VA, USA, 2003.

257 Wang, X. Y. and Sun, J. Q., On the fatigue analysis of non-Gaussian stress processes with asymmetric distribution. *Journal of Vibration and Acoustics*, vol. 127, pp. 556-565, 2005.

258 WAFO - Wave Analysis for Fatigue and Oceanography, ver. 2.1.1, Department of Mathematical Statistics, Lund University, SE, 2005.

259 Winterstein, S. R., Lange, C. H., and Kumar, S., Fitting: Subroutine to fit four-moment probability distributions to data SAND-94-3039, Sandia National Laboratories, 1995.

260 Meirovitch, L., *Elements of Vibration Analysis*, 2nd ed. McGraw-Hill, New York, NY, 1986.

261 Weaver W, Jr., Timoshenko, S. P., and Young, D. H., *Vibration Problems in Engineering*, 5th ed. John Wiley & Sons, Inc, 1990.

262 Spottswood, S. M., Wolfe, H. F., and Brown, D. L., The effects of record length on determining the cumulative damage of a ceramic matrix composite beam, *Sixth International Conference on Recent Advances in Structural Dynamics*, Southampton, UK, 1997.

263 Sweitzer, K. A. and Ferguson, N. S., Nonlinear random displacement and fatigue estimates using PDF transformations, *Ninth International Conference on Recent Advances in Structural Dynamics*, Southampton, UK, 2006.